This electronic thesis or dissertation has been downloaded from Explore Bristol Research, http://research-information.bristol.ac.uk

Author:
Levario Diaz, Victoria

Title:
Ultrasonic standing wave device for cellular and drug delivery applications and multipolar mitosis present in hPSCs

General rights
Access to the thesis is subject to the Creative Commons Attribution - NonCommercial-No Derivatives 4.0 International Public License. A copy of this may be found at https://creativecommons.org/licenses/by-nc-nd/4.0/legalcode This license sets out your rights and the restrictions that apply to your access to the thesis so it is important you read this before proceeding.

Take down policy
Some pages of this thesis may have been removed for copyright restrictions prior to having it been deposited in Explore Bristol Research. However, if you have discovered material within the thesis that you consider to be unlawful e.g. breaches of copyright (either yours or that of a third party) or any other law, including but not limited to those relating to patent, trademark, confidentiality, data protection, obscenity, defamation, libel, then please contact collections-metadata@bristol.ac.uk and include the following information in your message:

- Your contact details
- Bibliographic details for the item, including a URL
- An outline nature of the complaint

Your claim will be investigated and, where appropriate, the item in question will be removed from public view as soon as possible.

Ultrasonic standing wave device for cellular and drug delivery applications and multipolar mitosis present in hPSCs

Victoria Levario Diaz

A dissertation submitted to the University of Bristol in accordance with the requirements for the award of the degree of DOCTOR OF PHILOSOPHY in the Faculty of Science.

School of Chemistry, December 2020

Supervisors:

Professor M. Carmen Galan (School of Chemistry)

Dr Adrian Barnes (School of Physics)

Professor Rafael Carazo Salas (School of Cellular and Molecular Medicine)

Word count: 58,000

Abstract

Ultrasound-mediated devices are in rapid development to facilitate cellular trapping, manipulation and uptake of drugs in a non-invasive manner. However, the possible destructive effects that ultrasound and second-order factors i.e., cavitation, acoustic streaming, temperature and radiation forces have on the subjected (viable) cells are not fully known. A 1D ultrasonic device was designed and manufactured to explore particle and cell trapping using ultrasonic standing waves (USW). The operation and characterization of the ultrasonic device was carried out in order to obtain in a reliable cellular and microparticle trapping. Also, systematic optimisation studies were performed to evaluate cell viability and metabolic activity in a cancer cell line (HeLa) and in a healthy cell line Human Dermal Fibroblasts (HDF) as a function of time and applied voltage with a temperature regulator. The results demonstrate that high cell viability for both cell lines is achieved when the ultrasonic device is operated at the minimum trapping voltage while increasing in small steps 0.01 MHz the frequency to enhance the acoustic standing wave field at the trapping area. In addition, the optimised conditions to keep cell viability and metabolic activity close to control levels for both cell lines are 34°C with a driving voltage of 8 V_{pp} and acoustically exposed for 15 min. Furthermore, the mechanisms of particle uptake through ultrasound mediation are also not fully known, however, several studies suggest the involvement of a rearrangement of the cytoskeletal network as well as the particle internalization via endocytosis and transitional or lethal pore formation in the cell membrane. In this thesis, the dependence of cellular uptake depending on microparticle surface charge, employing the 1D custom-built ultrasonic device was investigated. Fluorescent carboxyl-polystyrene microspheres (~1μm) were coated with different formulations to obtain cationic, anionic and sugar-coated microspheres. The uptake of the conjugated microspheres by HeLa cells was evaluated using flow cytometry and, confocal fluorescence microscopy. Furthermore, transmission electron microscopy (TEM) was employed to visualize the cell's plasma membrane integrity after particle internalization. It was found that the cellular uptake by ultrasound exposure occurs through the transient formation of plasma membrane pores which reseal after treatment. Microparticle uptake of cells takes place via macropinocytosis and all treatments maintained their viability with no presence of toxicity from the conjugated microparticles. In general, this thesis highlights the importance of characterizing ultrasonic devices and the development of systematic and reliable acoustic protocols. In addition, it provided evidence of the mechanisms that support ultrasound-mediated delivery of microparticles.

Acknowledgements

Esta tesis se la dedico a mis papás, Guadalupe Diaz Montero y Victor Levario Medina y a mi hermano Bruno Levario Diaz, que siempre han estado apoyándome para cumplir mis sueños y alcanzar mis metas. Saben que son lo más importante en mi vida y que sin ustedes nada sería posible. Quiero que sepan que ustedes fueron mi motivación en todo momento y que mis logros son gracias a todos sus esfuerzos por darme todo lo que he necesitado y mucho más. Gracias por siempre brindarme su amor incondicional y saber que, aunque tenga muchos problemas, como fue el caso de esta experiencia, sin importar la distancia siempre estuvieron para mi dándome consejos e impulsándome a superarlos. Como diría el Dr Marcelo, hacen más falta papás como los de Bruno (y míos) ¡Los amo con todo mi corazón y muchas felicidades, lo logramos!

También se la quiero dedicar a mi pareja Laurens Jansen, que sin andar buscándonos nos encontramos en un punto intermedio y que desde entonces no nos hemos separado. Te quiero agradecer por todo tu apoyo durante todos estos años, sé que no ha sido nada fácil, pero lo logramos y espero que sigamos hacia adelante por mucho más tiempo. Que el cariño siga creciendo, que los logros individuales y conjuntos aumenten y que podamos disfrutar más la vida.

A mi gran amigo, Luis Felipe del Castillo que desgraciadamente falleció este año. Luisito como te diría mi tía Irma, *nos hizo falta tiempo*, como diría el también recientemente finado el gran maestro Armando Manzanero. Nos hizo falta vernos, reír, viajar, bailar y publicar más ciencia. No sabes el dolor que tengo de saber que ya no podremos realizar los planes que teníamos y de saber que no podremos festejar juntos el termino de mi doctorado. Te mando un gran abrazo hasta el cielo donde seguramente estarás bailando y gozando con nuestro gran amigo el señor Fares.

A mi madrina Margarita que desde que te perdimos dejaste un gran hueco en mi corazón. Todavía recuerdo el momento y lugar donde estaba cuando me entere y que lo ignore por que se me hacia una broma muy pesada. Ignore el comentario que leí por varios días y hasta que me lo confirmaron una o dos semanas después no lo asimile. Sigo pensando que pude haberte llamado, estar más al pendiente de ti, pero sabía que mi mama era tu apoyo y se me hizo fácil solo preguntar por ti. No sabes lo feliz que me hiciste cuando te despediste de mí y me dejaste con mucha paz con tu mensaje positivo durante el momento más difícil de mi doctorado. Se que nos sigues cuidando desde arriba y que nos volveremos a ver. Te mando un beso muy grande!

También quiero agradecer al Conacyt (México) por brindarme la oportunidad de estudiar en el extranjero y a toda la gente de México que con sus impuestos pude realizar mi sueño.

Mi doctorado fue la continuación de un cuento donde hubo una introducción, un nudo y un desenlace, pero más extendido y con eventos no tan buenos, pero al final se resolvieron gracias a mi familia y amigos. Primero fue mi introducción a un país extraño donde no se interactúa tanto como en mi bellísimo México, donde no es muy fácil que te ayuden, aunque te vean luchando y, que el color predominante es el gris. Mi introducción al mundo académico donde varias mentes, unas brillantes y otras no tanto, se reúnen y comparten ideas fantásticas para seguir impulsando la ciencia y el conocimiento, era hablado en otro idioma a mi lengua nativa. Introducción poco a poco de las personas que formarían parte de mi historia, de mis infortunios y mis éxitos. Aquí los personajes serian mis supervisores, Carmen, Adrian y en su principio Bruce y Monica Berry. Se darán cuenta que esta última se menciona con apellido y las razones vendrán más adelante. Este doctorado y la maestría antes realizada, fue empezado exactamente con mi introducción que Monica Berry hizo hacia Bruce, Carmen y Adrian con la propuesta de que una nueva estudiante de posgrado realizaría un proyecto excitante, donde ondas acústicas serian usadas para guiar células vivas y no dañarlas en el proceso. Esto se me hacía increíble y sacado de ciencia ficción ya que no tenía conocimiento previo de que las ondas acústicas ya eran utilizadas para otras aplicaciones como detectar defectos en materiales o que de hecho ya habían atrapado y guiado células vivas y más partículas.

Después de tener mi acercamiento a esta ciencia acústica y de realizar una maestría exitosa donde se me dio el titulo con distinción, decidí continuar con este proyecto tan excitante bajo la misma tutela, ya que pensaba que como me había ido tan bien durante la maestría entonces sería igual de increíble durante el doctorado. Sin embargo, un personaje, que a mi parecer perdió interés en la ciencia o en mí, eso no lo podría saber, pero Bruce acorto su estancia en esta historia ya que dejo de asistir a las juntas que ya no eran tan frecuentes para discutir mi progreso y los avances que iba teniendo. Este evento al principio me dejo desconcertada, pero sabía que podía pedir ayuda en el workshop de ingeniería con mi amigo Stan, aunque su nombre real es Miodrag Stanovich. Como su nombre era difícil de pronunciar todos lo conocen como Stan y él fue mi primer “salvador”. El me ayudo a diseñar y a fabricar el dispositivo ultrasónico y gracias a él, esta tesis pudo realizarse. Ya para ese entonces solo éramos 4 personajes, Carmen, Adrian y Monica Berry donde las discusiones de ciencia se volvieron platicas de dos amigos y de eventos que sucedían en la Universidad, pero no para todos los personajes. Carmen y yo hicimos un “click” y ella fue la me jalo e impulso a seguir trabajando en su laboratorio donde se encontraban personas maravillosas, entre ellas Imke, Sandra y David que siempre me apoyaron y como se verá más adelante, me defendieron ante el mal, de lo cual estoy agradecida con Carmen. Todo marchaba bien hasta que empezaron los cambios, más bien descontentos hacia mi persona por parte de Monica Berry. Todo esto empezó unos meses después de que empezara mi doctorado cuando me encontraba inmensamente triste porque no pasaría las vacaciones de invierno con mi familia en México y sumando los malos tratos hacia mi persona, se podría decir que me sentía miserable. Este sentimiento se prolongó con los comportamientos de Monica Berry que tenía hacia mí los cuales duraron **TRES AÑOS**. Durante ese tiempo iba sabiendo de las malas habladas que Monica Berry decía a mis espaldas como el que yo no era “buena”, sumando los gritos que sufría de la nada en medio de los pasillos, mis materiales que empezaron a “desaparecer” y “aparecer” en los botes de basura además mis células que cultivaba se empezaron a contaminar muy seguido. Al ver que estos eventos eran muy seguidos decidí hablar con Carmen naturalmente, ya que ella es la jefa del laboratorio donde yo estaba registrada pero también donde estaba trabajando Monica Berry que curiosamente ya estaba “retirada” desde que empecé el doctorado. Carmen tratando de no causar revuelto, y sumando a que Monica Berry ya no me quería en la oficina donde todos los estudiantes y postdoctorados trabajábamos, se decidió que lo mejor era que me cambiara de oficina la cual se encontraba al lado de la de Carmen. No fui a la única estudiante que se mudó en ese momento y aunque estaba más alejada de las personas con las que convivía, me sentía más tranquila. Sin embargo, el proyecto siguió siendo el mismo y por lo tanto la convivencia con Monica Berry fue la misma en el laboratorio donde cultivábamos las células y donde yo hacia todos mis experimentos. Recuerdo que sus modos de humor eran muy cambiantes y así como un día Monica Berry se veía contenta al otro estaba de mal humor. Se sabía que ella trataba muy bien a ciertos estudiantes, pero algo que note fue que eran todos varones.

Para no hacer la parte de terror más larga, decidí hablar con la directora mi programa doctoral, Annela para ver si se podía hacer algo o ayudarme de cierto modo porque ya no podía estar más en el mismo laboratorio trabajando al lado de Monica Berry con sus malos tratos. Su respuesta fue que aguantara y que hablara con Carmen para que se resolviera de algún modo. Su reacción fue muy desinteresada y distante pensando que, con darme unos chocolates, que no me acuerdo si los había comprado o se los habían regalado, mi llanto se borraría con mi memoria. Mas sin embargo eso no sucedió y no fue hasta que regresé de una de las únicas tres veces que fui en seis años, a ver a mi familia en mi bellísimo país que decidí poner una queja ante recursos humanos después de que Monica Berry una vez más me quería hacer la vida imposible. El camino para poner una denuncia no es fácil y menos si las personas designadas por la Universidad a ayudar, o ya no lo desempeñan o no se encontraban disponibles. Gracias al Profesor Mark de Life Sciences que me ayudo después de contarle esta historia. Su reacción nunca la olvidare, ya que se quedó con una mirada de ojos grandes y sacudía su cabeza todo el tiempo seguido de las palabras “no es posible”. Su primera pregunta hacia mi tampoco la olvidare y fue, como es tu relación con tu supervisor (Carmen)? A lo que yo respondí que era buena que no teníamos conflicto. Esto le impacto mucho más e inmediatamente estableció una comunicación vía email con las que es o era la encargada de recursos humanos de la Facultad de Ciencias, Stella. Ella respondió al email, pero mando a otra persona en representación, Laura, con la cual tuve una junta para explicar los hechos y razones de por qué ponía la queja contra Monica Berry. Su expresión ante lo contado tampoco la olvidare, y a partir de ese momento supe que lo más difícil estaba por venir. El proceso después de esa primera entrevista fue muy largo ya que duro desde finales de Febrero hasta a mediados de Julio donde la investigadora resolvió a mi favor después de escuchar los testimonios de mis amigos y compañeros que estuvieron presentes durante varios de los malos eventos. La Universidad me “regalo” un año más para compensar los años perdidos y poder acabar mi tesis doctoral. Para no hacer el cuento largo y ya para acabar esta historia quisiera agradecer con todo mi corazón a David por ayudarme a terminar mi doctorado, a Imke por brindarme su amistad y defenderme a capa y espada contra Monica Berry y a Sandra por su amistad, pero también por hacerme pasar ratos muy gratos sin parar de reír y sonreírle a vida a pesar de que las cosas no vayan muy bien.

Después de la resolución tuve que ir a terapia psicológica porque no me encontraba bien anímicamente y después de la primera evaluación donde resulto que mi condición era de moderada a grave, mis sesiones duraron por unos meses. Quiero enfatizar que todo esto sucedió en el extraño país y que mi familia no se encontraba físicamente cerca, pero si al mismo tiempo muy cerca de mi todo el tiempo con sus llamadas constantes de preocupación y con ganas de venir a salvarme. Gracias a ellos y por sobre todo a mi otro “salvador” de la historia, Terry McMaster, que me guio, ayudo, y estuvo en todas las juntas mientras se trataba de resolver esta situación conmigo, nunca bajaste la guardia. Terry, las palabras no me alcanzan para agradecerte por todo lo que hiciste por mí. Sabes que te considero mi amigo, un amigo que me trajo y estuvo cerca en toda mi duración en el Reino Unido y que espero que podamos seguir coincidiendo y comunicando. También quiero agradecer al Profesor Rafael Carazo Salas que fue mi último “salvador” al permitirme unirme a tu grupo sin conocer nada de mí, creo que viste en mis ojos una tristeza enorme y que tenía que salir del hoyo muy negro y profundo del que me encontraba al final de la resolución. Tu grupo también es maravilloso y tú eres un innovador que espero y pueda colaborar en un futuro contigo. Espero con ansias leer sobre tu ciencia y los avances que vayan realizando todos juntos.

Gracias Carmen y Adrian por ser los personajes principales que sin ustedes esto no hubiera sido posible y, aunque tal vez fueron momentos muy difíciles, podamos aprender de esta experiencia y asegurarnos que nadie más la viva. Gracias por su apoyo en la ciencia y creo que logramos tener resultados muy positivos al final y esperando publicar los que todavía nos faltan. Por último, agradecer a todas las personas que no pude mencionar por la falta de espacio que me ayudaron en todos estos años, con los que compartir y seguiré compartiendo experiencias, como Henkjan Gersen y Paul Verkade, mis dos profesores holandeses favoritos. Ojalá nuestros caminos se vuelvan a encontrar y que podamos reunirnos en persona sin el Coronavirus. Se que esta historia pudiera ser contada de manera diferente, ya que *cada quien la cuenta como le fue en la feria*, o podría ser censurada, pero creo que es importante que se sepa que estos eventos suceden y muy seguido en varias Universidades e Institutos de Investigación y que callar es lo peor que se puede hacer. Le dedico esta tesis también a todas esas mujeres en especial a las que dejaron la ciencia por discriminación, bullying o algún otro mal, esperando a que puedan regresar y continuar con sus estudios o trabajos en la ciencia.

ENGLISH VERSION: I dedicate this thesis to my parents and my brother who have always been supporting me to fulfil my dreams and achieve my goals. You know that you are the most important thing in my life and that without you nothing would be possible. I want you to know that you were and are my motivation at all times and that my achievements are thanks to all your efforts to give me everything I have needed and much more. Thank you for always giving me your unconditional love and knowing that, although I had problems, as was the case with this experience, regardless of the distance, you were always there for me, giving me advice and encouraging me to overcome them. As Dr Marcelo would say, more parents like Bruno's (and me) are needed. I love you with all my heart and congratulations, we made it!

I also want to dedicate it to my partner Laurens Jansen, who without looking for each other we found ourselves in an intermediate point and since then we have not separated. I want to thank you for all your support during all these years, I know it has not been easy at all, but we did it and I hope that we continue forward for much longer. May the love continue to grow, individual and joint achievements increase and that we enjoy life more.

To my great friend, Luis Felipe del Castillo, who unfortunately passed away this year. Luisito, as my aunt Irma would tell you, we needed time, as the great teacher Armando Manzanero, also recently deceased, would say. We needed to see each other, laugh, travel, dance, and publish more science. You don't know the pain I have of knowing that we will no longer be able to carry out the plans we had and knowing that we will not be able to celebrate the end of my doctorate together. I send you a big hug to heaven where you will surely be dancing and enjoying with our great friend Mr. Fares.

To my godmother Margarita, since we lost you, you left a big hole in my heart. I still remember the time and place where I was when I found out and that I ignored it because it made me very sad. I ignored the comment that I read for several days and until it was confirmed a week or two later, I did not assimilate it. I still think that I could have called you, be more aware of you, but I knew that my mother was your support, and it was easy for me to just ask about you. You don't know how happy you made me when you said goodbye to me and left me with a lot of peace with your positive message during the most difficult moment of my doctorate. I know that you continue to take care of us from above and that we will see each other again. I send you a really big kiss!

I also want to thank Conacyt (Mexico) for giving me the opportunity to study abroad and all the people of Mexico who, with their taxes, could make my dream come true.

My PhD was the continuation of a story where there was an introduction, a middle and a denouement, but more extended and with very bad events, but in the end, they were resolved thanks to the help of my family and friends. First it was my introduction to a strange country where people do not tend to interact as much as in my beautiful Mexico, where it is not very easy for them to help you, even if they see you struggling, and the predominant colour is grey. My introduction to the academic world where various minds, some brilliant and others not so much, get together and share fantastic ideas to continue promoting science and knowledge, was spoken in another language to my native language. Introduction little by little of the people who would be part of my story, my misfortunes and my successes. Here the characters would be my supervisors, Carmen, Adrian and initially Bruce and Monica Berry. You will notice that the latter is mentioned with a surname and the reasons will come later. This Ph.D. and the Master degree previously held, was started exactly with my introduction that Monica Berry made towards Bruce, Carmen and Adrian with the proposal that a new graduate student would carry out an exciting project, where acoustic waves would be used to guide living cells and not damage them in the process. This seemed incredible to me and out of science fiction since I had no prior knowledge that acoustic waves were already used for other applications such as detecting defects in materials or that in fact they had already trapped and guided living cells and more particles.

After having my approach to the acoustic science and completing a successful master's degree where I was awarded the title with Distinction, I decided to continue with this exciting project under the same tutelage, since I thought that how I had done so well during the master's degree then it would be just as amazing during the PhD. However, a character, who in my opinion lost interest in science or in me, I could not know, but Bruce shortened his stay in this story since he stopped attending the meetings that were no longer so frequent to discuss my progress and the advances that it was having. This event left me baffled at first, but I knew that I could ask for help in the engineering workshop with my friend Stan, even though his real name is Miodrag Stanovich. As his name was difficult to pronounce everyone knows him as Stan and he was my first "saviour". He helped me design and manufacture the ultrasonic device and thanks to him, this thesis could be done and finished.By then we were only 4 characters, Carmen, Adrian and Monica Berry where the science discussions became talks of two friends and of events that happened at the University, but not for all the characters. Carmen and I made a "click" and she was the pull me and the impulse to continue working in her laboratory where there were wonderful people, among them Imke, Sandra and David who always supported me and as it will be seen later, they defended me against him wrong, for which I am grateful to Carmen. Everything was going well until the changes began, rather unhappy towards me by Monica Berry. All this started a few months after I started my doctorate when I was immensely sad because I would not spend the winter holidays with my family in Mexico and adding the mistreatment of myself, you could say that I felt miserable. This feeling was prolonged by Monica Berry's behaviours towards me which lasted **THREE YEARS**. During that time, I was learning about the bad talk that Monica Berry said behind my back as the one that I was not "good", adding the screams that I suffered from nowhere in the middle of the corridors, my materials that began to "disappear" and " appear ”in the garbage cans and my cells that I cultivated began to be contaminated very often. Seeing that these events were very frequent, I decided to speak with Carmen naturally, since she is the head of the laboratory where I was registered but also where Monica Berry was working, which curiously had already been "retired" since I started my doctorate. Carmen trying not to cause a stir and adding to the fact that Monica Berry no longer wanted me in the office where all the students and postdocs worked, it was decided that the best thing was for me to change my office which was next to Carmen's. I was not the only student who moved in at that time and although she was further away from the people she lived with, I felt calmer. However, the project remained the same and therefore the coexistence with Monica Berry was the same in the laboratory where we cultivated the cells and where I did all my experiments. I remember that her moods were very changeable and just as one day Monica Berry looked happy the other, she was in a bad mood. It was known that she treated certain students very well, but one thing I noticed was that they were all male.

In order not to make the horror part longer, I decided to speak with the director of my doctoral program, Annela to see if something could be done or help me in a certain way because I could no longer be in the same laboratory working alongside Monica Berry with their mistreatment. Her response was for her to hang on and talk to Carmen to get it resolved somehow. Her reaction was very disinterested and distant, thinking that by giving me some chocolates, which I don't remember if I had bought them or given them to her, my tears would be erased by my memory. However, that did not happen, and it was not until I returned from one of the only three times, I went in six years, to see my family in my beautiful country, that I decided to file a complaint with human resources after Monica Berry once again I wanted to make my life impossible. The way to file a complaint is not easy, and less so if the people designated by the University to help, or no longer work or were not available. Thanks to Professor Mark from Life Sciences who helped me after telling him this story. I will never forget his reaction, as he was left with a big-eyed look and shook his head all the time followed by the words "not possible". I will not forget his first question to me either and it was, how is your relationship with your supervisor (Carmen)? To which I replied that it was good that we had no conflict. This impacted him much more and he immediately established a communication via email with whom she is or was the person in charge of human resources at the Faculty of Sciences, Stella. She responded to the email, but sent another person on her behalf, Laura, with whom I had a meeting to explain the facts and reasons why she was filing the complaint against Monica Berry. I will not forget her expression before what was said, and from that moment I knew that the most difficult was yet to come. The process after that first interview was very long since it lasted from the end of February to the middle of July where the researcher decided in my favour after hearing the testimonies of my friends and colleagues who were present during several of the bad events. The University "gave me" one more year to make up for the lost years and to finish my doctoral thesis. To end this story, I would like to thank David with all my heart for helping me finish my doctorate, Imke for offering me his friendship and defending me tooth and nail against Monica Berry and Sandra for friendship, but also for making me spend very pleasant moments without stopping to laugh and smile at life even though things are not going very well.

After the resolution I had to go to psychological therapy because I was not feeling well emotionally and after the first evaluation where it turned out that my condition was moderate to severe, my sessions lasted for a few months. I want to emphasize that all this happened in the strange country and that my family was not physically close, but at the same time very close to me all the time with their constant calls of concern and wanting to come and save me. Thanks to them and above all to my other "saviour" of history, Terry McMaster, who guided me, helped me, and was in all the meetings while it was trying to resolve this situation with me, you never let your guard down. Terry, words are not enough for me to thank you for everything you did for me. You know that I consider you my friend, a friend who brought me and was close throughout my duration in the United Kingdom and that I hope we can continue to coincide and communicate. I also want to thank Professor Rafael Carazo Salas who was my last “saviour” by allowing me to join your group without knowing anything about me. found at the end of the resolution. Your group is also wonderful, and you are an innovator who I hope and can collaborate with you in the future. I look forward to reading about your science and the progress that you are all making together.

Thank you, Carmen and Adrian, for being the main characters that without you this would not be possible and, although they were perhaps very difficult moments, we can learn from this experience and make sure that no one else lives it. Thank you for your support in science and I think we did it, we managed to have very positive results in the end, and we hope to publish the ones that are still missing.

Finally, thank all the people that I could not mention for the lack of space who helped me in all these years, with whom to share and I will continue to share experiences, such as Henkjan Gersen and Paul Verkade, my two favourite Dutch Professors. Hopefully our paths meet again and that we can meet in person without the Coronavirus. I know that this story could be told in a different way, since each one tells it as it was at the fair, or it could be censored, but I think it is important to let the reader know that these events happen and very often in various Universities and Research Institutes and that silence is what cannot be done. I also dedicate this thesis to all those women, especially those who left science due to discrimination, bullying or some other evil, hoping that they can return and continue their studies or work in science.

Author’s declaration

I declare that the work in this dissertation was carried out in accordance with the requirements of the University's *Regulations and Code of Practice for Research Degree Programmes* and that it has not been submitted for any other academic award. Except where indicated by specific reference in the text, the work is the candidate's own work. Work done in collaboration with, or with the assistance of, others, is indicated as such. Any views expressed in the dissertation are those of the author.

SIGNED: .... DATE: ....

Publications

The first chapters of this thesis are based on the following publications of which I am first author:

Chapter 2 & 3

V. Levario-Diaz, P. Bhaskar, M. C. Galan and A. C. Barnes (2020) Effect of acoustic standing waves on cellular viability and metabolic activity. *Scientific Reports*. **10**, 8493.

Chapter 4

V. Levario-Diaz, D. Benito-Alifonso, S. Medina, S. E. S. Michel, A. Leard, S. Cross, C. Neal, L. Sueiro-Ballesteros, A. Herman, P. Verkade, A. C. Barnes and M. C. Galan (2021) Acoustically enhanced cellular uptake of carboxyl-modified polystyrene microspheres using standing waves. *(to be submitted 2021).*

I have also contributed on the following publication during my PhD studies:

L. F. del Castillo, L. F. Martinez-Manzo and V. Levario-Diaz (2020) Thermodynamic Formulation of Living Systems and their Evolution II. *Journal of Modern Physics*. **11**, 1279-1300.

Table of Contents

Abbreviations

AB	- Alamar Blue
AM	- Acetoxymethyl
ANT	- Altered nuclear transfer
AS	- Araki-Sasaki human corneal epithelial cell line
BBB	- Blood-brain barrier
BSA	- Bovine serum albumin
$CDCl_3$	- Deuterated Chloroform
CIN	- Chromosomal instability
CRISPR/Cas9	- Clustered regularly interspaced short palindromic repeats
DLS	- Dynamic light scattering
DMEM	- Dulbecco's Modified Eagle's Medium
DMSO	- Dimethyl sulfoxide (DMSO)
DNA	- Deoxyribonucleic acid
ECM	- Extracellular matrix
EDC	- 1-ethyl-3-(3-dimethylaminopropyl)carbodiimide hydrochloride
EDTA	- Ethylenediaminetetraacetic acid
EM	- Extracellular matrix
ESC	- Embryonic stem cells
FBS	- Foetal bovine serum
FN	- Fibronectin
FUCCI	- Fluorescent ubiquitination-based cell cycle indicator
H2B-HaloTag	- Histone 2B – HaloTag
HCL	- Hydrochloric acid

HDF	- Human Dermal Fibroblasts
HeLA	- Human cervical cancer cell line
HIER	- Heat-induced epitope retrieval
hPSC	- Human pluripotent stem cell
HSQC	- Heteronuclear single quantum coherence
IF	- Immunofluorescence
IOBA	- human conjunctival epithelial cell line
iPSC	- Induced pluripotent stem cell
MDA	- Microtubule destabilising agent
MDCK	- Madin-Darby Canine Kidney
MTT	- 3-[4,5-dimethylthiazol-2-yl]-2,5-diphenyl tetrazolium bromide
MVA	- Mosaic variegated aneuploidy
MWCO	- Molecular Weight Cut Off
NMR	- Nuclear magnetic resonance
NSPC	- Neural stem / progenitor cell
PA	- Polyacrylamide
PBS	- Phosphate buffer saline
PBST	- Phosphate buffer saline tween
PCC	- Premature compaction
PDI	- Polydispersity Index
PEM	- Polymer electrolyte membrane
PET	- Polyethylene terephthalate
PI	- Propidium iodide
PIV	- Particle Image Velocimetry

PLL	- Poly-l-lysine
PMMA	- Poly (methyl methacrylate)
PPM	- Parts per million
PRF	- Primary radiation forces
PS-COOH	- Carboxyl polystyrene microspheres
PSC	- Pluripotent stem cell
PZT	- Piezoelectric transducers
ROCK	- Rho-associated protein kinase
SAC	- Spindle assembly checkpoint
SCNT	- Somatic cell nuclear transfer
SEC	- Secondary acoustic forces
SEM	- Scanning Electron Microscope
SRF	- Secondary radiation forces
TB	- Trypan Blue
TCPS	- Tissue culture polystyrene
TEM	- Transmission Electron Microscope
TTDDA	- 4,7,10-Trioxa-1,13-tridecanediamine
U2OS	- Osteosarcoma cells
UCA	- Ultrasound contrast agents
USW	- Ultrasonic standing waves

List of Figures

1 Introduction

This chapter is based on the first thesis topic – *Ultrasound*, and the principle is part of the work published in *Scientific Reports*[1] and work reported in Chapter 4 which will be submitted in due course[2] of which I am first author.

This thesis describes the progress in the manufacture, mode of operation and biological applications of a 1D ultrasonic device which will pave the way to future biomedical applications. Similar ultrasonic devices were previously developed and described at the University of Bristol; however, new advances and novel research are reported here. This first chapter gives an introduction to ultrasonics as a non-destructive research area and an overview of the physics behind the acoustic forces acting on the subjected objects. Furthermore, secondary factors (i.e., cavitation, sonoporation, streaming and temperature changes) produced by the acoustic waves are described in detail and explored in previous biological studies. An approach on how ultrasound is employed for mammalian cell trapping and manipulation with standing acoustic wave ultrasonic devices is reported, showing examples from previous work that successfully achieved the purpose of aligning and manipulating mammalian cells. In addition, a section on drug delivery using acoustic waves is described, differentiating between cavitation and sonoporation, secondary factor and ultrasound-induced effect that are commonly used for this purpose. The focus of this thesis is on the improvement in the manufacture and operation of the ultrasonic device and the exploration of its applications in trapping cells and delivering conjugated drugs to the cell. The advantages and limitations of the use of ultrasound devices in biomedical applications are reported by presenting the new research and the results done for this thesis.

1.1 Ultrasound history

Ultrasound, also known as *supersonics* in the early days, is the study of sound waves at frequencies above the average human hearing range, approximately 20 kHz, and their propagation in solids, liquids, and gases.[3-5] The history of ultrasound began in 1888, when the Curie brothers, discovered the direct piezoelectric effect by observing that when applying pressure to quartz, topaz and zincblende crystals an electrical surface charge was produced due to the mechanical stress and the polarization of the crystals (Figure 1.1 (**A**)).[85] Following the Curie brothers, G. Lippmann showed the converse or reverse piezoelectric effect when imposing an electric field on a crystal and observing its mechanical deformation and compression (Figure 1.1 (**B**)),[86,90] proportional to the imposed electric field. The word "piezo" derives from the Greek that means "press" and therefore the word piezoelectricity means "pressure electricity".[87] This ability of the crystals/materials to vary their electric polarization in response to the electrical/mechanical stress is called piezoelectricity.[88] The electric polarization is the result from the displacement of the negatively charged electrons in relation to the positive nuclei of the atoms, as depicted in Figure 1.1,[88] meaning that the material adapts to the perturbation by changing the position of the electrons and the nuclei resulting in the creation of dipoles.[85] The first time piezoelectricity was employed as an investigative tool was in 1894 when Marie Curie used a solution of piezoelectric quartz crystal in an ionization chamber to measure, with a quadrant electrometer, the radioactivity of uranium salts.[90]

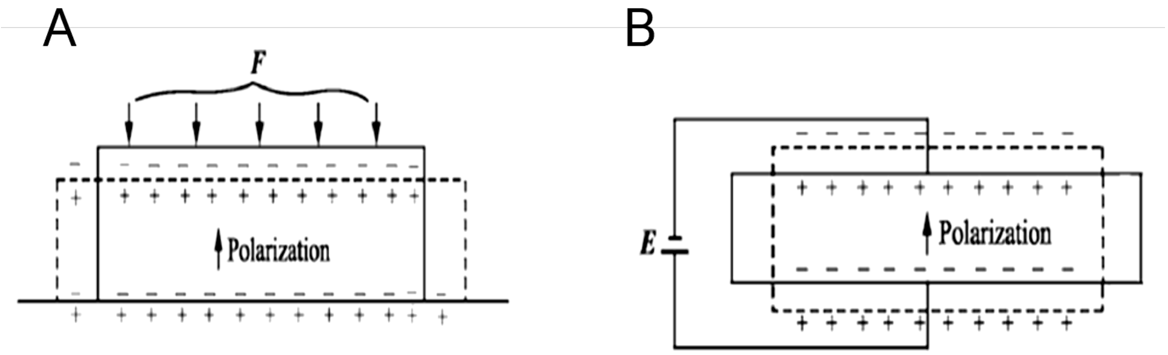

Figure 1.1: Piezoelectric effects. (**A**) Direct piezoelectric effect where an external force (*F*) is acting on the crystal. (**B**) Converse piezoelectric effect where an electrical field is acting on the crystal. Adapted from reference 88.

In World War I, ultrasonics became a subject of scientific research when in 1918 a French scientist named Langevin invented a 50 kHz vibrating ultrasonic transducer, *hydrophone*, for submarine detection, crediting him as the father of ultrasonics.[89] Later, from 1929 to 1935, Sokolov employed ultrasound waves to detect defects in metals and in 1935, Mulhauser used two piezoelectric transducers to detect internal flaws in solids, obtaining a patent.[3] Finally, in 1942 and 1945, Firestone and Simons, respectively, developed a pulse ultrasonic testing to localise ships by applying the sonic depth principle. After 1945, ultrasound was accepted as a very practical tool and became an established non-destructive technique.[3]

Piezoelectric materials are a type of dielectric material which can be polarised in the presence of an electrical field or mechanical stress. Ultrasonic transducers are the sound source and are piezoelectric ceramics that convert electrical energy to mechanical energy due to the applied electrical voltage across the material causing the transducer to vibrate (converse piezoelectric effect) and vice versa (direct piezoelectric effect) when detecting its echo back (Figure 1.1).[87,95] These vibrations create an acoustic waveform with compression and rarefaction zones (high- and low-pressure regions) (Figure 1.4 (**B**)) representing an elastic wave,[91] some examples are depicted in Figure 1.3. Moreover, the nature of these vibrations is sinusoidal as the path in function of time is a sine wave, as shown in Figure 1.4 (**C**).[92] Piezoelectric transducers (PZTs) are excited, and the acoustic waves are able to propagate when a coupling agent or glue is used[95] between the piezoelectric elements and the material to be inspected or boundary.

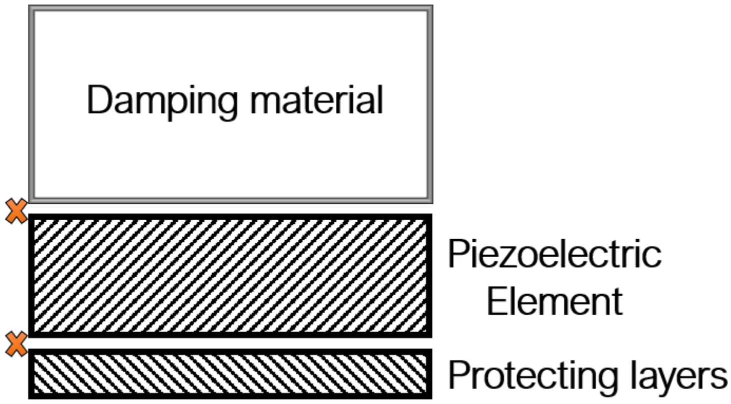

Figure 1.2: Typical piezoelectric element employed in ultrasonics. The layout of the mounting of a piezoelectric element using a damping material at the back of the transducer and the orange “X” are depicting the electrodes position. Adapted from reference 95.

Ultrasonic waves are elastic waves and need a medium in which they can propagate and be transmitted. The particles do not travel with the mechanical wave, they oscillate around their resting point and vibrate backwards and forwards (compression and rarefaction) in the direction or perpendicular to the wave motion.[89,92] Ultrasonic waves can be classified according to the direction of oscillation of the particles such as longitudinal waves where the particles oscillate in the same direction as the wave propagation (Figure 1.3 (**A**)). These waves are also called compressional or pressure waves because of the high- and low-pressure active regions. In the transversal or shear waves the particles oscillate perpendicular to the wave propagation due to a periodic shear force (Figure 1.3 (**B**)).[92,93] For these specific type of waves, the shear force is replacing the acoustic pressure of the longitudinal wave and is defined as the force per surface area. Longitudinal and transverse waves are plane waves, waves where the *phase* (i.e., the particles remain in the same state of motion) of the oscillation is the same as the propagation plane.[92]

The plane waves discussed above are thought to travel in unlimited cavities, however, when the propagation of the waves is disturbed by a limited cavity the travelling paths become more complex due to reflection and refraction of the waves. This limitation of wave propagation led to an additional classification of ultrasonic waves. Surface or Rayleigh waves, named after Lord Rayleigh, are the waves formed at the flat or curved boundary surfaces. The particles oscillatory motion is circular or elliptical due to a combination of longitudinal and transverse waves. Moreover, the amplitude of the wave decreases below the surface meaning that when the depth is on the order of the wavelength, the particles are at their resting position. Plate waves are similar to the surface waves but are generated when the thickness of the material is of a few wavelengths. There are several types of plate waves being Lamb waves the most common one. Lamb waves propagate parallel to the surface of the material and occur in two different modes, symmetrical or dilatational and asymmetrical or bending wave.[89,92]

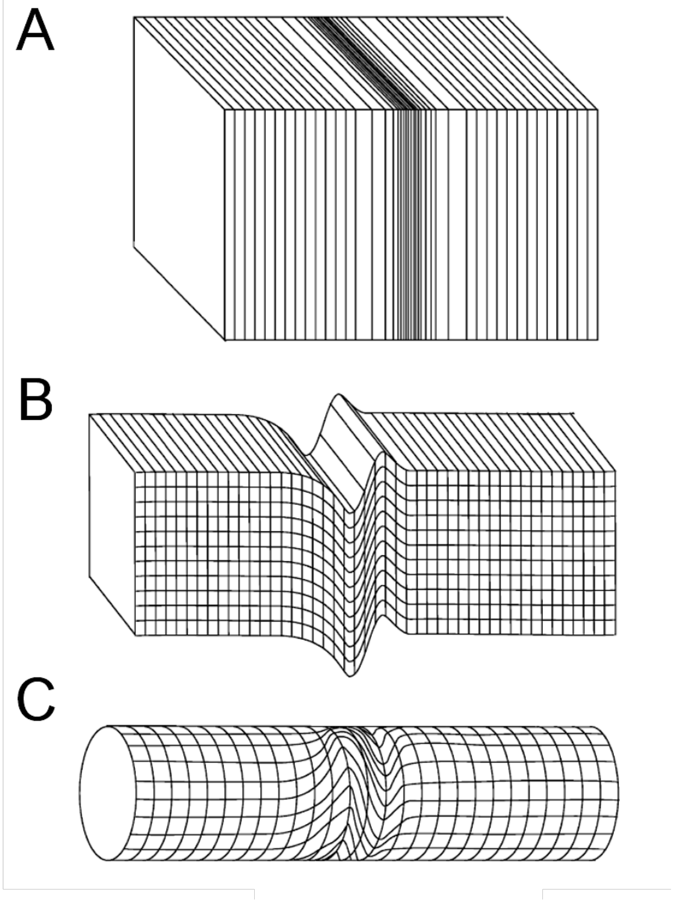

Figure 1.3: Acoustic waveforms. (**A**) longitudinal plane wave with compression and rarefaction zones, (**B**) shear transversal wave and (**C**) torsional wave. Adapted from reference 91.

The waves described above are examples when a single frequency is driven for a long period of time, however, if two sound waves are driven at the same frequency and amplitude but travelling from opposite directions, a standing wave is generated. A standing acoustic wave can also be generated by the constructive interference of the reflected sound wave between two solid planes traveling back and forth producing resonance (Figure 1.5) and the fundamental resonance is when the distance is separated by $\lambda/2$.[93] Both travelling waves or superimposed waves are longitudinal waves and the motion or displacement points where the waves cancel each other are called nodes while the regions of maximum amplitude are called antinodes. When the particles move towards the displacement nodes, the density and pressure of the particles are positive, while the counterpart is when the density of the particles decreases at the antinodes of motion creating a negative pressure. In terms of acoustic pressure, the motion antinodes coincide with the pressure nodes as the pressure is always zero and the particle density does not change (Figure 1.4 (**D**)).[92] When subjecting microparticles, microbubbles or mammalian cells to ultrasonic standing waves (USW) they will be directed to the pressure or antipressure nodes depending on their density by the acoustic radiation forces (explained in Section 1.1.1). These waves are widely used for particle, bubble and cell manipulation, separation and agglomeration,[94] further explained in the following sections.

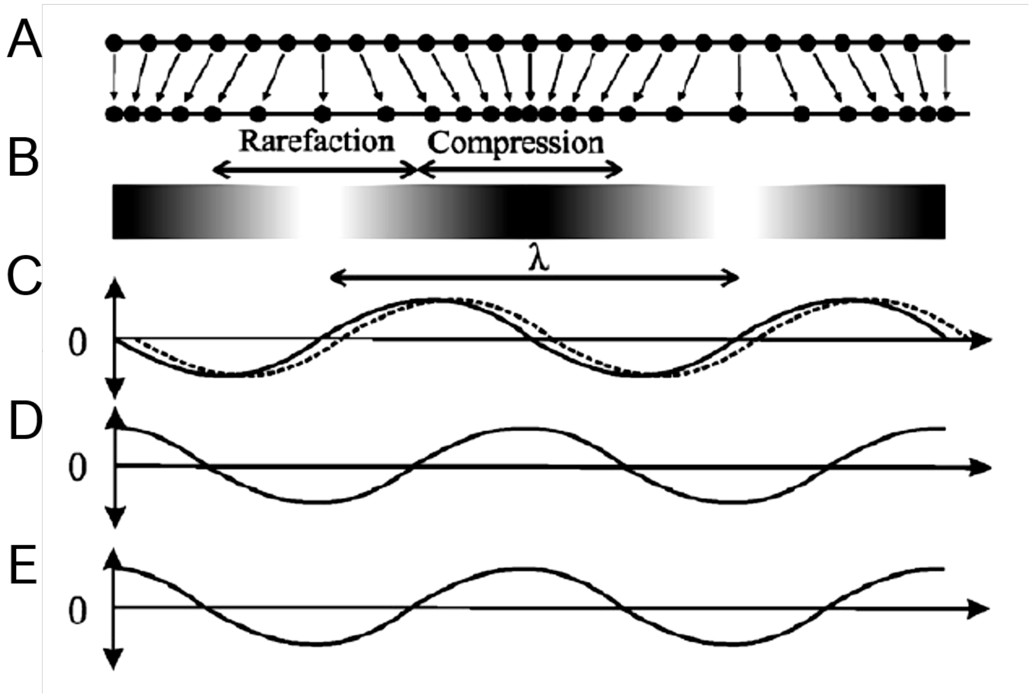

Figure 1.4: One-dimensional longitudinal wave at a single frequency. (**A**) The particles in the medium are at the equilibrium position and (**B**) displacement of the particles when the longitudinal wave is traveling through the medium depicting the high- and low-pressure zones where the darker regions are showing a higher particle density. (**C**) the sine wave representing the displacement of the particles and the separation of a wavelength between two equal motion states. (**D**) represents the acoustic pressure and (**E**) the particle velocity in the longitudinal wave. Adapted from reference 91.

The parameters of an ultrasonic wave are f*requency*, which is the number of complete oscillations for any given particle per second; *wavelength* which is the distance between two points where the particles of the medium are in the same motion state (i.e., compression) (Figure 1.4 (**C**)) and is inversely proportional to the frequency (i.e., at higher frequencies there will be shorter wavelengths). Another parameter is the *speed of sound* which is the velocity of the wave propagation, related to the wavelength and the frequency,[92,93] given by

$$c = f\lambda \tag{1}$$

As mention previously by exciting a piezoelectric transducer an ultrasonic wave is generated. By setting up multiple transducers different waves (i.e., standing acoustic waves) are generated even if excited at their resonant mode. When exciting continuously the piezoelectric transducers, an overheat can occur specially for the piezoceramic type as their polarization is lost.[93] These effects, time of ultrasound exposure and temperature, and how they impact ultrasonic devices are further explained in Section 1.1.4.

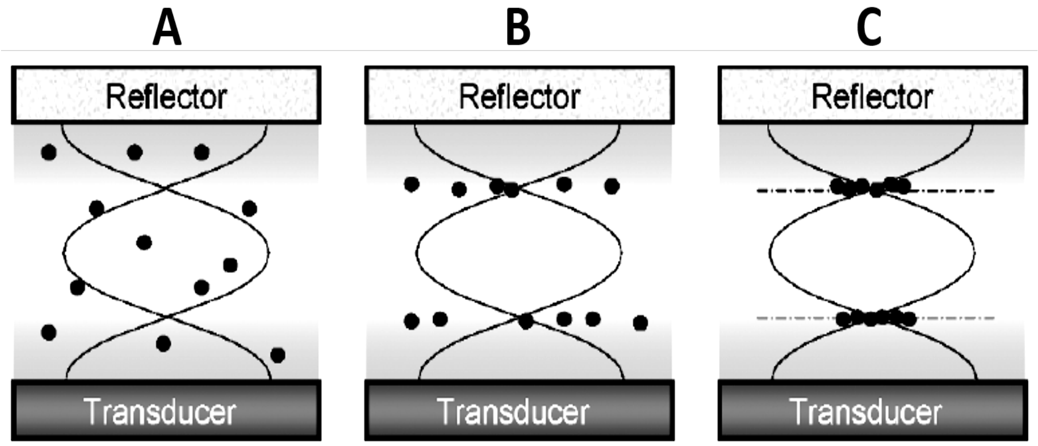

Figure 1.5: Particles guided and trapped in the pressure node of a standing acoustic wave. (**A**) a transducer is excited, and the longitudinal wave is being reflected forming a constructive interference. (**B**) the particles, denser than the host fluid, will be directed towards the pressure nodes of the standing acoustic wave and (**C**) particle agglomeration will be formed due to the secondary radiation forces. Adapted from reference 61.

1.1.1 Acoustic radiation forces

Acoustic radiation forces are an acoustic phenomenon that has been known to affect suspended particles within an ultrasonic field since the 19th century when Kundt and Lehman[61] acoustically trapped cork dust in a glass tube using standing acoustic waves.[62] The first demonstration of the biomedical application using acoustic radiation forces was done by Dyson, Woodward and Pond in 1971 by trapping erythrocytes *in vivo* in blood vessels separated by half a wavelength.[59,60] Particles in suspension drift, clump, attract or separate and repel each other due to hydrodynamic forces better known as acoustic radiation forces.[67] A change in the momentum of the traveling waves and the energy density produces acoustic radiation force similar to the electromagnetic waves. This phenomenon occurs due to reflections, scattering or absorption from the particles or the traveling waves.[62] The acoustic radiation forces which are experienced by the particles can be generated in both traveling and standing waves due to the nonlinear interaction between the scattering waves of the particles and the acoustic waves.[63] However, the radiation forces are greater in a standing acoustic field and therefore the focus is towards this type of acoustic waves due to their possible applications.[61,63]

Acoustic radiation forces are divided into two types, primary radiation forces (PRFs) and secondary inter-particle forces. Single cells are first subjected to PRFs moving towards the pressure nodes or antinodes of the standing acoustic waves and can form aggregates when attracted to each other or repel from each other due to the inter-particle secondary radiation forces (SRFs), [67] as shown in Figure 1.6.[94] In 1934, King[64] was the first to provide calculations of the primary radiation force for incompressible spherical particles suspended in a non-viscous fluid under the action of standing and traveling waves.[65] Kings' theory stated that rigid spheres will either move to the pressure antinode or node depending on the "relative density factor"[61] which is the relation between the density ratios of the host fluid and the particle. According to the predictions, the particle is incompressible if the density ratio between the particle and the fluid is less than 0.4 and the particle will move to a pressure antinode, whereas for ratios higher than 0.4 the almost-rigid particle will move towards the pressure node (depicted in Figure 1.7). Kings' approach is in agreement experimentally for solid particles in gas suspensions, however, it is not the case for particles that are not considered rigid in comparison to the host fluid.[61] Following and extending Kings' work, Yosioka and Kawasima provided an analysis for compressible particles, an important aspect for microbubble study in a resonant cavity.[65,66]

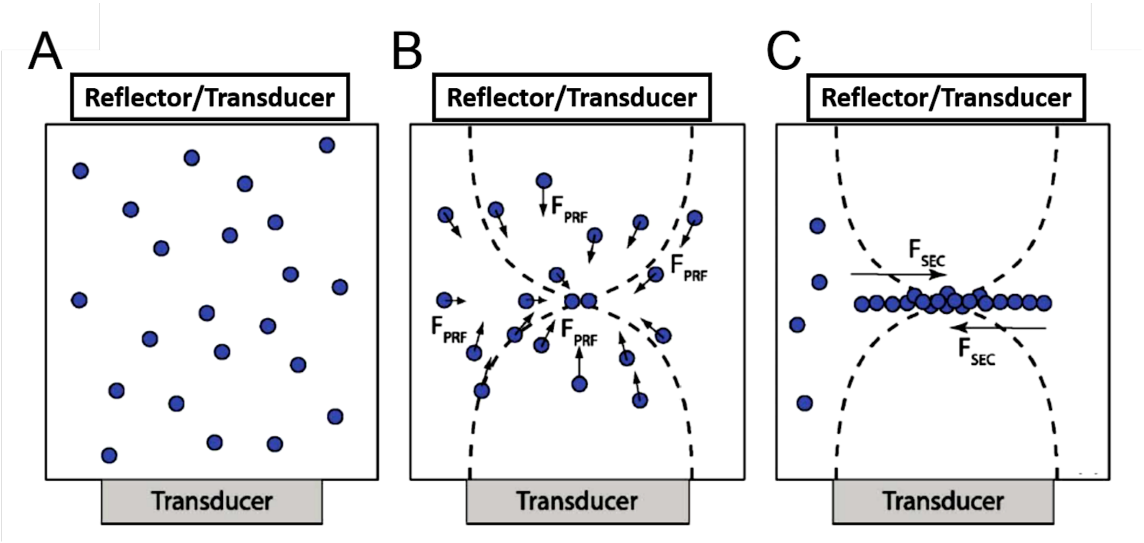

Figure 1.6: Acoustic radiation forces. (**A**) one transducer is excited and (**B**) the particles in the host fluid will be directed towards the pressure nodes (or antinodes for microbubbles) of the USW by the axial and lateral F$_{PRFs}$. (**C**) Secondary acoustic forces (F$_{SEC}$) contribute to the particle agglomeration. Adapted from reference 94.

They formulated an expression for a spherical particle in a 1D standing acoustic wave as

$$F_{AX} = 4\pi k \varepsilon r^3 \Phi(\beta, \rho) \sin(2kx) \tag{2}$$

where this time-average expression is given for a spherical particle with a radius of r at the position x and an acoustic energy density of ε. Moreover, the acoustic contrast factor $\Phi(\beta, \rho)$ and is given by

$$\Phi(\beta, \rho) = \frac{\rho_p + \frac{2}{3}(\rho_p - \rho_f)}{2\rho_p + \rho_p} - \frac{\beta_p}{3\beta_f} \tag{3}$$

Where ρ and β are the mass density and compressibility of the particle (p) and the host fluid (f). Compressibility, β, establishes the PRFs direction and is related to the speed of sound (c) as $\beta = \frac{1}{\rho c^2}$, additionally, the wave number (k) is same as $2\pi/\lambda$.[61] The theory of the radiation force relies on the summarized and generalized work of Gor'kov (1962),[68] who made an equivalent formulation to Yosioka and Kawasima, but derived a time-average radiation force $(F(r))$ relating the gradients of kinetic (E_{kin}) and potential (E_{pot}) energy densities on small spherical particles to a volume (V) in a position (r)[63] within a non-viscous fluid in an acoustic standing wave field:

$$F(r) = V\nabla\left(\frac{3(\rho_p - \rho_f)}{(2\rho_p + \rho_f)}E_{kin}(r) - \left(1 - \frac{\beta_p}{\beta_f}\right)E_{pot}(r)\right) \tag{4}$$

where V is the volume of the sphere, denoted by $4\,r^3/3$. E_{kin} and E_{pot} are factored by acoustic velocity and pressure in the standing acoustic wave weighted by functions of particle and fluid densities (ρ) and compressibility (β), respectively.[63] If the energy terms (E_{kin}, E_{pot}) are replaced by a rigid boundary ($x = 0$) then

$$E_{kin}(x) = \varepsilon \sin^2 (kx) \tag{5}$$

$$E_{pot}(x) = \varepsilon \cos^2 (kx) \tag{6}$$

The above theory only considers non-viscous fluids and thus Westervelt[69] extended this theory to be applied to viscous fluids where the relationship between the viscous drag and scattering forces from the rigid sphere are considered. Also, Doinikov[70] established a general derivation for acoustic radiation forces in viscous and thermally conducting fluids for both traveling and standing acoustic waves, adding divergent spherical fields. The formulation showed that for a rigid sphere and liquid drops that are compressible the viscosity and thermal effects are minor in a standing wave.[71,72]

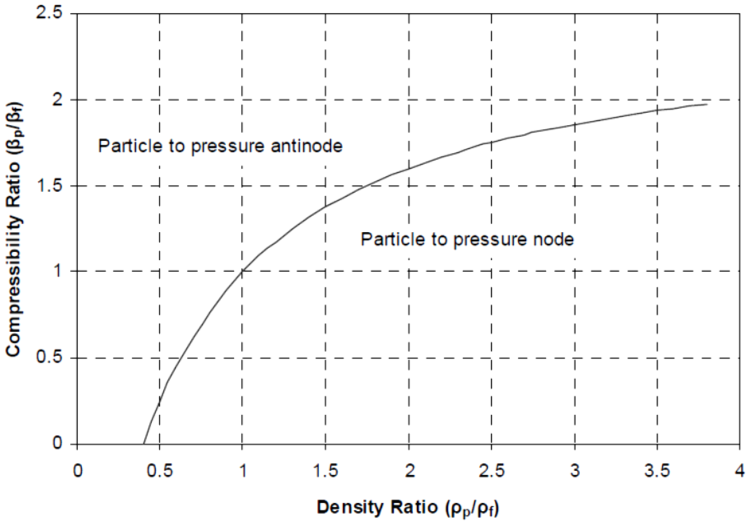

Figure 1.7: Plot as a function of density and compressibility of particle (ρ_p, β_p) and host fluid (ρ_f, β_f). Adapted from reference 61.

Suspended particles trapped under a standing acoustic field not only experience axial PRFs, which first direct the particles to pressure nodes or antinodes, but there are also lateral forces that move the particles to specific positions within the nodes that Schram referred to as hot spots.[61,73] The lateral forces can be generated by a source heterogeneity,[74] reduction of the localised energy density at the edges,[75,76] near-field effects produced by the interference patterning in different device geometries,[77] or due to the dimension of the acoustic mode (2D or 3D).[78] These forces may be desirable for particle trapping, however, detrimental effects can occur in the device operation. For a certain device geometry, there will be energy gradients in a *z* direction generated perpendicular to the standing wave and based on those gradients, lateral forces can be expressed as[79,80]

$$F_{Lat} = V\nabla\left(\frac{3(\rho_p-\rho_f)}{(2\rho_p+\rho_f)}\cos^2(kx) - \left(\frac{\beta_f-\beta_p}{\beta_f}\right)\sin^2(kx)\right) \tag{7}$$

This formulation states that the lateral radiation forces will direct particles considered as incompressible and dense, in relation to the host fluid, towards the maximum energy density points.[79]

In addition to the primary radiation forces (PRFs), the particles experience secondary forces from neighbouring particles. These forces are called secondary radiation forces

(SRFs) and are caused by the scattering waves from adjacent particles.[65] Furthermore, these interparticle forces become important when the distance between the particles decreases and scale up with the volume of two adjacent particles (α^3 indicates the radius in the case that both particles are the same size in Equation (8)).[80] Weiser *et al*[81] formulated an equation, based on the work of Crum,[82] combining the forces of a rigid spherical particle and a compressible particle where the radius of the particles and the distance between them is less than the acoustic wavelength and can be expressed as as[83]

$$F_{sec} = 4\pi\alpha^6 \left(\frac{\left(\rho_p - \rho_f\right)^2 (3\cos^2\theta - 1)}{6\rho_f d^4} \mathrm{v}^2(x) - \frac{\omega^2 \rho_f (\beta_p - \beta_f)}{9d^2} \mathrm{p}^2(x) \right) \tag{8}$$

where α is the radius of the particle, d is the interparticle distance, ω is the angular frequency and θ is the angle between the line of two particles and the centre line where the particle is trapped in the pressure node in the direction of the propagating acoustic waves, as shown in Figure 1.8.[80] The negative sign in the middle of the equation suggests an attractive interaction between particles, while for a positive sign it will be a repulsive force. Moreover, the first term of Equation (8) depends on the difference in density of the particles and the amplitude of the particle velocity $\mathrm{v}(x)$, while the second term refers to the difference in compressibility of the particles and the pressure amplitude of the acoustic waves $\mathrm{p}(x)$. The left density-based term depends on the angle (θ) which can scale strongly with the interparticle distance. As this is a velocity-dependent term, it decreases as the particle is being trapped in the pressure antinode which is the velocity node, which is significant for microbubble and lipid vesicle studies, and vice versa for solid particle studies where the particles are in the pressure nodes. When the particle is trapped in the pressure node the force will be attractive as the particle is trapped perpendicular to the direction of the wave propagation (θ= 90°) and will be repulsive when the particles are aligned in the same plane as the standing wave propagation (θ= 0°). The right compressibility-dependent term is the attractive force as the pressure is not affected by the orientation of the particle trapping.[80,83]

SRFs are usually very weak and are mainly present when the distance between the particles is very small, thus they are important in aggregation and sedimentation applications. After the PRFs guided the particles to the pressure nodes, the aggregates will enlarge and settle at the bottom of the device due to the forces of gravity dominating over the buoyancy. Additionally, these forces are also known as Bjerknes secondary forces named after C.A. Bjerknes and son V.F.K. Bjerknes, who were the first to study these forces theoretically and experimentally using bubbles.[84] Crum followed Bjerknes studies with bubbles under acoustic exposure and Weiser *et al* experimentally trapped red blood cells and investigated SRFs.[81,84]

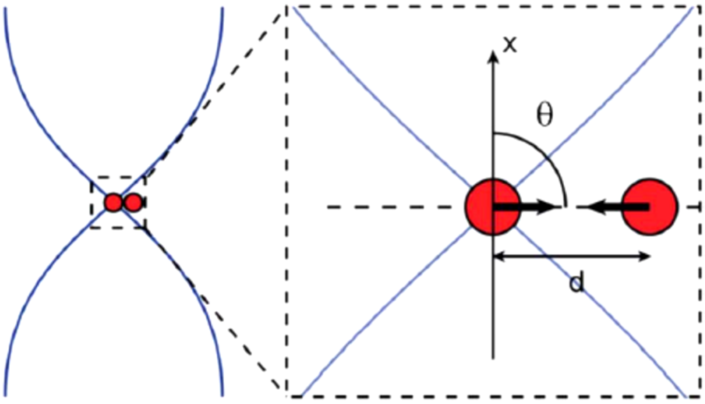

Figure 1.8: Secondary forces can cause agglomerates when the distance (d) between them reduces. The angle (θ) is indicated as half of the distance between the particles and the central line of the trapped particle in the pressure node. Adapted from reference 80.

1.1.2 Acoustic streaming

As mentioned previously, in standing wave ultrasonic devices the cells or particles are subjected to 2 main forces: acoustic radiation forces, explained above, and acoustic streaming related to the Stokes drag force.[14] Acoustic streaming is an ultrasound-induced second-order effect characterized by the energy, generated by the piezoelectric transducer, that is absorbed at the boundaries of the device and the bulk of the fluid.[5, 22] There are three types of acoustic streaming[23-25,5] that can affect particle trapping and manipulation: wavelength scale Rayleigh streaming,[3,5,27] boundary scale Schlichting streaming and cavity scale Eckart streaming, as shown in Figure 1.9 (**A**-

C). [3,5,28] Rayleigh streaming is generated when the energy is dissipated in the viscous boundary layer creating vortices on the scale of $\lambda/4$ and moving away the particles from the pressure nodes. [3,5,29] In 1945, Lord Rayleigh showed that the plane of the standing wave is confined in parallel to the walls and the $\lambda/4$ counter-rotating vortices are formed in the direction of the nodal planes.[3] Schlichting streaming or microstreaming forms a vortex flow inside the viscous boundary layer. The vortices are formed with a certain thickness up to twice the boundary layer.[3] These two types of streaming can occur at the same time and are driven by the absorbed energy in the boundaries of the device or near the surface of an oscillating bubble, most likely to be observed in ultrasonic microfluidic devices.[5, 26] Eckart streaming, also known as the ''quartz wind'', is generated when the energy is absorbed in the bulk of the fluid and the vortices are formed perpendicular to the front face of the piezoelectric transducer or the adsorber/reflector. For this type of streaming, energy absorption is required to occur over distances larger than the microfluidic scale; normally the fluid cavity length scale (l) is greater than the wavelength of the acoustic wave (λ), meaning $l >> \lambda$.[6,7]

Acoustic radiation force (F_{ra}) in Eq. 2 (Section 1.1.1) has to be strong to maintain the particles and cells trapped in the pressure nodes and not to be influenced by the streaming.[3] Acoustic device geometry, material properties and particles sizes are aspects to consider if the acoustic streaming-induced drag is not desirable when performing *in vitro* studies. Furthermore, the velocity of acoustic streaming depends on the properties of the employed fluid (viscosity, acoustic attenuation and the sound velocity) but also depends on the frequency, intensity and pressure amplitude.[10-12] This means that by increasing the viscosity of the fluid the acoustic streaming velocity will decrease and if the acoustic attenuation increases the velocity will increase as well.[12,13] Additionally, if the frequency is increased then the velocity will increase due to the increased energy transfer.[12] Bernassau *et al.*, [5] showed that Eckart streaming is the mechanism that can disturb particle manipulation within a multi-transducer ultrasonic device. They reported that this type of disturbance can be minimized either by reducing the size of the resonator or by reducing the depth of the fluid-filled cavity by adding a layer of epoxy at the bottom of the acoustic device.[5,8,9]

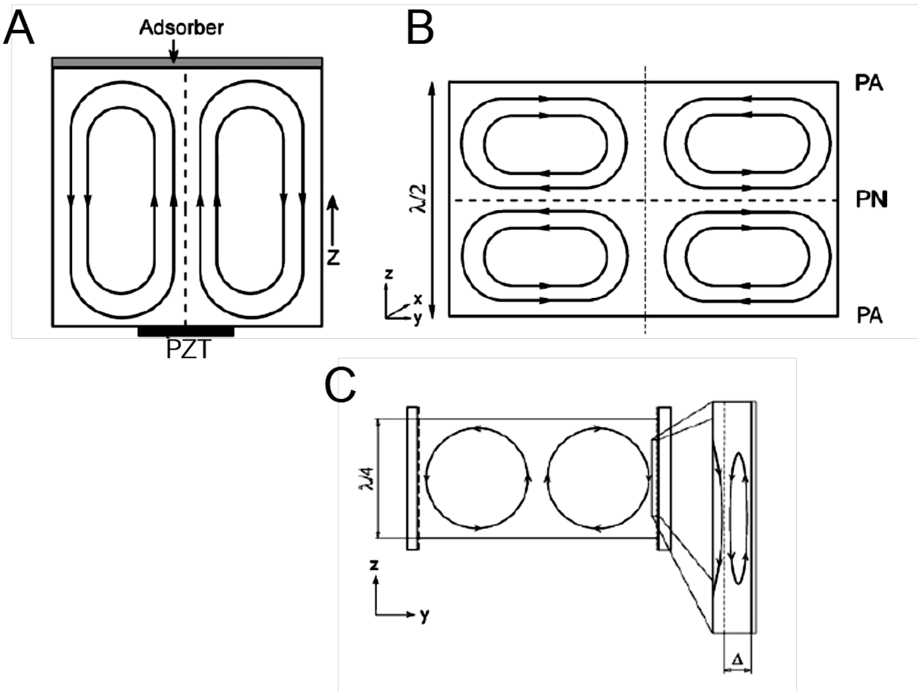

Figure 1.9 Diagram of the three different types of acoustic streaming. (**A**) Eckart streaming or "quartz wind", (**B**) Rayleigh streaming with vortices in λ/2 standing wave acoustic resonators and (**C**) Schlichting microstreaming formed at the boundary of the device depicted as Δ the thickness of the vortices. Adapted from references 3 and 4.

In standing wave ultrasonic devices, Schlichting streaming in combination with Rayleigh streaming can occur at the boundaries if the standing wave is parallel to the surface (along the *x* axis), as shown in Figure 1.10 (**A**). The pressure and antipressure nodes are fixed in the standing wave resulting in a steady viscous flow close to the boundaries of the cavity creating first a strong inner boundary layer streaming and moving towards the bulk of the fluid establishing an outer boundary layer streaming, Schlichting and Rayleigh, respectively. Boundary layer streaming generation depends on the wavelength (λ), the length scale of the device (h) and the viscous penetration depth (δ_v), meaning $\lambda >> h >> \delta_v$. The viscous depth depends on the kinematic viscosity (v) and the angular frequency (ω) of the acoustic wave.[15,17] This means that if the size of the fluid-filled cavity is reduced, the boundary layer streaming will be more pronounced, but the velocity will decrease.[15,18] Eckart streaming can also occur in a standing wave acoustic field due to the loss of acoustic energy over long distances, forming a jet in the bulk of the fluid and a steady flux.[15] However, the velocity will be slower because the Reynolds stress (parameter to describe flow characteristics)[7] generated in opposite directions will be steady and cancelling each other according to Wiklund *et al* [15] and Mulvana *et al*.[16]

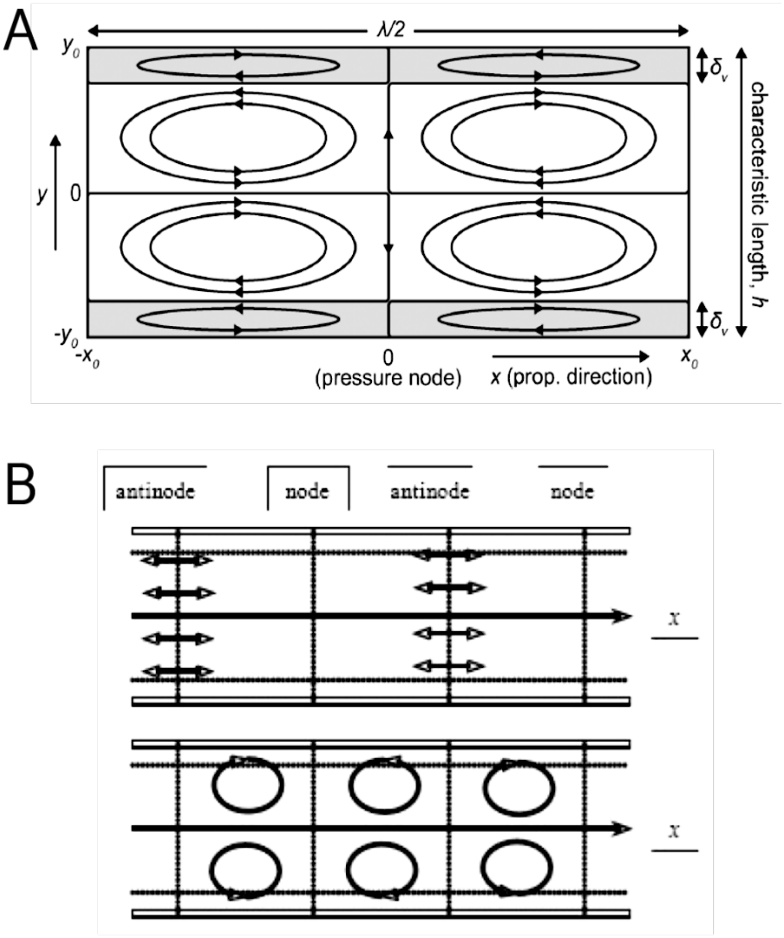

Figure 1.10: Acoustic streaming in an acoustic standing wave of *λ/2* cavity. (**A**) Thickness of Schlichting streaming vortices (in grey zones) and Rayleigh streaming vortices (white zones). The pressure node is represented as “0”. (**B**) The period of a standing wave is double in comparison to the counter-rotating vortices of the acoustic streaming. Adapted from references 7 and 15.

Acoustophoresis (acoustic motion of particles) has shown that acoustic streaming will dominate over the acoustic radiation forces when the particles are smaller than the wavelength (*λ*) or below 1μm.[14,19] Although in most of the *in vitro* studies acoustic streaming is not wanted, there are cases where the streaming induced drag can be used in a positive way. Cavitation microstreaming, which is the flow at the boundary layer of an oscillating microbubble produced by the viscous dissipation, is an example of a beneficial application of acoustic streaming that can enhance drug delivery into the cells.[7,20-21] Moreover, the shear stress of the microstreaming generated by the oscillating bubbles can produce transitional cell membrane pores with a mean size from nanometres to a few micrometres, termed sonoporation and further discussed in Section 1.1.3, increasing membrane permeability and thus the interaction between the cells and drugs.[7,]

1.1.3 Acoustic cavitation and sonoporation

Acoustic cavitation is the formation of oscillating gas bubbles. These microbubbles can be generated from pre-existing gas nuclei or gas bodies that stabilised in cracks of the impurities located in the fluid.[22] The gas inside the cracks of the impurities expands when the pressure of the fluid decreases forming microbubbles.[22,23] This unique phenomenon of ultrasound is a nonthermal interaction between the gas bubble and the propagating high-amplitude acoustic waves.[24] The microbubbles shrink and grow in accordance to the high and low pressure zones, compression and rarefaction respectively (Figure 1.11 (**A**)).[27] There are two types of cavitation microbubble movement: stable and inertial cavitation.[29] Stable cavitation or activation of the gas body is where the size of the microbubble is stable while it is subjected to periodic oscillations approximately at its resonant size, where the gas influx and gas efflux occurs in the expansion and compression zones, respectively, as shown in Figure 1.11 (**B**).[25,29] This type of cavitation allows the microbubble to oscillate for several cycles and not violently collapse, causing less damage to the exposed cells or tissue during sonoporation (Figure 1.12 (**A**)).[22] Inertial cavitation or transient cavitation is where the size of the microbubble can expand rapidly to a maximum radius and violently collapse even after 1μs of a single acoustic exposure leading to stronger biophysical damage to the cells (Figure 1.11 (**C**)).[22,25,28] Normally high ultrasound intensities are required for the gas body to activate in the inertial cavitation where it can be considered as gas nuclei because its smaller than the resonant size and this unstable gas body can fragment and generate more cavitation nuclei due to the high pressure and temperature inside the gas body. [29,30] During this inertial cavitation, the pressure and temperature concentrated in the microbubble can reach very high MPa and several degrees Kelvin that after collapsing, dissipates into the bulk of the fluid.[27] Moreover, the violent and asymmetric collapse of these microbubbles near the cells can generate microjets of liquid that travel at high speed where, in addition to permeabilizing the cell membrane, it can also cause detrimental effects on them (Figure 1.12 (**D**)).[27,31] The biological effects of these oscillating microbubbles to the subjected cells are due to the shear stress created by the micro-streamings surrounding the bubbles,[25] as shown in Figure 1.12 (**B**), specially at higher amplitudes where the shear stress can caused cell membrane rupture.[27] Inertial cavitation can also disrupt cells by significantly damaging organelles, like mitochondria, lysosomes, and dilating the rough endoplasmic reticulum, as shown in electron microscopy images.[25,53-55] This cavitation can also cause cell lysis, mainly in cells that undergo mitosis,[25,52] since the size of the pores reaches several microns, compared to stable cavitation that only reaches hundreds of nanometres.[25]

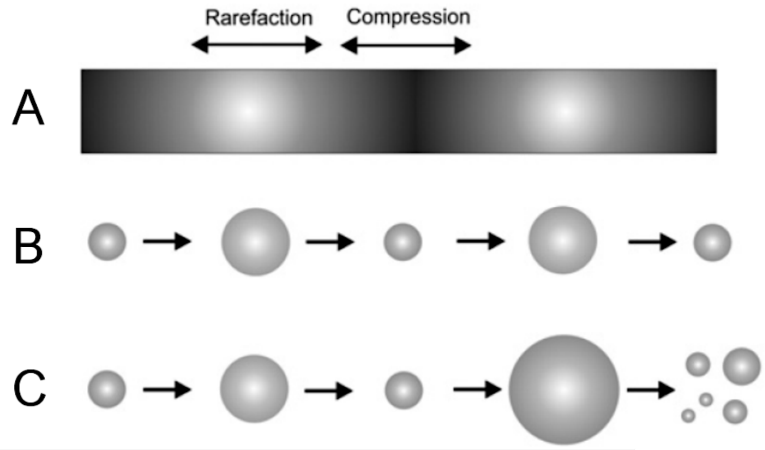

Figure 1.11: Acoustic cavitation where (**A**) is representing the acoustic pressure of a sound wave. (**B**) shows a stable cavitation and (**C**) shows an inertial cavitation of microbubbles. Adapted from reference 25 and 26.

The acoustic parameter that controls the microbubble response from stable to inertial cavitation is the pressure amplitude and the transition pressure is called inertial cavitation threshold.[22,23] Furthermore, the translational motion of the microbubbles within the acoustic field is the Bjerknes force[32-35] which in terms of pressure gradient is expressed as:

$$F_B = -\langle V \nabla p \rangle \tag{9}$$

where V is the volume of the microbubble and p is the acoustic pressure that would exist in the liquid at the centre of the microbubble. Bjerknes force is the average of the buoyancy force that is exerted on a bubble within a flowing fluid.[32,36] In standing waves, primary Bjerknes force occur where the bubbles, smaller than the resonant size, move to the pressure antinodes and, inversely, when the bubbles are larger than the resonant size, aggregates are in the pressure nodes.[32,37,38] This was first proved experimentally by Crum and Eller in 1970 where the velocities of the bubbles, smaller than the resonance size, translational motion were measured to the pressure antinodes[39] and is used to study single-bubble sonoluminescence, which is the light emission when the gas bubble collapse, employing acoustic levitation.[40]

New therapeutic methods have been reported employing gas-filled microbubbles encapsulated by a shell of lipids, proteins or polymers known as ultrasound contrast agents (UCAs).[25,41,42] These modified stabilised microbubble suspensions are used for diagnostic imaging, intracellular drug delivery and gene therapy which is facilitated by the transient pore formation in the cell membrane called sonoporation.[27] Sonoporation is an ultrasound-induced effect where the permeability in the cell membrane is increased by the stress waves (shock waves) caused by acoustic cavitation (Figure 1.12 (**C**)).[24] In addition, the change in permeability in the cell membrane can modify the ion exchange, where at an ultrasound exposure of 1.8 MHz a decrease in potassium ions was observed, leading to a sublethal alteration in the fibroblast cell membrane.[25,56] Sonoporation is not only caused by cavitation bubbles, but also by large molecules/particles that can cause sublethal damage to the cell membrane; however, a membrane reseal is followed by transient damage that increases cell survival. The membrane resealing has been reported to occur on the order of milliseconds to seconds after the ultrasound exposure is finished,[25,43-45] and it was shown that the cell membrane potential was restored after the decrease in calcium levels within the cell caused by the membrane pores.[25,43-46]

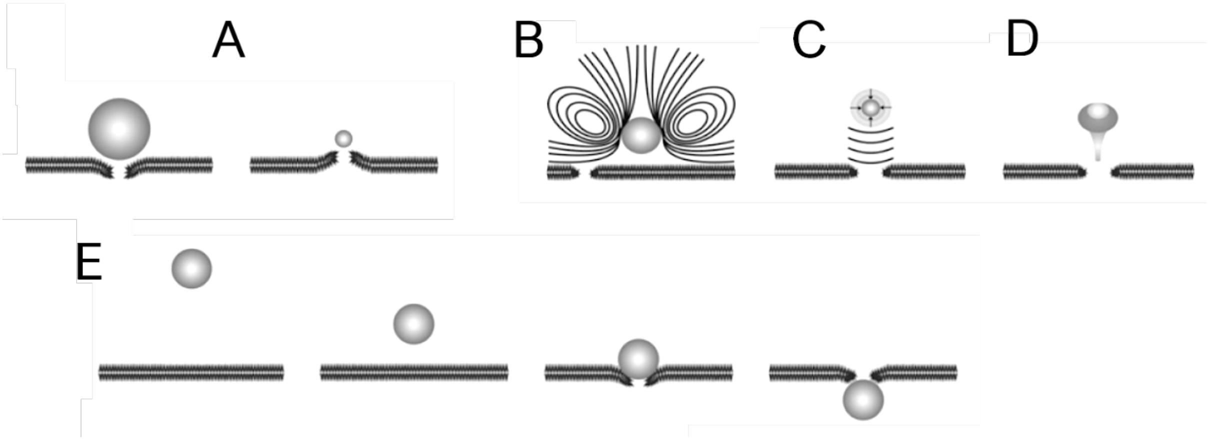

Figure 1.12: Microbubble stable and inertial cavitation cell membrane effects. (**A**) Cell membrane disturbed by the pushing and pulling movements of the bubbles during the rarefaction and compression zones in stable cavitation. (**B**) Microstreaming caused by the microbubble in a stable oscillation generating pores in the membrane. (**C**) Membrane rupture caused by shock waves when the microbubble collapse and (**D**) the formation of a liquid jet when the bubbles collapse asymmetrically, both in inertial cavitation. (**E**) During stable oscillations, acoustic radiation forces displace the microbubbles pushing against the cell membrane disrupting it with longer acoustic pulses. Adapted from reference 25 and 51.

The first Scanning Electron Microscope (SEM) images of cells showing pores in the cell membrane after low frequency ultrasound exposure were taken by Tachibana *et al*.[25,47] Moreover, endocytosis has been reported to be enhanced by ultrasound exposure in the absence of microbubbles.[25,48-50] In these studies, acoustic streaming may have been the main force acting as low intensities and high frequencies were applied where acoustic cavitation does not normally occur. This is a possible explanation where microstreaming and acoustic streaming can cause fluid phase endocytosis stimulation due to shear stress.[25,57] Another possible explanation is the rearrangement of the cytoskeleton occurs due to the plasma membrane deformation caused by the mechanical forces induced by ultrasound.[25,58] These changes in plasma membrane tension are detected by integrins and ion channels and directly influence subsequent intracellular processes, such as endocytosis and exocytosis, and can restore the plasma membrane. In the case of integrins which are transmembrane linkers between extracellular matrix (ECM) with the cytoskeleton, especially with bundles of actin filaments, can initiate a signalling cascade influencing endocytosis and exocytosis. Moreover, the binding and affinity between the specific ligands with the integrins depend on the cations (Ca^{2+} or Mg^{2+}) from the extracellular environment which lead to the Ca^{2+} influx and efflux mediated by the ion channels. Ion channels are transmembrane proteins that maintain homeostasis in the cell and their interaction with the external environment and thus respond to chemical or mechanical signals. When the membrane is ruptured by the shear stress produced by ultrasound, the levels of Ca^{2+} inside the cell increase due to passive diffusion, however, it has also been shown that the influx of Ca^{2+} is necessary for the resealing of the membrane.[25,122] Cell membrane ruptures with pores smaller than 0.2μm are believed to reseal by endocytosis as the tension stress on the cytoskeleton opposes the sealing. Furthermore, it has also been reported that exocytosis is triggered by ultrasound due to the influx of Ca^{2+} proposing that produces a relaxation in the membrane that facilitates repair where intracellular vesicles are recruited to the rupture site, fusing with each other and forming a larger vesicle to cover the wound, as observed by Schlicher *et al*[121]in Transmission Electron Microscope (TEM) images. This repair mechanism by exocytosis is proposed for larger membrane ruptures although the resealing of the membrane is not yet well understood.[25]

1.1.4 Acoustic exposure and temperature changes and their effect in mammalian cells

Temperature can increase when using acoustic devices as ultrasonic energy propagates through an attenuating material. This attenuation is the decrease of the pressure amplitude and depends on the absorption and scattering of acoustic waves as they travel through a medium. Absorption occurs when part of the mechanical energy is converted into heat and the scattering is when part of that mechanical energy changes direction.[96] The acoustic devices typically used for particle and mammalian cell trapping and manipulation are made of low-loss materials (i.e., glass and silicon) therefore the absorption is thought to be small when operating the PZTs at frequencies of 1-10 MHz.[97] Furthermore, the increase in temperature may be due to the dissipation of energy by the PZTs and the heat loss in the glue layers or polymer-based layers between the materials that support the acoustic resonators, therefore absorption by the host fluid and the layers of the device can occur, causing bioeffects on the subjected mammalian cells.[61,97] The properties of the materials and the layers used for the acoustic device, the input power, the size of the acoustic device and the material of the transducer are the parameters that will give the thermal behaviour of the acoustic device.[61] The increase in temperature can change the resonance frequency and, therefore, the performance of the ultrasonic device, as previously demonstrated by Augustsson *et al*,[98] where temperature changes of approximately 2°C / min promoted a shift of resonance peaks of around 1 kHz / °C and a temperature change of around 5°C can change the resonance modes. To tackle this issue, a Peltier element was attached to the bottom of the acoustic device to regulate the temperature by cooling down or heating up the system when necessary.

In general, mammalian cells have a broader tolerance for different temperature ranges compared to the body/tissues (Figure 1.13). For instance, it ranges from cryopreservation, which is a technique for storing cell lines in liquid nitrogen, to high temperatures where it can be lethal to the body but not to individual cells.[97,99] In particular for *in vitro* studies, heat shocks of a few degrees above the optimum temperature are required for protein expression and stability. Therefore, if the temperature rises and exceeds the optimal threshold, changes in the conformation of the proteins and incorrect folding can occur. These effects have an impact on various cellular mechanisms and internal responses that can lead to cell cycle arrest, slow growth,[97,100] reorganization of the cytoskeleton or organelle fragmentation[97,101] even though the cell membrane appears to be intact.

The tolerable temperature for mammalian cell studies is in the range of 33-39°C, however, the bioeffects above this range on individual cells depend on several factors such as exposure time, heating rate and cell type.[97] The temperature rise in the host fluid will be prolonged if the heating rate is greater than the rate of heat removal,[96] where the effects can range from increased cellular metabolic activity or cell cycle rate to denaturation of proteins and cell death.[97] Furthermore, at the sub-physiological temperature range (33-37°C), the biological effects may not be detrimental, since Al-Fageeh *et al*[102] reported that the "cold shock" responses of cultured cells can lead to a modulation of the transcription and translation processes and, therefore, the modification of cell metabolism, the cell cycle and the cytoskeleton. The exposure time factor in this temperature range is very important since in short period of times, although cell proliferation can decrease while maintaining cell viability, cell death can occur over prolonged periods if keeping the temperature below 33°C.[97]

When applying an ultrasound field to cultured mammalian cells, particular attention should be paid to the temperature in the trapping area. As mentioned above, acoustic resonance can be altered with increases in temperature, and therefore the device performance. Different strategies have been reported where a fan, a water circuit system or a Peltier element[98] were used to control the temperature. However, the temperature-controlled system depends on the size of the acoustic device and the rate of temperature rise.

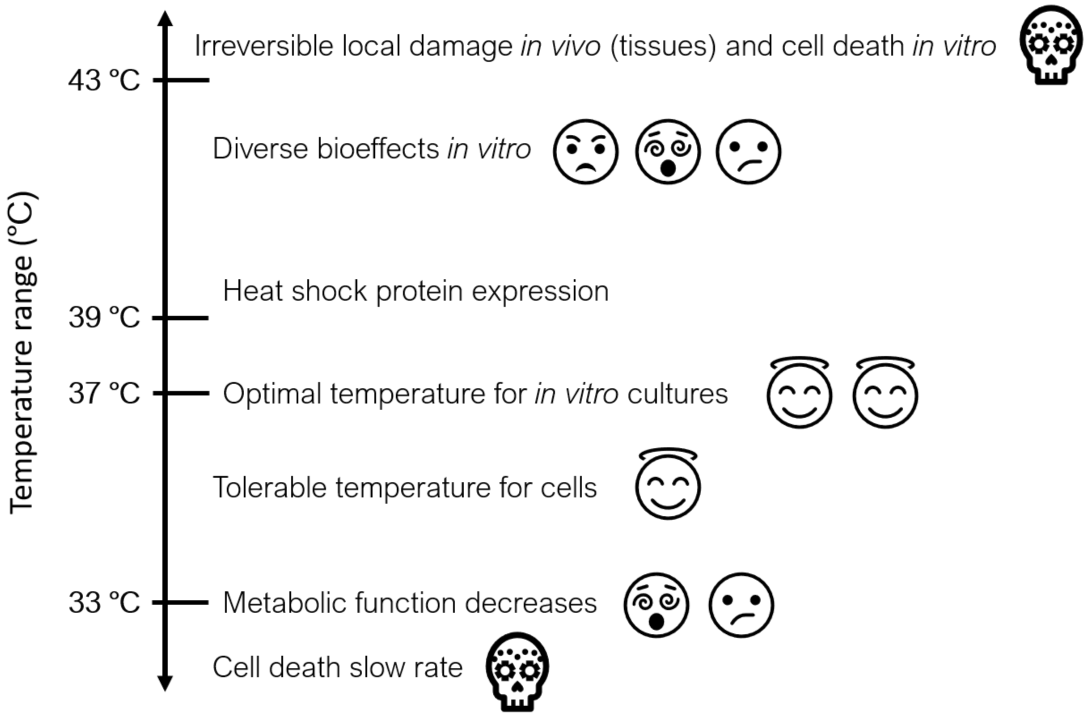

Figure 1.13: Bioeffects for mammalian cells according to the temperature range for *in vitro* studies. Adapted from reference 97.

Wiklund[97] has mentioned that for temperature increases of no more than 10-15ºC, the ultrasonic device should be operated at room temperature and when there are small increases in temperature generated by the ultrasonic field, this should be combined with an external heating system as long as the temperature in the trapping area it is kept at 37ºC. Furthermore, to monitor the temperature in the device, a thermocouple probe can be placed near the device or as Evander *et al*[103] demonstrated, rhodamine

B can be used to measure the temperature directly with the cells by measuring the fluorescence of the rhodamine, although thermocouple probes are more accurate.

During inertial cavitation, the effects are generally violent reaching high temperatures that can lead to cell destruction and eventually death. Also, the repetitive oscillation cycles of the microbubble in a stable cavitation can generate heat and microstreaming.[22,23] that is known to cause cell damage if the exposure is continuous. The magnitude of the high energy associated with inertial cavitation is comparable to ionizing radiation, which is capable of removing electrons from atoms,[97,104] and has been reported to cause Deoxyribonucleic acid (DNA) breaks or even necrosis. A problem with this type of cavitation is the ability to distinguish between the effects associated with cavitation and the thermal effects associated with the operation of the ultrasonic device. Therefore, it is important to maintain an optimal and constant temperature to maintain both the performance of the ultrasonic device and the viability and health of the cells and their environment.[97]

1.2 Ultrasound for particle and mammalian cell trapping

The increasing demand for controlled and precise manipulation of cells and particles has driven researchers to develop new microtechnologies in order for a better understanding of fundamental biological and chemical processes.[105,106] Contact-mediated force methods like micropipettes[107] and atomic force microscopy[108] are being used, however, damages in cell structure are observed and are not suitable for handling large particle amounts.[106] Therefore, moderate force micromanipulation techniques without physical contact are desirable where the particles are directed to a state of equilibrium, such as hydrodynamics, optical tweezers,[109] dielectrophoretic, magnetic and ultrasonic trapping[110] for biomedical and tissue engineering applications.

In particular, non-contact trapping and manipulation of mammalian cells and microparticles employing USW acoustic devices,[111] have been shown to be a low-cost and easy-to-assemble method.[110] Compared to other non-contact techniques, ultrasound trapping is non-invasive and large numbers of mammalian cells and particles can be trapped or manipulate simultaneously in short periods of time.[110]

Baker[115] and Coakley[116] showed that by employing USW red blood cells are trapped and separated in suspended fluids (Figure 2.1 in Chapter 2). Hertz,[117] Wu and Du[118] demonstrated the trapping of micron-sized particles employing two focused ultrasonic beams (Figure 2.2 in Chapter 2) where the latest also trapped frog eggs in clusters. However, for these early acoustic devices, no manipulation of microparticles was done and bulky systems were employed. Furthermore, in the late 90s Saito *et al*[119] employed USW for polymer composite fabrication after the trapped particles of various materials solidified and was one of the first examples for material fabrication.

Although acoustic trapping first emerged as a levitating tool nearly 50 years ago by NASA and ESA (European Space Agency) operating at frequencies in the range of kHz as a container-less technique.[112] However, it was not until the 1990s that Trampler *et al*[113] used a continuous flow acoustic levitation device to investigate transient hybridoma cell aggregates trapped in a contained chamber for antibody production. This flow-through device maintained almost 99% viability of the treated cells and antibody production of 5-fold increase was observed. Similar devices were reported by Doblhoff-Dier *et al*[114] where a single chamber and a two-chamber flow-through devices were developed in a layered piezoelectric configuration. The novelty of these devices was the introduction of an integrated cooling circuit system to reduce local thermal effects and therefore, ideal for long-term studies (Figure 1.14). Furthermore, an increase in cell viability and cell separation was reported added to the fact that large amounts of cell volume could be analysed. However, it was not until the early 2000s that acoustic trapping devices began to be scaled down for microscopic studies to be translated into portable applications.[94]

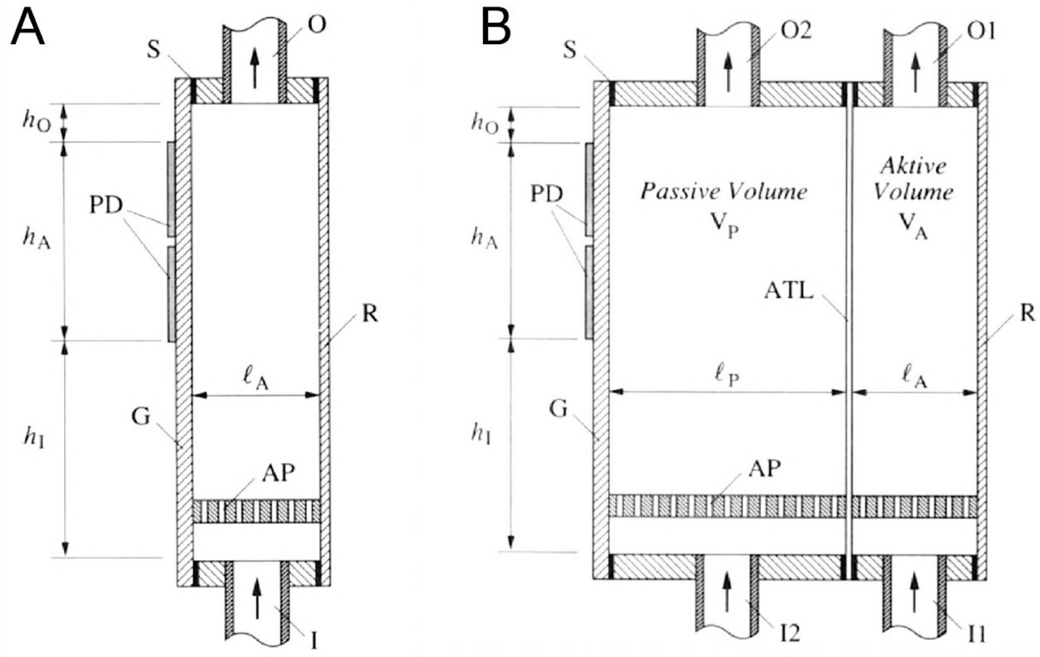

Figure 1.14: Flow-through acoustic devices with (**A**) one chamber and (**B**) two chambers. Similarities in both resonators are piezoelectric disks (PD) placed in the side of the glass (G). A reflector (R) was placed opposite the PD and the resonator was sealed (S) with a Viton rubber. The active volume (V_A) in both chambers were connected to a thermostat bath (not shown). The cooling water is running through the passive chamber (V_P) and the cells are trapped in the V_A. A CO_2 inlet was attached to the V_A (I1) to regulate the pH. Adapted from reference 114.

Drinkwater[120] made a recent classification of the dynamic acoustic manipulators employed for cellular and microparticle trapping into three main groups: acoustic beam, planar and in-plane manipulators. The first examples of acoustic manipulators mentioned above used focused acoustic beams to trap microparticles and cells which lead to bulkier acoustic systems due to the distance between the focus point and the transducers.[94] This class of acoustic manipulators requires two focused beams to be placed face to face to produce a standing acoustic wave due to the interference. Counter-propagation wave interference is similar to 1D plane acoustic traps, further explained; however, the main disadvantage is the application of beam manipulators due to the size required for the PZT assembly to trap the particles. Hence, in recent years new acoustic beam manipulators have been developed similar to optical tweezers employing high frequencies (< 200 MHz) with a low focal length to aperture size (*F*-number) and demonstrated to trap microparticles and single cells. (Figure 1.15

(**A**)).[120] Acoustic microbeam manipulators can also be used to explore the mechanical properties of individual cells, as shown by Hwang *et al*[123] by trapping a functionalized microparticle attached to the surface and measuring the stretching of the cell towards the microparticle. The costs of manufacturing the acoustic beam manipulators and the operation frequencies, normally from 30-200 MHz, have made the reports of studies and applications low, however, it is expected that their cost will be lower over time and that the demand will increase since their operating mode is more reliable.[120]

A similar beam manipulator has been developed by Baresch *et al*[124] but positioning the transducers in an array to create a 3D acoustic trap (Figure 1.15 (**B**)). In contrast to the acoustic beam manipulator operating in the Mie scattering regime, the scattering of particles whose diameter is greater than the wavelength, the array acoustic device operates in the Rayleigh regime, where the diameter of the particle is much less than the wavelength.[125] Moreover, the beam manipulator operates at high frequencies trapping the microparticles and cells against the surface while the array device operates at low frequencies creating an acoustic vortex in an axial 3D plane.[120]

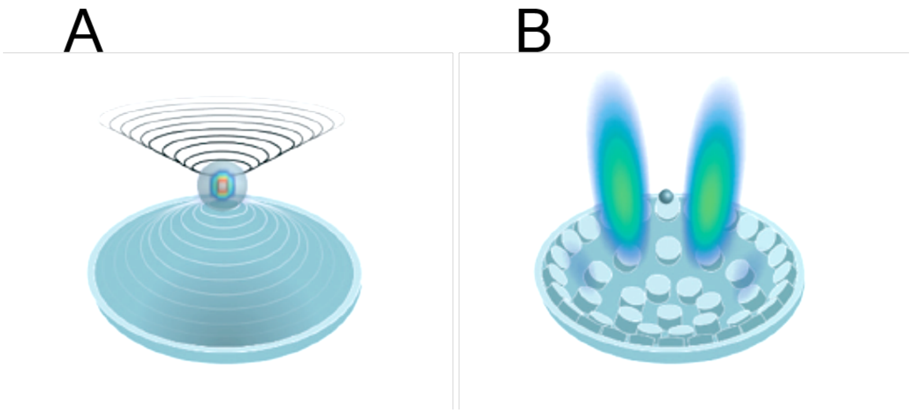

Figure 1.15: Vertical (**A**) micro-beam acoustic manipulator and (**B**) array acoustic manipulator. Adapted from reference 120.

Another classification of acoustic manipulators are the plane array or lateral manipulators. This type of acoustic manipulators were first introduced by Kozuka *et al*[126] in a 1D model when placing a PZT at a frequency of 2.9 MHz and an opposite reflector separated by 30 mm. Alumina microparticles (80 μm) were trapped in the nodes of the USW and by switching the PZT, the particles moved along the *x* axis.

These acoustic devices have the advantage of trapping the particles at a resonance and manipulating them in an orthogonal plane (2D) or in line (1D) to the trapping direction (Figure 1.16). More recent studies have manipulated microparticles at a microfluidic scale. Glynne-Jones *et al*[127] created a 1D microfluidic device were microparticle aggregates were trapped in the nodes at λ/2 resonance and moved in a lateral direction. A 2D array was developed by Qui *et al*[128] where a multilayer planar resonant device was operated at a frequency of 7.5 MHz with an opposite glass reflector for microparticle manipulation.

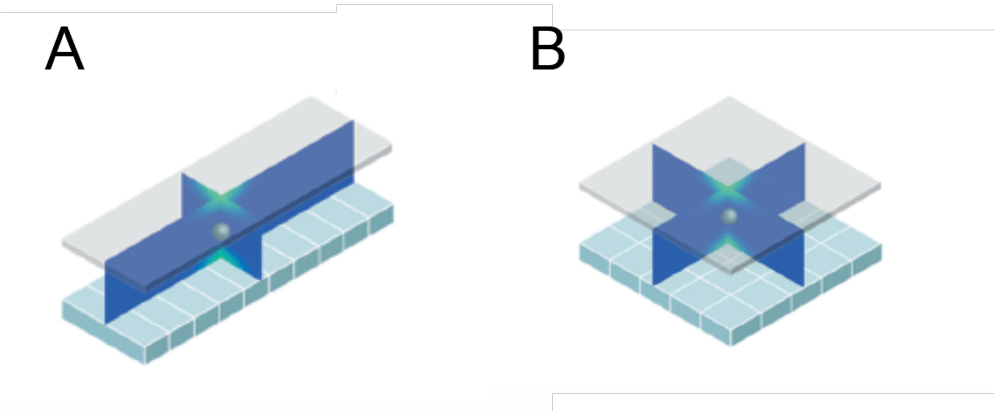

Figure 1.16: Planar array acoustic manipulators in (**A**) 1D and (**B**) 2D planes. Adapted from reference 120.

The last classification are the in-plane acoustic manipulators where the transducers are placed around the central chamber where the microparticle trapping occurs. The complexity of these devices depends on the number of PZT arranged at the periphery of the trapping area increasing the operation and patterning configurations. As shown in Figure 1.17 (A) the simpler in-plane device is when two PZT are placed opposite each other and generate a standing acoustic wave creating pressure nodes and antipressure nodes where dense particles are trapped. A more complex design is when two opposed orthogonal pairs of PZT generate a grid microparticle pattern due to the interference of the two orthogonal waves and compressed nodal lines at the centre of the trapping area are generated (Figure 1.17 (B)). For this type of in-plane manipulator, as the frequency increases the nodal lines will compress more at the centre of the device. The last example of in-plane manipulators is the circular array consisting of high potential nodes surrounding a low potential node at the centre (Figure 1.17 (C)) creating a 2D acoustic trap which in general is a more efficient device as the high intensity is focused on the small region at the centre of the device. These acoustic traps are not yet fully explored, however, few examples as Hong *et al*[129] were able to create a circular vortex and trap microparticles at the centre of the device.[120]

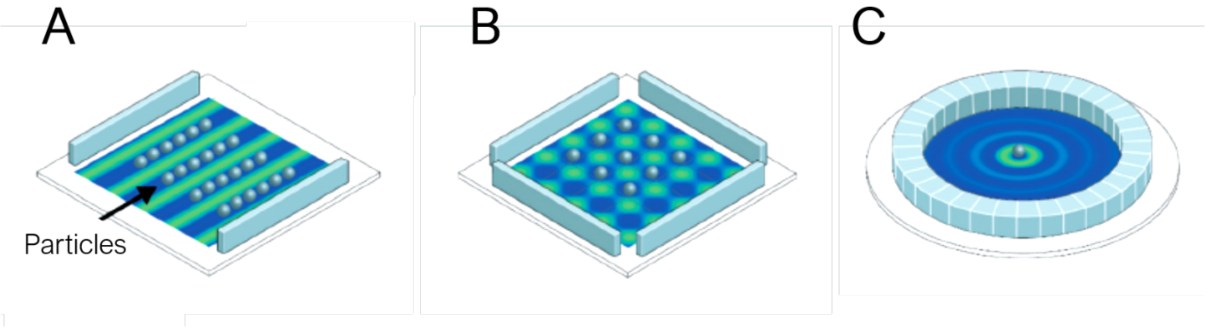

Figure 1.17: In-plane 1D acoustic manipulators. (**A**) where two PZT are placed at the side of the acoustic trapping zone and (**B**) with four PZT in all sides of the device. While (**C**) represents a circular array of PZT surrounding the trapping area. Adapted from reference 120.

In addition, acoustofluidics can also be considered as another classification of acoustic manipulators, as it is defined as ultrasound exposure in a microfluidic system. Particular attention has been paid to these acoustic traps since they can be used to separate mammalian cells according to their mechanical properties without the need to be labelled. However, the physical variables have to be scaled down from a millimetre acoustic system to a micrometre range, so Bruus[130] provided a study of scaling laws for designing and model microfluidic systems. These scaling laws are related to the dimensions of the device and the variables involved in a classical continuum flow rate of a fluid (i.e., velocity, pressure and density). A common design of an acoustic-fluidic system is similar to that previously reported by Trampler *et al*[113] and Doblhoff-Dier *et al*[114] (Figure 1.14) where a PZT is placed on one wall of the device with a coupling layer and in front on the other wall a reflector (multilayer approach, Figure 1.18)[133] or another PZT is placed operating with the same frequency, however, these first resonators were larger in size. It was not until 1992 when Yasuda and colaborators[131] first reported and patented a small half wavelength microfluidic resonator operating at a MHz frequency (Figure 1.19). A standing wave device was developed where particles are trapped at the pressure nodes within the fixed microfluidic channel in a continuous or steady fluid flow. A capillary tube was placed inside the microfluidic tube by moving the support rods to collect selectively the particles that were trapped in the nodes from the particles at the loops.[132]

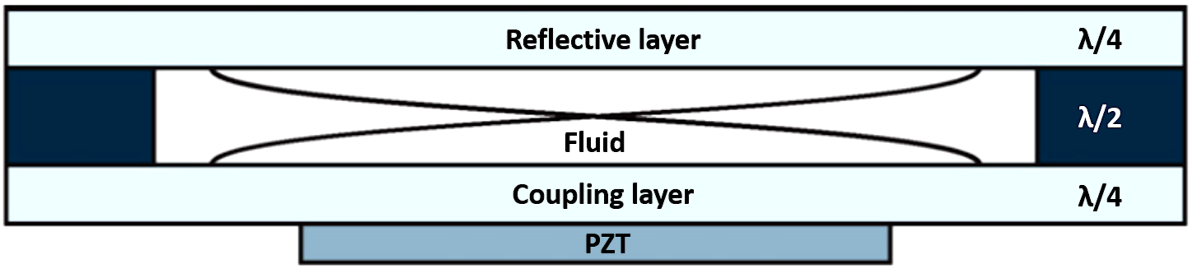

Figure 1.18: Scheme of a multilayer resonant acoustofluidic device where the standing wave is formed in the plane perpendicular to the continuous flow. Adapted from reference 133.

The reduction in the dimensions of the acoustic device also reduces the scaling laws of the axial PRFs where the acoustic force is proportional to the frequency as demonstrated in Equation (10), described in a previous work. For acoustic devices of half wavelength operating in MHz regime, which in a 1D resonance mode is expressed as

$$F_{AX} = 4\pi R^3 E k \sin(2kx)\phi \tag{10}$$

where F_{AX} is the primary acoustic radiation force, R is the radius of the particle, E is the acoustic energy and x is the position where the particle is located in the direction of the wave propagation. Furthermore, $k = 2\pi f / c_0$ where f is the employed frequency and c_0 is the speed of sound in the fluid. The acoustic contrast factor (ϕ) includes the speed of sound of the particle and the densities of the particle and the fluid.[132] So, as the frequency increases and therefore the acoustic force, manipulation of particles and mammalian cells in a continuous flow is possible. The contrast factor (ϕ) will determine the direction of the force acting on the microparticles either directing them towards the pressure or anti pressure node where in a standard microparticle trapping the microparticles will be directed towards the pressure nodes. Furthermore, the Reynolds number that is defined as $Re = \rho v l / \mu$ where μ is the viscosity dynamics, l is the scale of the acoustic system and v is the velocity, is used to describe the flow characteristics in a microfluidic system. In the case of an acoustofluidic device the Re number is very small, so turbulence phenomena will not be generated though a formation of a vortex rotational movement may occur.[7] Since the first work of Yasuda *et al*[131] and from the first lab-on- a-chip acoustofluidic devices that were used as filters to separate cells, new applications have been developed such as trapping and sorting of microparticles and cells,[134] forensic and food analysis,[135,136] as well as cell synchronization and differentiation.[137,138]

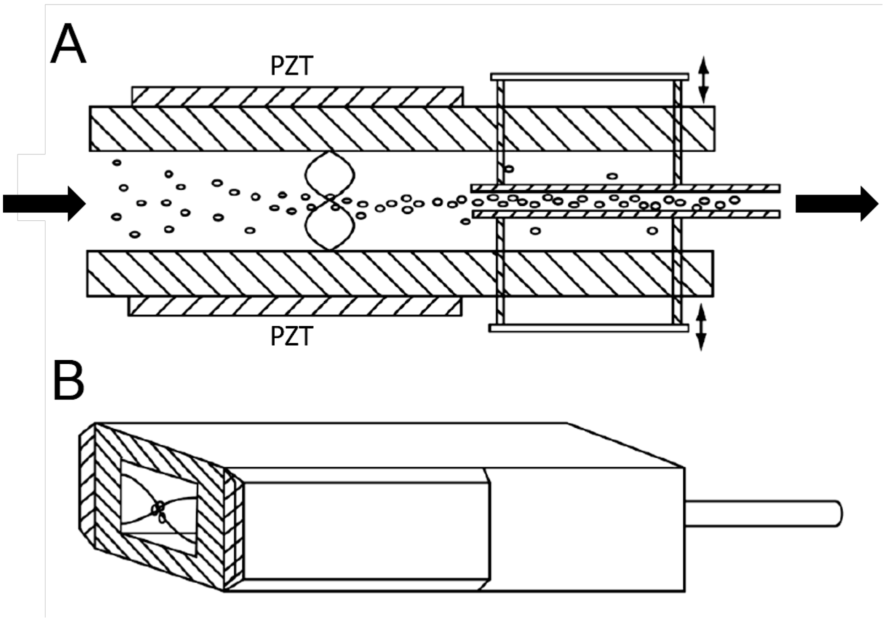

Figure 1.19: Schemes of the acoustofluidic device from Yasuda et al[131] where (**A**) an internal and (**B**) an external view of the device, are represented. The arrows indicate the flow of the fluid where the inlet and outlet are located. Adapted from reference 131.

1.3 Ultrasound for drug delivery applications

Ultrasound is also employed as a versatile tool for drug delivery applications. Ultrasound-mediated drug delivery systems have been developed to increase the uptake of therapeutic agents efficiently, controlled and to minimise toxicity in targeted cells/tissues. Drug delivery devices have versatile designs and configurations that range from a millimetre-wide ultrasound beam to a multi-transducer system that can be used to expose large areas.[139] This research area has increased since the ultrasound contrast agents (UCAs) enable the non-invasive diagnostic and therapeutic clinical applications. These micron-sized shell agents are gas-filled spheres that act as carriers of drugs and genes that have been used in the treatment of transdermal insulin delivery,[140] gene therapy to treat cancer[141] and cardiovascular disease,[142] drug delivery across the blood-brain barrier (BBB),[143] among other applications. As mentioned in Section 1.1.3, acoustic cavitation is a nonthermal mechanism in which the formation of microbubbles, including UCAs, their oscillation and collapse generally occurs by two types of cavitation forms, stable and inertial cavitation. These cavitation mechanisms are considered a category for ultrasound-mediated drug delivery where sonoporation, temporary increase in permeability and porosity of the cell membrane induced by ultrasound, leads to an increase in the cellular uptake of formulated drugs (Figure 1.20 (**A**)).[139] Moreover, sonophoresis which is defined as the ultrasound enhanced transdermal drug delivery,[144] and sonochemistry where ultrasonic waves enhance chemical reactions at different rates depending on the acoustic conditions,[145] are also cavitation phenomena.

Another category of ultrasound-mediated drug delivery is the use of active liposomes or UCAs which, when disrupted and destroyed, the therapeutic drug contained internally is released into the cells of interest. In this particular case, the surface of these drug carriers is decorated with specific ligands that can bind directly to specific receptors on the cell membrane to achieve a more accurate targeting (Figure 1.20 (**D**)). Also, in this category, positively charged drug carriers can be noncovalently bound to DNA (Figure 1.20 (**B**)) and an oily layer between the gas layer and the carrier can be added to load hydrophobic formulated drugs and be stabilised by the membrane of the carrier (Figure 1.20 (**C**)).[139] Ultrasound can also be used in sonodynamic therapy which is the combination of a chemical sonosensitiser and high intensity ultrasound exposure. This therapy is used for the treatment of cancer and is used *in situ* directed to the tumour where reactive oxygen species can attack and induce apoptosis and necrosis to cancer cells. The most common sonosensitiser in this cancer therapy is doxorubicin, which in combination with ultrasound can be targeted and internalise into the cancer cells.[146]

The categories mentioned above are ultrasound-mediated microbubble drug delivery, however, sonoporation also can be induced by fluorescent probes and plasmids in the absence of microbubbles.[147] Although this mechanism remains unexplored, some studies have shown that effective drug delivery can be achieved using standing acoustic waves and microstreaming where increased porosity in the cell membrane was observed after exposure.[148,149] These results are in agreement with a previous work where the dynamics of sonoporation in *Xenopus* eggs was explored during ultrasound exposure and it was observed that the permeability of the cell membrane presented current variations in relation to the time of ultrasound exposure.[150] This sonoporation method is thought to maintain cell viability as the cell membrane can be resealed (Section 1.1.3) which may be an advantage over the microbubble-mediated drug delivery that can lead to cell death depending on the acoustic conditions.[147]

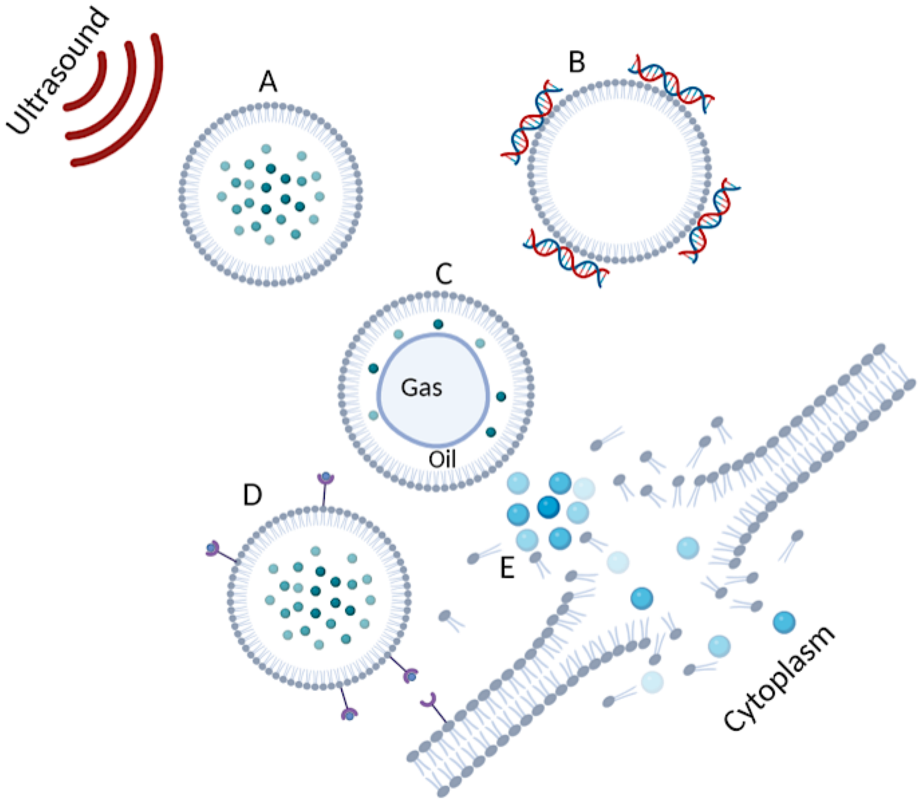

Figure 1.20: Schemes of ultrasound-mediated drug delivery. (**A**) represents microbubbles loaded with the formulated drugs, (**B**) DNA can be covalently bound to the microbubble surface and (**C**) hydrophobic drugs are inside the oily layer between the gas and the membrane of the microbubble where a ligand can be attached to the surface for accurate targeting as depicted in (**D**). (**E**) represents sonoporation in the absence of microbubbles where the materials can increase the porosity of the cell membrane and be internalised. Adapted from reference 137 and created with Biorender.

1.3 Conclusions and thesis aims

As discussed in the previous sections above, ultrasound trapping offers a wide range of possible biomedical applications as a non-destructive technique. Progress has been made throughout the years in the areas of drug delivery and mammalian cellular manipulation and trapping employing acoustic waves, however, further development and research still remains to be done towards these areas. An important aspect of ultrasound research is the development of reliable acoustic devices and their operation mode without affecting the viability of the cells and the safe delivery of drugs. Although there is a plethora of described ultrasonic devices, questions arise about the advantages and limitations of ultrasonic devices applied in biomedical applications due to practicality and unexplored secondary factors that must be addressed and investigated prior to cellular treatments.

The aims of this research project are:

- Improve the design of the ultrasonic device previously developed at the University of Bristol School of Engineering.
- Systematic studies (i.e. frequency, voltage and time) to determine the mode of operation for 1D cellular and microparticle acoustic trapping.
- Explore cellular acoustic trapping and drug delivery using solid conjugated-microspheres maintaining cellular viability.

Moreover, a special chapter is added for stem cell research and the presence of multiple mitotic spindles. Although this chapter is not related to the main topic of this thesis, it provides an opportunity for further research and a possibility to study this phenomenon employing ultrasound, further described in Chapter 7. The results of this project are described in the following chapters:

Chapter 2 describes the design, fabrication and characterisation of the 1D ultrasonic device. A background of similar standing acoustic wave devices are reported, and the operation mode of the device is detailed considering the materials used for the fabrication and their acoustic properties. In this chapter the advantages and limitations of this acoustic device are described highlighting the importance of investigating the operation mode and acoustic properties of the employed materials for an optimal acoustic trapping.

Chapter 3 reports the results of the evaluation of secondary acoustic factors in cancer cells and healthy cells subjected to acoustic exposure. Systematic and optimization studies were carried out based on time, voltage and temperature. Cell viability and metabolic activity were measured in both cell lines for 3 different exposure times and different driving voltages. In addition, further investigation of acoustic factors (i.e., acoustic cavitation and flow) was performed prior to conducting cell studies.

Chapter 4 describes the application of ultrasound-mediated drug delivery and presents the results of acoustically enhanced delivery of fluorescent microspheres conjugated to a cancer cell line (HeLa). These conjugations were modified to present a different surface charge and to investigate the uptake by HeLa cells using electron microscopy and flow cytometry assay. This chapter provides further evidence of ultrasound-mediated drug delivery in the absence of microbubbles.

Chapter 5 presents the conclusions of the previous results obtained in the chapters of ultrasound. It also presents a discussion of the advancement of this science and its applications with an outlook to the future focusing on the design and applications of ultrasonic devices.

Chapter 6 is an additional thesis topic that I did during my last year of PhD studies and demonstrates the multipolar mitosis and mitotic defects observed in human pluripotent stem cells (hPSCs). The results include quantifications of the mitotic defects of undifferentiated hPSCs analysing a 4-day time-lapse imaging and immunofluorescence assays of cellular components involved in the mitotic process.

Chapter 7 presents the conclusions of the results obtained in the previous chapter and provides an outlook for an opportunity to evaluate the mitotic defects and multipolar mitosis employing acoustic trapping. This final chapter provides some examples of literature reporting on acoustically exposed stem cells and their effects.

1.4 References

1. V. Levario-Diaz, P. Bhaskar, M.C. Galan and A.C. Barnes, *Sci Rep*, 2020, **10**, 8493.
2. V. Levario-Diaz, D. Benito-Alifonso, S. Medina, S. E. S. Michel, A. Leard, S. Cross, C. Neal, L. Sueiro-Ballesteros, A. Herman, P. Verkade, A. C. Barnes and M. C. Galan., Acoustically enhanced cellular uptake of carboxyl-modified polystyrene microspheres using standing waves*. (to be submitted 2021).*
3. L. A. Kuznetsova and W. T. Coakley, *Biosensors and Bioelectronics*, 2007, **22**, 1567-1577.
4. J. Spengler and M. Jekel, *Ultrasonics*, 2000, **38**, 624-628.
5. A.L. Bernassau, P. Glynne-Jones, F. Gesellchen, M. Riehle, M. Hill and D.R.S. Cumming, *Ultrasonics*, 2014, **54**, 268-274.
6. J. Lei, P. Glynne-Jones and M. Hill, *Lab Chip*, 2013, **13** (11), 2133-2143.
7. J. Wu, *Fluids*, 2018, **3** (4), 108.
8. T. Xu, J. Jin, C. Gregory, J. J. Hickman and T. Boland, *Biomaterials*, 2005, **26**, 93–99.
9. V. T. Ribeiro-Resende, B. Koenig, S. Nichterwitz, S. Oberhoffner and B. Schlosshauer, *Biomaterials*, 2009, **30**, 5251–5259.
10. W.L-M. Nyborg, Acoustic Streaming, Ed. P.M Warren, Physical Acoustics, Academic Press, vol. 2, part B. 1965.
11. K.R. Nightingale, P.J. Kornguth and G.E. Trahey, *Ultrasound Med Biol.* 1999, **25**, 75-87.
12. L. Clarke, A. Edwards and EL. Graham, *Ultrasound in Med & Biol*., 2004, **30** (4), 559-562.
13. X. Shi, R. Martin, S. Vaezy, P. Kaczkowski and L. Crum, *Ultrasound Med Biol*. 2001, **27**, 1255-1264.
14. P. B. Muller, R. Barnkob, M. J. H. Jensen and H. Bruus, *Lab Chip*, 2012, **12**, 4617-4627.
15. M. Wiklund, R. Green and M. Ohlin, *Lab Chip*, 2012, **12**, 2438-2451.
16. H. Mulvana, S. Cochran and M. Hill. *Adv Drug Deliv Rev*. 2013, **65** (11-12), 1600-10.
17. L. D. Landau, E. M. Lifshitz, Fluid Mechanics, Course of Theoretical Physics, Vol. 6, Butterworth-Heinemann, 2nd Ed. 2006.

18. K.D. Frampton, S.E. Martin and K. Minor, *Appl. Acoust*., 2003, **64**, 681–692.
19. A. Lenshof, M. Evander, T. Laurell and J. Nilsson, *Lab Chip*, 2012, **12**, 684.
20. L.A. Kuznetsova, and W.T. Coakley, *Biosens. Bioelectron*., 2007, **22**, 1567–1577.
21. J. Marshall and J. Wu, *Phys. Fluids*, 2015, **27**, 103601–1036021.
22. Z. Izadifar, P. Babyn and D. Chapman, *Ultrasound in Med. & Biol*., 2017, **43** (6), 1085-1104.
23. D. Dalecki, *Annu Rev Biomed Eng*, 2004, **6**, 229–248.
24. D.L. Miller, S.V. Pislaru and J.F. Greenleaf, *Somatic Cell and Molecular Genetics*, 2002, **27**, 115-134.
25. I. Lentacker, I. De Cock, R. Deckers, S.C. De Smedt and C.T.W. Moonen, *Advanced Drug Delivery Reviews*, 2014, **72**, 49-64.
26. I. Lentacker, S.C. De Smedt and N.N. Sanders, *Soft Matter*, 2009, **5**, 2161-2170.
27. H-D. Liang, J. Tang and M. Halliwell, *Proceedings of the Institution of Mechanical Engineers Part H Journal of Engineering in Medicine*, 2010, **224**, 343-361.
28. H. Flynn, *J Acoust Soc Ame*., 1982, **72**, 1926–1932.
29. M.W. Miller, D.L. Miller and A.A. Brayman, *Ultrasound in Med & Biol*., 1996, **22** (9), 1131-1154.
30. J. Rooze, E.V. Rebrov, J.C. Schouten and J.T.F. Keurentjes, *Ultrasonic Sonochemistry*, 2013, **20**, 1-11.
31. S.G. Zhang, J.H. Duncan and G.L. Chahine, *J. Fluid Mechanics*, 1993, **257**, 147-181.
32. O. Louisnard, *Ultrasonics Sonochemistry*, 2012, **19**, 66-76.
33. V.F.K. Bjerknes, Fields of Force, 1906, Columbia University Press, New York.
34. S.A. Zwick, *J. Math. Phys*., 1958, **37**, 246–268.
35. I. Akhatov, R. Mettin, C.D. Ohl, U. Parlitz and W. Lauterborn, *Phys. Rev*., 1997, **55** (3), 3747–3750.
36. J. Magnaudet and I. Eames, *Ann. Rev. Fluid Mech*., 2000, **32**, 659–708.
37. T. G. Leighton, A.J. Walton and M.J.W. Pickworth, *European Journal of Physics*, 1990, **11**, 47-50.
38. T.G. Leighton, M.J.W. Pickworth, A.J. Walton and P.P Dendy, *Phys. Med. Biol*., 1988, **33**, 1239-1248.
39. L.A. Crum, A.I. Eller, *J. Acoust. Soc. Am*., 1970, **48** (1), 181–189.

40. B.P. Barber, R.A. Hiller, R. Löfstedt, S.J. Putterman, K.R. Weninger, *Phys. Rep.*, 1997, **281**, 65–143.
41. K. Ferrara, R. Pollard and M. Borden, *Annu. Rev. Biomed. Eng.*, 2007, **9**, 415–447.
42. S. Hernot and A. Klibanov, *Adv. Drug Deliv. Rev.*, 2008, **60**, 1153–1166.
43. C. Deng, F. Sieling, H. Pan and J. Cui, *Ultrasound Med. Biol.*, 2004, **30**, 519–526.
44. Y. Zhou, J. Cui and C. Deng, *Biophys. J.*, 2008, **94**, 3.
45. Y. Zhou, R. Kumon, J. Cui and C. Deng, *Ultrasound Med. Biol*, 2009, **35**, 1756–1760.
46. Y. Zhou, J. Shi, J. Cui and C. Deng, *J. Control. Release*, 2008, **126**, 34–43.
47. K. Tachibana, T. Uchida, K. Ogawa, N. Yamashita and K. Tamura, *Lancet*, 1999, **353**, 1409.
48. J. Hauser, M. Ellisman, H.-U. Steinau, E. Stefan, M. Dudda and M. Hauser, *Ultrasound Med. Biol.*, 2009, **35**, 2084–2092.
49. V. Lionetti, A. Fittipaldi, S. Agostini, M. Giacca, F. Recchia and E. Picano, *Ultrasound Med. Biol.*, 2009, **35**, 136–143.
50. D.M. Paula, V.B. Valero-Lapchik, E.J. Paredes-Gamero and S.W. Han, *J. Gene Med.*, 2011, **13** (7–8), 392–401.
51. A. Delalande, S. Kotopoulis, M. Postema, P. Midoux and C. Pichon, *Gene*, 2013, **525** (2), 191–199.
52. P. Clarke and C. Hill, *Exp Cell Res*,1969, **58**, 443–444.
53. Dvorak M and Hrazdira I. *Z Mikrosk Anat Forsch*,1966, **75**, 451–460.
54. I. Hrazdira, Changes in cell ultrastructure under direct and indirect action of ultrasound. In: Bock J, Edler I, Ossoinig K, (eds). Societas Internationalis pro Diagnostica in Ophthalmologia. Ultrasonographia medica Vienna: Verlag der Wiener Medizinischen Akademie; 1971. p. 457–463.
55. K.J.W. Taylor and J.B. Pond, Primary sites of ultrasonic damage on cell systems. In: Reid M, Sikov MR, (eds). Interaction of ultrasound and biological tissues, vol. 3. Washington, DC: DHEW; 1972.
56. I. Chapman, *Br J Radiol*, 1974, **47**, 411–415.
57. P.F. Davies, *Physiol. Rev.*, 1995, **75**, 519.
58. G. Apodaca, *Am. J. Physiol.*, 2002, **282**, 90.
59. A. Sarvazyan, *Ultrasonics*, 2010, **50**, 230-234.
60. M. Dyson, B. Woodward and J.B. Pond, *Nature*, 1971, **232**, 572–573.

61. M. Hill and N.R. Harris (2007) Ultrasonic Particle Manipulation. In: Hardt S., Schönfeld F. (eds) Microfluidic Technologies for Miniaturized Analysis Systems. Springer, Boston, MA.
62. A.P. Sarvazyan, O.V. Rudenko and W.L. Nyborg, *Ultrasound in Med. & Biol*., 2010, **36** (9), 1379–1394.
63. P. Glynne-Jones, R.J. Boltryk and M. Hill, *Lab Chip*, 2012, **12**, 1417.
64. L.V. King, *Proc. R. Soc. A Math. Phys. Eng. Sci*., 1934, **147**, 212–240.
65. G. Simon, M.A.B. Andrade, M.P.Y. Desmulliez, M.O. Riehle and A.L. Bernassau, *Micromachines*, 2019, **10**, 431.
66. K. Yosioka and Y. Kawasima, *Acustica*, 1955, **5**, 167–173.
67. A.A. Doinikov, *Recent Res. Devel. Acoustics*, 2003, **1**, 39-67.
68. L.P. Gor’kov, *Sovlet Physics Doklady*, 1962, **6**, 773–775.
69. P.J. Westervelt, *Journal of the Acoustical Society of America*, 1951, **23** (4), 312–315.
70. A.A. Doinikov, *Journal of the Acoustical Society of America*, 1997, **101** (2), 713–721.
71. A.A. Doinikov, *Journal of the Acoustical Society of America*, 1997, **101** (2), 722–730.
72. A.A. Doinikov, *Journal of the Acoustical Society of America*, 1997, **101** (2), 731–740.
73. C.J. Schram, (1991) Manipulation of particles in an acoustic field. In Advances in Sonochemistry (Mason, T.J., ed), Elsevier, Amsterdam.
74. M. Gröschl, Acustica, 1998, **84** (3), 432–447.
75. D. Bazou, G.A. Foster, J.R. Ralphs and W.T. Coakley, *Molecular Membrane Biology*, 2005, **22** (3), 229–240.
76. J. Morgan, J.F. Spengler, L. Kuznetsova, W.T. Coakley, J. Xu, J, and W.M. Purcell, *Toxicology In Vitro*, 2004, **18** (1), 115–120.
77. T. Lilliehorn, U. Simu, M. Nilsson, M. Almqvist, T. Stepinski, T. Laurell, J. Nilsson, and S. Johansson, *Ultrasonics*, 2005, **43** (5), 293–303.
78. R.J. Townsend, M. Hill, N.R. Harris and N.M. White, *Ultrasonics*, 2006, **44**, 467–471
79. S. M. Woodside, B. D. Bowen and J. M. Piret, *AIChE J*., 1997, **43**, 1727–1736.
80. B. Hammarstrom, T. Laurell and J. Nilsson, *Lab Chip*, **12**, 4296-4304.

81. M. A. H. Weiser, R. E. Apfel and E. A. Neppiras, *Acustica*, 1984, **56**, 114.
82. L. A. Crum, *J. Acoust. Soc. Am.*, 1971, **50**, 157.
83. T. Laurell, F. Petersson and A. Nilsson, *Chem. Soc. Rev.*, 2007, **36**, 492-506.
84. L.A. Crum, *Journal of the Acoustical Society of America*, 1975, **57** (6), 1363–1370.
85. R.S. Dahiya, M. Valle, Robotic Tactile Sensing, Springer, Science +Business Media Dordrecht 2013.
86. S. Katzir, The discovery of the piezoelectric effect in the beginnings of piezoelectricity: a study in mundane physics. The Netherlands: Springer; 2006. p. 15–64.
87. K. Uchino, Introduction to Piezoelectric Actuators and Transducers, Penn State University (2003), 41.
88. A.S. Ahmad, M.M. Usman, S.B. Abubakar and A.Y. Gidado, *Journal of Advanced Research in Applied Mechanics*, 2017, **33** (1), 9-19.
89. V.N. Bindal. (1999). Transducers for Ultrasonic Flaw Detection. New Delhi: Narosa Publishing House.
90. N. Waingankar, E. Goldenberg and B.R. Gilbert, Ultrasound of the Male Genitalia, Springer, Science +Business Media New York 2015.
91. T.G. Leighton, *Progress in Biophysics and Molecular Biology*, 2007, **93**, 3-83.
92. J. Krautkramer and H. Krautkramer, Ultrasonic Testing of Materials, Third Edition, Springer-Verlag Berlin Heidelberg New York 1983.
93. W.N. McDicken and T. Anderson, 2011. Basic physics of medical ultrasound. Blood, 1570 (1.61), p.105.
94. M. Evander and J. Nilsson, *Lab Chip*, 2012, **12**, 4667-4676.
95. J. Dual and D. Moller, *Lab Chip*, 2012, 12, 506.
96. W.D. O’Brien Jr., *Progress in Biophysics and Molecular Biology*,2007, **93**, 212–255.
97. M. Wiklund, *Lab Chip*, 2012, **12**, 2018–2028.
98. P. Augustsson, R. Barnkob, S.T. Wereley, H. Bruus and T. Laurell, *Lab Chip*, 2011, **11**, 4152.
99. S.B. Barnett, G.R. Ter Haar, M.C. Ziskin, W.T. Nyborg, K. Maeda and J. Bang, *Ultrasound Med. Biol.*, 1994, **20**, 205–218.
100. K. Richter, M. Haslbeck and J. Buchner, *Mol. Cell*, 2010, **40**, 253–266.

101. D. M. Toivola, P. Strnad, A. Habtezion and M. B. Omary, *Trends Cell Biol.*, 2010, **20**, 79–91.

102. M.B. Al-Fageeh, R.J. Marchant, M.J. Carden and C.M. Smales, *Biotechnol. Bioeng.*, 2006, **93**, 829–835.

103. M. Evander, L. Johansson, T. Lilliehorn, J. Piskur, M. Lindvall, S. Johansson, M. Almqvist, T. Laurell and J. Nilsson, *Anal. Chem.*, 2007, **79**, 2984–2991.

104. National Toxicology Program, U.S. Department of Health and Human Services, 14th Report on Carcinogens, November 3rd, 2016.

105. Yongquiang Qiu, *et al*. *Sensors*, 2014, **14**, 14806-14838.

106. J. Nilsson, M. Evander, B. Hammarstrom, T. Laurell. *Analytica Chimica Acta*., 2009, 141-157.

107. R. C. McMaster, (1959) (Ed). Nondestructive Testing Handbook (2 Vols.), New York: Ronald Press.

108. A.L. Bernassau, C.-K. Ong, Y. Ma, P.G.A. MacPherson, C.R.P. Courtney, M. Riehle, B.W. Drinkwater and D.R.S. Cumming, *IEEE Trans Ultrason Ferroelectr Freq Control*, 2011, **58** (10), 2132-2138

109. C.M. Lin, Y.S. Lai, H.P. Liu, C.Y. Chen, A.M. Wo, *Analytical Chemistry*, 2008, **80**, 8937–8945.

110. D. Bazou, A. Castro and M. Hoyos, *Ultrasonics*, 2012, **52**, 842-850.

111. David N. Cheeke. (2010). Fundamentals and Applications of Ultrasonic Waves. Florida: CRC Press.

112. E. G. Lierke, *Acustica*, 1996, **82**, 220–237.

113. F. Trampler, S.A. Sonderhoff, P.W. Pui, D.G. Kilburn and J.M. Piret, *Biotechnology (N Y)*, 1994, **12** (3), 281-284.

114. O. Doblhoff-Dier, Th. Gaida, H. Katinger, W. Burger, M. Groschl and E. Benes, *Biotechnol. Prog.*, 1994, **10**, 428-432.

115. N.V. Baker, *Nature*, 1972, **239** (5372), 398-399.

116. W.T. Coakley, D.W. Bardsley, M.A. Grundy, F. Zamani and D.J. Clarke, J. Chem. Tech. Biotechnol., 1989, 44, 43-62.

117. H.M. Hertz, Applied Physics Reviews, 1995, 78 (8), 4845-4849.

118. J. Wu and G. Du, *Proc. R. Soc. A*, 1990, **87** (3), 997–1003.

119. M. Saito, T. Daian, K. Hayashi, S. Izumida, *J. Appl. Phys.*, 1998, **83**, 3490.

120. B.W. Drinkwater, *Lab Chip*, 2016, **16**, 2360.

121. R.K. Schlicher, J.D. Hutcheson, H. Radhakrishna, R.P. Apkarian and M.R. Prausnitz, *Ultrasound Med Biol.*, 2010, **36** (4), 677-692.

122. V. Idone, C. Tam, N. Andrews, *Trends Cell Biol.*, 2008, **18**, 552–559.

123. J. Hwang, C. Lee, K. Lam, H. Kim, J. Lee and K. K. Shung, *IEEE Trans. Ultrason. Ferroelectr. Freq. Control*, 2014, **61** (3), 399–406.

124. D. Baresch, J.-L. Thomas and R. Marchiano, *Phys. Rev. Lett.*, 2016, **116** (2), 024301.

125. D.J. Lockwood, (2015) Rayleigh and Mie Scattering. In: Luo R. (eds) Encyclopedia of Color Science and Technology. Springer, Berlin, Heidelberg.

126. T. Kozuka, T. Tuziuti, H. Mitome and T. Fukuda, Acoustic micromanipulation using a multi-electrode transducer, in MHS’96 Proceedings of the Seventh International Symposium on Micro Machine and Human Science, *IEEE*, Nagoya, Japan, 1996, pp. 163–170.

127. P. Glynne-Jones, C. Demore, C. Ye, Y. Qiu, S. Cochran and M. Hill, *IEEE Trans. Ultrason. Ferroelectr. Freq. Control*, 2012, **59** (6), 1258–1266.

128. Y. Qiu, H. Wang, S. Gebhardt, A. Bolhovitins, C. E. M. Demore, A. Schonecker and S. Cochran, *Ultrasonics*, 2015, **62**, 136–146.

129. Z. Y. Hong, J. Zhang and B. W. Drinkwater, *Phys. Rev. Lett.*, 2015, 214301.

130. H. Bruus, Governing Equations in Microfluidics, Microscale Acoustofluidics, The Royal Society of Chemistry, 2015, Ed. Thomas Laurell and Andreas Lenshof.

131. K. Yasuda, S. Umemura, K. Kawabata, K. Takeda, K. Uchida, Y. Harada, M. Kamahori and K. Sasaki, US Pat., US6216538B1, 1996.

132. A. Lenshof, M. Evander, T. Laurell and J. Nilsson, *Lab Chip*, 2012, **12**, 684.

133. J. Nilsson, M. Evander, B. Hammarström, T. Laurell, *Analytica Chimica Acta*, 2009, **649**, 141-157.

134. T. Franke, S. Braunmueller, L. Schmid, A. Wixforth and D.A. Weitz, *Lab Chip*, 2010, **10**, 789–794.

135. J. V. Norris, M. Evander, K. M. Horsman-Hall, J. Nilsson, T. Laurell and J. P. Landers, *Anal. Chem.*, 2009, **81**, 6089–6095.

136. C. Grenvall, P. Augustsson, J. R. Folkenberg and T. Laurell, *Anal. Chem.*, 2009, **81**, 6195–6200.

137. P. Thevoz, J. D. Adams, H. Shea, H. Bruus and H. T. Soh, *Anal. Chem.*, 2010, **82**, 3094–3098.

138. P. Augustsson, R. Barnkob, C. Grenvall, T. Deierborg, P. Brundin, H. Bruus and T. Laurell, Measuring the acoustophoretic contrast factor of living cells in microchannels, in ed. S. Verporte, H. Andersson, J. Emneus and N. Pamme, Proc. 14th MicroTAS, 3–7 October 2010, Groningen, The Netherlands, CBMS, 2010, pp. 1337–1339.

139. E.C. Pua and P. Zhong, *IEEE Eng Med Biol Mag*. 2009 Jan-Feb **28** (1), 64-75.

140. J. Kost, *Diabetes Technol Ther*., 2002, **4** (4), 489–497.

141. Y. Taniyama, K. Tachibana, K. Hiraoka, M. Aoki, S. Yamamoto, K. Matsumoto, T. Nakamura, T. Ogihara, Y. Kaneda, and R. Morishita, *Gene Ther*., 2002, **9** (6), 372–380.

142. S. Bao, B. D. Thrall, and D. L. Miller, *Ultrasound Med. Biol*., 1997, **23** (6), 953–959, 1997.

143. S.Y. Wu, C. Sanchez, G. Samiotaki, *et al*. *Sci Rep*, 2016, **6**, 37094.

144. S. Mitragotri, D. Blankschtein and R. Langer, *Science*, 1995, **269**, 850-853.

145. C. Gong an D. P. Hart, *Journal of the Acoustical Society of America*, 1998, **104**, 1-16.

146. Horise Y, Maeda M, Konishi Y, Okamoto J, Ikuta S, Okamoto Y, Ishii H, Yoshizawa S, Umemura S, Ueyama T, Tamano S, Sofuni A, Takemae K, Masamune K, Iseki H, Nishiyama N, Kataoka K and Muragaki Y., *Front. Pharmacol*., 2019, **10**, 545.

147. H. Mulvana, S. Cochran and M. Hill. *Adv Drug Deliv Rev*. 2013, **65** (11-12), 1600-10.

148. S. Rodamporn, N.R. Harris, S.P. Beeby, R.J. Boltryk, T. Sanchez-Elsner, *IEEE Transactions on Biomedical Engineering*, 2011, **58**, 927-934.

149. D. Carugo, D.N. Ankrett, P. Glynne-Jones, L. Capretto, R.J. Boltryk, X. Zhang, P.A. Townsend, M. Hill, *Biomicrofluidics*, 2011, **5**, 044108-044115.

150. H. Pan, *et al*. *Ultrasound in medicine & biology*, 2005, **31** (6),849-56.

2 Ultrasonic 1D device

This chapter is based on work published in *Scientific Reports*, of which I am first author,[1] where a further explanation can be found in the supplementary information. In this work, I designed and built the ultrasonic device with P. Bhaskar at the School of Engineering, University of Bristol, and assisted Dr Adrian Barnes at the School of Physics, University of Bristol with the ultrasonic device characterization.

2.1 Introduction

This chapter introduces the first ultrasonic devices developed at the School of Engineering, University of Bristol and the works they were based upon. The idea of continuing with the research and applying ultrasound for biomedical purposes was conceived after previous works successfully developed an ultrasonic standing wave device (USW) to trap and align inorganic materials. Furthermore, the design, manufacture and characterisation of the employed ultrasonic device and its components for microparticle trapping is reported. The operation mode of the ultrasonic device is detailed according to the relationship of the properties of the sound waves, the materials and the medium used, employing a pair of piezoelectric transducers working at the resonant frequency (third harmonic) around 6.7 MHz. Electric impedance measurements, mathematical models and microscopy images validated microparticle trapping and provided further insight into the advantages and limitations of the ultrasonic device. Moreover, these results highlight the relevance and necessity of developing well characterised and defined acoustic protocols.

2.2 Ultrasonic 1D device fabrication

In the search for an optimal and reliable USW device to trap microparticles and cells, several designs, geometries and materials from previous literature were examined chronologically (Section 2.2.1). The chosen design consists of a dynamic acoustic field device considering the configuration and positioning of a pair of piezoelectric transducers to produce in-plane standing waves. Static-field and dynamic devices usually adopt simple geometries and generate 1D acoustic pressure variations along the fluid-filled central chamber. [2,3] The acoustic field is established by the superposition of the two counter-propagating waves traveling from opposite directions forming the standing acoustic waves, where the resulting pressure nodes and antinodes (minimum and maximum energy areas) are thus the trapping positions for the tested particles. For micrometre scale applications, the wavelengths are in function to the resonant frequencies in the range of MHz and are usually larger than the particles being trapped, in the order of hundreds of micrometres (i.e., λ= 220 µm for 6.77 MHz, in water). Successful cell agglomeration and separation has been achieved employing these dynamic and static-field devices, [4,5] following Gor'kov formulation on acoustic radiation forces previously explained (Section 1.1) and further demonstrated (Section 2.2.2).

2.2.1 Standing wave acoustic traps

In the 19th century, Kundt [6] first observed the acoustic standing waves and the acoustic radiation forces acting on cork dust particles experimentally demonstrated in a resonant cylinder (Kundt's tube).[7] But it was not until Baker[8] and Coakley[9], in 1972 and 1989, respectively, when the first horizontal standing wave devices were developed for *in vitro* red blood cell manipulation in suspension employing low frequencies (1-3 MHz) and high frequencies (5-9 MHz) (Figure 2.1). In the later device, erythrocyte trapping was observed to be occasionally disrupted due to cavitation effects at low frequencies (1 MHz) and it was already known that this effect occurs when the amplitude of the sound pressure exceeds a threshold.[9,12] Hertz[10] further developed a 3D confocal standing wave acoustic trap where glass microparticles with a mean size of 2.1 and 8 µm were acoustically trapped in water and imaged with a Helium-Neon (HeNe) laser. In an attempt, red blood cells were also stably trapped in the pressure nodes. Acoustic streaming was observed and minimised by the addition of two thin plastic walls near the trapping area (Figure 2.2). From these studies, second-order effects (i.e., cavitation and acoustic streaming) due to ultrasound were investigated and cell trapping in suspension was achieved using standing waves. The advantages of ultrasonic traps as a non-destructive technique were introduced and was the starting point to exploit ultrasonic standing waves for biological studies allowing this flexibility in design and device fabrication.

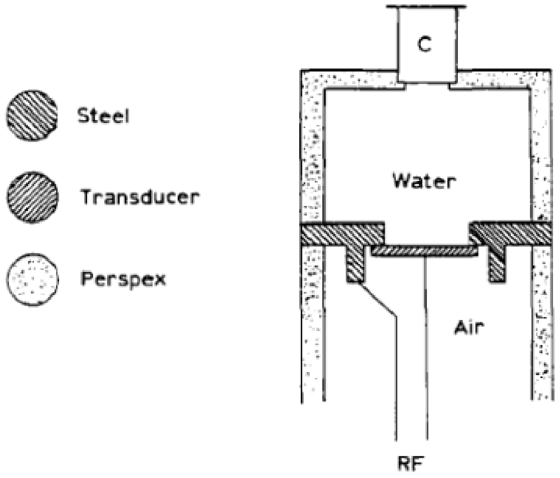

Figure 2.1: The vertical cylinder made of Perspex (indicated in C) was 35 mm long with and internal diameter of 13 mm. On the top of the cylinder, a coverslip was placed to act as a reflecting surface and was in contact with the red blood cell suspension. A 12 μm thick clingfilm was the base of the cylinder. Adapted from reference 9.

At the University of Bristol, Courtney and collaborators[11] developed a new ultrasonic device combining acoustic levitation and standing waves to suspend 5 μm polystyrene particles in a liquid medium and manipulate them in the *x*- axis. Similarities in design with the first standing wave devices from Coakley and Hertz were observed, as a glass plate acted as a reflector at the top of the device and a large piezoelectric transducer was placed at the bottom to levitate the microparticles, as depicted in Figure 2.3. Additionally, two acrylic windows were enclosing the fluid-filled cavity, although the approach of the windows was not to minimise the acoustic streaming but to produce a close environment while microparticle acoustic trapping occurred.

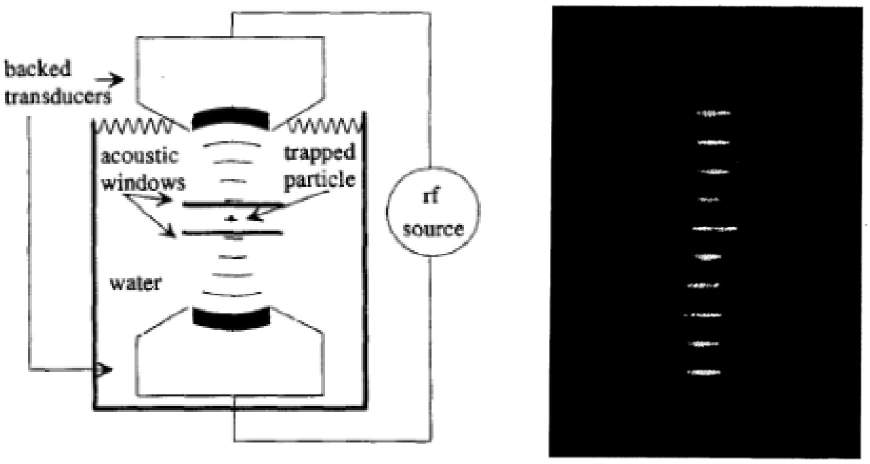

Figure 2.2: Diagram of the confocal standing wave ultrasonic device setup and the photograph of glass particles (θ= 2.1 μm) trapped in the pressure nodes of the standing wave. Adapted from reference 10.

The devices previously described proved that in fixed geometries using two active piezoelectric transducers or a reflector with one front-faced piezoelectric transducer, standing acoustic waves are generated to trap and levitate microparticles in a liquid medium. However, complex setups and over-sized designs showed to be a disadvantage for bench research. Bernassau[13] with collaborators at the University of Bristol, manufactured an ultrasonic device termed “sonotweezer”. The heptagonal geometry of the device allowed a multiple transducer approach in a constrained space and was initially employed to trap and manipulate 10 μm polystyrene beads by varying the relative phase (ΔΦ) of the piezoelectric transducers. Different combinations and configurations of simultaneously active piezoelectric transducers were performed, which were operated at the same frequency (4 MHz) with a voltage of 8 V_{pp} (Figure 2.4).

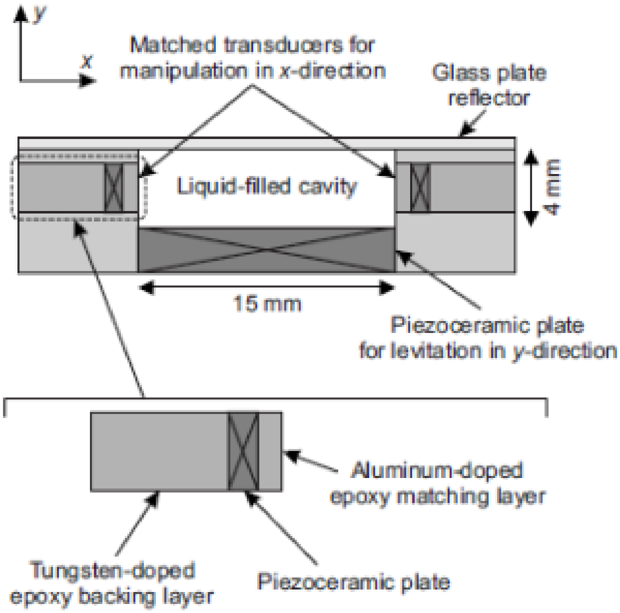

Figure 2.3: Diagram of the ultrasonic device for particle manipulation. This cross-section of the device shows the acoustic levitation stage where a 15 mm piezo transducer was placed at the bottom and two acoustically matched piezo transducers are collocated at the lateral sides to produce the counter propagating waves to manipulate the microparticles in the *x*-axis. Adapted from reference 11.

In the combination 1-2 while trapping the microparticles in the heptagonal shape sonotweezer (Figure 2.4), acoustic streaming was observed, and a layer of agar was later added at the bottom of the device to minimise the streaming effect. This modified acoustic device was also employed for patterning and manipulating cells,[14] functionalised microparticles, emulsions and microbubbles,[15] exciting the piezoelectric transducers at 4 MHz in all experiments but with different voltages. For the patterning of Madin-Darby Canine Kidney (MDCK) cells, the device was rinsed with 70% ethanol followed by several washes with sterile water before use. A glass coverslip, previously coated with poly-l-lysine, was placed on top of the agar layer to attach the patterned cells. Cell viability and cell metabolism were not measured, instead a phase shift of 180° from the initial position was performed and the displacement of the “loose” cells, denominated as not viable, was tracked by Particle Image Velocimetry (PIV) software. The temperature was also measured inside the central cavity to demonstrate that the cell viability was not affected by the heat generated during ultrasonic exposure. A final temperature of 26°C was recorded when the different combinations of active piezoelectric transducers were excited, showing a 0.7°C increase from the initial room temperature.

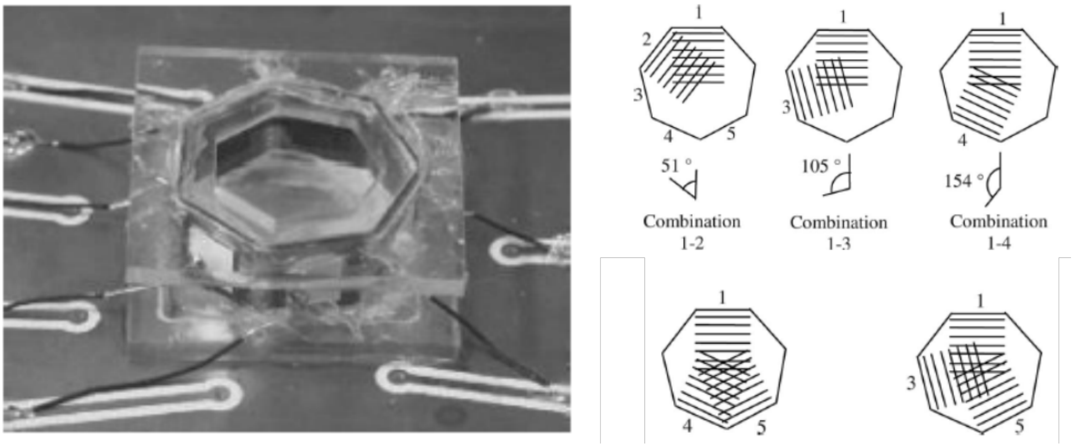

Figure 2.4: Photograph of the heptagonal shape ultrasonic trap. A flexible circuit, supporting the seven piezoelectric transducers (PZT), is being pressed by two poly (methyl methacrylate) (PMMA) plates and mounted on a printed circuit board to connect each piezoelectric transducer. Diagrams of the different combinations and configurations (below) of the active piezoelectric transducers. The combinations were produced by exciting only two PZT simultaneously and the configurations by exciting three PZT. Adapted from reference 13.

Surface charge of 10 µm and 6 µm polystyrene beads was modified by adding amino (NH_3^+ groups) and carboxylate (CO_2^- groups) to obtain positive and negatively charges, respectively. The acoustic patterning when performing the different combinations of active PZT of the functionalised polystyrene microbeads was identical to the non-functionalised microparticles.[13] However, the tendency to form small clusters while being aligned in the pressure nodes, was not observed in the charged microparticles as they repelled each other.[15] Emulsions, made of water, vegetable oil and isopropanol, were trapped in the areas of maximum energy (pressure antinodes) and microbubbles, injected into the deionised water-mineral oil interface, would be either trapped in the pressure nodes or antinodes depending on their resonant frequency and the employed ultrasound frequency.[15,16] Although the asymmetry of the heptagonal shape and the combinations 1-2 produced the acoustic streaming effect, that later was minimised by adding a layer of agar, Bernassau and Courtney[16] developed an octagonal shape sonotweezer to reduce the generation of adverse effects that could interfere with the microparticle acoustic trapping and to create more complex patterning shapes. Non-functionalised microparticles and microbubbles were trapped in the octagonal sonotweezer demonstrating that particle trapping, patterning and manipulation can be achieved with precision in a multiple transducer setup, in agreement with computational models that predicted the pressure zones. Additionally, acoustic streaming was not observed due to the balanced arrangement of the combinations of the active PZT, concentrating the standing waves in the trapping zone.

The standing wave “sonotweezer” traps described offered multiple advantages over the earlier ultrasonic devices. The devices compact size in the order of centimetres, the biocompatibility with cell culture and the possibility of trapping several microparticles at the same time, made them some of the first versatile acoustic traps suitable for biomedical applications. Although the manufacture of the sonotweezer devices was simpler than the earlier acoustic traps, Scholz[17] developed a new and simpler standing wave ultrasonic device in order to assemble glass fibres into thin layers of anisotropic material in polymeric fluids (i.e. epoxy) that later polymerised so the cast could be extracted. The ultrasonic device was made of a PMMA frame mounted on a standard microscope slide, where the central cavity was the trapping area, and a pair of piezoelectric transducers were placed at opposite sides to create the standing waves. The two adjacent cavities were filled with water as a heat sink and were separated by a 5 mm PMMA boundary from the central cavity to protect the electronics from the resin polymerisation, as shown in Figure 2.5.

A variety of microparticles with different shapes, sizes and materials were also acoustically trapped in different host fluids.[18] Spherical and cylindrical microparticles were aligned in parallel lines in all tested fluids, however, a few particles were observed to be unaffected by the standing waves or delayed in motion due to the frictional effects with the glass bottom (Figure 2.6). Additionally, particle tracking was done by using a previously reported software where an algorithm was design to track particles in motion against a background with large variations in light[19] to corroborate friction effects observed under an optical microscope.

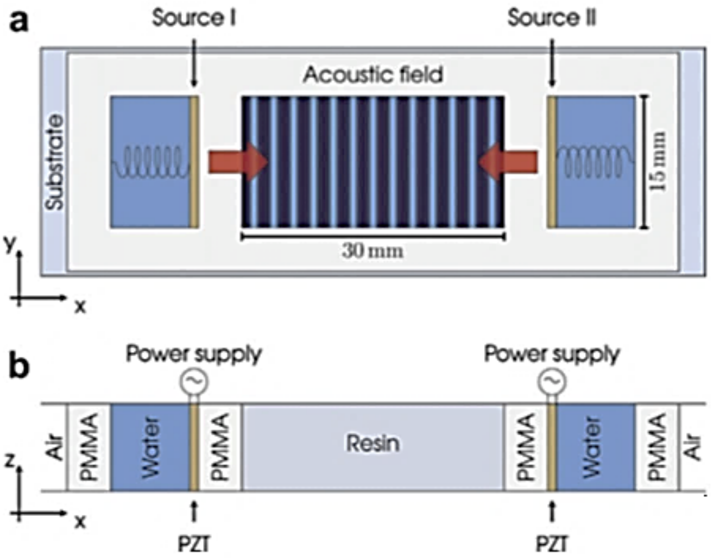

Figure 2.5: Standing wave ultrasonic device. (**a**) the acoustic field is generated in the central cavity by two opposing transducers, placed in the adjacent cavities, submerged in water and pressed against the PMMA wall by metallic springs. (**b**) diagram of a 1D model by ordering the material layers: air (∝), PMMA (5mm), water (9.025 mm), PZT (0.975 mm), PMMA (5 mm), resin (30 mm), PMMA (5 mm), PZT (0.975 mm), water (9.025 mm), PMMA (5 mm), air (∝). Adapted from reference 17.

Furthermore, a 2D acoustic modelling analysis was performed with the Comsol Multiphysics software (Comsol Inc., Burlington, USA) to predict the acoustic resonant behaviour of the device. This software contains the interface “Acoustic-Piezoelectric Interaction” and requires the geometrical and physical features of the ultrasonic device and the piezoelectric transducer specifications in order to obtain the acoustic forces and the absolute pressure maps along the trapping zone (Figure 2.7). The central cavity was considered to be a water-filled space for all cases. A mesh using rectangular elements to cover the zones 1-9 and triangular elements for the zone 10 (glass bottom) (Figure 2.7 a) was done for the Comsol modelling in terms of the wavelength with a value of λ/10 to cover the geometry of the device. The 2D pressure map was extracted analysing two conditions: covering the trapping zone with a coverslip, denoted as hard boundary, and leaving the trapping zone in contact with air, denoted as soft boundary (Figure 2.7 b and c), respectively. Both analyses, computational and experimental, agreed in the results of the pressure zones equally spaced (λ/2) in the trapping zone near the bottom of the device indicating that this ultrasonic device is suitable to trap particles denser than the host fluids, as a less strong trapping was observed when moving to the top (z > 0) in particular in the soft boundary condition.

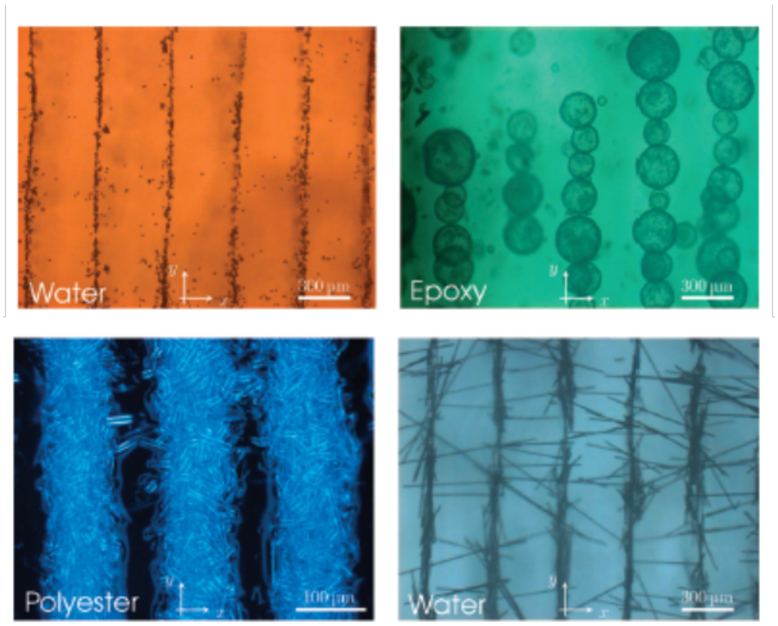

Figure 2.6: Ultrasonic assemble and aligning of 10 μm polystyrene beads in water, polyurethane (PU) and polyurethane foam infill (PUF) microcapsules with a mean diameter of 113 μm in epoxy, glass fibres (50 μm long and 14 μm diameter) in a polyester fluid and carbon fibres with a diameter of 7 μm with a length of 750 μm in water. For all cases, a separation of half wavelength was observed. Scale bars (100 μm and 300 μm) are indicated. Adapted from references 17 and 18.

Additionally, maximum pressure in the trapping area was evaluated experimentally and compared with the Comsol software. A needle hydrophone was used to evaluate the acoustic pressure distribution as a function of frequency in the trapping cavity along the *x*- axis with step size of 0.3 μm and every 25 μs. A frequency range (from 1–2.5 MHz) was employed in both computational modelling and experimental analysis.[18] Both results defined 4 main high-pressure peaks at 1.23 MHz, 1.58 MHz, 1.78 MHz and 2.27 MHz, with 26 kPa, 16 kPa, 41 kPa and 36 kPa, respective pressures. Also, a further evaluation of the central cavity resonance as a function of the frequency was done by modifying the thickness of the PMMA walls, separating the central cavity from the electronics (piezoelectric transducers), with a range from 2 mm to 7mm and in consequence, altering the dimensions of the central cavity from 1 mm to 30 mm. The obtained results from this analysis was that the PMMA walls add an additional damping to the system as sharper resonance peaks were observed when the PMMA boundary walls were thinner. This attribute, therefore, allows the particle trapping even when there are temperature shifts or there are polymerization processes taking place at the central cavity. Overall, the extensive characterisation experimentally and computational, made the ultrasonic device a more suitable and reliable option to trap and manipulate a wide range of particles and observe the acoustic trapping in real time under an inverted microscope due to the glass slide bottom.

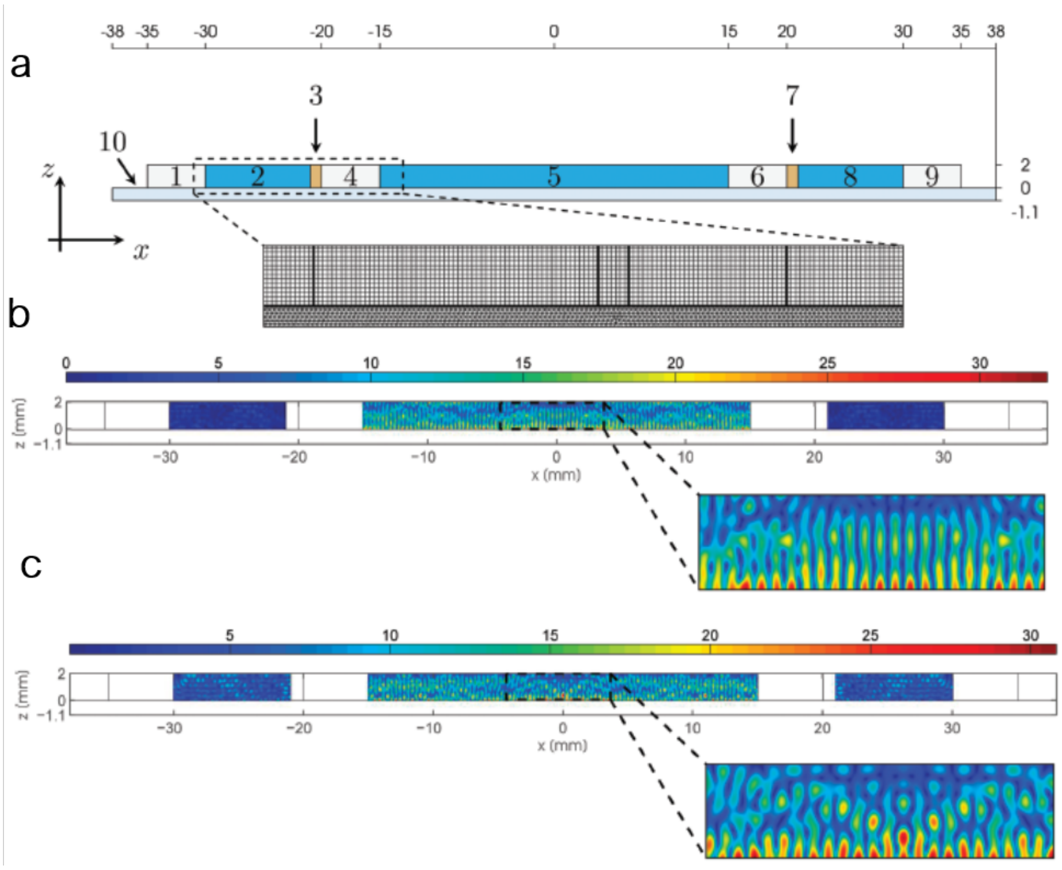

Figure 2.7: Comsol Multiphysics results. (**a**) Mesh distribution according to the geometry of the ultrasonic device and 2D acoustic pressure maps extracted with a (**b**) hard boundary (central cavity covered by a glass coverslip) and a (**c**) soft boundary (central cavity exposed to air) at a frequency of 2.36 MHz with a voltage of 1V. Adapted from reference 18.

At the School of Biomedical Sciences in collaboration with the School of Engineering at the University of Bristol, an ultrasonic device for cellular trapping was developed (internal UoB report). The front faced piezoelectric transducers were attached to a 3D printed frame and the whole device was submerged in a cell culture petri dish. Although a strong cellular trapping and aligning in the pressure nodes was observed, the cell viability was compromised and not maintained. These problems were due to the non-sterile conditions of the frame, the direct contact of the electronics with the cells and the culture media and possibly to the heat increased in the cavity. To overcome these problems, Hughes and White (internal UoB report), developed and constructed an ultrasonic device based on the Scholz device[17] employing the same geometrical shape and number of chambers or cavities. A laser cut 3 mm PMMA frame was mounted in a glass slide with a 3D printed cast to hold the ultrasonic device and the electrical connectors of the piezoelectric transducers. The piezoelectric transducers were pressed against the PMMA walls with two 3D printed “X” and a layer of medical ultrasound gel was placed in between the walls and the piezoelectric transducers as a coupling agent to transmit efficiently the acoustic energy and fill the air gap between the layers.

They also developed a second ultrasonic device with a square geometry with four lateral cavities and constructed to the size of three standard microscope slides joined together. In the central cavity, 8 µm polystyrene beads, Araki-Sasaki (AS) and human conjunctival epithelial (IOBA) cells were successfully aligned in parallel lines with 2 active transducers. Then, a 2 mm thick aluminium reflector was placed at 45° in the central cavity to produce 2D grid patterns. The polystyrene beads and both cell lines were initially aligned for 90s at three different voltages 4 V_{pp}, 6 V_{pp} and 8 V_{pp}. After the short ultrasound exposure, the cells were left to adhere for 30 min to the previously coated fibronectin coverslip placed at the bottom of the device. Further ultrasound exposures of 2 min, 15 min, 30 min and 1 hour were also tested with both cell lines. Also, pulsed ultrasound exposure was evaluated only for the AS cell line for 1 hour alternating 100 milliseconds on and off at 8 V_{pp}. Cell viability studies were performed in all conditions employing Calcein AM dye to label viable cells and unexposed cells were taken as control. Relative fluorescence from both cell samples (exposed and unexposed) were read and the viability percentage was calculated. Cell viability was maintained in both cell lines when the ultrasound exposures were performed for short periods at the three voltages tested. However, when applying constant ultrasound for 1 hour, the cell viability decreased 50% at 6 V_{pp} and 8 V_{pp} while at 4 V_{pp} cells remained viable. For the pulsed 1-hour ultrasound exposure at a constant voltage, AS cells maintained their viability around 95%, suggesting that the constant exposure for longer periods of time may be detrimental for the cell health. Particle distributions were analysed with a computational circular analysis of rose plot histograms to analyse the direction of the particle alignment in the *x*, *y* planes. Temperature variation measurements were performed using a digital thermometer during a 90 min ultrasound exposure at 8 V_{pp} in the central and adjacent cavities where the piezoelectric transducers were placed. The temperature was recorded every 10 min and it was done while trapping particles and cells. In all cavities, the temperature raised in the first 10 min by 1.6°C and 2.8°C at the central cavity and the adjacent cavities, respectively. The experimental evaluations were done at an initial room temperature of 21°C and the final recorded temperature in the central cavity was 24°C, still below the biological standard.

This simple, non-resonant 1D device has several advantages over early ultrasonic devices. Manufacture with flexible and inexpensive materials allows easy assembly and configuration for microparticle and cell studies. Additionally, the ability to clean and sterilize the device using 70% ethanol without damaging the piezoelectric transducers, as they can be removed to properly clean the device. Furthermore, it is possible to perform continuous studies of living cells once they have been acoustically trapped and attached to the treated surfaces. However, further systematic investigations employing cells and microparticles are necessary in order to develop a reliable ultrasonic device.

2.2.2 Ultrasonic device proof of concept

Initial ultrasonic devices were manufactured with three different geometries: square, equilateral and angled triangles (Figure 2.8) for my Masters project. Successful honeycomb-like patterns were achieved when trapping 8 μm polystyrene beads (Figure 2.10 **b-c**) and HeLa cells (θ= 13 μm) (Figure 2.11) in both equilateral and angled triangle devices, as previously demonstrated by Bernassau and collaborators employing the heptagonal sonotweezer when the configuration with three active piezoelectric transducers was done (Figure 2.4).[13] The acoustic device with a square geometry was based on the Scholz,[17] Hughes and White (internal UoB report) devices and as expected, a linear patterning was achieved (Figure 2.10 **a**). All three ultrasonic devices were designed with the Autodesk Inventor software and laser cut in Polyethylene terephthalate (PET) sheets with a width of 2 mm. The dimensions of the ultrasonic devices were adjusted to fit and be mounted in a double width glass slide (Magnacol Ltd, UK) to observe the acoustic patterning under an inverted microscope. The material choice for PET was due to its availability, that it can be sterilised with 70% ethanol for cell studies and has an acoustic impedance value of ~3.2 - 3.4 $MPasm^{-1}s$, the same as PMMA.[20,21]

The acoustic setup of the devices was the same as Hughes and White where a layer of ultrasound gel was placed in between the lead zirconate titanate piezoelectric transducers (15 x 2 x 1cm, Noliac group, NCE51) and the 3 mm PET walls as a coupling agent and to properly transmit the acoustic energy to the fluid-filled cavity. Before and between experiments, the devices were thoroughly cleaned with Virkon disinfectant and sterilised with 70% ethanol without damaging the electronics. Additionally, further deionised water washes were made, and a fresh layer of ultrasound gel was added. Prior to the experiments, impedance measurements were performed in air, water and with ultrasound gel for the piezoelectric transducers, connected to the same Impedance Analyser (Trewmac Systems TE1000) in order to obtain a mean working resonance frequency. Although the obtained resonant frequencies in all mediums presented slight differences, an optimal value was acquired. The standing waves were generated at a frequency of 6.74 MHz (wavelength of 196 μm) with a voltage of 5 V_{pp} where the output impedance was 50 Ω and monitored with an oscilloscope (Agilent Technologies DS03152A) during the 1-min exposure for the microparticle and HeLa cell trapping. Furthermore, a hard boundary setup, previously explained,[18] was done where the acoustic device is open and in contact with air while the microparticles and HeLa cells are being trapped at room temperature.

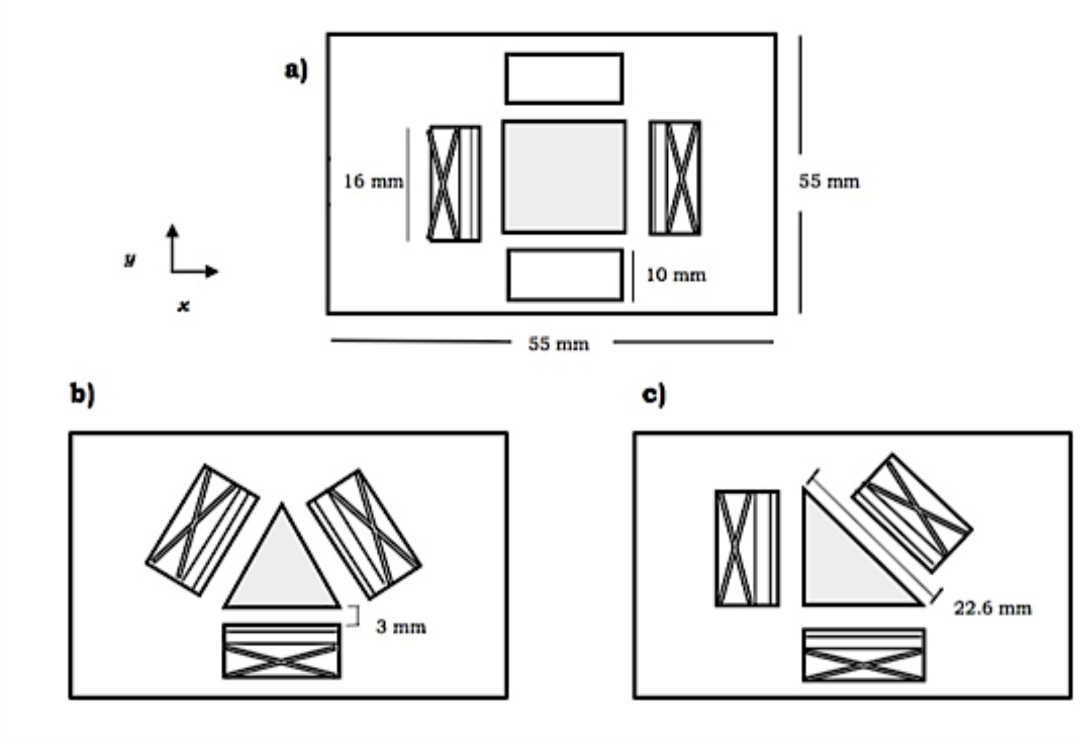

Figure 2.8: Diagrams of ultrasonic devices. The PZT transducers were pressed by 3D printed “X” in all devices against the PET walls. a) In the square design the acoustic field is formed in the central cavity by placing two opposing PZT elements. b) In the equilateral triangle and c) angled triangle the acoustic field is made by three active front-faced PZT transducers. However, in the corners of the device, the microparticles and cells were accumulated and out of the trapping field.

A 5 mm boundary wall PET device was previously tested without successful microparticle alignments and a 2 mm boundary wall PET device was designed and laser cut, however, the boundary walls were not straight and broke due to the V-shape result from the concentrated heat at the top of the 2 mm PET sheet. So, a 3 mm boundary ultrasonic device was found to be a better design to be laser cut, and a strong microparticle alignment was later observed when experimentally tested (Figure 2.10). As mentioned above, the resonance in the central cavity can be modified depending on the thickness of the boundary walls. Previous evaluations have shown that for thinner boundary walls, sharper resonance peaks can be obtained, resulting in better microparticle trapping. [18]

To predict the behaviour of the acoustic devices, MATLAB modelling was performed to evaluate the pressure distributions along the central cavities of the devices (Figure

2.9 **a-c**). The computational code was written and provided by Professor Bruce Drinkwater from the School of Engineering, University of Bristol.

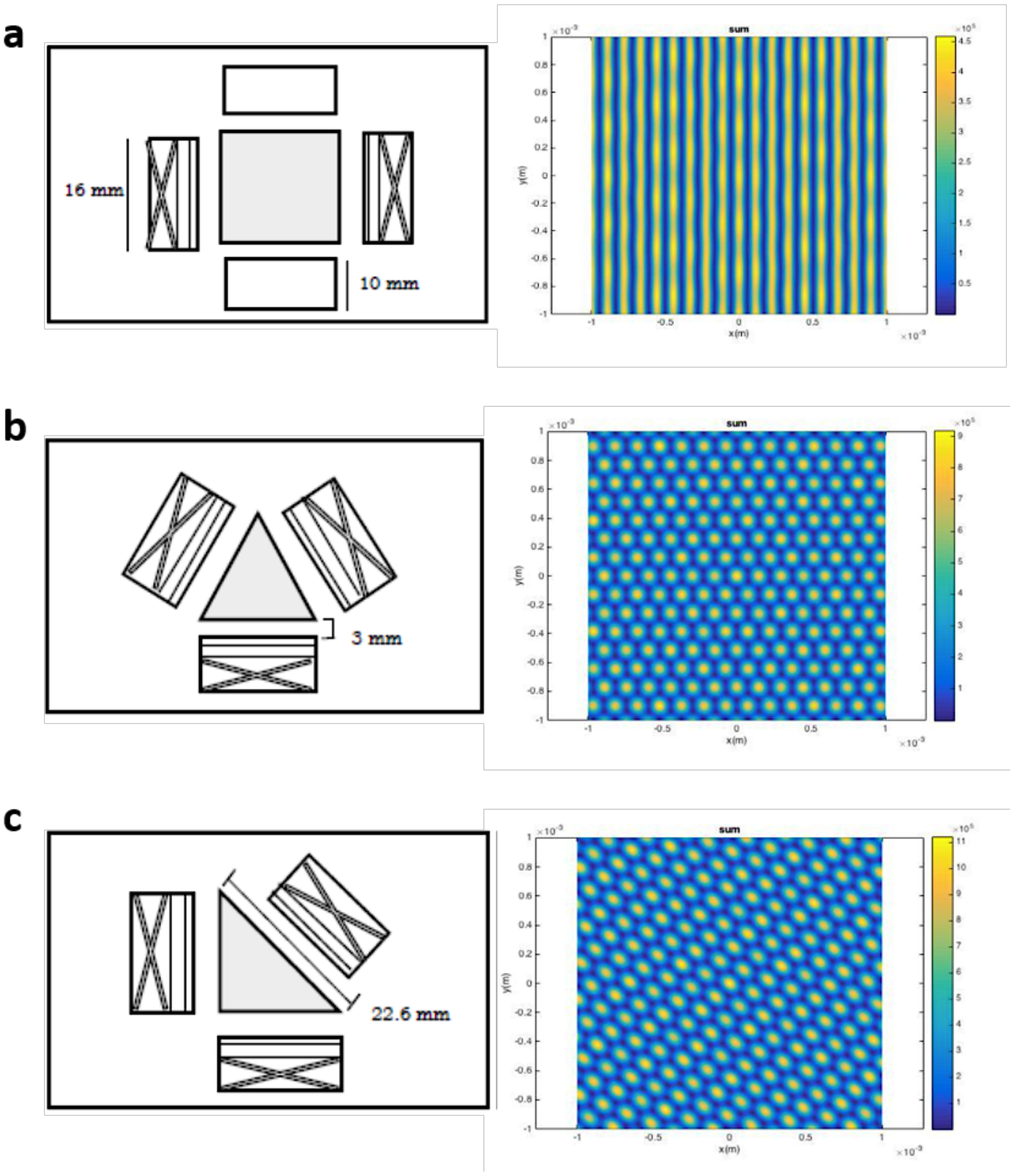

Figure 2.9: Diagrams of ultrasonic devices with a) square b) equilateral and c) angled triangle geometries with the central region modelled in MATLAB demonstrating a linear and honeycomb-like patterns with two and three front faced transducers, respectively, operated at 6.74 MHz and 5V$_{pp}$. High acoustic pressure is shown in blue and low in yellow.

The operating resonant frequency of the piezoelectric transducers previously obtained by the impedance measurements, density of water, speed of sound in water, density and radius of the polystyrene microspheres were the parameters considered for the computational code. Each piezoelectric transducer was modelled as a series of point sources, better known as Huygens Principle. Additionally, a Fast Fourier transform was performed employing the obtained images from the experiments with the polystyrene microspheres in phosphate buffer saline (PBS) to analyse the acoustic patterns in ImageJ (Figure 2.10 **B**).

The second step was to evaluate the cellular trapping with the ultrasonic devices. As mentioned before, HeLa cells were employed after being trypsinized and suspended in PBS. Successful honeycomb-like patterns were achieved in the central cavity of the equilateral triangle ultrasonic device (Figure 2.11) where the cells were stably trapped at the pressure nodes. However, the patterning of HeLa cells was not as well defined as the polystyrene microspheres due to their compressibility. Previous studies have measured the compressibility of polystyrene microspheres and different types of cells (i.e., cancer and healthy) and have determined that, although both have a positive acoustic contrast factor, the moving speed towards the pressure nodes is different. They found that the cancerous cells have relatively high compressibility values ($>4X10^{-10}Pa^{-1}$) compared to the healthy cells ($<4X10^{-10}$ Pa^{-1}) while for the polystyrene microsphere it is between 2.1 and $2.4X10^{-10}Pa^{-1}$.[22-24] Possible explanations for the difference in the compressibility of the cancerous and healthy cells is due to the changes in stiffness. Cancerous cells are less stiff and have a weaker cytoskeletal structure associated with the partial loss of microtubules [22,27] and the reduction of the F-actin filaments, both stress fibres along with the intermediate filaments, provide mechanical stability.[22,28] Furthermore, the acoustic trapping of red blood cells, with a compressibility value of 3.36 to $3.48X10^{-10}Pa^{-1}$,[22,25,26] has been demonstrated and mentioned that the cells were not considered as spheres and rigid particles as the acoustic theory defines.[10]

After successfully demonstrating HeLa acoustic trapping, slight modifications were made to the dimensions of the square ultrasonic device, as shown in Figure 2.12. The central region and the adjacent cavities, where the front-faced PZT are placed, were enlarged by 3 mm in order to fit an 18-mm coverslip to perform cellular adhesion studies after ultrasound exposure. The maximum volume in the central cavity is 800µl and was separated by a 3-mm PET walls from the electronics. The choice to continue using only the square ultrasonic device for further cellular adhesion studies was due to the fact that is widely described and computational modelled in previous works carried out within the University and a simpler pattern can be beneficial for initial cellular evaluations.

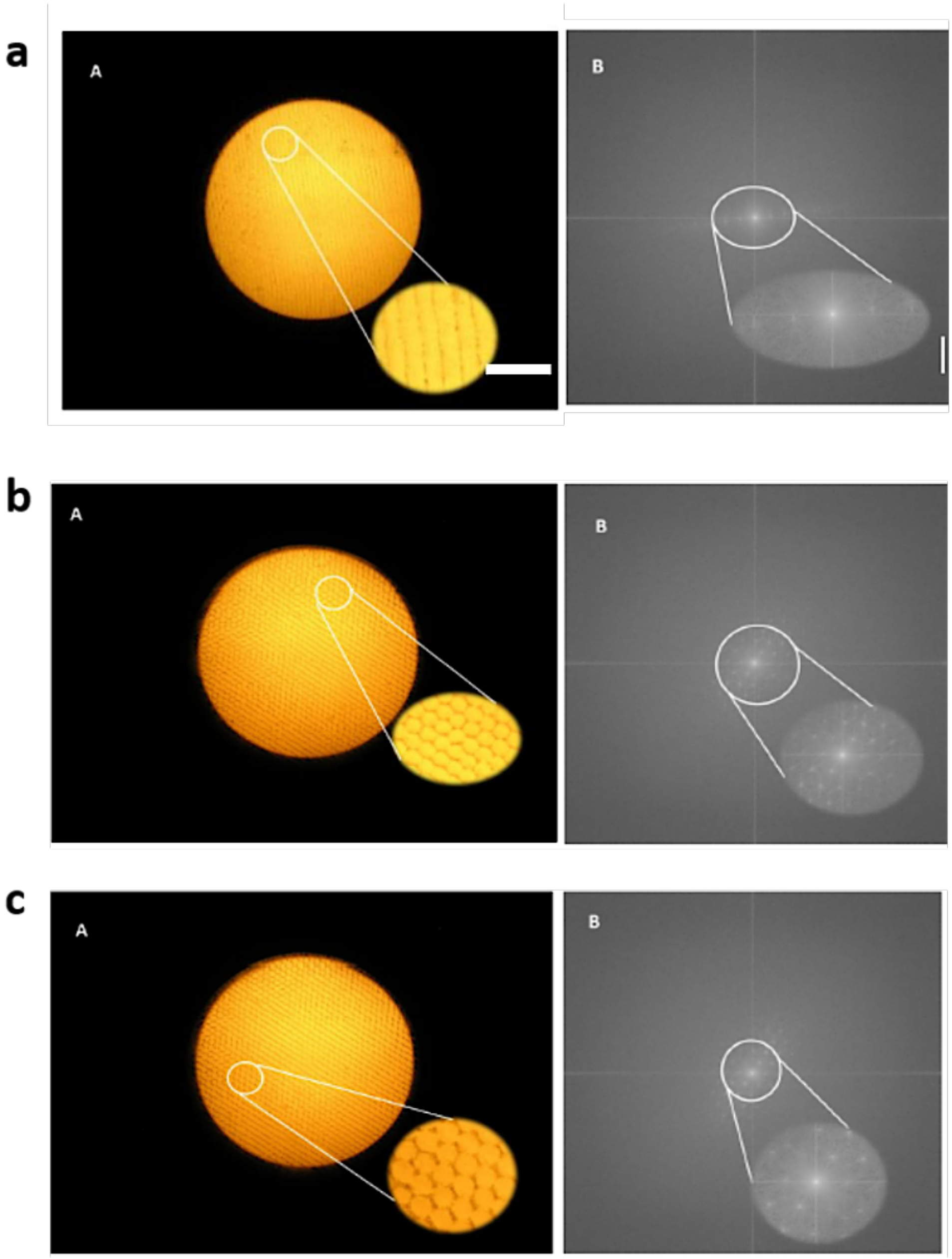

Figure 2.10: Polystyrene beads with a mean size of 8μm aligned in **a**) parallel and **b-c**) honeycomb-like patterns with two and three front faced transducers driven at 6.74 MHz and $5V_{pp}$. B) Fast Fourier transform analysis was made detecting the direction and orientation of each pattern. Scale bar 50μm closer view.

Impedance measurements were made for a new pair of PZT, and a mean resonant frequency of 6.84 MHz, identified in air, was obtained. A combination of ultrasound exposure with 7 V_{pp} for 5 min followed by 10 min of 2 V_{pp} was performed for a total of 15 min in the initial cell adhesion studies. A voltage of 10 V_{pp}, was used for longer periods of ultrasound exposure as previous literature reported a higher voltage (8 V_{pp}) for live cell trapping and a 24-hour kept alignment.[29] In order to adhere HeLa cells after ultrasound exposure and incubate the cells overnight for further observations, 18 mm coverslips were treated overnight with two different solutions: fibronectin and poly-l-lysine. Fibronectin (FN) is a glycoprotein of the extracellular matrix (EM) that binds to the transmembrane receptor proteins named integrins and plays a role in cell adhesion, migration, growth and the differentiation process.[30-32] The interaction of fibronectin with other macromolecules permits the cell adhesion and spreading *in vitro*.[33] Poly-l-lysine (PLL) is a widely used synthetic amino acid chain positively charged.[34] The cellular adhesion is possible due to the adsorption of the cationic poly-l-lysine molecules on the substrate and the interaction of the anionic sites of the cell membrane with the substrate.[35] The treated coverslips were washed and maintained in PBS prior experiments. Images of the FN-coated coverslips showed poor adherence of HeLa cells to the substrate after 15 min of ultrasound exposure, while for PLL-coated coverslips, good cell adhesion and a linear pattern were observed (Figure 2.13). A possible explanation for this result is that the adhesion to the FN-coated coverslips depends on the ability of the cells to interact with the FN molecules via integrins while being subjected to the acoustic radiation forces and the PLL cationic charges interact with the cell membrane anionic charge. Previous literature have reported conformational changes of the FN molecules after being adsorbed on different substrates affecting their biological activity and ultimately leading to receptor-ligand affinity modifications.[36-41] Furthermore, the FN surface density on the coverslip and the short time left for cell deposition may be other possible causes for the poor cell attachment.

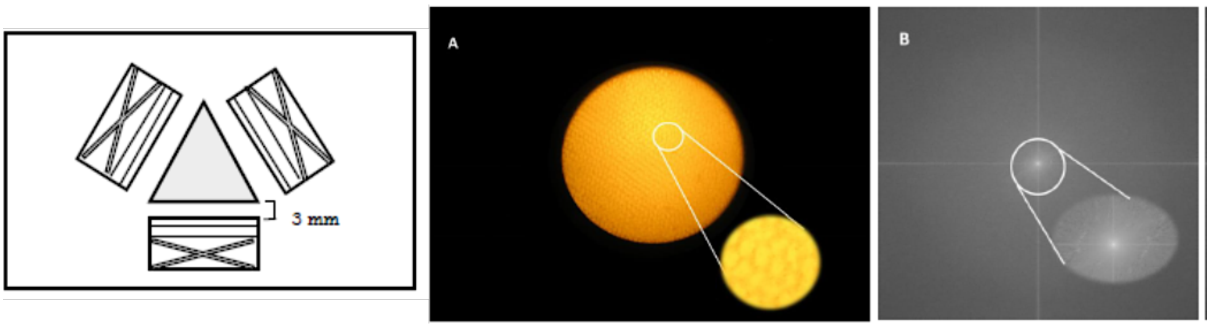

Figure 2.11: **A**) HeLa cells in PBS aligned in a honeycombs-like pattern employing the equilateral triangle ultrasonic device. The frequency of the three-front faced piezoelectric transducers was 6.74 MHz at 5V_{pp}. **B**) Fast Fourier transform is shown to analyse the obtained pattern.

These results showed that the cell adhesion to PLL-coated coverslips is the treatment to follow. Also, two HeLa cell concentrations (5x10^4 and 5x10^5 cells ml^{-1}) were tested in order to obtain a linear patterning with a little distance separating the cells instead of cell agglomerations trapped in the same pressure node, being 5x10^5 cells ml^{-1} the ideal cell concentration for this ultrasonic device. A further 30 min and 1-hour continuous ultrasound exposure were tested, following the previous work from Gesellchen *et al,* [29] and the attached HeLa cells were transferred to a 6-well plate for an overnight incubation. Images taken from both ultrasound exposure treatments with a voltage of 10 V_{pp} demonstrated that linear patterning was achieved, however, the cells from the 1-hour ultrasound treatment presented the morphology of non-viable cells and cell debris was observed in the medium (Figure 2.14). Other voltages were not tested for the 30 min and 1-hour ultrasound exposure as 10 V_{pp} was taken as the closest voltage used for continuous exposure from previous works. [29,50]

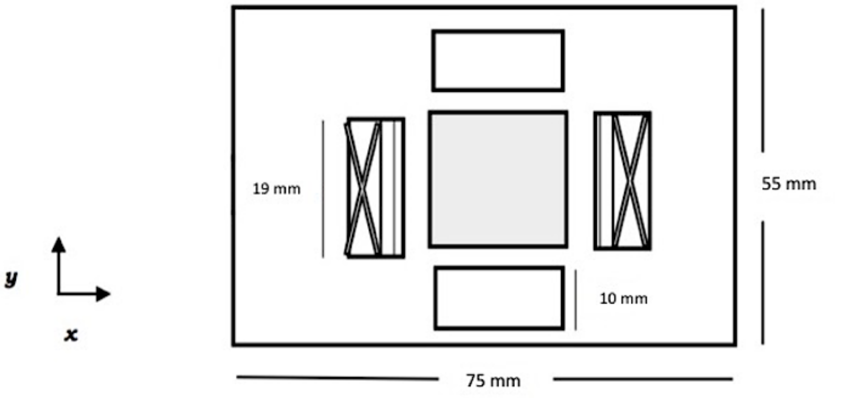

Figure 2.12: Square device with modifications. A 19 mm central chamber (shown in grey) where the suspended cells are aligned and 4 adjacent cavities where the two active transducers are placed front face.

After the 30 min and 1-hour acoustic exposure of HeLa cells with an overnight incubation, the linear patterning was kept. A second ultrasonic exposure and alignment of the daughter cells was proposed to form a mesh-like structure after the 24-hr incubation. The daughter cells are denominated as the product of the mitotic division of the parental cells that were previously exposed and aligned. The alignment of the daughter cells was performed placing two opposite PZTs in the upper and lower cavities with reference to the central cavity. The active PZT were driven at a frequency of 6.7 MHz with a voltage of 10 V_{pp} for 30 min and 1 hr. Inverted microscope observations of the second ultrasonic exposures at both times showed no daughter cell alignment and cell viability studies, performed with Alamar Blue (AB), demonstrated a drastic decrease in viability for both treatments (further explained in Section 3.4.2). The idea of a second ultrasound exposure originated from previous work[29] that demonstrated a complex cell patterning in a “tartan” arrangement employing different configurations of active PZT in the same ultrasonic device. The hypothesis formulated was that HeLa cells enter into mitosis and focal adhesions in the cell membrane are lost where the cell adopts a spherical shape. The daughter cells resulting from this division, which have not yet fully adhered to the PLL substrate, are guided to the pressure nodes by the acoustic radiation forces. Dix *et al* [42] explored the dynamic adhesion changes that cells undergo throughout mitosis, since they enter until the daughter cells are formed. They observed that despite the disassembled and re-assembly of the focal adhesion complexes when entering the mitosis, the cells remained attached to the substrate by stable retraction fibres located under the cell body (Figure 2.15).[44] The ends of these thin fibres revealed having β1-integrins that remained at the same position where the lost focal adhesions were located. The β1-integrins serve as the molecular memory for the cell shape and adhesion pattern.[42,43] Finally, the formed daughter cells adhere to the substrate throughout mitosis due to long and thick fibres which also helped with the cell spreading.

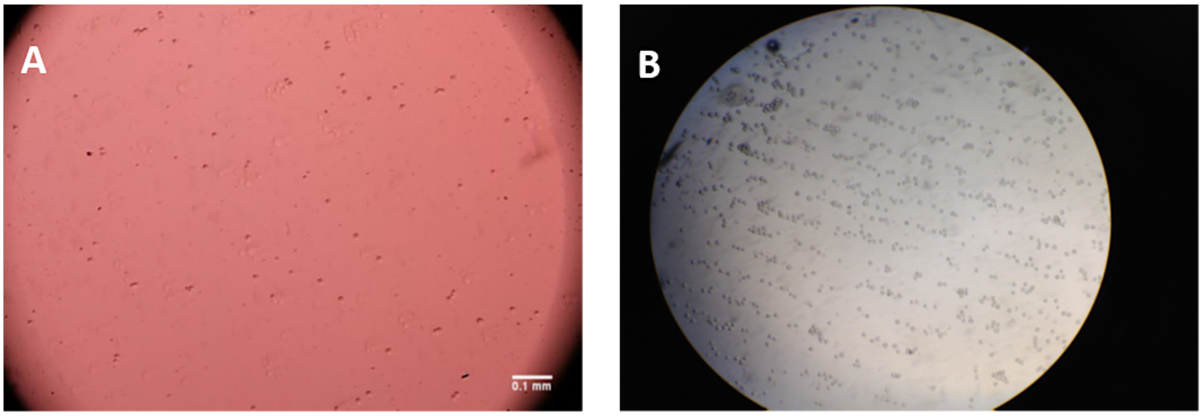

Figure 2.13: A) Fibronectin-coated coverslip with very few attached and aligned HeLa cells after ultrasound exposure. B) PLL-coated coverslip with a strong cell attachment and a clear linear patterning. Both samples were exposed for 15 min. Scale bars 0.1µm.

Furthermore, cellular adhesion mechanisms on charged polymeric substrates are known to be facilitated by the interaction of integrins with the adsorbed serum proteins from the cell medium. Previous literature has demonstrated differences in cell adhesion depending on the charge of the polymeric surfaces and the serum content in the cell medium. It was found that the adsorption of negatively charged proteins on the surface layer of HeLa cells is promoted by electrostatic forces on the cationic substrates when the cell medium is serum-free. For serum-containing cell media, cell adhesion in cationic polymeric substrates can be facilitated either by integrin receptor mechanism or a non-integrin receptor mechanism. By blocking the integrin receptor interaction with Ethylenediaminetetraacetic acid (EDTA), it was observed that HeLa cells adhered to the cationic substrate and the adherence force was over 800 pN, suggesting a stronger non-integrin interaction.[45] Couchman has reported that protein-protein interactions may also involve a type of ancient transmembrane proteoglycan receptors that are present in the focal adhesions named syndecans, however, further studies are necessary. [45,46]

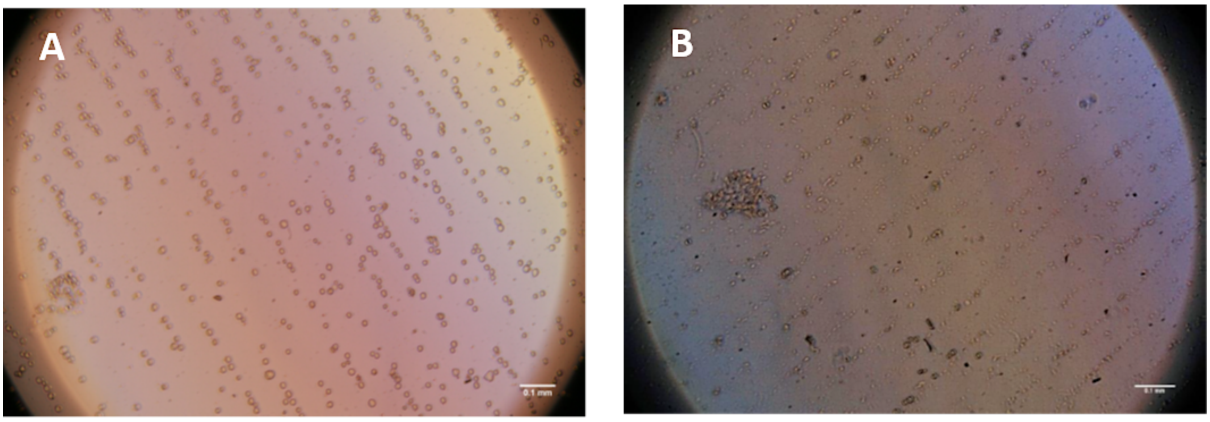

Figure 2.14: A) HeLa cell alignment and adherence after 30 min of ultrasonic exposure and B) after 1-hr exposure. In both exposed times, the employed cell concentration was the same ($5x10^5$ cells ml^{-1}) and the coverslip was coated with poly-l-lysine prior patterning. A clear change in cell morphology is observed between the samples. Scale bars 0.1μm.

Adhesion of HeLa cells to PLL-coated glass coverslips in the ultrasonic device is difficult to overcome using acoustic radiation forces once the cells have adhered. Previous work employing a similar square ultrasonic device, measured the forces exerted on 8 μm silica micro-beads when exposed to acoustic standing waves employing optical tweezers. A range of voltages (2–6 V_{pp}) were tested and showed these forces to be in the order of 0.5–1 pN V−1 with respect to the amplitude.[47] These acoustic forces are minimal in comparison with the adherence force of HeLa cells to PLL substrates mentioned above. Furthermore, Touhami and collaborators[48] have reported that adhesion forces of bacterial cells to PLL-coated surfaces are on the order of a few hundreds of pN, which are closer to the value obtained for HeLa cells.[45] The acoustic forces achieved with this ultrasonic device suggest being considerably less than 100 pN that are known to cause cellular rupture.[49]

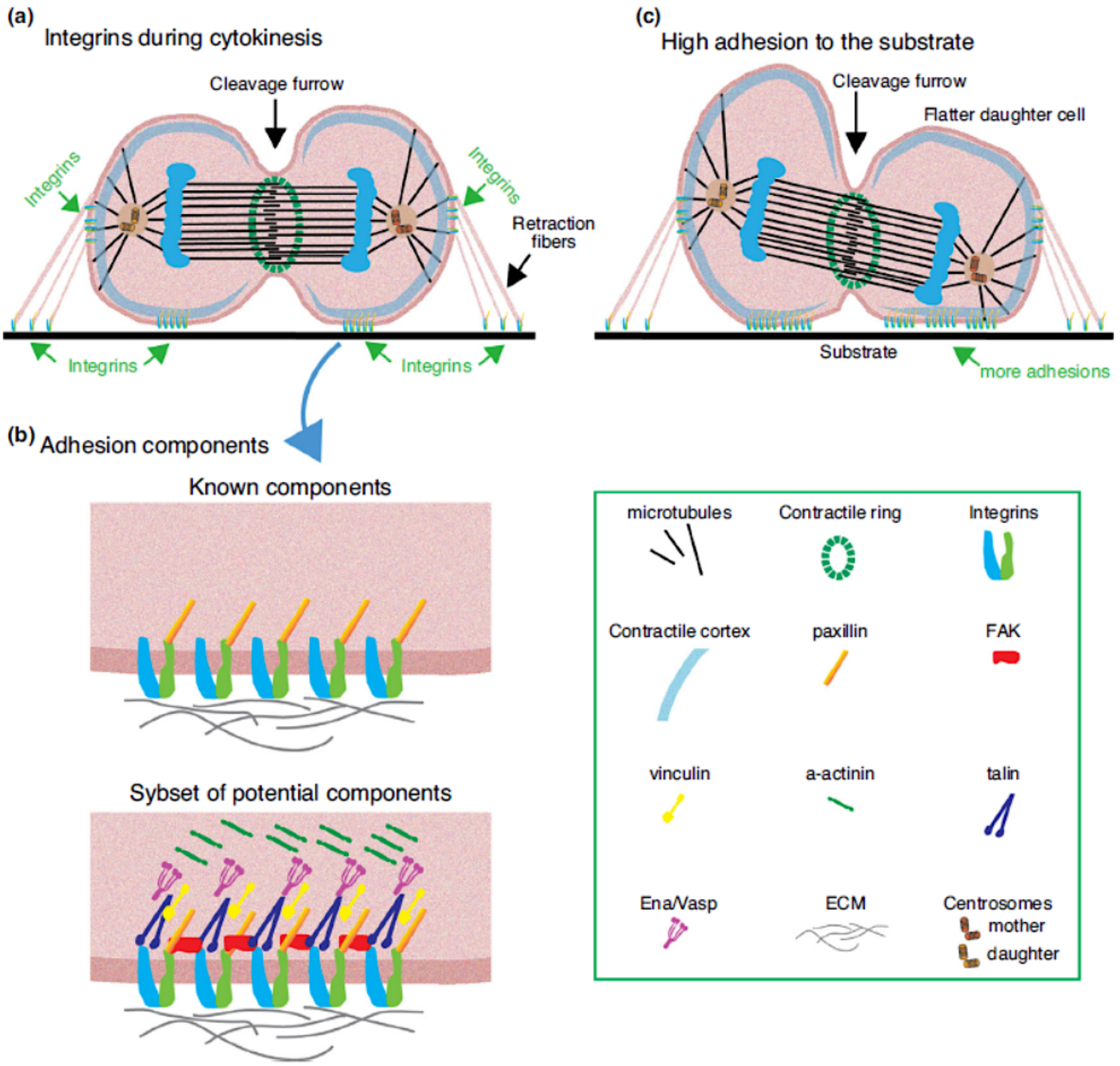

Current Opinion in Cell Biology

Figure 2.15: Diagram of a cell and adhesion components during cytokinesis. **a**) Lateral view of a cell in division indicating active integrins (green arrows) at the bottom of the cell body. **b**) a closer view at the bottom of the cell and the components involved to the substrate adhesion. **c**) further adhesion to the substrate from the mother centrosome from a daughter cell while dividing. Adapted from reference 44.

A further exploration of the ultrasonic device was performed using the same geometry. A new rectangular 2D PMMA acoustic trapping device was designed and manufactured while maintaining the dimensions of the PET device due to material availability. As mentioned before, the acoustic impedance of both materials is the same (3.4 MPasm^{-1}s) and sterile conditions can be achieved by cleaning the device with Virkon disinfectant and 70% ethanol prior experiments. The new PZT pair was coupled with ultrasound gel and pressed against the 3 mm-boundary walls with two wooden pieces glued together (Figure 2.16). Further explained in Section 3, cellular trapping was successfully carried out in 1D in parallel rows to the PZT, that were operated at an optimum temperature, voltage and close to their anti-resonance frequency, 6.77 MHz, determined previously by impedance measurements. The acoustic operation of this device is further explained in Section 2.3 where I assisted Dr Adrian Barnes in the experimental section and acoustic setup. Furthermore, Dr Adrian Barnes performed the SPICE modelling and the electrical impedance measurements.

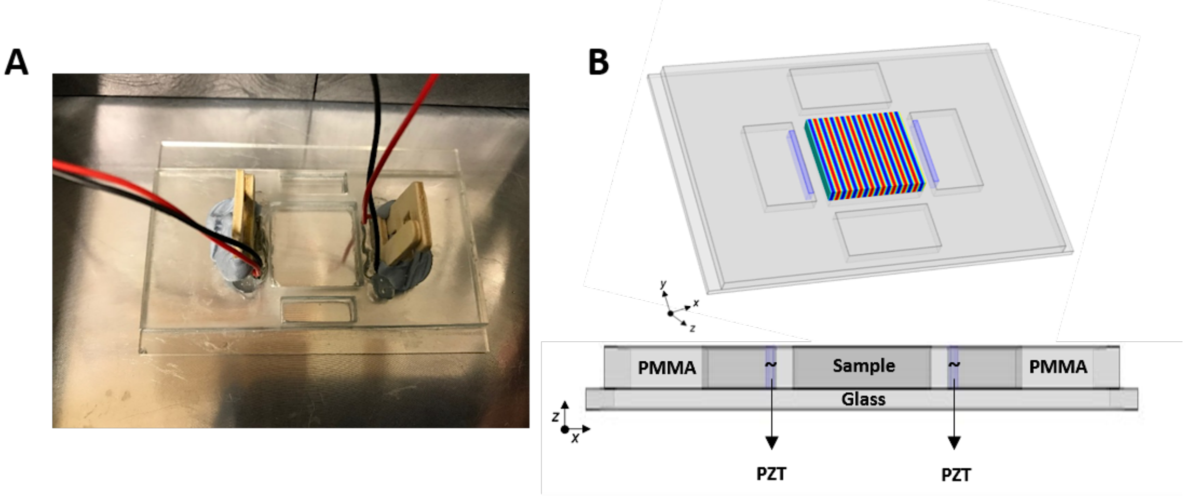

Figure 2.16: Diagram of the PMMA ultrasonic device. **A**) Picture of the 2D ultrasonic device with two wooden pieces pressing the PZT against the PMMA boundary walls. **B**) Top: 3D view of the device with the acoustic pressure field scheme in the central cavity. Bottom: a lateral view of the employed materials. Adapted from reference 1.

2.3 Operation of ultrasonic device

2.3.1 Acoustic resonant cavity

The square PMMA ultrasonic device was operated with a pair of active PZT with a reverse piezoelectric effect, where the piezoelectric material expands and contracts (rarefaction and compression) by applying an alternating voltage across the crystals at the same frequency as the applied signal. The PZT were operated closer to their anti-resonant frequencies (6.69 MHz to 6.74 MHz) generated by one signal generator in parallel and monitored with an oscilloscope. The ultrasonic device was operated at a cavity resonance of *w*/λ dominating the acoustic trapping field and were separated by approximately 0.1 MHz. Impedance measurements were performed and although a mean resonant frequency (6.77 MHz) was obtained, the frequency was adjusted in small steps of 0.01 MHz until HeLa cell alignment was observed in the inverted microscope. When a voltage of 10 V_{pp} was applied, the maximum electrical power delivered to the central cavity of the device was around 1 W. To achieve a maximum acoustic transmission, ultrasound gel was employed as a coupling layer to reduce the gap between the boundary walls and the PZT. Moreover, as demonstrated in the previous work,[18] the PMMA boundary walls acted as a damping barrier to the acoustic system maintaining a strong cellular trapping even if resonance changes occurred in the central cavity due to the absorption of more power at the cavity resonance where changes in the electrical properties of the device will be observed.

In a 1D central cavity device, acoustic pressure as a function of position can be represented in terms of the acoustical equivalent of the optical Fabry-Perot Cavity,

$$P \sim P_0 \frac{1}{\left(1-\sqrt{r_1 r_2 e^{-\alpha f^2 d}}\right)^2 + 4\sqrt{r_1 r_2} e^{-\alpha f^2 d} \sin^2\left(\frac{\pi d}{\lambda}\right)} \tag{1}$$

where r_1 and r_2 are the reflection coefficients of the PMMA walls, λ is the wavelength, α is the linear attenuation coefficient of the wave, d is the length of the cavity and f is the frequency of the acoustic wave. Modeling of the maximum pressure as a function of frequency at the central cavity is shown in Figure 2.17 for different values of $r =$

$r_1 = r_2$. The order of r values is typically from 0.8 – 0.9 if in a given device the employed transducers are away from their operating resonance frequency, where considerable changes in the peak pressure can be obtained with small frequency changes. As further mentioned in Section 3.3, the PZT are also a heating source to the acoustic system and the magnitude of the USW and the velocity of sound in the employed fluid are dependent on the temperature. The ultrasound gel was placed in between the PMMA walls and the PZT, also acted as a heat sink to prevent sudden temperature increases and, therefore, the resonance frequency. This is a topic further discussed in Section 3.3 where a heating block was used as a temperature-control regulator and ensure the HeLa cell acoustic trapping.

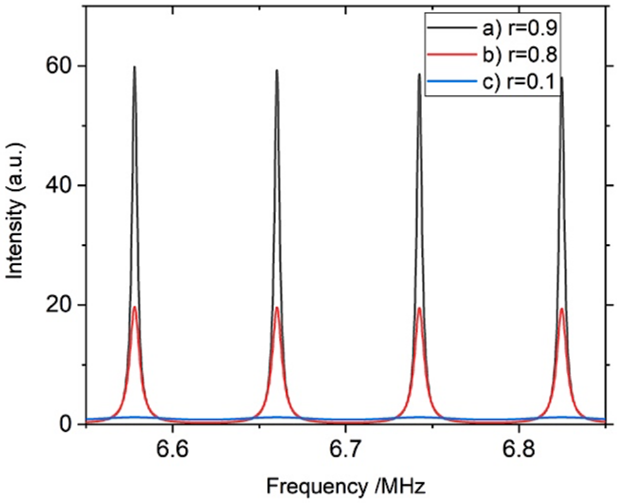

Figure 2.17: Maximum intensities as a function of frequency at the central cavity containing water with a length 18mm. a) a reflection coefficient of r=0.9 similar to the PZT walls away from the transducer resonance frequency, b) reflection coefficient of r = 0.8 corresponding to silica walls and c) for r = 0.1 corresponding to PMMA walls.

Experimentally, is difficult to establish and maintain the ultrasonic device at a certain cavity resonance due to the large uncertainty in the applied relative pressure to a trapped particle. Although the previous work[18] employed a needle hydrophone along the *x*-axis of the trapping zone and 4 main high-pressure peaks were obtained, any small change in voltage, frequency or temperature in a resonant ultrasonic device will result in large variations in pressure.

2.3.2 Electrical impedance measurements

Electric impedance |Z| measurements were performed under the same experimental conditions used for HeLa cell and microparticle in order to investigate the above-mentioned effects (large variations in acoustic pressure as a function of frequency and acoustic coupling). As shown in Figure 2.18 (**A**), when the central cavity is absent of fluid (water or cell media), the electrical impedance (red line and blue line) of the ultrasonic device is in agreement when both PZT are connected in parallel but with a slight difference in their resonant frequencies. However, once the fluid is added to the central cavity (black lines) an impedance modulation with a frequency separation of around 60 kHz is observed in accordance with the 18mm length of the cavity. These experimental results demonstrate that this ultrasonic device works at a strong cavity resonance and agrees with the observations of the previous work modelling similar geometry and same material of the ultrasonic device.[18] Therefore, substantial variations in the acoustic pressure with small changes in frequency (less than 10 kHz used for acoustic trapping) employing this ultrasonic device, can cause stress on the subjected HeLa cells.

Other possible variations in acoustic pressure were evaluated experimentally considering the volume of fluid in the central cavity. In Scholz *et al*,[18] computational analysis was carried out assuming it to be a full-fluid cavity reaching the top of the ultrasonic device, and the acoustic pressure variations at the bottom of the device were obtained by either leaving the central cavity in contact with air (soft boundary) or by placing a coverslip at the top (hard boundary) (Figure 2.7). However, acoustic pressure variations may also depend on the reflection effects at the top of the device and hence the height reached by the fluid at the central cavity. The variations in the impedance measurements are shown in Figure 2.18 (**B**) where the resonance fringes are the 20µL steps of water added to the central cavity, starting from slightly underfilled (<650µL) to slightly overfilled (~1mL).

Variations close to the anti-resonant frequency (<6.6MHz and >6.8MHz) were smaller than the changes around the frequency (6.77 MHz) where a strongest alignment of HeLa cells was observed, suggesting that variations in acoustic pressure at the bottom of the device where the HeLa cells are trapped, as previously shown in Figure 2.7, is also subjected to the volume of the fluid in the ultrasonic device.

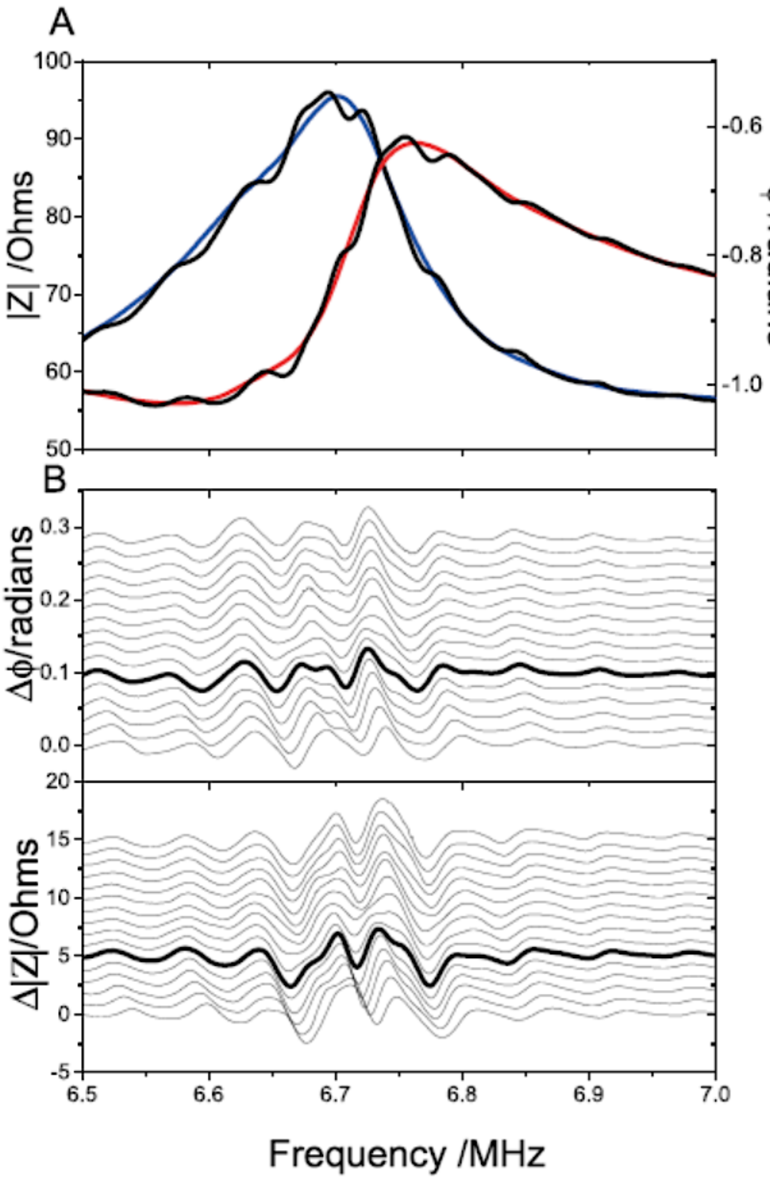

Figure 2.18: Graphs from (**A**) the electrical impedance |Z| (red line) and the phase angle ϕ (blue line) for both PZT connected in parallel with a fluid absent central cavity. The black lines depict the corresponding electric impedance once the water is added to the cavity. The variation of the impedance is clearly observed, with a period of ~60 kHz, due to cavity resonance. (**B**) Changes in the impedance measurements as the volume of water is increased in 20μL steps. The lowest line corresponds to the underfilled device (<650μL). The bold line corresponds to the level surface in which the device was used in the experimental measurements. The unfilled central cavity electrical impedance lines [red and blue lines in (**A**)] have been subtracted for (**B**) and

the measurements were offset by +0.05Ω (| Z |) and +0.001 radians (ϕ) for each 20μL step. The large variations in the impedance are observed close to the operating resonant frequency of the device (6.77 MHz).

Afterwards, a final evaluation of the acoustic pressure variations due to the acoustic coupling was made. The ultrasonic device, previously set up with the PZT coupled with ultrasound gel and pressed against the boundary walls with an empty central cavity, was left undisturbed overnight. After, the central cavity was filled with water and impedance measurements were made without additional disturbance or movement of the ultrasonic device, however, no impedance modulation was observed. The ultrasonic device was dismantled, and it was observed that the ultrasound gel had dried out and a very poor acoustic coupling was obtained between the PZT and the device. After cleaning the device and re-assembling it with a fresh layer of ultrasound gel new impedance measurements were made. The results obtained were the same as those shown in Figure 2.18 (**B**) for 6.77 MHz, which shows that adequate acoustic coupling must be ensured before conducting an experiment or measurement. Precise operating acoustic conditions are difficult to define, as many factors can contribute and therefore inconsistent results would be obtained.

Furthermore, by measuring the electrical impedance as a function of frequency, the resonant behaviour of the ultrasonic device can be explored. If the acoustic resonance is absent, then the impedance would correspond to two independent PZT connected in parallel. To test this behaviour, a 1D transmission line model in SPICE was performed to calculate the impedance for two PZT using the same experimental resonant frequencies (6.69 MHz and 6.74 MHz) (Figure 2.19). The results obtained from the modelling correspond to the electrical impedance measurements from Figure 2.18 (**A**) when there was no fluid in the central cavity. Moreover, in Figure 2.20 a 1D transmission line modelling was done including the fluid filled cavity and the PMMA boundary walls separating the central cavity and the PZT. For this test, the modelling results correspond to the behaviour of a resonant cavity separated from the PZT and to the impedance measurements at 6.77 MHz, depicted in bold lines in Figure 2.18 (**B**). The weaker interference effects are also observed in the smaller features of the modelling due to the reflections between the posterior face of the PZT and the PMMA boundary walls. If the whole central cavity was in resonance, then this would be the expected impedance measurement result.

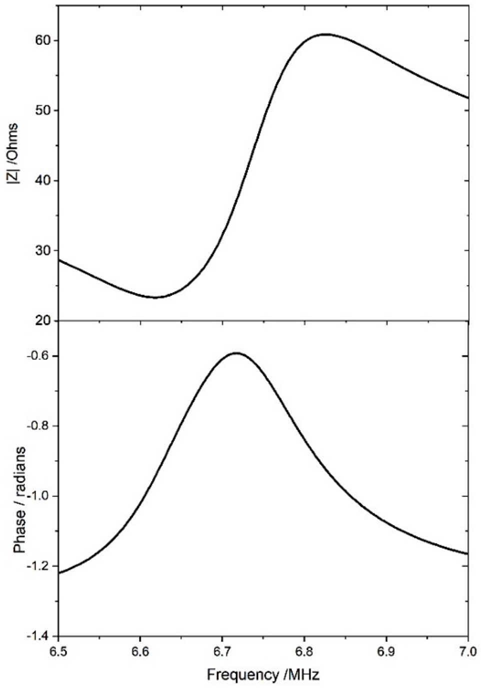

Figure 2.19: SPICE modelling of impedance was calculated for two PZT in the ultrasonic device with no fluid in the central cavity. This can be compared with the electrical impedance measurements shown in Figure 2.18 (A) with the red and blue lines.

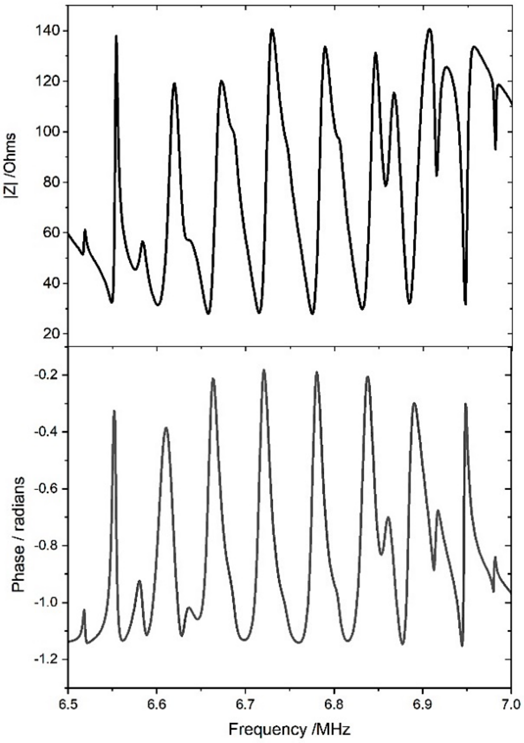

Figure 2.20: A calculation of the transmission line for the electric impedance of the ultrasonic device adding PMMA walls and a water filled central cavity.

These strong resonant effects in the whole central cavity have not been observed in the experimental results which is in agreement with previous work where a Finite Element Analysis was performed and showed that only a small volume closer to the bottom of the central cavity presented a strong resonant behaviour.[18] Therefore, a modification was made to the transmission line model, separating the device into two parts connected in parallel: a non-resonant part where the behaviour is similar as shown in Figure 2.17 and a resonant part which is shown in Figure 2.19. The impedance calculation resulting from the SPICE modelling is shown in Figure 2.21 which is similar to the observed impedance spectra in this ultrasonic device. The fraction of the radiating surface in the resonant part was set as 1/20 compared to the non-resonant part for this model. Strong variations in the acoustic pressure as a function of frequency were observed in the modelling results showing the characteristics of an acoustically resonating central cavity with the position, width, electric impedance sharp dips and peaks in the phase angle.

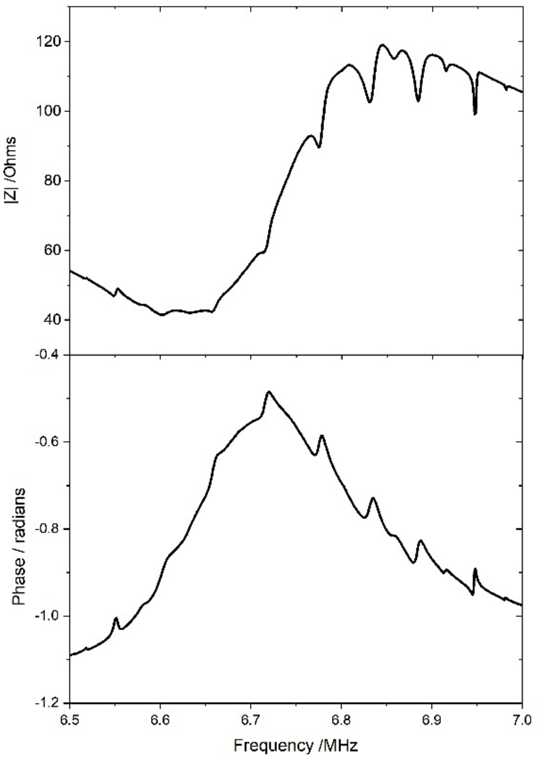

Figure 2.21: Modified transmission line calculation of the ultrasonic device assuming the fraction is 1/20 of the resonant part to non-resonant part of the cavity.

Furthermore, a comparison of the calculated impedance measurements with the experimental measurements was made. Impedance measurements were made when the PZT are in contact with the fluid in the central cavity, meaning no PMMA boundary walls are modelled. As shown in Figure 2.22, the sharp dips in the electrical impedance (|Z|) and the peaks in the phase angle (φ) are similar to the previously calculated in Figure 2.21. The same modelling is shown in Figure 2.23 but emphasising the effect of the cavity resonance due to the removal of the broad background of the PZT impedance. The very narrow sharp dips and peaks in the phase angle of the resonance correspond to the active layer of the ultrasonic device and is in agreement with the above mentioned where subtle variations in the operating conditions of the device will lead to great variations in acoustic pressure. Large variations in the impedance were observed when the central cavity was under and over filled with water while near the optimum volume (~650-700μl) where the strongest impedance response was obtained.

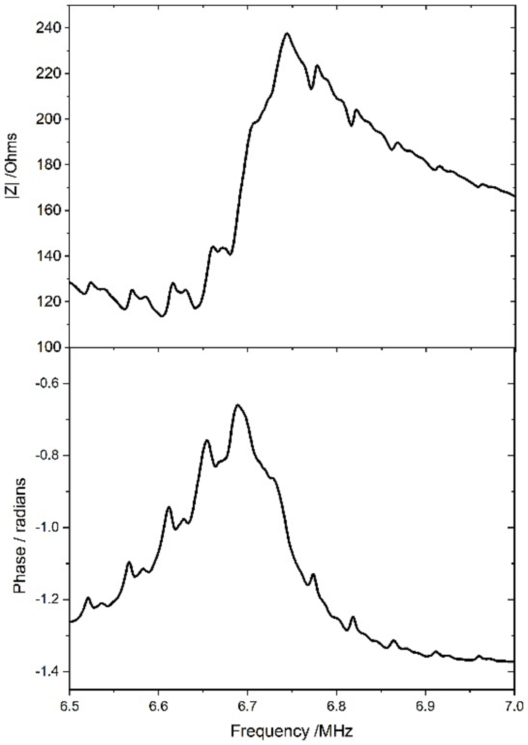

Figure 2.22: Impedance measurements for a 1D ultrasonic device without boundary PMMA walls and the PZT are in direct contact with the fluid at the central cavity.

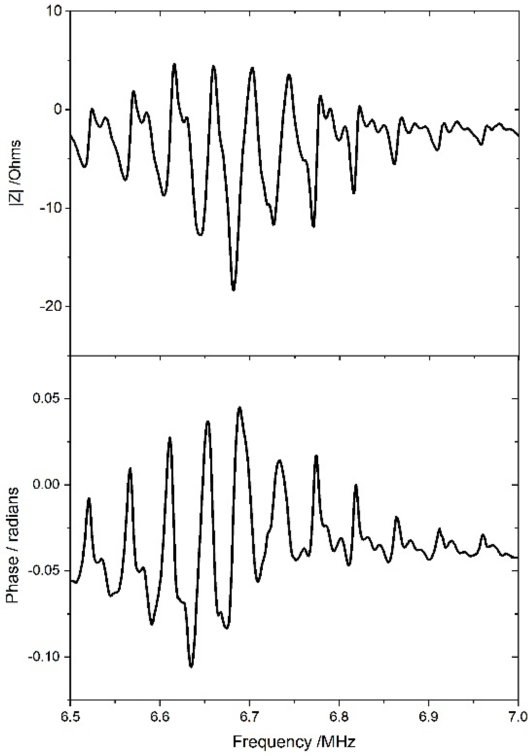

Figure 2.23: Smooth background from the PZT resonances has been removed from the data shown in Figure 2.22 emphasising the effect from the cavity resonance.

Additionally, impedance measurements as the volume of water is increased in 100µL steps from the baseline volume (~650-700µl) in the experiments with HeLa cells and microspheres were done following what is shown in Figure 2.18. The results depicted in Figure 2.24 showed what Scholz *et al* [18] reported previously where a strong resonance is found in a small volume closer to the bottom of the ultrasonic device. As done before, Figure 2.25 shows impedance measurement when the background contributed by the PZT resonances is removed. In both Figures (2.24 and 2.25) the width of the dips and the peaks correspond to the PZT separation in the device.

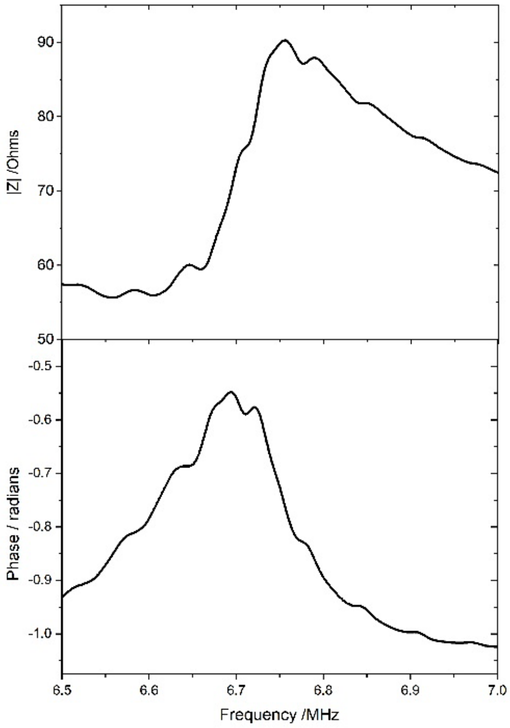

Figure 2.24: Impedance measurements for the ultrasonic device when the water volume is increased with 100µL steps until a level surface is reached.

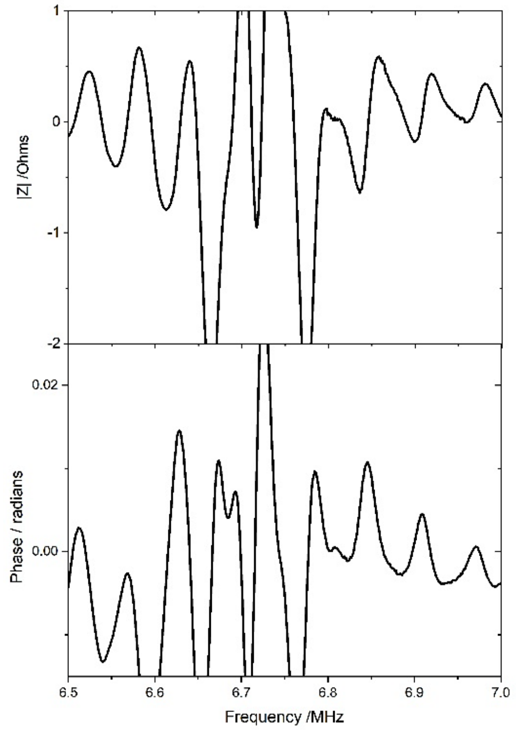

Figure 2.25: The same data shown in Figure 2.24 after removing the background from the PZT resonances.

2.4 Chapter conclusions

In the results presented, the spacing and the sharpness of the peaks are consistent with the high resonance cavity when two PZT are opposite each other. The small variations in the peaks are due to the reflections from the PMMA boundary walls (Figure 2.21) and with higher frequencies the resonance of the device appears to be stronger. However, there is a great variation in the impedance measurements when the volume in the central cavity is modified and the ultrasonic device is built with or without boundary walls. These variations lead to difficulties when performing consistent and reliable experiments on cells and microparticles. Moreover, the operation principle of this type of ultrasonic trapping devices (USW) in particular for particle manipulation at the employed frequencies is detailed in previous work.[51] Manipulation is when the particles are spatially translated independently by changing the relative phase of the PZT and the requirements are that the PZT need to operate precisely at their resonant frequency where there are almost no reflections or a quarter of a wavelength of anti-reflection coating is employed. This particular ultrasonic device employs PZT that can be poorly matched and no anti-reflection coatings are used. For this ultrasonic device, strong particle trapping can be achieved as demonstrated before using two opposed and well-coupled PZT creating multiple reflections between them. Furthermore, special attention to the construct of the device and the acoustic properties of the materials (glass, PMMA, ultrasound gel, etc) should be considered when operating at an optimum acoustic condition.

2.5 References

1. V. Levario-Diaz, P. Bhaskar, M.C. Galan and A.C. Barnes, *Sci Rep*, 2020, **10**, 8493.
2. P. Glynne-Jones, R.J. Boltryk and M. Hill, *Lab Chip*, 2012, **12**, 1417-1426.
3. B.W. Drinkwater, *Lab Chip*, 2016, **16**, 2360-2375.
4. S. Peterson, G. Perkins and C. Baker, *IEEE/Eight Annual Conference of the Engineering in Medicine and Biology Society*, 1986, 154.
5. T. Laurell, F. Petersson and A. Nilsson, *Chem. Soc. Rev.*, 2007, **36**, 492-506.
6. A. Kundt and O. Lehmann, *Ann. Phys. Chem.*, 1874, **153**, 1.
7. A.P. Sarvazyan, O.V. Rudenko and W.L. Nyborg, *Ultrasound in Med. & Biol.*, 2010, **36** (9), 1379–1394.
8. N.V. Baker, *Nature*, 1972, **239** (5372), 398-399.
9. W.T. Coakley, D.W. Bardsley, M.A. Grundy, F. Zamani and D.J. Clarke, *J. Chem. Tech. Biotechnol.*, 1989, **44**, 43-62.
10. H.M. Hertz, *Applied Physics Reviews*, 1995, **78** (8), 4845-4849.
11. C.R.P. Courtney, C.-K. Ong, B.W. Drinkwater, P.D. Wilcox, C. Demore, S. Cochran, P. Glynne-Jones and M. Hill, *J. Acoust. Soc. Am.*, 2010, **128** (4).
12. R. Esche, *Acoustica*, 1952, **2**, 208-218.
13. A.L. Bernassau, C.-K. Ong, Y. Ma, P.G.A. MacPherson, C.R.P. Courtney, M. Riehle, B.W. Drinkwater and D.R.S. Cumming, *IEEE Trans Ultrason Ferroelectr Freq Control*, 2011, **58** (10), 2132-2138.
14. A.L. Bernassau, F. Gesellchen, P.G.A. MacPherson, M. Riehle and D.R.S. Cumming, *Biomed Microdevices*, 2012, **14** (3), 559-564.
15. A.L. Bernassau, P.G.A. MacPherson, J. Beeley, B.W. Drinkwater and D.R.S. Cumming, *Biomed Microdevices*, 2013, **15**, 289-297.
16. A.L. Bernassau, C.R.P. Courtney, J. Beeley, B.W. Drinkwater and D.R.S. Cumming, *IEEE International Ultrasonics Symposium (IUS)*, 2013, 1903-1906.
17. M.-S. Scholz, B.W. Drinkwater and R.S. Trask, *Ultrasonics*, 2014, **54**, 1015-1019.
18. M.-S. Scholz, B.W. Drinkwater, T.M. Llewellyn-Jones and R.S. Trask, *IEEE Trans Ultrason Ferroelectr Freq Control*, 2015, **62** (10), 1845-1855.

19. S.S Rogers, T.A. Waigh, X. Zhao, and J.R. Lu, *Phys. Biol.*, 2007, **4** (3), 220–227.
20. J.A. Slotwinski, Handbook of Reference Data for Nondestructive Testing. DS68. *ASTM International*, 2002.
21. G. Destgeer, J.H. Jung, J. Park, H. Ahmed, K. Park, R. Ahmad and H.J. Sung, *RCS Adv*, 2017, **7**, 22524.
22. D. Hartono, Y. Liu, P.L. Tan, X.Y.S. Then, L-Y.L Yung and K-M. Lim, *Lab Chip*, 2011, **11**, 4072.
23. F. Petersson, L. Aberg, A.M. Sward-Nilsson and T. Laurell, *Anal. Chem*., 2007, **79**, 5117–5123.
24. S. Hirawa, T. Masudo and T. Okada, *Anal. Chem*., 2007, **79**, 3003–3007.
25. M.A.H. Weiser and R.E. Apfel, *J. Acoust. Soc. Am*., 1982, **71**, 1261–1268.
26. K. K. Shung, B. A. Krisko and J. O. Ballard, *J. Acoust. Soc. Am*., 1982, **72**, 1364–1367.
27. M. Lekka, P. Laidler, D. Gil, J. Lekki, Z. Stachura and A. Z. Hrynkiewicz, *Eur. Biophys. J*., 1999, **28**, 312–316.
28. Q.S. Li, G.Y.H. Lee, C.N. Ong and C.T. Lim, *Biochem. Biophys. Res. Commun*., 2008, **374**, 609–613.
29. F. Gesellchen, A.L. Bernassau, T. Dejardin, D.R.S. Cumming and M.O. Riehle, *Lab Chip*, 2014, **14**, 2266.
30. W. Yi, E. Xiao, R. Ding, P. Luo and Y. Yang, *Oncology Reports*, 2016, **36**, 3145-3153.
31. M.D. Pierschbacher and E. Ruoslahti, *Nature*, 1984, **309**, 30-33.
32. R. Pankov and K.M. Yamada, *J. Cell Sci*, 2002, **115**, 3861-3863.
33. E. Ruoslahti, *Cancer Metastasis Reviews*, 1984, **3**, 43-51.
34. Poly-L-Lyisne A-005-C ©2020, Merck, UK.
35. D. Mazia, G. Schatten and W. Sale, *J. Cell Biol*., 1975, **66**, 198-200.
36. A.J. Garcia, M.D. Vega and D. Boettiger, *Molecular Biology of the Cell*, 2017, **10** (3), 785-798.
37. F. Grinnell and M.K. Feld, *J. Biomed. Mater. Res*., 1981, **15**, 363-381.
38. D.J. Iuliano, S.S. Saavedra and G.A. Truskey, *J. Biomed. Mater. Res*., 1993, **27**, 1103-1113.
39. P.A. Underwood, J.G. Steele and B.A. Dalton, *J. Cell Sci*., 1993, **104**, 793-803.

40. D.K. Pettit, A.S. Hoffman and T.A. Horbett, *J. Biomed. Mater. Res.*, 1994, **28**, 685-691.
41. A.J. Garcia, P. Ducheyne and D. Boettiger, *J. Biomed. Mater. Res.*, 1998, **40**, 48-56.
42. C.L. Dix, H.K. Matthews, M. Uroz, S. McLaren, L. Wolf, N. Heatley, Z. Win, P. Almada, R. Henriques, M. Boutros, X. Trepat and B. Baum, *Developmental Cell*, 2018, **45**, 132-145.
43. J.G. Lock, M.C. Jones, J.A. Askari, X. Gong, A. Oddone, H. Olofsson, S. Goransson, M. Lakadamyali, M.J. Humphries and S. Stromblad, *Nature Cell Biology*, 2018, **20**, 1290-1302.
44. N. Taneja, L. Rathbun, H. Hehnly and D.T. Burnette, *Curr Opin Cell Biol.*, 2019, **56**, 45-52.
45. T. Hoshiba, C. Yoshikawa and K. Sakakibara, *Langmuir*, 2018, **34**, 4043-4051.
46. J.R. Couchman, *Nat Rev Mol Cell Biol.*, 2003, **4** (12), 926-937.
47. P.G. Bassindale, D.B. Phillips, A.C. Barnes and B.W. Drinkwater, *Appl. Phys. Lett.*, 2014, **104**, 163504.
48. A. Touhami, M.H. Jericho, J.M. Boyd and T.J. Beveridge, *J. Bacteriol.*, 2006, **188**, 370-377.
49. A. Pierres, P. Eymeric, E. Baloche, D. Touchard, A-M. Benoliel and P. Bongrand, *Biophysic J.*, 2003, **84**, 2058-2070.
50. I. Iranmanesh, H. Ramachandraiah, A. Russom and M. Wiklund, *RCS Adv*, 2015, **5**, 74304.
51. C.R.P. Courtney, C.-K. Ong, B.W. Drinkwater, A.L.Bernassau, P.D. Wilcox and D.R.S. Cumming, *Proc. R. Soc. A.*, 2012, **468**, 337-360.

3 Effect of acoustic standing waves on cellular viability and metabolic activity

This chapter is also based on the work published in *Scientific Reports* of which I am first author.[1] The experimental methods in this chapter were conceived alongside with Professor Carmen Galan and Dr Adrian Barnes. I performed all cellular deposition studies, systematic temperature-dependent measurements and cell viability and metabolic activity analysis during and after ultrasound exposure at the School of Chemistry, University of Bristol. The 1D ultrasonic device previously described in Chapter 2 was employed for all experiments.

3.1 Introduction

In the previous chapter, the characterization of the 1D ultrasonic device was performed in order to achieve a clear and reliable trapping of microparticles and cells. However, concerns were raised about the possible destructive effects that ultrasound and second-order factors i.e., cavitation, acoustic streaming, temperature and radiation forces have on the subjected viable cells. Systematic and optimisation studies were therefore performed and, cell viability and metabolic activity in a healthy cell line (Human Dermal Fibroblasts, HDF) and in a cancer cell line (HeLa) were measured. In this chapter, temperature-controlled measurements were made as a function of ultrasound exposure time and voltage, ranging from 4 V_{pp} to 10 V_{pp}. Moreover, a further exploration of acoustic streaming and cavitation phenomena was performed employing microscopy imaging, while for acoustic radiation forces, absolute pressure maps were taken from previous work [2] performed at the School of Engineering, University of Bristol. The obtained results demonstrate that in order to maintain high cell viability in both cell lines, the ultrasonic device has to be driven at a sinusoidal signal of minimum voltage and matched carefully to accomplish a strong cavity resonant operation (previously explained in Chapter 2). Furthermore, both cell lines were found to maintain their viability and metabolism after 15 min of ultrasonic exposure, while detrimental effects on cell metabolism and viability were observed due to small changes in temperature and voltage during shorter periods of acoustic exposure.

3.2 Cellular alignment deposition

In the previous chapter, the design, manufacture and characterisation of the operation mode of the 1D ultrasonic device was presented and discussed. This ultrasonic device was designed considering the size range for cells and particles to be trapped in the pressure nodes (>1µm). Acoustic primary radiation forces are weaker when trapping smaller particles (<1µm) and other forces such as acoustic streaming will dominate due to the acoustic force being proportional to the volume of the particles.[3] As mentioned in Section 1.1.2 there are three different types of acoustic streaming (Rayleigh, Schlichting and Eckart) that can influence the particle trapping. This phenomenon is caused by the absorption of acoustic energy in viscous fluids, creating vortices that are flow patterns present in the trapping region. In contrast to microfluidic devices where Rayleigh and Schlichting streaming occur closer to the boundaries of the device and the vortices are λ/4, [3] experimental observations while performing particle trapping showed that Eckart streaming occurs in this device (Figure 3.1 **B**). Eckart streaming is produced when the length scale of the fluid cavity (l) is larger than the wavelength of the acoustic wave (λ) and the circular flows are formed perpendicular to the front face of the PZT with the main fluid jet traveling in the direction of the acoustic waves propagation (Figure 3.1 **A**).[5,6] Moreover, Eckart streaming can be generated with standing acoustic waves although the velocity of the flow is lower due to the steady Reynolds stress from opposite directions partly cancelling each other. [6]

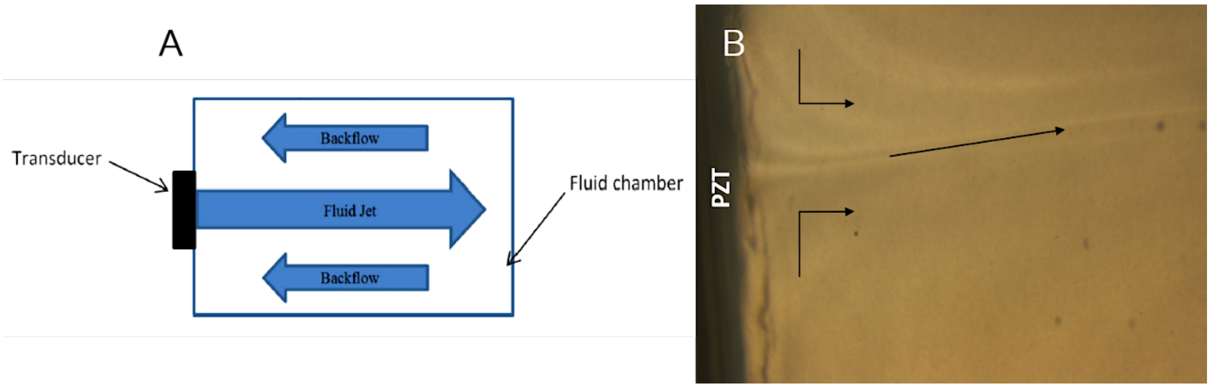

Figure 3.1: (**A**) Diagram of Eckart streaming direction of the main fluid jet and the back flow.6 (**B**) Picture of Eckart streaming present in the central cavity of the ultrasonic device. The main fluid jet is depicted in the centre perpendicular to the front face of the PZT. Eckart streaming for this device is negative for cell and particle trapping as

they will be trapped in the bulk of the fluid and not at the bottom where the pressure nodes are formed.

Previous work reduced Eckart streaming in a multi-transducer acoustic device by adding a layer of agar at the bottom of the device. The height of the fluid at the central cavity was minimised and a very clear particle trapping (6 and 10 μm) was observed with the lowest volume of water-particle in the central cavity (0.6 ml). [3] Gravity begins to affect the trapping when particles are bigger than 20 μm in the trapping area and the rate of deposition depends on the density of the particles in relation to the density of the employed fluid.[4] However, in the previous work carried out by Bernassau et al, [3] gravity helped in the sedimentation of 6 μm and 10 μm particles and, the acoustic primary radiation forces (PRF) along with the slow acoustic streaming drag force guided the particles to the pressure nodes while for the 1 μm particles, acoustic streaming was the dominant force over the PRF. For this ultrasonic device, HeLa cells with a mean diameter of 12 μm were employed to evaluate the possible influence of acoustic streaming on cellular trapping. As shown in Figure 3.2 **B**, strong HeLa cell trapping was observed at the bottom of the device although Eckart streaming affected in the positioning of the cells in the pressure nodes while the cells settled at the bottom. These experimental observations were similar to the previous work[3] for the lowest volume, where the fluid volume in this device was 650-700 μl. Furthermore, the HeLa cell alignment agreed with the modelling predictions previously made for the acoustic pressure distribution (Figure 3.2 **A**).

Additionally, ultrasound can also cause cavitation, which is the formation and collapsing of bubbles in the media.[1,32] This phenomenon is dependent on the frequency and the intensity of the ultrasound exposure and since the effect is proportional to $1/\sqrt{f}$, at high frequencies. cavitation will decrease. Furthermore, as this is a standing wave acoustic device, the bubbles produced from the cavitation will be guided towards the anti-pressure nodes opposite to the cells which are guided to the pressure nodes, therefore, it is expected that the cells will not be affected as it is at the bottom of the device where the alignment takes place. It was not possible to obtain optical images of the possible bubbles formed in the device, however, as the frequencies employed in this ultrasonic device were higher than 1 MHz, it can be stated that there is no cavitation produced.[1,33]

HeLa cell deposition studies were then performed to evaluate the deposition rate to the bottom of the device where the acoustic trapping takes place due to the high-pressure distribution (previously explained in Section 2.2.2) and to optimise acoustic parameters for cellular trapping. HeLa cells were seeded at a concentration of 5×10^4 cells ml^{-1} in the central cavity and the deposition rate was timed and video recorded under optical microscope observation. The total time for the cells to deposit at the bottom of the device was 3 min without any acoustic input. As the cell concentration increases, the cell agglomeration will increase and diffuse linear patterning will be observed.

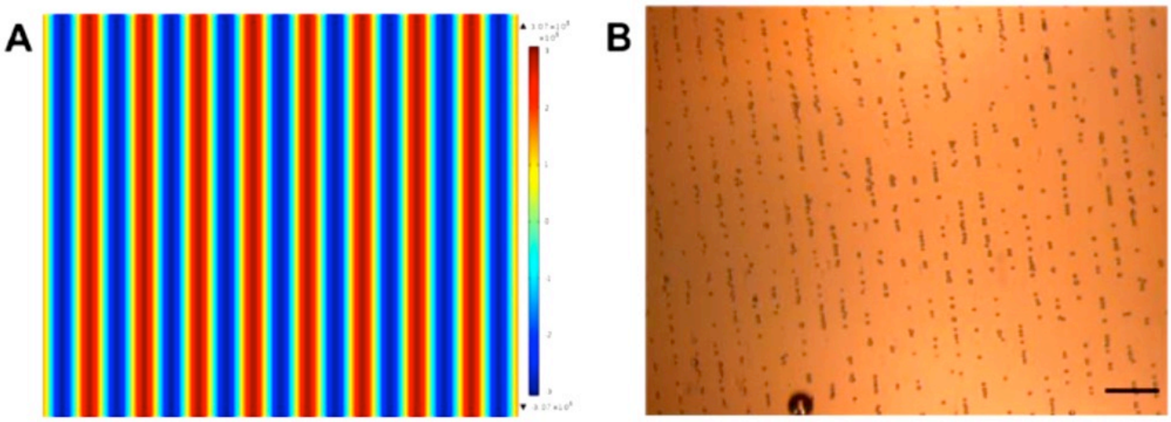

Figure 3.2**:** (**A**) Comsol modeling of the acoustic pressure distribution in the central cavity when two PZT are active. As depicted in the pressure scale, red lines are the pressure nodes and blue lines are the anti-pressure nodes. (**B**) Linear HeLa cell patterning is achieved by trapping the cells in the pressure nodes of the USW. The scale bar is 100 µm and the objective was 4X. Adapted from reference 1.

Then, three different acoustic exposure times were tested (5, 10 and 15 min) with a pair of PZTs driven at a frequency of 6.77 MHz with an amplitude of 6 V_{pp} and the produced parallel lines were separated by a wavelength of 110 µm. The hypothesis behind testing shorter acoustic exposure times is that cell viability will be maintained since previous experimental work showed that cell viability is reduced at 30 min and one hour (further explained in Section 3.4.2). Furthermore, two acoustic protocols were performed in which the acoustic field was switched on before seeding the cells and after 3 min allowing the cells to deposit at the bottom. Images taken with an optical microscope throughout the cellular trapping and adherence at the bottom surface showed that linear cell patterning and stable acoustic trapping were obtained at 5, 10 and 15 min for both acoustic protocols (Figure 3.3). However, a less defined and more diffuse cell patterning was observed at 10 and 15 min when letting the cells deposit for 3 min before the acoustic field was switched on. These results suggest that once HeLa cells deposit at the bottom of the device, they adhere to the PLL-coated glass coverslips in a very short time and then difficult to overcome with the acoustic forces. As previously explained in Section 2.2.2, previous work measured the forces exerted on micro-beads while being trapped in a similar square acoustic device employing two active PZT. Measurements were made with optical tweezers testing a range of voltages (2-6 V_{pp}) and the results showed that the forces were between 0.5-1 pN V.[7] Moreover, cellular adhesion forces on PLL-coated surfaces are greater than 800 pN[8] in agreement with Touhami *et al* [9] who reported that bacterial adhesion forces on the same coated surfaces are of a few hundred of pN. The results of previous works and the observations made in this ultrasonic device suggest that the acoustic forces exerted on the cells are less than 100 pN where it is known that cell rupture can occur.[10]

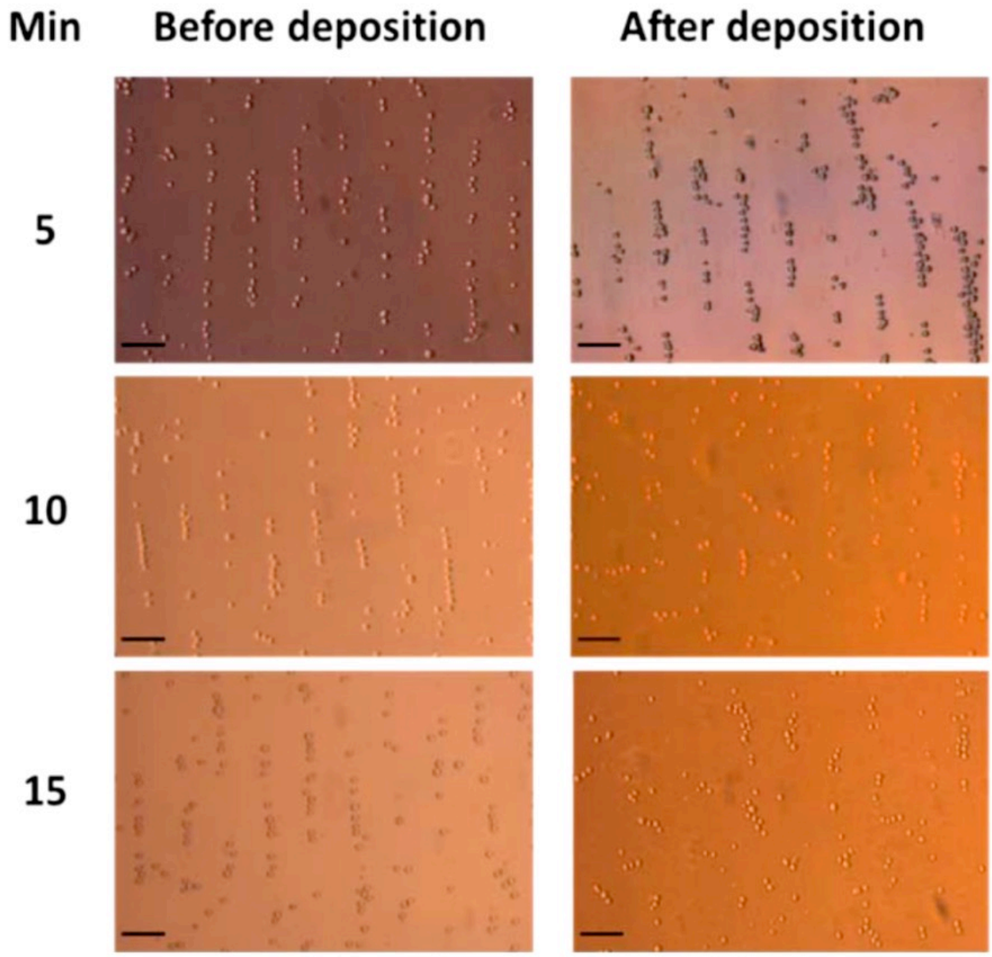

Figure 3.3: HeLa linear patterning at three times (5, 10 and 15 min) when exposing the cells before and after being deposited at the bottom. Scale bars are 50 µm and the objective was 10X. Adapted from reference 1.

An optimum protocol for a clear cellular alignment was thus acquired where the acoustic field switched on before seeding the cells into the cavity. Additionally, no difference in cell number or linear patterning was observed for the three tested times under these acoustic field conditions, suggesting that this ultrasonic device can be reliably employed for single cell or tissue engineering studies as reported in previous literature.[11] As shown in Figure 3.4, after a 24 h incubation from the 5-min acoustic exposure after deposition at an amplitude of 6 V_{pp}, the linear patterning and orientation of HeLa cells were maintained.

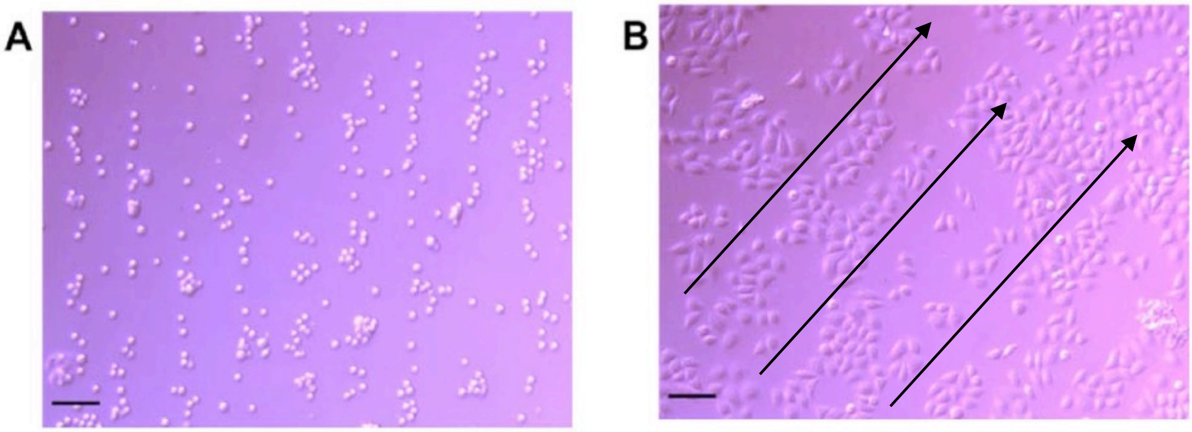

Figure 3.4: (**A**) Hela cells aligned in parallel lines for 5 min at an amplitude of 6 V_{pp} after being seeded. (**B**) linear patterning kept after an overnight incubation; black arrows depict the direction of linear patterning. The scale bars are 100 μm and the objective was 10X. Adapted from reference 1.

3.3 Temperature-dependent measurements

Mechanical energy is converted into heat by the absorption of ultrasound by a material, although at low frequencies normally in the range 1-10 MHz, the absorption is known to be small due to the low-loss materials (i.e. glass and silicon) and the high Q factor ultrasound transducers.[12] The quality factor (Q) of a transducer (PZT) is defined as the ratio of energy stored to the energy dissipated affecting the bandwidth and the peak amplitude per cycle at resonance when the system is not damped and can be expressed as[13,14]

$$Q = \frac{f_r}{\Delta_f} = \frac{\omega_r}{\Delta_\omega} \tag{2}$$

where f_r is the resonant frequency of the PZT and Δ_f is the half of the maximum power bandwidth as depicted in Figure 3.5, where the energy is dissipated by the PZT at a certain frequency and the amplitude across the PZT equals $1/\sqrt{2}$. If the peak of the amplitude is sharp, then the Q factor will increase and viceversa.[14] The Q factor can be modified by adding a layer of i.e., epoxy at the rear face of the PZT as a mechanical damping material to reduce oscillations and should be well-matched to the acoustic impedance of the PZT.[15] Moreover, by matching the acoustic impedance of the front and the back layers with the PZT, the bandwidth of the amplitude can increase. However, the attenuation can also increase when multiple matching layers are added to the system although the matching increases the efficiency of energy transfer between the PZT and the media. To minimise this attenuation, the reverberation (reflection of sound waves from surfaces)[16] losses should be low between the matching layers.[17] For this ultrasonic device, a coupling agent (ultrasound gel) was added at the front face of the PZT between the PMMA walls and the PZT due to its close acoustic impedance and low attenuation for an efficient energy transfer to the central cavity.

Previous work at the University of Bristol, performed a finite element modelling employing a similar ultrasonic device where the acoustic parameters of the materials and the PZT were incorporated to evaluate the acoustic behaviour of the device, as previously mentioned in Chapter 2. The device was made of a PMMA frame mounted on a frictionless modelled glass substrate. Water was taken as the fluid domain in the trapping area and the PZT were submerged in the adjacent cavities. The Q factor for the PZT as a function of frequency was extrapolated form previous literature[18] (Q=80) separated from the Q factors for glass and PMMA and, a constant dissipation factor (loss rate of energy) was determined to be $\tan\delta = 1/80$ across the PZT. The model was solved with a range of frequencies (1-2.5 MHz) at a voltage of 1V where 4 wide bands in the frequency were identified. The results of the modelling and later demonstrated experimentally showed stronger resonant peaks as the boundary PMMA walls were thinner. The PMMA walls are acting as additional damping to the ultrasonic system allowing maintenance of the particle trapping even when there are changes in resonance due to i.e. temperature shifts or polymerization of a material. Moreover, particle alignment was found at the bottom of the device suggesting that this type of ultrasonic device should be use with particles denser that the host fluid.[2]

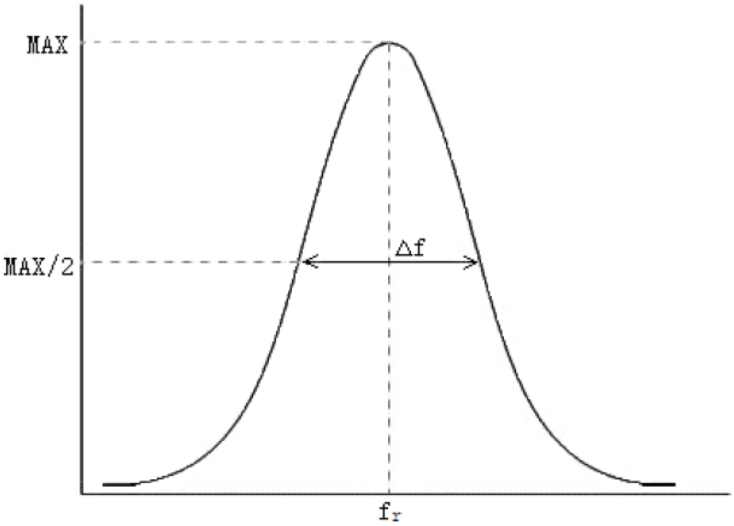

Figure 3.5: Scheme depicting the frequency band width at half of the maximum power. Adapted from reference 14.

It can be assumed that this ultrasonic device has the same acoustic characteristics as the one described above and therefore knowing its behaviour, this ultrasonic device can be also be used to evaluate secondary acoustic factors such as temperature. According to Wiklund,[12] during ultrasound exposure temperature can rise from the heat generated by the electromechanical energy loss of the PZT, as explained above, and due to the heat loss in the glue layers that are in between the layers of the PZT. To evaluate the temperature in the ultrasonic device, a Type K thermocouple was placed in the fluid (culture medium) in the central cavity while the acoustic field was switched on at room temperature (20°C) and when the temperature was set at 34°C with a temperature-controlled stage (heating block). The temperature of the culture medium was evaluated as a function of time (maximum 30 min) at a range of voltages (4-10 Vpp) generally suitable for cellular trapping and manipulation (Figure 3.6). Room temperature measurements showed in Figure 3.6 (A) exhibited a rise of ~2 °C when the amplitude was 10 Vpp reaching an equilibrium after 10 min approximately. However, by placing the ultrasonic device in a temperature-controlled stage initially set at 33°C and later reaching a final temperature of 34°C based on the thermocouple reading, the temperature variations in the central cavity were less than 0.25°C regardless of the operating voltage as shown in Figure 3.6 (B), also reaching an equilibrium after 10 min. The final temperature reached by the temperature-controlled stage (34°C) was considered as the physiological temperature closest to the biological standards range (33°C - 39°C) where cellular health is believed to be maintained. [12]

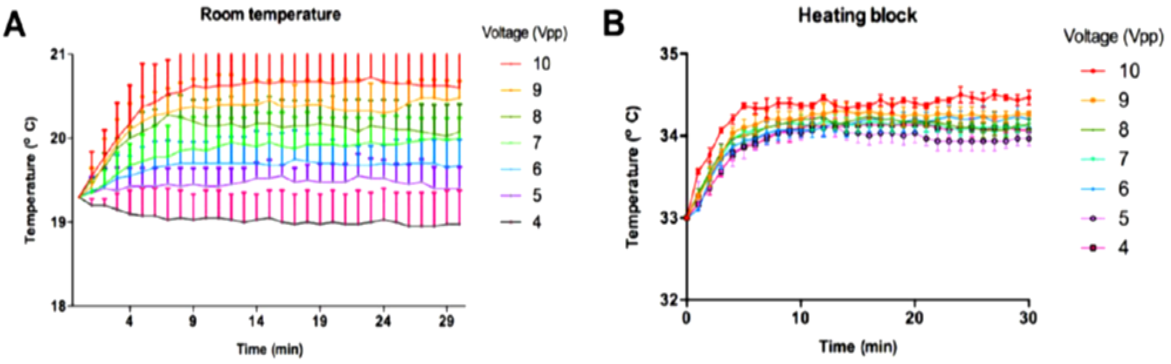

Figure 3.6: Temperature monitored in the fluid filled cavity at (**A**) room temperature (20°C) and at (**B**) a physiological temperature of 34°C set in a temperature-controlled stage for 30 min at a range of 4-10 V_{pp}. Adapted from reference 1.

As mentioned in a previous work, small changes in temperature can modify the acoustic resonance frequency in the trapping area.[2] The PZTs were operated in parallel at their third harmonic frequency (6.74 MHz) and the frequency was adjusted in steps of 0.01 MHz until cellular alignment was observed, operating close to their anti-resonance frequency of 6.77 MHz. A localised heating around the cells is not expected to occur in this device as the frequencies that were employed are in the range where low absorption takes place, as previously mentioned.[12] These measurements also demonstrated the relation between the energy dissipated and the frequency as the temperature increased in the culture medium due to the absorption. Moreover, the rise in temperature is shown to be dependent on the acoustic wave amplitude as demonstrated in $A = A_0 e^{i \propto t}$ and the time required to reach a final temperature is given by the attenuation coefficient that depends on the frequency (f), density (ρ) and speed of sound (c) of the employed fluid, given by[18]

$$\alpha = \frac{2\mu(2\pi f)^2}{3\rho_m c^3} \tag{3}$$

Furthermore, the cavity resonance must be operated at $\upsilon = nv/w$ in terms of the frequency where v is the velocity of sound. As an example, the velocity of sound in water at room temperature is around 1500 m s^{-1} and changes with small temperature variations at a rate of ~3 m s^{-1} °C^{-1} demonstrating that with a slight temperature change of 1°C the resonance will shift by ~0.01 MHz and the device will no longer operate at the optimum resonance. Hence, for optimal and reliable experimental conditions an optimum voltage and a temperature-controlled stage are necessary while also operating close to the resonance frequency.

3.4 Cell viability and metabolic activity measurements

3.4.1 Standard cellular viability and metabolic assays

Alamar blue (AB) or "resazurin reduction test" [19] is a widely used *in vitro* colourimetry cytotoxicity assay based on the reduction in the cytosol of the non-fluorescent blue water-soluble dye called resazurin (oxidised form) to resorufin (reduced form), which is a highly fluorescent pink dye.[20,21] Resorufin can be further reduced to hydroresorufin which is non-fluorescent and uncoloured. [19] Changes in cell culture fluorescence are analysed by a microplate reader and the reduction is the result of the metabolic activity of healthy and viable cells. This assay is very stable, easy to use, and can be employed to monitor cell cultures for a long period of time due to its non-toxic property.[21.22] Another common assay is 3-[4,5-dimethylthiazol-2-yl]-2,5-diphenyl tetrazolium bromide (MTT) which provides similar information about the cell health and is based on the reduction of the tetrazolium salt to formazan (purple colour). The intensity of the dye indicates the enzymatic activity of viable cells and a total number of living cells can be obtained.[23,24] However, due to the use of Dimethyl sulfoxide (DMSO) or isopropanol / hydrochloric acid (HCl) required, no further cell culture observations or maintenance is possible as it is highly toxic and therefore AB is the preferred cytotoxicity assay.[20,21]

Previously, a chromium (^{51}Cr) release assay was widely used specially to measure the cytotoxicity *in vitro* of T cells in their response to tumours and phage’s lytic activity.

This assay is based on the release of chromium from dead cells into the supernatants or the retention in live cells. However, a major disadvantage of this method is the use of radioactive compounds and, therefore, their disposal and handling.[25] A safer alternative fluorescent assay is Calcein-acetoxymethyl (Calcein-AM).[26] This cytotoxicity assay is based in the non-fluorescent and hydrophobic acetoxymethyl ester that crosses the cell membrane by passive transport. Once in the cytosol is hydrolysed by the intracellular esterases into calcein which is an insoluble polar fluorescent product. This green dye is well-retained in viable cells with no damage in their membranes and no dye transfer between the cells occurs, however, the dye is released by the non-viable cells and fluorescence can be read from the supernatants, similar to the chromium (51Cr) release assay.[25,27]

3.4.2 HeLa and HDF viability and metabolic activity measurements

Prior to exposing HeLa cells and human dermal fibroblasts (HDF) to the acoustic field, which is discussed in more detail below, the cell viability of both cell lines was measured by the dye exclusion assay, Trypan Blue (TB). In this assay, the blue dye labels dead cells while leaving live cells are uncoloured. Cell viability is then measured with an automated cell counter or with a haemocytometer under an optical microscope.[23,28] The results for HeLa and HDF cells indicated a 97% and 98% cell viability, respectively.

As previously mentioned in Section 2.2.2, HeLa cells were exposed to a mean resonant frequency of 6.7 MHz at an amplitude of 10 V_{pp} for 30 min and 1 hour when initially testing the ultrasonic device. However, the percentage of viable cells that was measured with the AB assay and as shown in Figure 3.7, was less than 20% after 30 min of ultrasonic exposure and approximately only 10% for the 1-hour exposure. After a further 24-hour incubation, a second acoustic exposure was made, and the cellular viability was measured again showing that for the extra 30 min (A30) HeLa cells recover reaching a 50% viability while for the 1-hour (A1) cells presented the same viability percentage as for the initial exposure. Temperature variations as a bioeffect of ultrasound may be the possible explanation for the low percentages in cell viability, since the exposures to ultrasound were carried out at room temperature and modifications at the molecular level may occur due to the fact that their metabolism decreases at temperatures below 33°C.[12] Although cells are more tolerant at temperatures that would have detrimental effects *in vivo*, previous work has reported that at sub-physiological temperatures the cells experience a “cold shock” which can affect some cellular processes such as cell cycle, metabolism and actin filaments organization, to mention a few. However, this work also mentions that in some cases not all temperature bioeffects have negative outcomes as it has been reported that recombinant protein production increases at lower temperatures.[12,29]

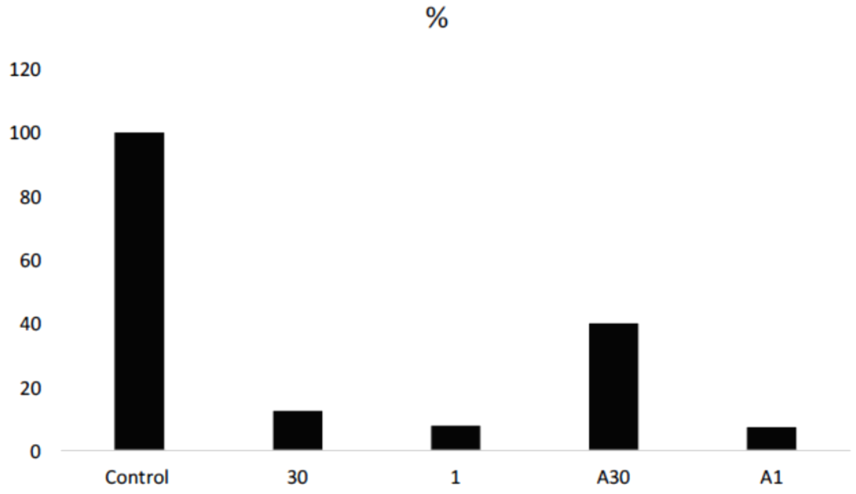

Figure 3.7: Cytotoxicity assay with Alamar blue (AB) showing the percentage of viable HeLa cells after a first continuous exposure to ultrasound for 30 min (30) and 1 hour (1). After a 24-hour incubation, the percentages of viable cells were taken after a second exposure to ultrasound for 30 min (A30) and 1 hour (A1). Unexposed HeLa cells were taken as a control.

The impact of low temperatures depends on the cell type since in some cells the viability can be maintained for longer periods of time even though their proliferation rate stops. However, an eventual slower cell death occurs if the temperature is kept below physiological temperatures.[29,30] In addition, it is known that the metabolic rate decreases as the temperature decreases and the cells become more susceptible to changes in the supply of nutrients and oxygen when the temperature is 37°C, the biological standard, than when the temperature is lower.[12] Following the above, the possibility for low cell viability after the second ultrasound exposure is that HeLa cells returned to standard biological conditions 24 hours prior exposure, however, at shorter ultrasound exposure of 30 min (A30), the viability seems to be recovering.

The thermal mechanism and how it is produced is relatively well understood, but its effect depends on the on the type of ultrasonic device and its characteristics, therefore, it should be evaluated under various acoustic exposure conditions. After optimizing the cell deposition rate with the acoustic field and the temperature as a function of time and voltage, the impact of the acoustic field on the viability and metabolism of HeLa and HDF cells was further evaluated. The cancer cell line (HeLa) and a healthy cell line (HDF) were exposed at three different times (5, 10 and 15 minutes) at a frequency of 6.77 MHz and at three voltages of 6, 8 and 10 Vpp. Cell viability was evaluated after acoustic exposures were carried out at room temperature (20°C) and at 33°C, but reaching a final temperature of 34°C. Both temperatures were monitored with the thermocouple and the temperature close to the biological standard was established with the temperature-controlled stage (heating block). In addition, the three different times were chosen to minimize the period of acoustic exposure to the cells since a clear cell alignment can also be obtained in times less than 30 min where cell death can occur. To measure the viability of both cell lines of exposed and control samples (unexposed cells), Calcein-AM assay was employed. The results shown in Figure 3.8 (**A**) demonstrate that the cell viability is maintained in HDF cells at room temperature for all times and voltages tested. However, when the temperature was maintained at 34°C, cell death occurred after 10 min of acoustic exposure at 10 and 8 V_{pp}, as shown in Figure 3.8 (**C**), where HDF cell viability with respect to unexposed cells decreased by approximately 50% and only approximately 60% remained viable after 15 min of exposure at 10 V_{pp}.

The viability of HeLa cells, on the other hand, was more varied at both temperatures, times and voltages with respect to the unexposed cells. As shown in Figure 3.8 (**B**), HeLa viability decreased by 50% after 5 min of acoustic exposure at 8 V_{pp} and increased slowly at 10 and 15 min. For 6 and 10 V_{pp} cell viability was maintained at the three times tested, only a slight decreased of approximately 10% was observed for 10 Vpp after 15 min but overall, at these two driving voltages HeLa cells maintained their viability at 20°C. A similar behaviour was observed when the ultrasonic device was kept at 34°C as shown in Figure 3.8 (**D**). Only when the driving voltage was 10 V_{pp}, after 10 min of acoustic exposure, cell viability decreases by 50% while for 5 min and 15 min of acoustic exposure approximately 70% of the HeLa cells remained viable. Interestingly, the viability of HeLa cells remained at high percentages at 5, 10 and 15 minutes when the driving voltages were 6 and 8 V_{pp}.

The initial temperature variations in this device according to previous measurements, occur in the first 10 min of ultrasound exposure and later reach an equilibrium at room temperature (2°C for the highest voltage) and at 34°C (± 0.2°C at 10 V_{pp}). A possible explanation for low cell viability percentages, mainly after 10 min of exposure and in a few cases after 5 min and 15 min for both cell lines, may be due to these "cold shocks" that the cells are subjected to initially before reaching the equilibrium, instead of an overheating for the temperature-controlled cell viability percentages. As discussed below, the impact of temperature variations depends also on the type of cell, since they have different biophysical and mechanical properties.

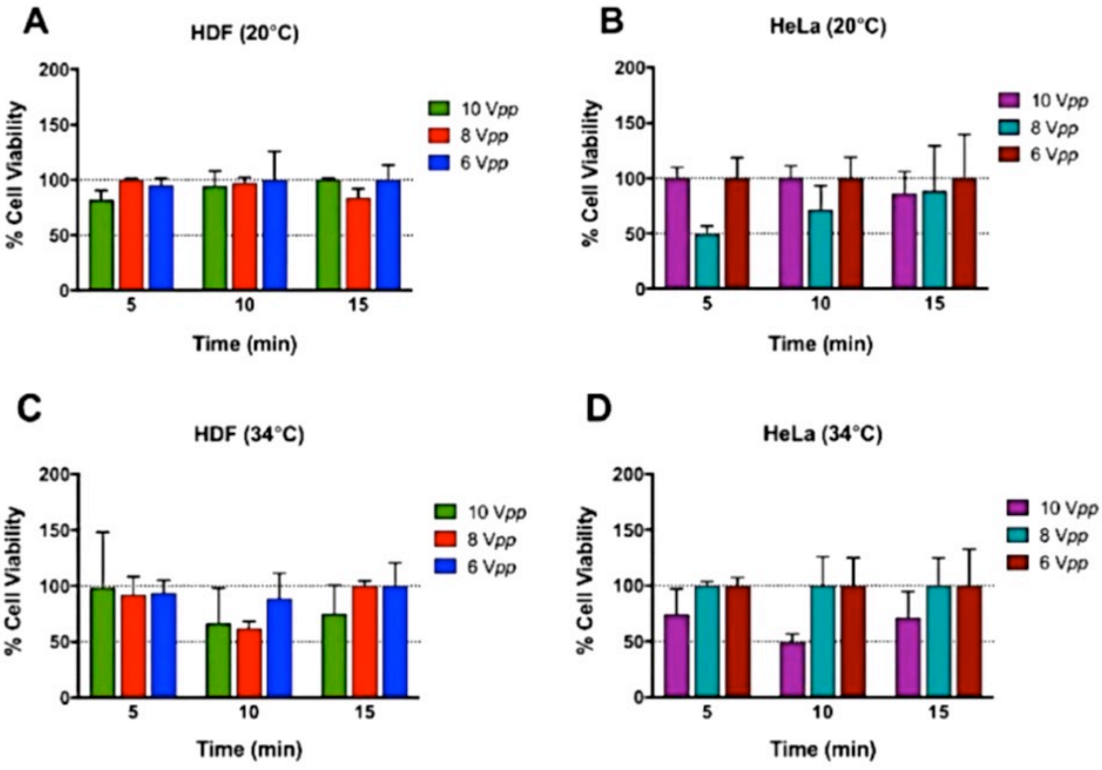

Figure 3.8: HeLa and HDF viability graphs relative to unexposed cells as controls after acoustic exposure. Calcein AM readings were made at room temperature for HDF (**A**) and HeLa (**B**) and while maintaining the temperature at 34°C for HDF (**C**) and HeLa

(**D**). Triplicates were made for each treatment and data is shown as mean ± SD. Adapted from reference 1.

The AB assay was then performed to evaluate the metabolic activity of both cell lines, which is an indicator of cytotoxicity, after ultrasound exposure and compared with unexposed cells (Figure 3.9). In the case of HDF and HeLa cells at 20°C, a great variability of metabolic activity was observed, especially when the driving voltage was 10 V_{pp} during the first 5 and 10 min, and just after 15 min of exposure, the metabolic activity rate of both cell lines were closer to the controls, as observed in Figure 3.9 (**A**) and (**B**), respectively. For HeLa cells when exposed at 6 and 8 V_{pp}, the percentage of metabolic activity remained closer to 100% for the three exposure times, however, for HDF an increase in metabolic activity values was obtained for the same voltages and times, indicating toxicity or altered metabolism. In contrast, fewer changes in metabolic rate were observed for both cell lines when the temperature was maintained at 34°C and ultrasonic exposures at the three different voltages (Figure 3.9 (**C**) and (**D**)), although HeLa cells seem to do better at this temperature at the tree tested times. Metabolic activity appears to be dependent on time and temperature, as it appears to be maintained after 15 minutes of acoustic exposure, suggesting an adaptation of the cells to initial "shock" temperatures. This short adjustment period is in agreement with previous observations made for cell viability, where is generally maintained better after 15 min of exposure and at all voltages.

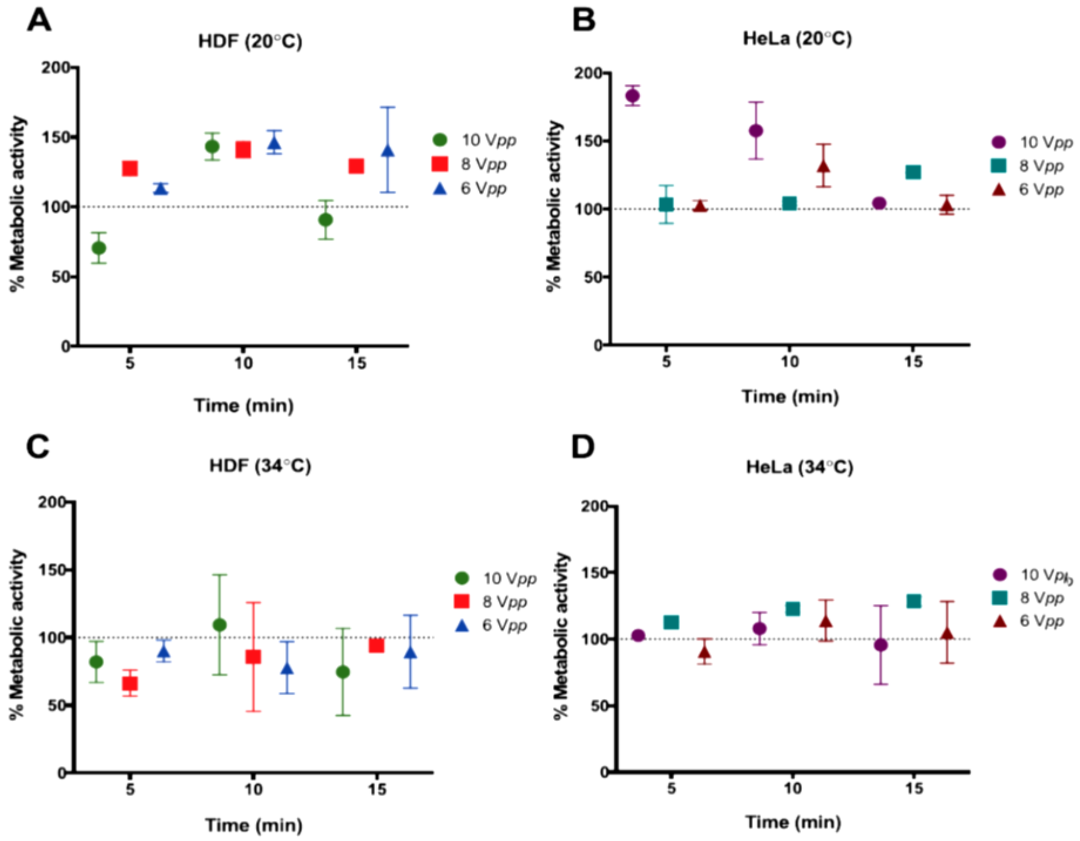

Figure 3.9: Alamar blue assay to evaluate the reductive metabolism of HDF and HeLa in relation to controls after acoustic exposure. Three different times were tested (5, 10 and 15 min) at three voltages (6, 8 and 10 V_{pp}). Evaluations were made at room temperature for HDF (**A**) and HeLa (**B**) and at 34°C for HDF (**C**) and HeLa (**D**). Triplicates were made for each treatment and data is shown as mean ± SD. Adapted from reference 1.

The results showed that the combinations of exposure to ultrasound voltage, time and temperature affect cells differently. This can be expected since the properties of cells differ according to their origin and therefore their susceptibility to changes will also vary. It has been reported that the effect of ultrasound on single cells depends on the frequency and intensity applied.[31,32] Moreover, previous experimental studies have shown that cancer cells are more susceptible than healthy cells when exposed to ultrasound and variations in temperature inside the trapping zone influence cellular membranes depending on their stiffness.[31,12,32] The difference in cell membrane rigidity can be used to mechanically separate tumorigenic cells and normal cells,[31] however, since a clear correlation between voltage, acoustic exposure time and temperature has not been observed in these results for both HeLa and HDF, more in-depth cellular studies are suggested at a molecular level to discriminate the acoustic factors that impact the cells. As discussed at the beginning, there are several secondary factors derived from acoustic exposure that can have a detrimental impact on cell viability and metabolism, such as streaming, temperature, cavitation, or even the materials used in the ultrasonic devices (discussed in Section 2.3). The variations of these factors also affect the cells differently and may be the explanation for the inconsistencies observed in both cell lines.

3.5 Chapter conclusions

In summary, this resonant ultrasonic device was employed for the study of secondary acoustic factors and their effect on the viability and metabolic activity of one cancerous cell line and one normal cell line, HeLa and HDF, respectively. Inconsistencies in the response from both cell lines were observed and it is largely attributed to the difficulty in tuning accurately high resonance devices like this in particular. As discussed in Chapter 2 from the acoustic impedance measurements, significant effects on the acoustic pressure can be obtained with small variations in the acoustic parameters. Therefore, the study of acoustic streaming, cavitation and temperature were performed and their possible effects on cells. Eckart streaming was found to be produced in this device, as previously observed in a similar device by Bassindale *et al*,[7] however no cell damage or major disturbance was found with the frequencies employed. There was also no clear evidence of the production of bubbles due to cavitation effect which is expected to be minimum in this device due also to the frequencies used. However, temperature variations during acoustic exposure were happening through time in the trapping area and the resonant frequency had to be finely tuned in steps of 0.01 MHz for the cells to be trapped. Furthermore, employing this experimental set up, a 15-minute acoustic exposure was found to be the optimum for both cell lines, switching on the acoustic field before seeding the cells into the central cavity and employing a temperature-controlled stage to maintain the temperature close to the biological standard. However, it is recommended to work at ±1°C from 37°C when exposing the cells so the biological processes can be measured reliably and not affected.[12] Robust protocols for ultrasonic exposure are necessary if the applications are for therapeutic or clinical diagnosis. Based on these results, the driving voltage should be kept at minimum values and the resonant frequency has to be carefully tunned maybe at smaller steps than 0.01 MHz in order to trap the cells while maintain their cell viability high. Moreover, when designing and manufacturing a new ultrasonic device, systematic measurements considering all the acoustic parameters and their secondary factors under physiological conditions must be done.

3.6 References

1. V. Levario-Diaz, P. Bhaskar, M.C. Galan and A.C. Barnes, *Sci Rep*, 2020, **10**, 8493.
2. M.-S. Scholz, B.W. Drinkwater, T.M. Llewellyn-Jones and R.S. Trask, *IEEE Trans Ultrason Ferroelectr Freq Control*, 2015, **62** (10), 1845-1855.
3. A.L. Bernassau, P. Glynne-Jones, F. Gesellchen, M. Riehle, M. Hill and D.R.S. Cumming, *Ultrasonics*, 2014, **54**, 268-274.
4. A. Lenshof, M. Evander, T. Laurell and J. Nilsson, *Lab Chip*, 2012, **12**, 684.
5. J. Wu, *Fluids*, 2018, **3** (4), 108.
6. M. Wiklund, R. Green and M. Ohlin, *Lab Chip*, 2012,**12**, 2438-2451.
7. P.G. Bassindale, D.B. Phillips, A.C. Barnes and B.W. Drinkwater, *Appl. Phys. Lett.*, 2014, **104**, 163504.
8. T. Hoshiba, C. Yoshikawa and K. Sakakibara, *Langmuir*, 2018, **34**, 4043-4051.
9. A. Touhami, M.H. Jericho, J.M. Boyd and T.J. Beveridge, *J. Bacteriol.*, 2006, **188**, 370-377.
10. A. Pierres, P. Eymeric, E. Baloche, D. Touchard, A-M. Benoliel and P. Bongrand, *Biophysic J.*, 2003, **84**, 2058-2070.
11. J. P. K. Armstrong, *et al*. *Adv. Matter*, 2018, **30**, 1802649.
12. M. Wiklund, *Lab Chip*, 2012,**12**, 2018-2028.
13. C. Chen and B. Choubey, *2018 IEEE SENSORS*, New Delhi, 2018, 1-4.
14. Z. Chaoyue, A. McDowell and T. Hubing, EMI Source Modeling of the John Deere CA6 Motor Driver, 2011.
15. S. Cochran, Piezoelectricity and basic configurations for piezoelectric ultrasonic transducers, *Woodhead Publishing*, 2012, 3-35.
16. Katrin E. Kroemer Elbert, Henrike B. Kroemer and Anne D. Kroemer Hoffman, Chapter 5 - Human Senses, Ergonomics (Third Edition), *Academic Press*, 2018, 171-252.
17. V.T. Rathod, *Sensors*, 2020, **20**, 4051.
18. W. D. O’Brien Jr, *Prog Biophys Mol Biol*. 2007, **93**, 212–255.
19. J. O’Brien, I. Wilson, T. Orton and F. Pognan, *Eur. J. Biochem*, 2000, **267** (17), 5421-5426.
20. F. Bonnier, M. Keating, T. P. Wrobel, K. Majzner and M. Baranska, *Toxicology in Vitro*, 2015, **29**, 124-131.

21. S. Al-Nasiry, N. Geusend, M. Hanssens, C. Luyten and R. Pijnenborg, *Human Reproduction*, 2007, **22** (5), 1304-1309.
22. S. A. Ahmed, R. M. Gogal and J. E. Walsh, *J Immunol Metho*, 1994, **170**, 211-224.
23. S. B. Iloki Assanga, *et al*. *International Journal of Biotechnology and Molecular Biology Research*, 2013, **4**(4), 60-70.
24. T. Mossman, *Journal of Immunological Methods*, 1983, **65**, 55-63.
25. S. Neri, E. Mariani, A. Meneghetti, L. Cattini and A. Facchini, *Clinical and Diagnostic Laboratory Immunology*, 2001, **8** (6), 1131-1135.
26. M. M. Roden, K-H. Lee, M. C. Panelli and F. M. Marincola, *Journal of Immunological Methods*, 1999, **226**, 29–41.
27. N. G. Papadopoulos, G. V. Z. Dedoussis, G. Spanakos, A. D. Gritzapis, C. N. Baxevanis and M. Papamichail, *Journal of Immunological Methods*, 1994, **177**, 101-111.
28. V. J. Rodriguez, V. O. Vicente and M. J. Canteras, *Patología*, 1997, **30** (1), 18-27.
29. M. B. Al-Fageeh, R. J. Marchant, M. J. Carden and C. M. Smales, *Biotechnol. Bioeng*., 2006, **93**, 829–835.
30. H. Kaufmann, X. Mazur, M. Fussenegger and J. E. Bailey, *Biotechnol. Bioeng*., 1999, **63**, 573–582.
31. Fraldi, M., Cugno, A., Deseri, L., Dayal, K. & Pugno, N. M, *J. R. Soc. Interface*, 2015, **12**, 20150656.
32. A. Schuster, T. Schwab, M. Bischof, M. Klotz, R. Lemor, C. Degel, K-H. Schafer, *Ann. Anat*. 2013, **195**, 57–67.
33. S. B. Barnett, *et al*. *Ultrasound in Med. & Biol*, 1994, **20**, 205–218.

4 Acoustically enhanced cellular uptake of modified microspheres using USW

This chapter is based on the work to be submitted in 2021 of which I am first author. The experimental methods in this chapter were conceived alongside with Professor Carmen Galan and Dr David Benito-Alifonso. The 1D ultrasonic device previously described in Chapters 2 and 3 was used for cellular and microsphere trapping. For the formulation and characterization of fluorescent carboxyl polystyrene microspheres, Dr Sandra Medina and Dr Sarah Michel performed the procedures, respectively, and I assisted in the process. The flow cytometric analysis of the microsphere uptake was carried out by me with the help and training of Lorena Sueiro-Ballesteros and the person in charge of the facility, Andrew Herman. I obtained the confocal images with the training and assistance of Alan Leard and microsphere infiltration analyses were performed by Stephen Cross, both members and technicians of the Wolfson Imaging Centre in the School of Biomedical Sciences at the University of Bristol. Finally, Transmission Electron Microscopy (TEM) was performed with the help and training of Dr Judith Mantell, Chris Neal and Professor Paul Verkade also from the School of Biomedicine at the University of Bristol.

4.1 Introduction

In previous chapters, the characterization and use of the 1D ultrasonic device was described and demonstrated to achieve defined trapping of HeLa and HDF cells while maintaining their viability at 8 V_{pp} when exposed for 15 min under temperature-controlled conditions. Based on these results, it was decided to explore the potential of the ultrasonic device for drug delivery applications. As discussed in Chapter 1, ultrasound is known to increase cellular uptake of micron-sized therapeutic agents in a controlled manner, targeting specific cells or tissues without inducing toxicity through cavitation and sonoporation mechanisms. Moreover, previous literature has reported that endocytosis, which is a set of mechanisms used for the intracellular transport of particles and macromolecules via vesicles into the cytoplasm,[1] can be acoustically enhanced by increasing the permeability of the plasma membrane even in the absence of microbubbles.[2-5] However, the endocytic mechanisms involved in microparticle uptake by standing acoustic waves (USW) remains unexplored.

Therefore, for this research, fluorescent polystyrene carboxyl microspheres with a mean diameter of ~1 μm were used and conjugated. The surface charge of the microspheres was modified to study the cellular absorption mechanism when both were exposed to ultrasound and cellular uptake was measured by the flow cytometry technique for all microsphere conjugations. In addition, confocal images were taken to observe internalization after exposure and with these images a microsphere infiltration analysis was performed to obtain a total count of internalized particles, bound to the cell membrane and to the exterior of the cell. Finally, TEM sections were made to observe the interior of the sectioned cells, locate the position of the conjugated microspheres and visualize the integrity of the plasma membrane

4.2 Carboxyl-modified polystyrene microspheres formulation and characterisation

In previous chapters, the design, manufacture and characterisation of the operation mode of the 1D ultrasonic device was presented and discussed. Moreover, it was demonstrated that HeLa cells can be acoustically trapped and aligned in parallel to the PZTs maintaining their viability and metabolic activity. This ultrasonic device was designed according to the size range for cells and particles to be trapped in the pressure nodes (>1μm) which are guided to the pressure nodes by the acoustic primary radiation forces and aggregate by the secondary radiation forces. The size of the particles to be used in an endocytosis investigation is one of the most important factors to consider, since the cell regulates its entry gates through the plasma membrane according to size, charge, among other considerations. This interface allows communication, uptake of nutrients between cells and their external environment and with other neighbouring cells. Micro and nanoparticles are internalised by the invagination of the plasma membrane and transported in vesicles derived from the same which is an energy dependent mechanism (Figure 4.1).[1] Depending on the size of the particles there are different pathways of internalization within the pinocytosis mechanism which is the extracellular fluid uptake. Endocytosis offers the advantage of non-specific uptake of particles by adsorption and it can be divided in three pathways: macropinocytosis, caveolae-mediated and clathrin-mediated endocytosis.[1] Endocytosis also includes phagocytosis, but it can only be used by phagocytic cells such as macrophages, whereas endocytic pathways are used by all other cell types.[7] The clathrin-mediated endocytosis pathway, the most characterized mechanism,[7] is crucial to regulate the transport and internalization of small proteins and ions, maintaining homeostasis in the cell, also important for intracellular communication and for the continuous absorption of essential nutrients such as low-density lipoproteins which is regulated by the receptor-ligand complex. This pathway involves the formation of clathrin-coated pits after the ligand binds to the specific receptor and induces the recruitment and assembly of coated pit proteins, with clathrin being the main unit. These clathrin-coated pits pinch off from the plasma membrane carrying receptor-ligand complexes by a polygonal clathrin cage.[1] Furthermore, nanoparticles up to 200 nm are also being uptake by this pathway,[14]

Caveolae-mediated endocytosis was first reported in the 1950s, flask-shaped invaginations were observed in endothelial cells.[15] This endocytic pathway is characterised by the structural organization of the dimeric protein, caveolin that gives rise to the flask-shaped caveolin pits by binding to cholesterol and forming an inner pocket of the plasma membrane.[16] This pathway, involved in the intracellular transport of cholesterol and uptake from lipid rafts, is present in many cells and only small particles (50-60nm) can be taken up at a rate >20min, suggesting that it is a highly regulated pathway.[1]

In macropinocytosis, the plasma membrane ruffles and large volumes of extracellular fluid with particles are absorbed when the two protrusions of the membrane fuse (Figure 4.1, sequence depiction).[7,8] This mechanism is not selective and suspended macromolecules can be absorbed by being engulfed and internalized by vesicles in the plasma membrane called macropinosomes with a maximum reported size of 5μm.[7,9] Furthermore, macropinocytosis is induced by a signalling cascade of the Rho family GTPases which is a subgroup of the Ras family,[6] therefore, triggering the membrane protrusion that is an actin-driven formation.[1] It has been reported that some Rho GTPases are overexpressed in cancer cell lines such as breast cancer,[11] and promote oncogenesis.[6] Moreover, cancer cells use preferentially macropinocytosis pathways for extracellular protein internalization and be used as a source of energy for their metabolism.[12,13]

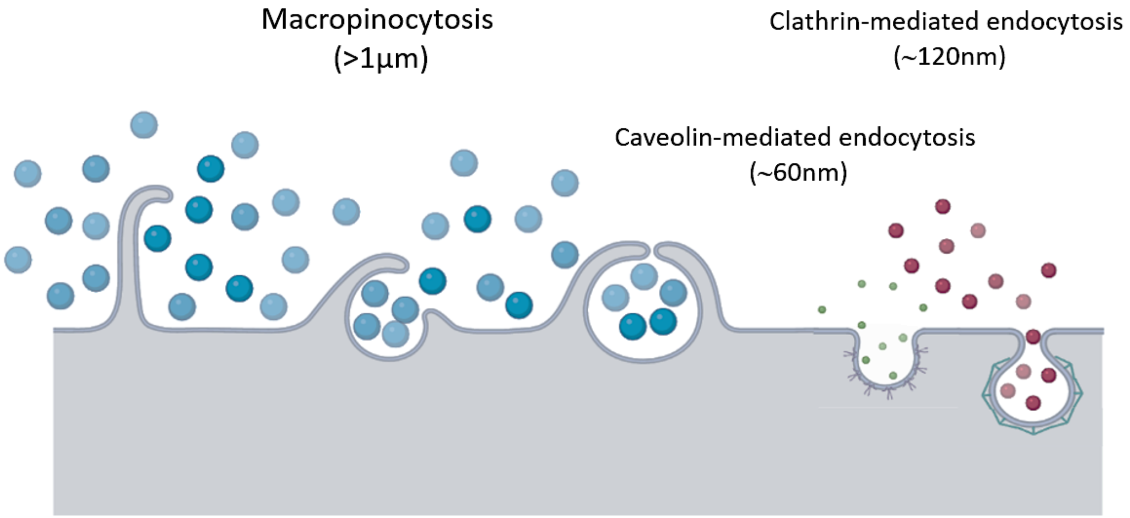

Figure 4.1: Endocytic pathways regulated by the plasma membrane. Sequence of the macropinocytosis mechanism is depicted where the membrane starts to ruffle and at the end the particles (>1µm) are uptake and engulfed. Macropinosome is formed and responsible for the intracellular transport. Caveolin-mediated endocytosis uptake vesicles of ~50-60nm and clathrin-mediated endocytosis up to 200nm nanoparticles are transported into the cell. Adapted from reference 1.

4.2.1 Carboxyl-modified polystyrene microsphere formulation

Another important factor to consider when studying endocytosis mechanisms specially for drug delivery purposes is the surface charge of the particles. This property is of great interest as micro and nanoparticles can be applied to clinical therapies for drug and gene deliveries.[17] For this research, carboxyl polystyrene fluorescent microspheres (PS-COOH) were used as the model for surface charge conjugations. As reported in the previous literature, [26,27] these microspheres are one of the ideal models since they are commercial and have properties that make them reliable, such as their presentation in different sizes, they are internally labelled with dyes and are non-toxic. According to the manufacturer's information (Tech Note 103, Bangs Laboratories, Inc.) carboxyl polystyrene microspheres are internally labelled after being synthetised (Figure 4.2 **c**). Polystyrene microspheres are swelled in an organic solvent where the water-insoluble dye is diffused and the dye entrapment occurs when the solvent is removed either through evaporation or by being transfer to an aqueous phase. In addition, it has been seen that they form stable and monodisperse suspensions in cell media without presenting dye leakage.[26,27] For this reason, dragon green-fluorescent carboxyl polystyrene microspheres with a mean size of ~1µm, were used to explore the mechanism of cellular uptake under the influence of USW. Different complete and partial conjugations were made to modify their surface charge and so amino dextran, 4,7,10-Trioxa-1,13-tridecanediamine (TTDDA) and amino lactose were used to form cationic, anionic and sugar-coated microspheres (Figure 4.2 (**a**)), respectively. Dextran has proven to be a safe material to be used as an applied drug delivery vehicle for clinical applications. Dextran also allows the particles to be further chemically modified due to the modification of hydroxyl groups to amino groups that will generate positively charged microspheres.[28] Cationic microparticles are promising carriers for effective drug delivery after the interaction and uptake by cells due to their positive net characteristics.[29]

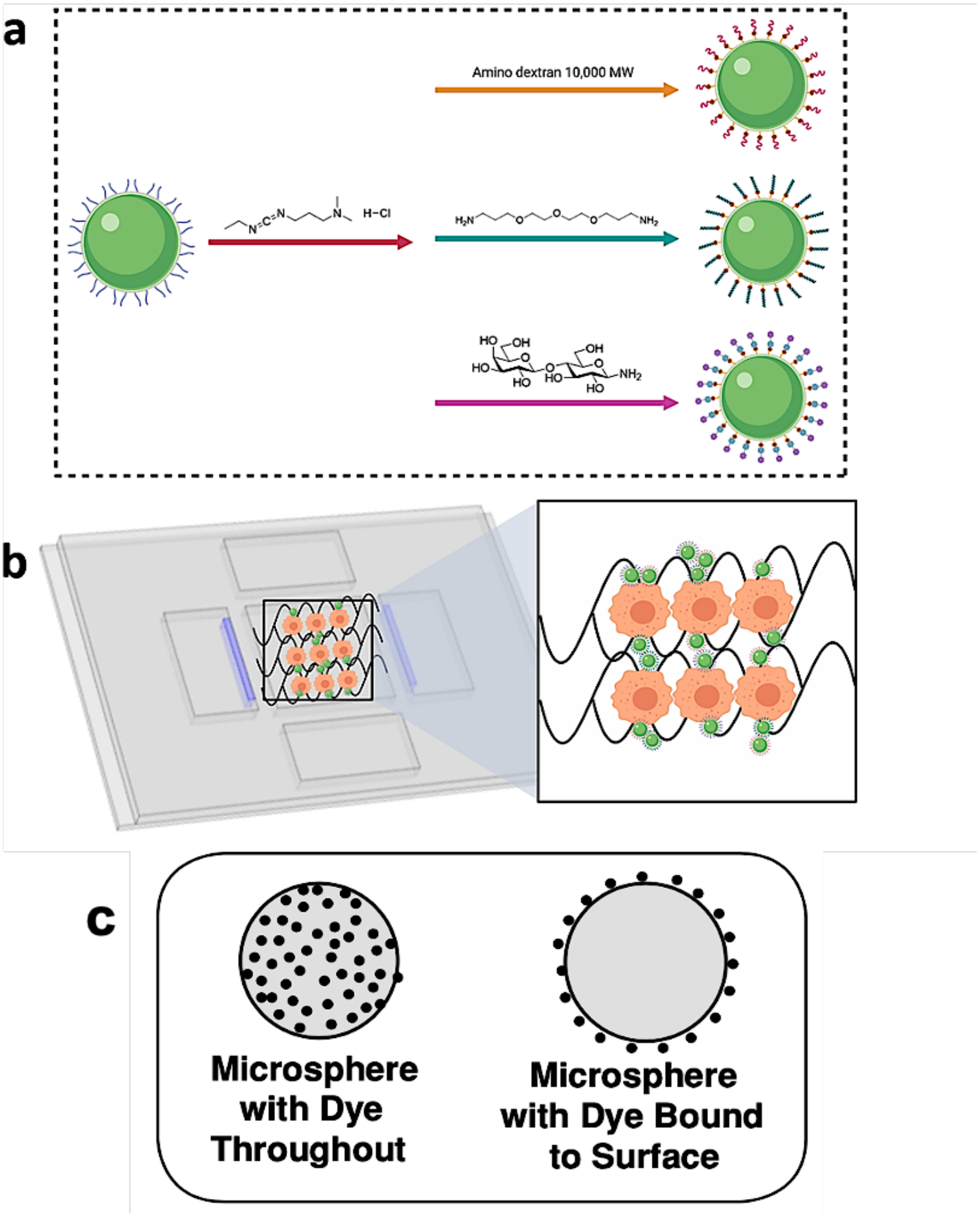

Figure 4.2: (**a**) Green fluorescent carboxyl polystyrene microspheres conjugated with EDC and with three different surface charge formulations. Indicated with an orange arrow are the Amino dextran microspheres, with a green arrow are the TTDDA microspheres and lastly, pointed out with a pink arrow are the lactose microspheres. (**b**) Acoustic trapping and alignment of HeLa cells and surface-modified microspheres aggregates at the pressure nodes of the standing acoustic waves (USW). (**c**) depicts two different methods for dye loading by diffusion according to the manufacturers tech

note data. For the carboxyl polystyrene microspheres employed in this work, internal labelling was done.

Trioxa-tridecanediamine (TTDDA) has been used for dendritic structure synthesis to create an amine surface.[31] This molecule gives rise to cationic surface charge particles and is more dependent on the pH of the surrounding medium as ions can interact with the amine groups and generate a positively charged particle. To obtain an anionic surface charge using nanoparticles partially conjugated with TTDDA, it has been reported that for colloidal silica nanoparticles where in the range of 3-13 the pH of the surrounding medium resulted in a highly negative surface charge of the NP[32] when the cell medium has a pH of 7. Lactose-modified microspheres were conjugated as a sugar-coated microcarrier due to the biocompatibility with the cells. It is known that the outer cell membrane presents carbohydrates which are involved in intercellular and matrix communication, and organelle interaccion.[33-36] Lactose is a disaccharide which is composed of galactose and glucose and it can be employed to target the cell membrane and be recognised by the carbohydrate receptors that are associated with uptake and intracellular mechanisms.[37] The coupling method that was followed to join these three molecules to the carboxyl polystyrene microsphere was the 1-ethyl-3-(3-dimethylaminopropyl)carbodiimide hydrochloride) better known as EDC. Is an inexpensive method and is employed for the coupling of carboxyl groups to primary amine groups.[38-41] This method was employed to couple the carboxyl groups from the commercial microspheres to the amine groups of amino dextran, trioxa-tridecanediamine (TTDDA) and amino lactose and modify their surface charge.

4.2.2 Carboxyl-modified polystyrene microspheres characterisation

As mentioned above, the surface charge of the microspheres was modified to elucidate the cellular uptake mechanism after acoustic exposure and incubation process. The microsphere conjugations (TTDDA-, dextran- and sugar-coated) were confirmed by NMR (Appendix A.4). Furthermore, the microspheres after conjugation were also characterized by measuring their size, polydispersity index and ζ- potential in PBS and DMEM media. It is important to mention that the employed DMEM media was not supplemented with foetal bovine serum (FBS) since the ζ- potential can be modified due to the protein adsorption on the surface of the conjugated microspheres, as reported in previous literature.[18-20] Zeta potential measurements in PBS and DMEM solutions showed that there are no significant differences for all micro-spheres (Appendix Table A.1 and Figure 4.3 (**a**) and (**d**)). Furthermore, amino dextran-coated microspheres with a zeta potential of 7.14 mV and 8.9 mV in DMEM and PBS (Appendix Table A.1), respectively, were the only positive conjugate microspheres, while lactose-, TTDDA-, and acid-coated microspheres presented a negative surface charge ranging from -9.6 mV to -46.6 mV (Appendix Table A.1). The results shown in Appendix Table A.1.1 and Figure 4.3, also demonstrate that there are no significant changes in the microspheres size values in PBS and DMEM solutions (Figure 4.3 (**b**) and (**e**)), respectively. Surface-modified microspheres (lactose, amino dextran and TTDDA) were found to be slightly above 1µm while the acid-coated and commercial microspheres were found to be around 0.9µm to 1µm. As a control, acid-coated microspheres were employed by dialyzing the commercial microspheres with pure water to remove the surfactants and to ensure the achievement of proper surface conjugations. The TTDDA partially conjugated microspheres remained monodispersed and homogenous in PBS (Appendix Table A.1; 0.09) and DMEM (Appendix Table A.1; 0.1) solutions. Although lactose and amino dextran conjugated microspheres tended to form small aggregates in both solutions, they remained within the standard range to describe a monodispersed and uniform solution (Appendix Table A.1 and Figure 4.3 (**c**)and (**d**)).[21]

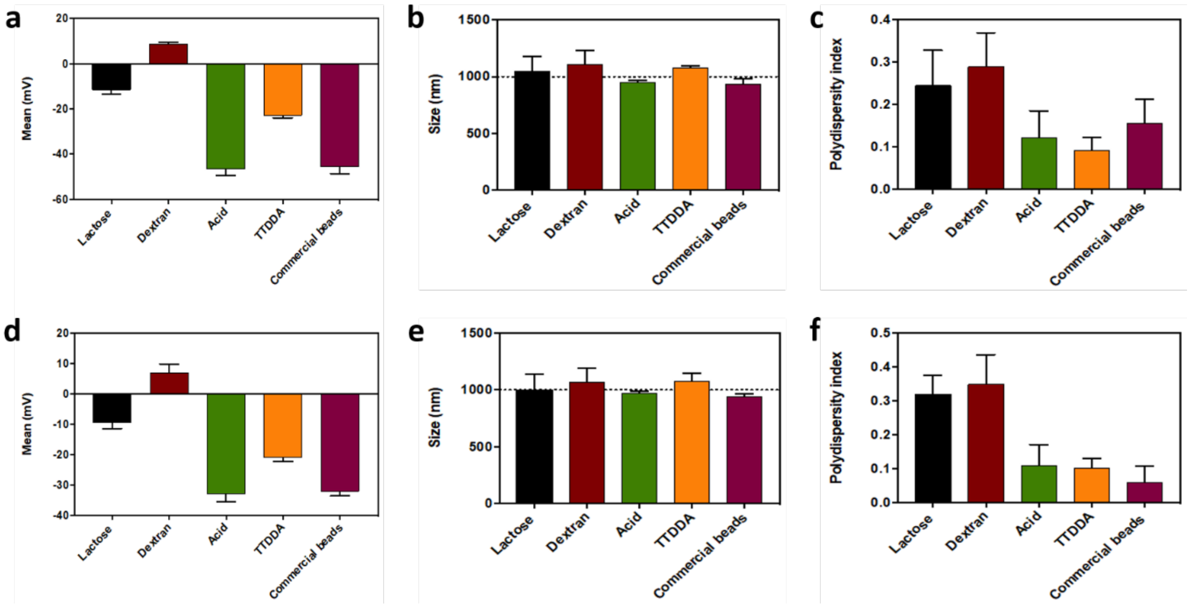

Figure 4.3: ζ- potential, hydrodynamic size and polydispersity index graphs of non-conjugated and conjugated microspheres in PBS solution (**a**, **b**, and **c**) and in DMEM media not supplemented with FBS (**d**, **e**, and **f**). The graphs represent the average of three measurements.

4.3 Energy dependent cellular uptake and inhibition

HeLa cells were chosen for this study because they have been a widely used model for microparticle uptake studies,[26] in addition to being cancer cells and, as mentioned above, the Ra-activated pathway stimulates their macropinocytosis. This Rho GTPases subgroup of the Ras family regulates the assembly of focal adhesions, motility, polarity and cell-cycle progression, meaning they are responsible for the cytoskeleton arrangement.[11] In order to properly elucidate if the endocytic mechanism, macropinocytosis, is involved in the ultrasound-mediated and basal endocytosis uptake is necessary to perform an assessment with pharmacological inhibitors. This assessment allows the establishment of the uptake mechanism and relate the endocytic pathway to intracellular mechanisms.[7] For this specific study, the inhibitor colchicine was used, which blocks the endocytic pathway macropinocytosis. This inhibitor is a microtubule destabilising agent (MDA) as its binding site is in a key position that prevents the extension of the tubulin fibres; therefore, the straight fibre structure and assembly is lost. The mechanism of this inhibitor was first found by Ravelli *et al*[42] by observing the crystal structure of colchicine interacting with the tubulin complex noticing that the binding pocket was a hydrophobic site.[23] Moreover, it has been reported that colchicine prevents microtubule polymerization which also reduces the ruffling of the membrane.[43-45]

4.4 Ultrasound exposure and cellular uptake

In order to study the cellular enhanced uptake of conjugated microspheres, the 1D ultrasonic device, previously explained in Chapters 2 and 3, was employed following the results obtained in both Chapters where HeLa cells deposit and align when the acoustic field is switched on before seeding them and maintained their viability and metabolic activity when the PZTs were driven at their resonant frequency (~6.77 MHz) at 8 V_{pp} for 15 min and under temperature-controlled conditions. For this chapter investigation, four treatments with HeLa cells were performed to elucidate the uptake mechanism when cells are exposed to ultrasound and cell-microsphere aggregates form. The categories were: acoustic exposure, basal endocytosis, inhibitor acoustic and inhibitor basal endocytosis. All acoustic treatments were exposed with the conditions mentioned above and the basal endocytosis refers to the incubation of conjugated microspheres with the cells for 15 min at 37°C. This was taken as the mechanism of macropinocytosis that normally occurs in cells. Inhibitor treatments were performed by incubating the cell with macropinocytosis inhibitor, prior the conjugated microspheres exposure / incubation. These cell-microsphere interactions were expected to be enhanced when exposed to USW where the primary and secondary acoustic forces guide both cells and particles (Figure 4.2 (**b**)). Additionally, the acoustic force triggers the pore formation and, the conjugated microsphere is being internalised into the cell.

4.4.1 Flow cytometry technique

This powerful technique allows measurement of the optical and fluorescent characteristics of individual cells as they pass through a detector in a constant fluid flow. The principle of flow cytometry is the relationship between light scattering and fluorescence emission that occurs when the laser beam (excitation source) hits the cells / particles when passing by. The morphology and structural properties of the cell, which can also be measured, are detected by light scattering, whereas the fluorescence emitted by the fluorescent particle is derived from the fluorescence emission being proportional to the amount of internal fluorescent microsphere or bound to the cell.[46,47] To analyse the results generated by flow cytometry, gates and regions can be determined to analyse subpopulations in a numerical and graphical way. Some of these properties that can limit the populations and make the divisions are the cell size and granularity.[46,48] This method of gating strategy also allows to eliminate results from dead cells if treated with propidium iodide (PI), described below and make a distinction.

Propidium iodide (PI), which is an impermeable membrane dye used to exclude viable cells, can be used in combination with flow cytometry. This dye binds to the DNA of apoptotic cells and, the fluorescence emission of the dye is proportional to the nucleic acids. This fluorescence presents a broader distribution that is very easy to recognize from viable cells where its fluorescence distribution is narrow. Although there may be fragments of DNA or even necrotic cells where there is DNA degradation, PI staining is a reliable exclusion technique to quantitatively evaluate the cell viability within the sample and is easy to use.[30]

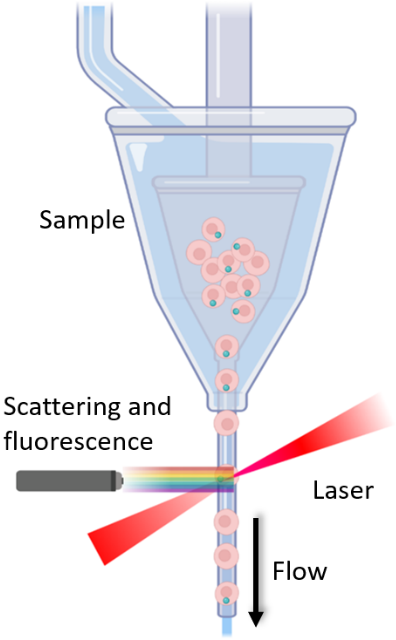

Figure 4.4: Diagram of the principle of flow cytometry. Adapted from reference 46 Created with Biorender.

Flow cytometry was used to quantitatively analyse cell uptake and distinguish between cell internalization or cell membrane binding of conjugated microspheres from cells that did not present microspheres. Before flow cytometric analysis, quenching of the conjugated microspheres was tested with TB, however, the microspheres, as mentioned previously, are internally labelled where quenching was not possible. Therefore, the populations of HeLa with internalised and bound fluorescent microspheres were compared to control samples where no fluorescent microspheres were added. As mentioned above, HeLa cells were subjected to four different treatments (acoustic, basal endocytosis, and colchicine inhibitor treatment for both mechanisms) for 15 min. Prior to flow cytometric analysis, HeLa cells were dissociated using Accutase and then processed on a BD LSR11 flow cytometer detecting a minimum of 3,000 live cells per treatment and adding PI to label the apoptotic cells. The gating strategy done for this study, for each cellular treatment is found in Appendix A.5 with the density plots for each parameter. The density plots are labels as: **A**-acoustic, **BE**- basal endocytosis, **Inh A**- inhibitor acoustic and **Ihn BE**- inhibitor basal endocytosis. Percentages of live and single cells were analysed and within that population the cells with dragon green-fluorescent microspheres (positive) were quantified and statistical analysis was performed.

To analyse microsphere uptake, frequency of Dragon green positive HeLa cells was analysed (Figure 4.5) and found that amino dextran -coated microspheres were preferentially uptake in all treatments while lactose-coated, that were the less negatively charged microspheres, was preferentially uptake in basal endocytosis treatment but was the lowest in the acoustic treatment. The clear difference in uptake frequency of conjugated microspheres between acoustic and basal endocytosis treatment is the difference with lactose-conjugated microspheres. This may be occurring because the sound waves are reported to deform the cell membrane[49] due to the mechanical forces acting on it and the carbohydrate receptors are not able to attach to the sugar molecule. This is only a speculation and more research in this area is needed. Lactose is being uptake in high frequency when its only incubated with the cells (basal endocytosis) which an integral cell membrane shown in Figure 4.11 is in agreement that the endocytic pathway acting with this size particles is macropinocytosis as a membrane protrusion is observed.

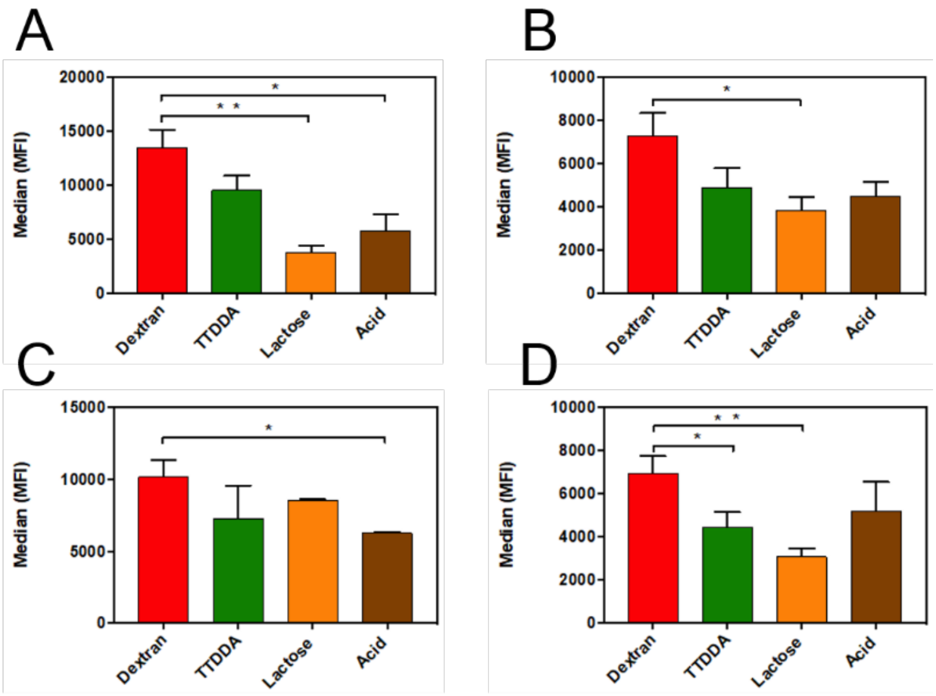

Figure 4.5: Fluorescent microsphere uptake was evaluated by using flow cytometry after treatments. The median fluorescence intensity (MFI) from single cells with positive green microspheres are shown as mean values with ±SD from 3 independent replicates (**A**- Acoustic, **B**-Inhibitor Acoustic, **C**-Basal Endocytosis, and **D**-Inhibitor Basal Endocytosis). One-way Anova analysis was done in conjunction with a Tukey's test (*p* <0.05).

For the inhibitor treatments, when the cells were acoustically exposed with the microspheres a similar trend in frequency was observed as acoustic treatment having a significant difference between the amino dextran and lactose-conjugates microspheres. For the inhibitor basal endocytosis, the trend was not observed as the acid microspheres were uptake more frequent than lactose which can be explained as the inhibitor is affecting the cytoskeleton structure therefore the attached carbohydrate receptors are being affected.

Furthermore, the percentage of the fluorescent microspheres internalised or bound to the membrane was obtained for each treatment. Figure 4.6 clearly shows as expected that amino dextran was the most found microsphere in all treatments, either internalised or bound to the membrane, while once again lactose-coated microspheres were the least uptake or bound except in the inhibitor acoustic treatment where it was the TTDDA-conjugated microspheres the lowest. This can represent the distribution of the uptake frequency in comparison to controls and other cellular treatments.

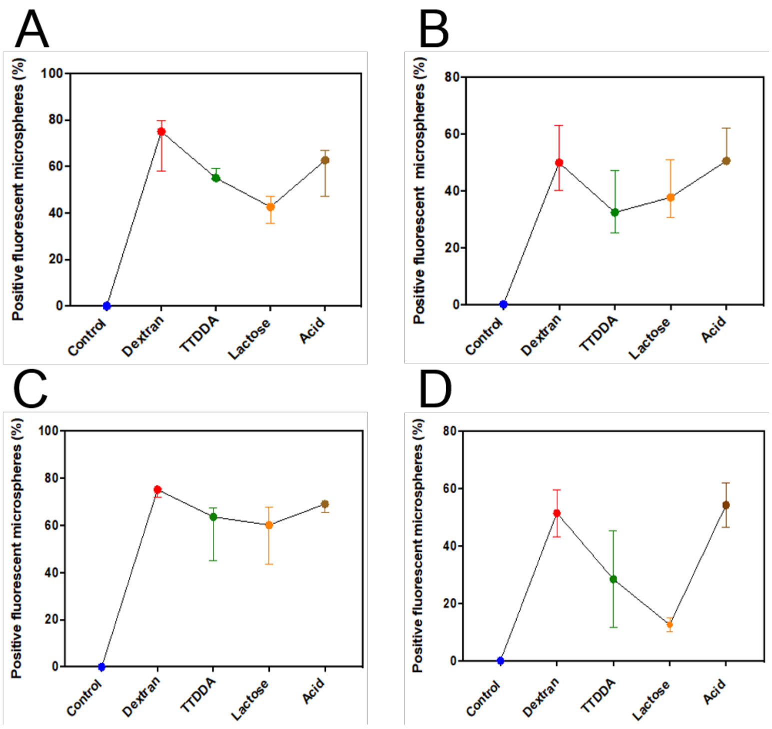

Figure 4.6; Fluorescent microsphere uptake was evaluated by using flow cytometry after treatments. The percentage of the total live and single HeLa cells with positive green-fluorescent microspheres are shown (**A**-Acoustic, **B**-Inhibitor Acoustic, **C**-Basal Endocytosis, and **D-I**nhibitor Basal Endocytosis).

Propidium iodide (PI) dye was used to label the DNA from the apoptotic cells. As it does not discriminate between the different death cell types as it labels the free DNA as it is no permeable, the live cell quantification can be obtained from the dye exclusion assay. As shown in Figure 4.7, all cellular treatments maintained their cell viability and is in agreement with the results presented in Chapter 3 for the specific conditions of 8 V_{pp}, 15 min of acoustic exposure or incubation under temperature-controlled stage.

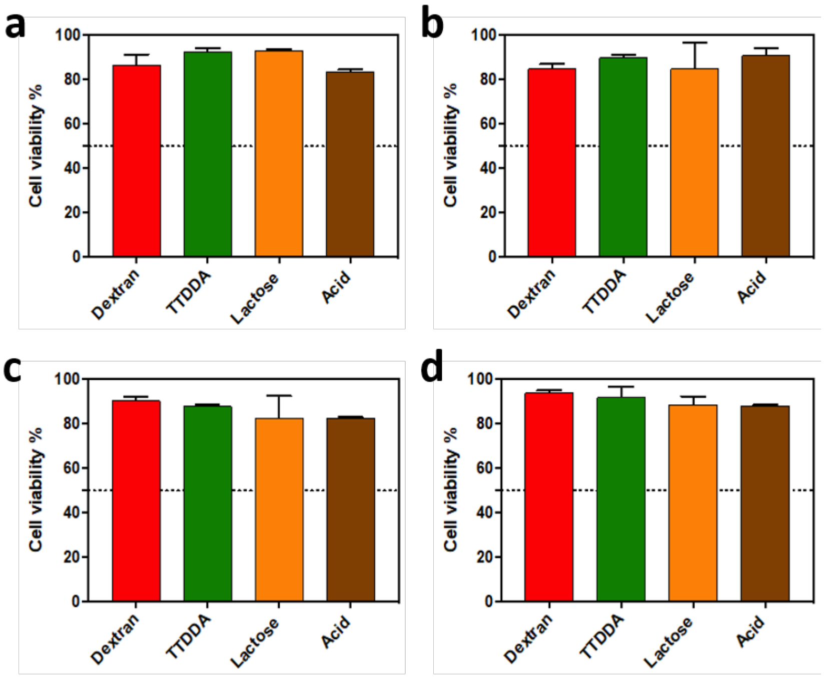

Figure 4.7: HeLa cell viability analysed by propidium iodide (PI) measurements after (**a**) treated with ultrasound, (**b**) when inhibiting cellular transport and acoustically exposed, (**c**) basal endocytosis treatment and (**d**) inhibiting macropinocytosis.

Furthermore, toxicity results were obtained when comparing the percentage of live cells of all treatments to control samples, which were not exposed nor treated with fluorescent microspheres. As shown in Figure 4.8, the cell viability for all treatments was maintained close to the controls. Overall, these results also are in agreements with those previously mention, where the polystyrene microspheres are used as a biocompatible model for drug delivery as they are non-toxic.

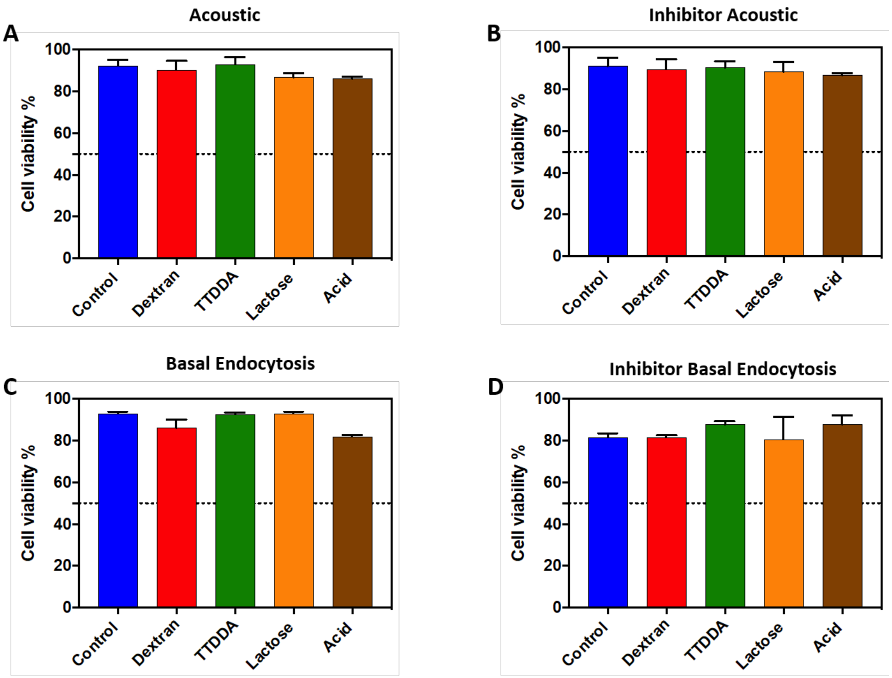

Figure 4.8: Toxicity assay of conjugated microspheres when compared to control samples (untreated and unexposed HeLa cells).

4.5 Confocal and electron microscopy

To observe microsphere internalization, confocal microscopy images with orthogonal views (*x*, *y*) were taken for all HeLa treatments. As shown in Figure 4.9, four cellular treatments were performed and imaged: cells exposed to ultrasound, basal endocytosis as the active cellular transport mechanism, and colchicine inhibitor treatment to determine if the cellular uptake was dependent on macropinocytosis (>150 nm)[18] for both treatments. As reported previously, colchicine inhibits microtubule polymerization preventing membrane ruffling and decreasing the straight tubulin structure.[22,23] In Figure 4.9, the cells look rounder in all inhibitor treatments, losing the straight tubulin structure as mentioned before but maintaining their viability. All treatments except for the controls have fluorescent microspheres either internalized or near the cell surface. In the cells exposed to USW, all surface-modified microspheres seem to be internalized and located in the cytoplasm, while with the rest of the treatments all microspheres seem to be adjacent or bound to the outer cell membrane, with some exceptions for inhibitor acoustic treatment with amino dextran and acid-coated microspheres. It is important to mention that the observed number of fluorescent microspheres in the acoustically exposed cells was higher than the rest of the treatments, meaning that the alignment of the cells and the micro-spheres in the acoustic pressure nodes allows more cell-particle contact in comparison to the basal endocytosis treatment where HeLa cells were incubated with the fluorescent microspheres, exhibiting a more scattered pattern. The bright and prolonged fluorescence of the microspheres indicates that there is no dye leakage from the microspheres as they are internally dyed according to the manufacturer (data not shown, Tech Note 103, Bangs Laboratories, Inc.).

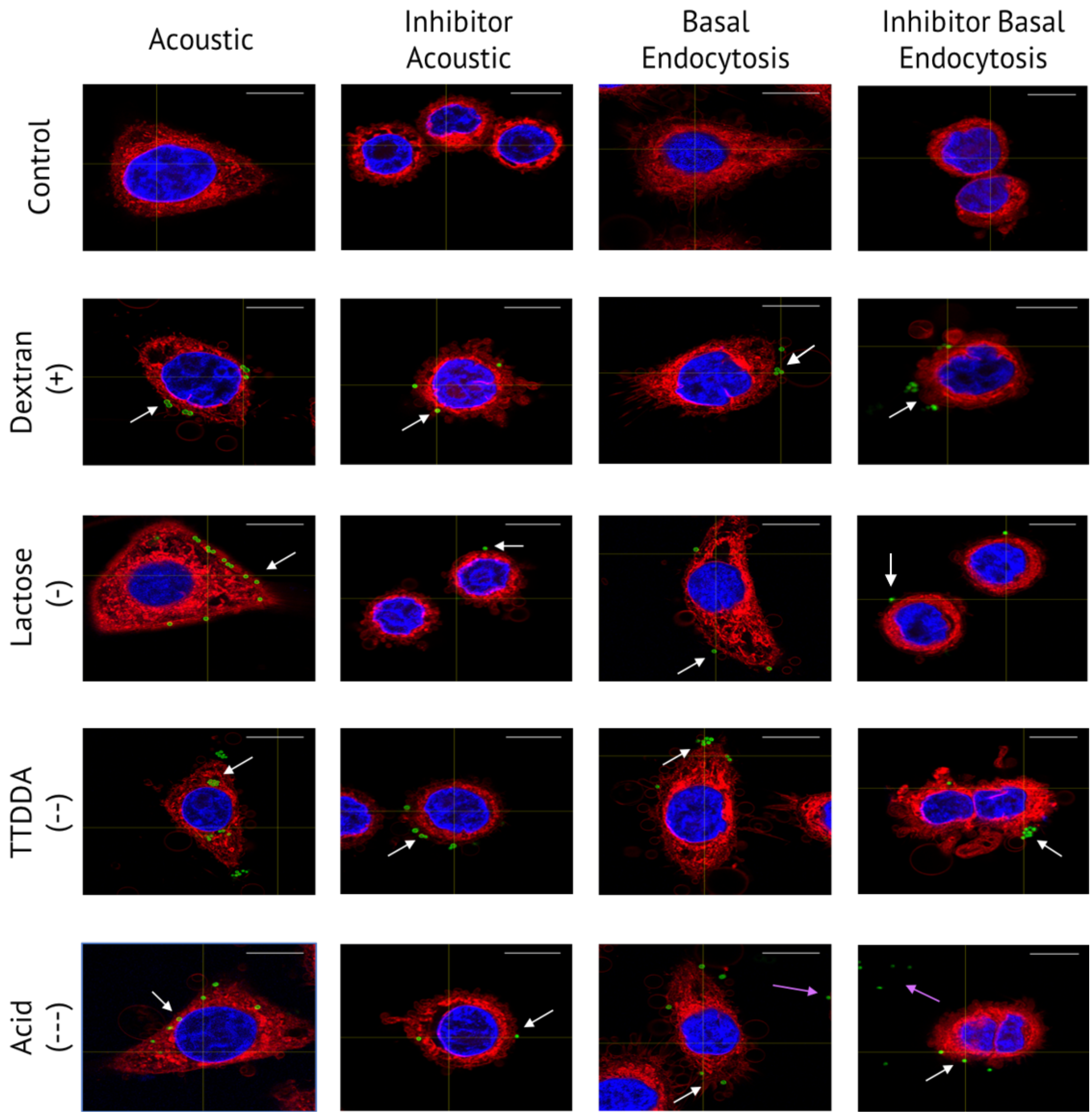

Figure 4.9: Control and fixed HeLa cells for all treatments were stained with red cell mask for plasma membrane and DAPI for the nucleus. The white arrows indicate the conjugated microspheres internalized or at the edge of the plasma membrane, while

the two purple arrows at the bottom right are indicating the microspheres that were not internalized in basal endocytosis and inhibitor basal endocytosis. Scale bars 10µm.

Microsphere infiltration quantifications of deconvoluted confocal images were performed to elucidate whether surface-modified microspheres internalized into the cytoplasm or bound to the cell surface in basal and acoustic endocytosis treatments. This analysis was carried out with the deconvoluted images of three individual HeLa cells for each surface-modified microsphere in all treatments. HeLa cell and microsphere size limits were identified and any objects larger or smaller than the established threshold were excluded. As shown in all Figures in Appendix A.2, the cell membrane was delimited and marked in purple by the computational analysis while a different colour delimitation was employed for the internalised microspheres (red), bound to the cell membrane (yellow) and outside of the cell membrane (blue). In all treatments, 3D stacks of the cells were analysed, and all the microspheres were categorised and labelled. Afterwards, graphs of the total count for all microspheres in all treatments produced by the computational analysis were made and the median was calculated (Appendix A.3). As expected from the images produced by the analysis, almost all microspheres were found to be either internalised or bound to the cell membrane with very few cases outside of the cell observed in the acid- and lactose-surface modified microspheres. For the acoustic treatment, all surface modified microspheres were found to be either internalised or at the edge of the cell membrane, while for the basal endocytosis treatment most of the microspheres were mainly bound to the cell membrane. Amino dextran microspheres were mostly localised at the edge of the cell membrane with fewer cases inside the cell with both inhibitor treatments. Acid-modified microspheres were internalised in both inhibitor treatments; however, few microspheres were also found on the border or outside of cells. Finally, most of the lactose- and TTDDA-surface modified microspheres treated with colchicine were bound to the cell membrane with some microspheres outside and inside the cell, respectively. These results suggest that by applying the acoustic field, the microspheres are trapped closer to the cell and a cell-microsphere contact can be made if compare with the basal endocytosis treatments. Furthermore, this analysis is useful for an initial scope of microsphere internalization, as it quantifies deconvolved images of individual cells. However, this analysis is limited as it cannot analyse more than two cells in the same field and therefore large cell samples cannot be analysed.

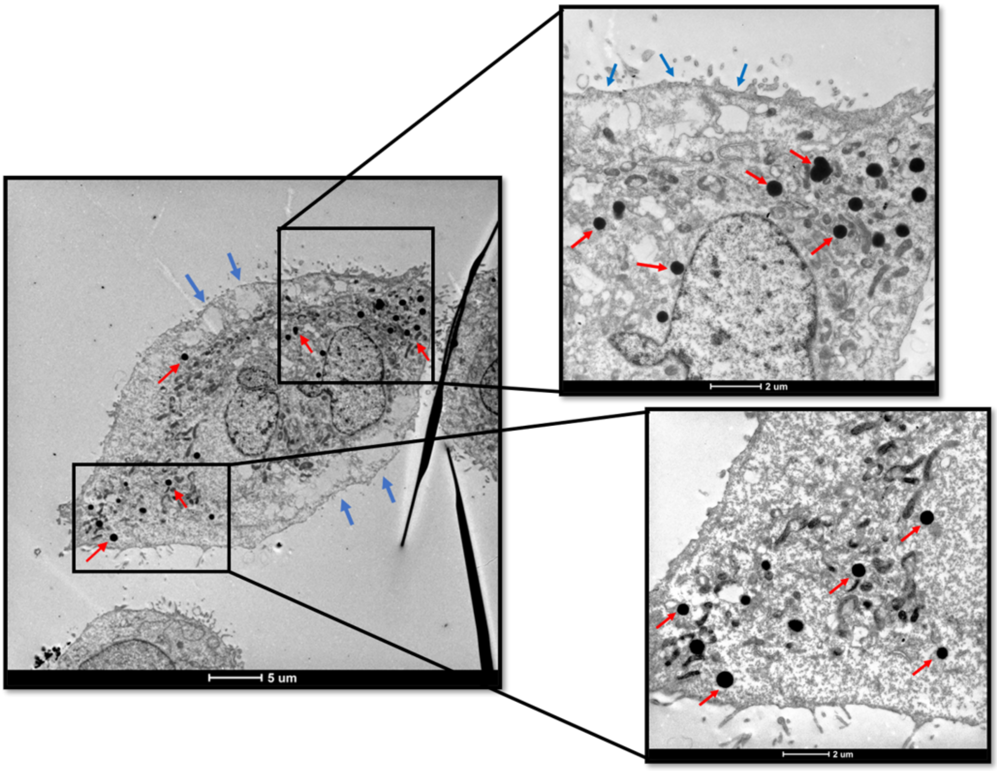

Figure 4.10: TTDDA-conjugated microspheres acoustically guided inside a HeLa cells. Two closer views are depicted from the top and the bottom end of the cell where with red arrows the conjugated microspheres are indicated and, with blue arrows the transitional pores induced by ultrasound are indicated. Scale bars 5 μm and 2μm, respectively.

Transmission electron microscopy (TEM) was also used to elucidate the endocytic mechanism and observe the integrity of the cell membrane for all treatments. The first images obtained with the TTDDA- acoustic treatment (Figure 4.10), the microspheres were internalized and were mainly at the ends or periphery of the plasma membrane. In particular the observation of pores in the membrane and in the periphery of the cytosol that can indicate the formation of transitional pores in which some were sealed, and the integrity of the plasma membrane was re-established. This result is in agreement with the previous literature where the first SEM images showed that ultrasound induced the formation of pores in the tumour cell membrane.[10] In addition, lactose-conjugated and incubated microspheres were also imaged without acoustic exposure or inhibitor. An image could be captured where it is observed that the plasma membrane is intact and there was no pore formation. Furthermore, the microsphere appears to be engulfed by a membrane protrusion and it is possible that the macropinosome was forming at that time (Figure 4.11).

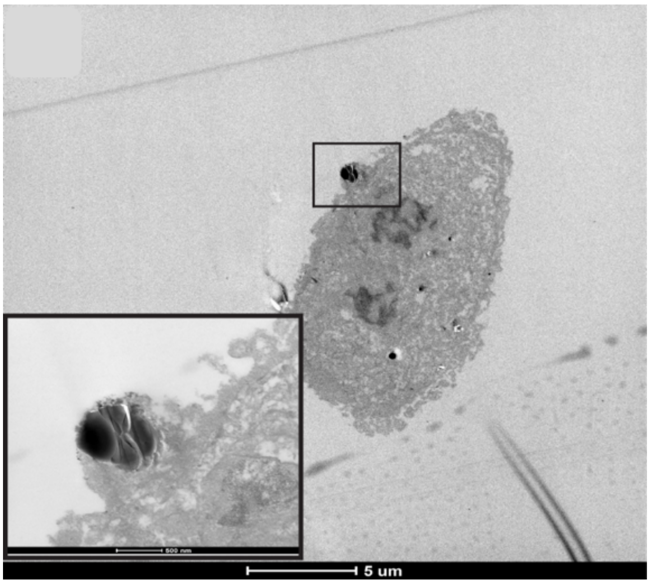

Figure 4.11: Lactose-conjugated microsphere inside the HeLa cell with a basal treatment. The closer view can confirm the uptake by macropinocytosis as the plasma membrane is engulfing the microsphere and the plasma membrane is intact. Scale bar 5 µm, inset 500 nm.

Furthermore, Figure 4.12 shows HeLa cells with internalised conjugated microspheres when acoustically exposed. Amino dextran microspheres were the most uptake by the cell (**A**) located mainly at the periphery inside in the cytoplasm. As observed, at the top of the cell, microsphere aggregates were found, and it can be due to the electrostatic interaction between microparticle join with the secondary acoustic forces which are the interparticle forces. This is in agreement with Polydispersity Index (PDI) measurements where amino dextran microspheres tend to form aggregates in solution but within the standards to still be considered a monodispersed solution. TTDDA- and lactose-conjugated microparticles (**B** and **C**) were also internalised and membrane pores are observed at the periphery of the cell. In lactose- (**C**) treated cell, the particle is shown to be closer to the nuclear envelope suggesting that it was transported by the macropinosome as seen by the very thin membrane around the particle that is not well-defined and is also observed in the amino dextran-conjugated microspheres (**A**). However, that is not the case for TTDDA- and acid-microspheres where the latter one is also close to the nucleus. It is important to mention that the expulsion of conjugated microspheres from the cells was not observed but this idea cannot be ruled out since for this research the cells were fixed after being treated with the microspheres. However, by these results it is suggested to further incubate the cells with the internalised microspheres and evaluate with TEM if there are microspheres taken out by the cells which will mean the exocytosis pathway is acting and, will lead to more a structural and molecular detail for ultrasound-mediated drug delivery employing solid particles. More TEM images are in process for the rest of the cellular treatments but so far it can be speculated that high intensity ultrasound indeed also enhances delivery by forming transitional membrane pores which may be triggered by mechanical forces that induce the Ra-activating pathway and cytoskeleton rearrangement.

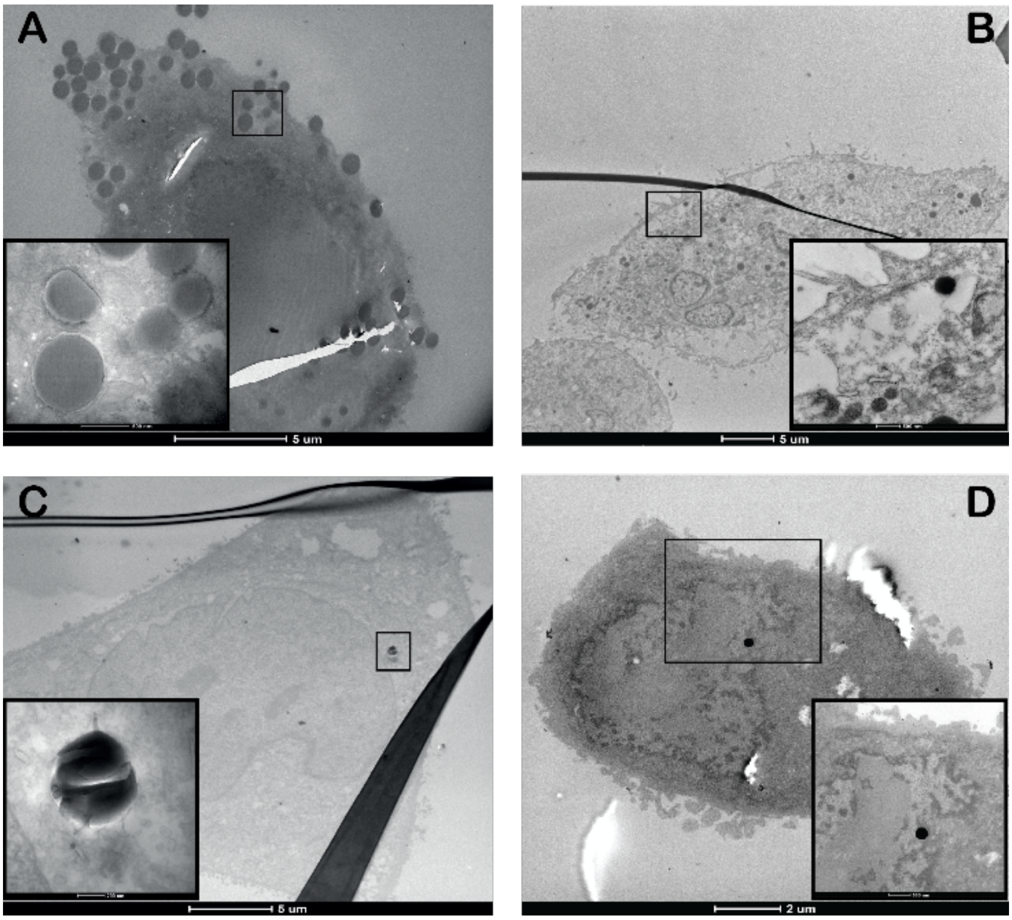

Figure 4.12: HeLa cells after ultrasound exposure with (**A**) amino dextran-conjugates microspheres, (**B**) TTDDA-conjugated, (**C**) lactose-conjugates and (**D**) acid microspheres. As observed in (**A**) and (**C**) the conjugate microspheres present a very thin and not well-defined membrane around them. In all treated samples, pores in the membrane are observed and in (**C**) and (**D**) the conjugated microspheres are located near the nuclei. Scale bars are 5μm and 2 μm for the closer views.

4.6 Chapter conclusions

To conclude, this chapter offers a possible approach to the mechanisms of endocytosis and enhancement of USW-induced microparticle uptake. As seen in the microscopy images, the membrane pores appeared to form after exposure to ultrasound, indicating that they may be transient, as resealing is observed when the conjugated microspheres were internalised. Also, the endocytic pathway that was found to uptake the 0.9-1μm conjugated microspheres was macropinocytosis where a membrane protrusion is observed while maintaining the integrity of the plasma membrane. These protrusions are believed to fuse together forming the macropinosome fusing again with the plasma membrane although this last exact mechanism is not yet fully known. Furthermore, these results showed particle uptake when exposed to ultrasound and when inhibiting the endocytic pathway. Cell viability was not affected, and the conjugated microspheres were not toxic to the cells as the propidium iodide analysis showed, although more viability and more importantly metabolic activity measurements are needed to fully guarantee their survival. There are only a few reports of low-intensity ultrasound,[24,25] used for imaging, improving cell motility, and thus promoting wound closure[24] and activating the inducing phagocytosis of the Rho family in macrophages.[25] As mentioned in Chapter 1, is believed that in low intensity acoustic exposures, acoustic streaming may be the phenomenon enhancing fluid phase uptake due to the shear stress and the constant oscillations that are produced near the plasma membrane. However, and as discussed previously, although there is Eckart acoustic streaming produced in this ultrasonic device, the microspheres and therefore the cells are not affected and are trapped at the bottom of the device where the USW are generated. Another explanation described in the previous Chapter was the rearrangement of the cytoskeleton which is triggered by the mechanical forces acting on the cell are induced by ultrasound which increases the permeability of the membrane. This reasoning may be appropriate for this research since, as mentioned above, macropinocytosis is activated by a signalling cascade of Rho GTPases that regulate cellular mechanisms such as actin organization, cell polarity and motility, focal adhesions.[24] This can only provide a start point as more research is needed on signalling pathways after ultrasound exposure and also on exocytosis pathways in order to broaden the field of nanomedicine using solid particles.

4.7 References

1. S. D. Conner and S. L. Schmid, *Nature Review*, 2003, **422**, 37-43.
2. I. Lentacker, I. De Cock, R. Deckers, S.C. De Smedt and C.T.W. Moonen, *Advanced Drug Delivery Reviews*, 2014, **72**, 49-64.
3. J. Hauser, M. Ellisman, H.-U. Steinau, E. Stefan, M. Dudda and M. Hauser, *Ultrasound Med. Biol*., 2009, **35**, 2084–2092.
4. V. Lionetti, A. Fittipaldi, S. Agostini, M. Giacca, F. Recchia and E. Picano, *Ultrasound Med. Biol*., 2009, **35**, 136–143.
5. D.M. Paula, V.B. Valero-Lapchik, E.J. Paredes-Gamero and S.W. Han, *J. Gene Med*., 2011, **13** (7–8), 392–401.
6. J. L. Huang, G. Jiang, Q. X. Song, *et al*., *Nat Commun*, 2017, **8**, 15144.
7. D. Vercauteren, R. E. Vandenbroucke, A. T. Jones, J. Rejman, J. Demeester, S. C. De Smedt, N. N. Sanders and K. Braeckmans, *Molecular Therapy*, 2010, **18** (3), 561-569.
8. A. T. Jones, *J Cell Mol Med*, 2007, **11**, 670-684.
9. S. Grimmer, B. van Deurs and K. Sandvig, *J Cell Sci*, 2002, **115** (14), 2953-2962.
10. K. Tachibana, T. Uchida, K. Ogawa, N. Yamashita and K. Tamura, *Lancet*, 1999, **353**, 1409.
11. P. Burbelo, A. Wellstein, and R. G. Pestell, *Breast Cancer Research and Treatment*, 2004, **84**, 43–48.
12. C. Commisso, *Nature*, 2013, **497**, 633-637.
13. J. Son, *et al*., *Nature*, 2013, **496**, 101-105.
14. J. Rejman, V. Oberle, I. S. Zuhorn and D. Hoekstra, *Biochem J*, 2004, **377** (1), 159-169.
15. E. Yamada, *J. Biophys. Biochem. Cytol*., 1955, **1**, 445-458.
16. R. G. Anderson, *Annu. Rev. Biochem*., 1998, **67**, 199-225.
17. S. Mura, J. Nicolas and P. Couvreur, *Nat. Mater*., 2013, **12**, 991-1003.
18. T. dos Santos, J. Varela, I. Lynch, A. Salvati, K. A. Dawson, *PLoS ONE*, 2011, **6** (9), e24438.
19. T. Patiño, J. Soriano, L. Barrios, *et al*., *Sci Rep*, 2015, **5**, 11371.
20. F. Wang, *et al., Nanomedicine*, 2013, **9**, 1159–68.
21. M. Danaei, M. Dehghankhold, S. Ataei, F. Hasanzadeh Davarani, R. Javanmard, A. Dokhani, S. Khorasani and M. R. Mozafari, *Pharmaceutics*, 2018, **10** (57), 1-17.

22. H. Herd, N. Daum, A. T. Jones, H. Huwer, H. Ghandehari and C-M. Lehr. *ACS Nano*. 2013, **7** (3), 1-21.
23. H. Guo, X. Li, Y. Guo and L. Zhen, *Medicinal Chemistry Research*, 2019, **28**, 927–937.
24. P. Atherton, F. Lausecker, A. Harrison and C. Ballestrem, *Journal of Cell Science*, 2017, **130**, 2277-2291.
25. S. Zhou, M. G. Bachem, T. Seufferlein, Y. Li, H. J. Gross and A. Schmelz, *Cell Signalling*, 2008, **20**, 695-704.
26. T. dos Santos, J. Varela, I. Lynch, A. Salvati, K. A. Dawson, *Small*, 2011, **7** (23), 3341-3349.
27. M. G. Bexiga, J. A. Varela, F. Wang, F. Fenaroli, A. Salvati, I. Lynch, J. C. Simpson and K. A. Dawson, *Nanotoxicology*, 2011, **5** (4), 557-67.
28. H. V. Nguyen, K. Campbell, G. F. Painter, S. L. Young and G. F. Walker, *Pharmaceutics*, 2020, **12**, 1150.
29. E. Bilensoy, *Expert Opin. Drug Deliv.*, 2010, **7**, 795-809.
30. C. Riccardi and I. Nicoletti, *Nature Protocols*, 2006, **1** (3), 1-4.
31. M. Pawlaczyk and G. Schroeder, *Molecules*, 2020, **25**, 2660.
32. K-M. Kim, *et al.*, *International Journal of Nanomedicine*, 2014, **9**, 29-40.
33. B. Kang, K. T. Opatz, Landfester and F. R. Wurm, *Chem. Soc. Rev*. 2015, **44**, 8301-8325.
34. Y.-L. Xie, M.-J. Wang and S.-J. Yao, *Langmuir*, 2009, **25**, 8999–9005.
35. N. Sharon and H. Lis, *Sci. Am.*, 1993, **268**, 82–89.
36. S. Q. Ye, C. Y. Wang, X. X. Liu and Z. Tong, *J. Biomater. Sci., Polym. Ed.*, 2005, **16**, 909–923.
37. D. Benito-Alifonso, S. Tremel, B. Hou, H. Lockyear, J. Mantell, D, J. Fermin, P. Verkade, M. Berry and M. Carmen Galan. *Angew Chem Int Ed Engl.*, 2014, **53** (3), 810-814.
38. M. P. Wickramathilaka and B. Y. Tao, *J Biol Eng*, 2019, **13**, 63.
39. G. T. Hermanson, Bioconjugate techniques: Academic press; 2013.
40. J. D. Carter and T. H. LaBean, *Journal of nucleic acids*. 2011.
41. S. S. Ghosh, P. M. Kao, A. W. McCue and H. L. Chappelle, *Bioconjug Chem*. 1990, **1**, 71–6.

42. R. B. Ravelli, B. Gigant, P. A. Curmi, I. Jourdain, S. Lachkar, A. Sobel and M. Knossow, *Nature*, 2004, **428**, 198–202.
43. I. A. Khalil, K. Kogure, H. Akita and H. Harashima, *Pharmacol Rev*. 2006, **58**, 32–45.
44. A. Piasek and J. Thyberg, *J Cell Sci*. 1980, **45**, 59–71.
45. A. Piasek and P. Oblakowski, *Haematol Blood Transfus*.,1985, **29**, 511–513.
46. A. Adan, G. Alizada, Y. Kiraz, Y. Baran, and A. Nalbant, *Crit Rev Biotechnol*, 2017, **37** (2), 163–176.
47. M. G. Macey (2010). Principles of flow cytometry. Flow cytometry: principles and applications In: Macey MG, ed. Totowa (NJ): Humana Press, 1–15.
48. M. J. Wilkerson *Vet Clin North Am Small Anim Pract*, 2012, **42**, 53–71.
49. L. M. López-Marín, B. E. Millán-Chiu, K. Castaño-González, *et al*., *J Membrane Biol*, 2017, **250**, 41–52.

5 Conclusions and outlook: Ultrasound

To conclude this thesis topic -*Ultrasound*, it can be said that since the discovery from the Curie brothers of the piezoelectric effect, through the first applications as an investigative tool experimentally demonstrated by Marie Curie and when it became a scientific subject as a hydrophone was employed for submarine detection during World War I by the father of ultrasonics, Pierre Langevin, ultrasound has evolved. Its evolution has implied reducing the scale of the first devices to be able to be translated into biological applications and to generate non-invasive therapies.

Standing acoustic waves have proven to be a widely used category in the field of ultrasound since in the 19th century, Kundt[6] observed in his tube that dust particles could get trapped and stay "still." This fact caused interest and began the studies and formulation of physical expressions to explain this phenomenon. The use of the acoustic forces, primary that guides the particles to either the pressure or antipressure nodes and the secondary forces which permits the agglomeration of particles in the nodes is known due to the studies of King in 1934. He was the first person to provide calculations of the primary radiation forces acting on a spherical particle in a non-viscous fluid. This formulation later expanded the area of ultrasound study and it was Gor'kov who formulated the theory of acoustic radiation in 1962 and years later Yosioka and Kawasima expanded it. This implied that researchers began to play with the designs and the geometries to be able to generate more complex alignment patterns under various ultrasonic operating conditions. The range of frequencies used for the trapping of biological materials has not changed, since the first experiments carried out by Baker and Coakley in the early 70s and late 80s, the range has remained from 1-10 MHz. It is clear that depends on the piezo transducers that one uses, which is the acoustic source, but as the size of the device decreases, the size of the piezo transducers also decreases.

The physical laws were also reduced, and phenomena were found to act because of acoustic waves. These so-called acoustic phenomena began to be studied with their implications in biological and non-biological materials. Some of them like the acoustic streaming, which are oscillations observed in the bulk fluid, which can not only disturb particle entrapment, but can also benefit in gene delivery applications within acoustic contrast factors. This allowed the commercialization to create these stable gas spheres to be able to introduce the drugs or genes and be carried to the cell or tissue of interest. The effects of acoustic streaming are that they generate porosity in the membranes by another acoustic phenomenon called cavitation and allows the entry of drugs due to their constant oscillations of fluid creating a shear stress force. This increased in membrane permeability termed sonoporation is one of the most studied areas within ultrasound. Another bioeffect that was found to be detrimental for biological samples was the overheating in the exposure area. This rise in temperature due to high intensity ultrasound later became a therapeutic subject to treat different types of cancer or being used in lithotripsy a method to break down kidney stones.

The operating condition of the ultrasound showed great variability for all the referenced literature, which also hinders the reproducibility and follow-up of the studies in the area. It was also found that more systematic methods are needed to create a certain order and clarify various fundamental aspects of ultrasound, such as its phenomena with its implications. It is also necessary to carry out more studies that expose biological materials, following the above, in a systematic way and using various techniques to correctly evaluate the benefits or harms of acoustic waves. Drug delivery studies using solid particles and ultrasound are very few to date. A plethora of studies related to the uptake of solid micro and nanoparticles in various types of cells and with various sizes, shapes and forms were found without ultrasound, which their results would provide us with an approximation. But also, within these studies, a great variability was found using the same characteristics of micro and nanoparticles but obtaining opposite results.

To conclude, it is necessary to create protocols and systematic studies in the operation and acoustic conditions for each developed ultrasonic device, covering its phenomena and its implications in various materials. Also, explore several applications employing the same ultrasonic device so it will be possible to transfer the technology to a tangible and portable device. The science of ultrasound has been oriented according to the needs that are emerging in society as shown in the first applications. Its potential is yet to be exploited in various areas of biomedicine, especially applied to gene therapies and personalized medicine that are emerging. For the latter, ultrasound can be used for a personalized patient device that can treat and target medications to a specific tissue / organ without the need to go to hospitals or clinics.

6 Multipolar mitosis in human pluripotent stem cells (hPSCs)

This chapter presents an additional thesis topic in which multipolar cell divisions were observed in human pluripotent stem cells (hPSCs), a phenomenon exhibited by cancer cell lines that is thought to be linked to tumorigenesis, aneuploidy and therefore genomic instability. For this work, I was supervised by Prof. Rafael Carazo Salas from the School of Cellular and Molecular Medicine at the University of Bristol and quantified multipolar mitosis and mitotic defects in undifferentiated hPSCs based on previous results obtained in the Carazo Salas group by Rosie Maddock (rotation student) and comparing them with the new results I acquired during time-lapse confocal imaging. In addition, I performed immunofluorescence assays to label and visualize the cellular components involved in the mitotic process to be able to observe the anomalies during the process that lead to mitotic errors and defects. The hPSC cell line that was used expressed a FUCCI (fluorescent ubiquitination-based cell cycle indicator) reporter genetically encoded to highlight the G1 / S / G2 / M phases of the cell cycle and a Histone 2B (H2B-HaloTag) reporter was also genetically introduced, which was covalently coupled with a HaloTag JF646 ligand to label the chromatin of live cells. Both constructs were previously made by Dr Seongmin Kim, senior postdoc in the Carazo Salas group, using the CRISPR/Cas9 knock-in technology.

6.1 Introduction

Pluripotent stem cells (PSCs) are highly relevant for tissue engineering and regenerative medicine studies as they can be used for 2D and 3D tissue and organoid culture due to their multi-lineage differentiation potential. This organoid approach despite their immense potential for therapeutic applications has not been fully established. Moreover, hPSCs have shown genomic instability when cultured *in vitro* for long periods of time (culture adaptation). This chapter introduces and exemplifies the mitotic defects and multipolar divisions that have been observed in hPSCs from previous works. Additionally, a new visualization approach is introduced with a genetically encoded fluorescent three-colour reporter system to investigate and monitor individual hPSCs during a 4-day time-lapse confocal imaging. Quantifications of total mitosis, mitotic defects, and multipolar divisions were obtained from undifferentiated hPSCs and the first generation of daughter cells resulting from division. A general table for the undifferentiated hPSCs was constructed from the quantifications of two different time-lapse data sets. In addition, immunofluorescence assays were performed to label cellular structures involved in the mitotic process in fixed hPSCs after time-lapse imaging. The focus of this chapter is to introduce the mitotic defects that hPSCs can suffer and, although these results are not enough to conclude on which cellular structures contribute to genomic instability, they indicate that such defects could be potentially involved in causing genomic instability and tumorigenic potential in hPSC cultures. Therefore, more research is needed to investigate the limitations and risks of using hPSCs before transferring this technology to therapeutic scenarios.

6.2 Human pluripotent stem cells (hPSCs)

Human embryonic stem cells (hESCs) are the isolated and cultivated cells derived from the inner cell mass of the blastocyst. When the zygote, which is the result of fertilization of an oocyte by a spermatozoon, undergoes several mitosis, it generates a morula consisting of 32 to 64 totipotent cells. After the morula, a blastocyst is developed where the embryonic membranes and the placenta are derived from the peripheral cells called the trophoblast and the foetus is formed from the inner cell mass. As shown in Figure 6.1, embryonic stem cell cultures are established from this inner cell mass which are considered pluripotent stem cells (PSCs)[1] as they can be used to generate different types of mature somatic cells through lineage differentiation techniques. If the development of the embryo continues to generate a complete multicellular organism, after the blastocyst a gastrula is formed that is composed of three germ layers, ectoderm, mesoderm and endoderm. From the ectoderm, the nervous system, the epidermis and neural-derived tissues are generated. From the mesoderm, connective tissue, cartilage, axial skeleton and blood will be formed and the endoderm will give rise to the respiratory, gastrointestinal and urinary systems.[2]

Embryonic stem cells (ESCs) have the unique ability to indefinitely self-renew in an undifferentiated state through various passages in cell cultures while maintaining their pluripotency. As mentioned before, they are also able to differentiate into several stem or progenitor cell types that are used for developing drugs or tissue engineering.[3,4] The first cultivated ESC lines were established in 1981 from mouse embryos[7,8] and in the late 90s the first human ESC line was generated from donated frozen human blastocysts produced by in vitro fertilization.[9] Furthermore, it has been demonstrated that mature somatic cells can be reprogrammed to return to a pluripotent state and differentiate into different cell types by several methods: cloning and somatic cell nuclear transfer (SCNT), altered nuclear transfer (ANT), cell fusion or by introducing transcription factors using viral and non-viral vectors that are involved in the maintenance of ESC pluripotency.[10,15] The resultant reprogrammed cells from the latter technique are called induced pluripotent stem cells (iPSCs) and it is believed that they have equal phenotype, gene expression and developmental characteristics as the ESCs.[5]

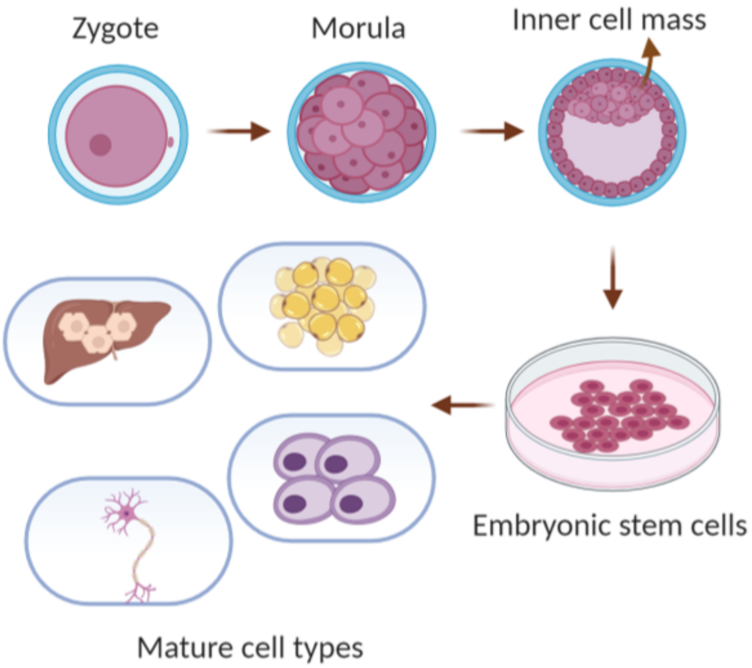

Figure 6.1: Cultivation of human embryonic stem cells (hESCs). The zygote undergoes several cell divisions forming the blastula where the stem cells are extracted from the inner cell mass. These cells are pluripotent and can be differentiated into other types of cells. Adapted from reference 1 and created with Biorender.

The SCNT or cloning technique is when the nucleus from a mature adult cell is transplanted into an enucleated oocyte to reprogram the somatic nucleus to the pluripotent state.[11] In 1962, the first SCNT work was demonstrated in amphibians by Nobel Prize winner (2012) Sir John B. Gurdon.[12] In this incredible work, different species within the *Xenopus* genre were employed, *Xenopus tropicalis* and *Xenopus* *laevis*, respectively, where the nuclei of differentiated cells of the intestinal epithelium of *X. tropicalis* were injected into *X. laevis* enucleated eggs. Sir John B. Gurdon followed the nuclear transplantation method previously described in 1960 by Elsdale *et al*[13] and showed that the egg with the foreign nucleus formed a fully functional tadpole (juvenile stage). This landmark discovery proved that the nucleus from a mature and differentiated cells can return to a pluripotent state because it stores genetic information necessary to develop a viable individual. Following the work of Sir John B. Gurdon, the first SCNT in mammals was performed by Wilmut *et al*[14] in the late 1990s where a live lamb named Dolly was born after the transfer of a mammary gland nucleus into an enucleated oocyte and implanted into an adult ewe (female sheep). They reported more than 50% of foetal loss during pregnancy in the other treated sheep and approximately 10% or perinatal loss. In addition, they observed that the lambs that were alive had characteristics of the donor nucleus and not the recipient oocyte, which means that they did not resemble their birth sheep. This technique provided more insight and paved the way for future research in developmental biology and stem cells. However, it has the disadvantage of being unpredictable as several attempts must be made to generate viable organisms, which raised ethical issues as these organisms did not survive long.[15]

Altered nuclear transfer (ANT) is similar to the SCNT as it involves the transfer of a somatic nucleus from a mature cell into an oocyte without nucleus. However, the main difference between these two techniques is that in ANT either the somatic nucleus from the donor cell, the cytoplasm of the oocyte or both have to be modified or altered before the transfer to produce a hybrid pluripotent cell.[10,15] These modifications can either be at the DNA level of the nucleus from the donor cell or the environment of the recipient oocyte.[15] Also, a hybrid pluripotent cell can be generated by the fusion of ESCs with somatic cells (i.e., fibroblasts) where a stable tetraploid DNA structure is maintained and the hybrid PSCs present similar characteristics in morphology, antigen expression and growth rate to the original ESCs.[16,17] Previous works have demonstrated with both techniques that reprogramming factors are present in ESCs or oocytes or perhaps both.[18]

Takahashi and Nobel Prize winner (2012) Yamanaka[6] screened 24 candidate genes expressed in ESCs that can induce reprogramming and were able to generate functionally equivalent pluripotent stem cells, which they termed induced pluripotent stem cells or iPSCs from mouse embryonic and adult fibroblasts by adding a cocktail of four transcription factors (Oct3/4, Sox2, c-Myc and Klf4) in a retroviral vector, an example is depicted in Figure 6.2. This work represented a breakthrough in the field due to the discovery of two central transcription factors essential to generate iPSC, Oct3/4 and Sox2, although Nanog is known to be essential for maintaining pluripotency,[19,20] providing the first means to artificially produced PSCs from adult somatic cells *in vitro*. They mention that the overexpression of these four Yamanaka factors are necessary for the generation of iPSC, but that their continued overexpression can be counterproductive for their self-renewal. Furthermore, Takahashi and Yamanaka demonstrated that reprogramming takes place in the nucleus and not in the cytoplasm, since these factors are already highly expressed in ESCs, and showed that they can differentiate *in vivo* and *in vitro* when having the retroviral vectors. Later, Thomson and collaborators found that by adding Lin28 to the cocktail of Oct3/4, Sox2 and Nanog, iPSCs can also be generated.[21]

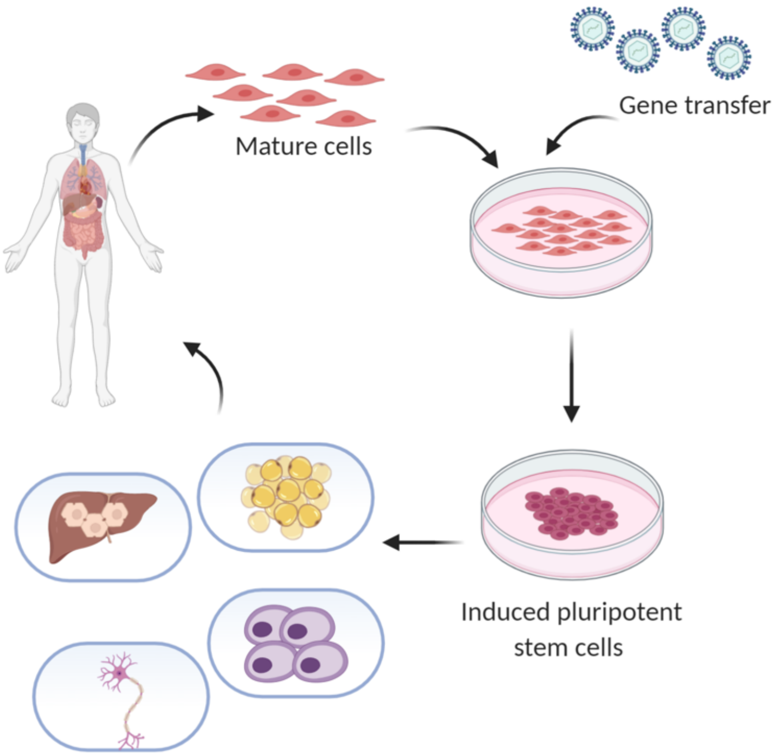

Figure 6.2: Generation of induced pluripotent stem cells (iPSCs) by adding a genetic vector to mature cells to induce pluripotency. This technology has the advantage of

generating autologous cells for therapeutic treatments. Adapted from reference 1 and created with Biorender.

Since the establishment of techniques for the manipulation and generation of hPSCs added to their self-renewing and pluripotency characteristics, there has been a rapid development of clinical trials in the last decade.[22] The first PSCs clinical trials were made by Geron for spinal cord injuries, Advanced Cell Technology and the Kobe Centre for Developmental Biology for macular degeneration.[24] Therapies employing hPSCs require to scale-up the cultivation and production of stem cells and differentiate them into a specific cell type to generate an autologous transplant. However, there are outstanding problems when using hPSCs for patient specific therapies that include maintaining genetic stability during culture before and after being differentiated without tumorigenic potential,[23] as discussed further.

6.2.1 Multipolar mitosis in cancer cell lines

Cancer cells present six main common characteristics that alter their cellular physiology and that jointly develop a malignant growth, these are known as the hallmarks of cancer and were described by D. Hanahan and R. A. Weinberg.[25] These hallmarks (i.e., evading apoptosis, metastasis and tissue invasion, grow without external signals and unaffected by growth inhibitors, sustained angiogenesis and limitless division potential maintaining their telomerase length) allow cancer cells to survive and proliferate. Although hallmarks are still being added to the existent list, to date the characteristics that allow them to be generated are genomic instability and inflammation promoting tumorigenesis.[26] The genomic instability that cancer cells develop is the result of accumulated mutations during multiple cell divisions.[27] This genomic instability includes numerical (i.e., gaining or losing chromosomes) and structural chromosomal rearrangements (i.e., deletions, amplifications or translocations) that cause chromosomal instability (CIN) leading to aneuploidy which is irreversible and tumour development.[28]

The mechanisms that cause CIN in cancer cells include defects in the spindle assembly checkpoint (SAC), defects in the kinetochore-microtubule attachment, supernumerary centrosomes and chromatid cohesion defects.[29] The cellular division in mammalian cells is carried out by sequential protein activations and deactivations regulating the cell cycle progression. The cell cycle consists of an interphase that consists of 4 phases (G0, G1, S and G2), and of the M phase, which is the mitotic process where an equal distribution of genetic information (chromosomes) and cytoplasm between two daughter cells (cytokinesis) is ensured. Moreover, mitosis also consists of 5 phases (prophase, prometaphase, metaphase, anaphase and telophase).[30] Cell cycle checkpoints detect defects that occur throughout DNA replication or later stages up to mitosis and induce cell cycle arrest in response to those defects.[31] The arrest of the cell cycle allows the repair mechanisms to correct chromosomal defects and if this is not possible then the cell-checkpoints trigger processes such as apoptosis or senescence to prevent the damaged cells from propagating. Checkpoints are well established throughout cell cycle phases to maintain genome stability, such as the G1 / S checkpoint that prevents damaged cells from initiating S phase (synthesis) or triggers apoptosis or senescence while checkpoint S minimise errors by delaying DNA replication. Another very important checkpoint is the G2 / S, which prevents mis-segregation of chromosomes by stopping cells from entering mitosis prematurely.[30]

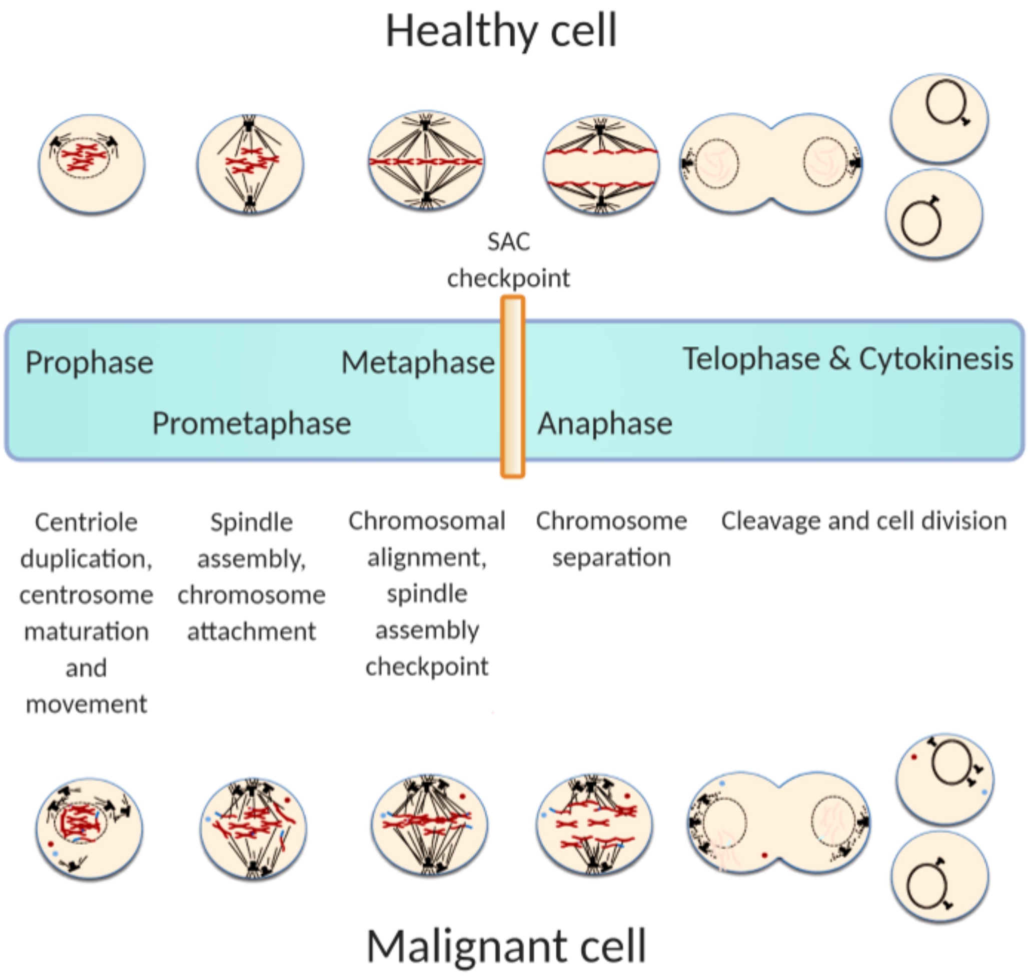

Figure 6.3: Mitosis in a healthy and a malignant cell depicting the sequential cellular process to ensure a proper chromosomal segregation and formation of two daughter cells. Adapted from reference 30 and created with Biorender.

As shown in Figure 6.3, the mitotic checkpoint or SAC is a highly conserved mechanism responsible for ensuring proper chromosomal segregation by preventing the cell from initiating anaphase until the spindle microtubules have been attached to the kinetochores. The kinetochores are large protein complexes where the centromeres, chromosomal locus that holds the chromatids arms, are assembled and are essential for the chromosome alignment and separation.[32] Each kinetochore is attached to around 25 microtubules in human cells, therefore, the SAC ensures that the kinetochores are bound to enough microtubules before the chromatids separation (Figure 6.4 (**C**)).[33] However, several cancer cell lines with CIN have revealed that their SAC was functional and had no defects. Therefore, it is not yet fully known how common SAC defects and mutations are occurring in tumours since very few studies have reported the silencing of the SAC gene by methylation causing mis-segregation leading to a very rare cancer syndrome called mosaic variegated aneuploidy (MVA). This syndrome is caused by the mutation of the gene inactivating the BUBR1 protein.[32,34] Some of these studies have reported a dysregulation of SAC components that leads to mitosis perturbations and therefore aneuploidy.[56] For example, some SAC proteins can either be over expressed or knock-down such as MAD2, BUBR1, as mentioned before, and AURORA KINASE B, that are linked to the cell cycle and as a result sister chromatids separation is premature or mitotic defects like chromosomal bridges or even cytokinesis can occur.[57]

Centrosome amplification or supernumerary (more than 2 per cell) centrosomes is a recognized feature of cancer cell lines since Van Beneden[35] and Boveri[36] were the first to identify its potential role in causing aneuploidy and promoting tumorigenesis. These organelles are the nucleation and organization centres of microtubules, involved in cell polarity, migration and division. Each centrosome is composed by two orthogonal centrioles surrounded by the pericentriolar matrix. The duplication of the centrioles occurs in S phase where the newly formed centrioles grow next to existing ones elongating and migrating to the opposite poles during mitosis.[37] Abnormalities in the structure, such as over-elongation of centrioles, and number of the centrosomes are associated with chromosomal instability generating multipolar cell divisions. In contrast to healthy cells where they stop proliferating and eventually die in the presence of multiple centrosomes, cancer cells will cluster extra centrosomes during mitosis as a survival mechanism enabling the formation of transient multipolar or pseudo-bipolar spindles (Figure 6.4 (**A**)).[32,37] These multipolar spindles increase merotelic attachments, where a single kinetochore is attached to multiple microtubules that arise from both spindle poles, generating a chromosomal mis-segregation (Figure 6.4 (**A** and **B**)). However, since the kinetochores attach to several microtubules, the SAC is often misguided, and the cell continues to the S phase.[38]

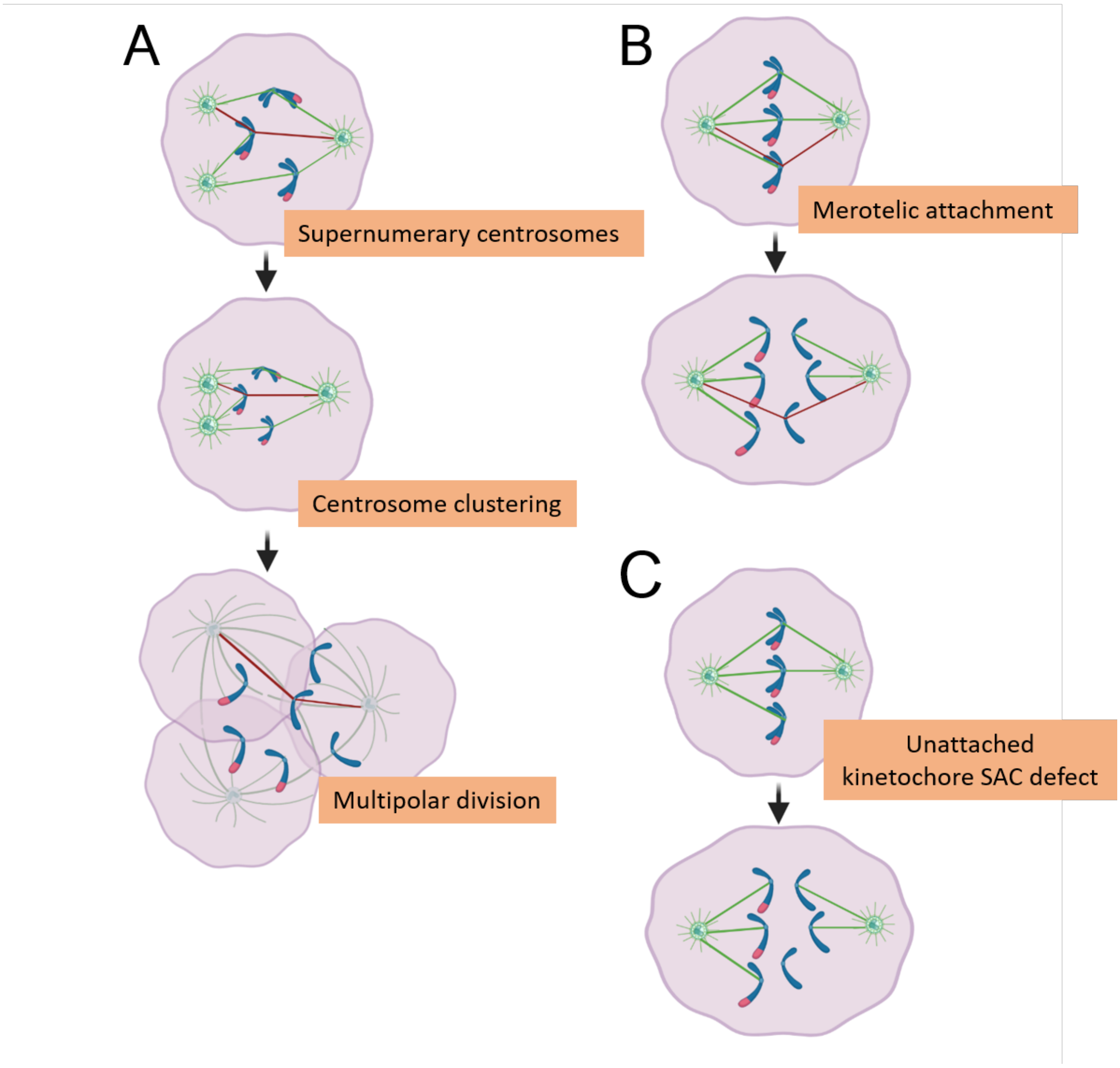

Figure 6.4: The cancer cells can become aneuploid by presenting (**A**) supernumerary centrosomes where a cluster occurs during mitosis and creates pseudo-bipolar spindles increasing merotelic attachments (**B**). Also, by presenting (**C**) defects in the SAC where the cell is compromised when entering anaphase with misaligned chromosomes. Adapted from reference 32 and created with Biorender.

Merotelic attachments and CIN are also linked to defects in kinetochore-microtubule attachments. This process is reversible and can be corrected by the rate-limiting step which is the release of the microtubule from the kinetochore. The chromosomes remain stable in the spindle microtubules although individual microtubules suffer a continuous association and dissociation from prometaphase to anaphase as the kinetochores are attached to a large number of microtubules (Figure 6.5).[38] These attachment errors are related to chromosomal mis-segregation and have been demonstrated to be restored in cancer cells with CIN where two microtubule depolymerizing kinesins, Kif2b and MCAK were able to restore the kinetic-microtubule dynamics in U2OS cells (osteosarcoma), however, a high frequency of lagging chromosomes, mitotic defect, was observed.[39] Overall, aneuploidy in cancer cells is caused by the relation between the merotelic attachments and chromosomal mis-segregation.[38]

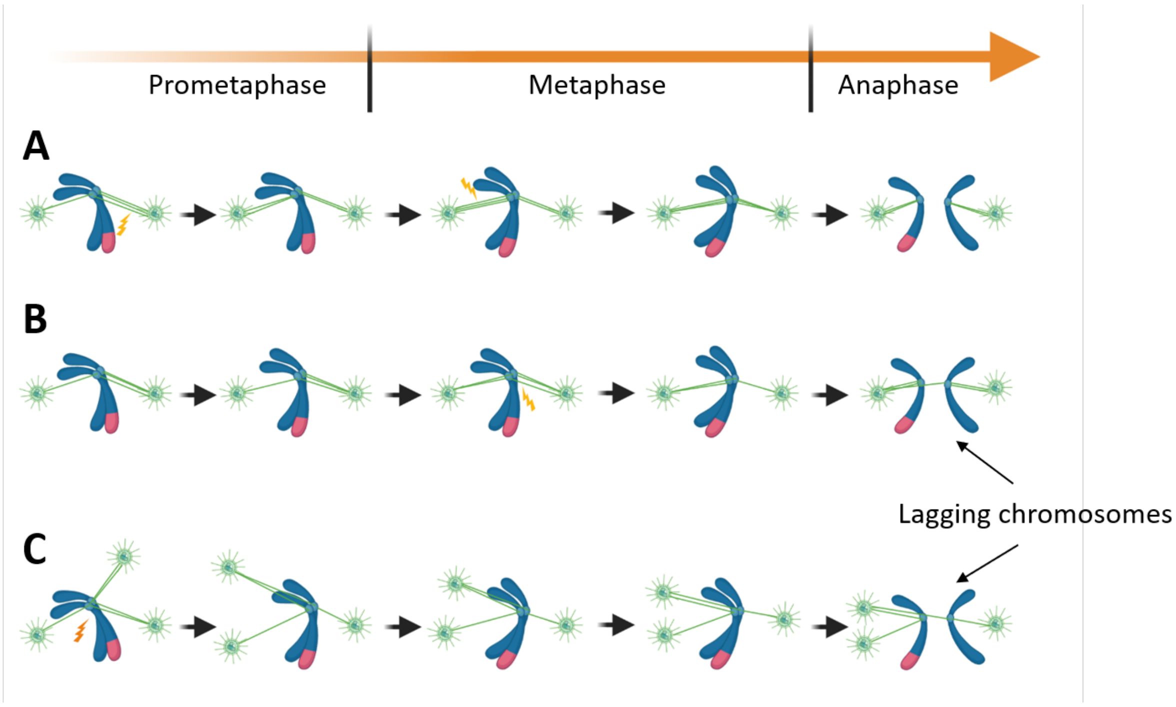

Figure 6.5: Merotelic attachments in the early mitosis phases for (**A**) normal bipolar divisions, (**B**) cancer cells presenting CIN and (**C**) cells presenting extra centrosomes. The correction of the bi-orientation of the chromosomes can be induced for an error-free chromosomal segregation (depicted with lightning bolts). It is known that the attachment of kinetochore-microtubule in cancer cells is really stable, therefore it is harder to establish a correct orientation. Adapted from reference 38 and created with Biorender.

Cancer cell lines have also demonstrated to present mitotic defects mainly in anaphase such as lagging chromosomes, which is the most common defect, and chromosomal bridges. Lagging chromosomes are single chromosomes that did not segregate as the kinetochore is attached to microtubules at the opposite pole of the spindle caused by a merotelic attachment,[38] while chromosomal bridges are fused chromosomes or sister chromatids where both have been suggested to cause aneuploidy or polyploidy and therefore CIN (Figure 6.6).[40] In the case of lagging chromosomes, as there are more microtubules attached to the kinetochore from one pole of the spindle, there will be more traction force from that pole of the spindle halting the segregation to a daughter cell that generates the lagging chromosome. Depending on the cleavage site, the lagging chromosome has been observed that it is segregated to the correct daughter cell. In the case it is not taken up by any daughter cell, it will generate its own nuclear envelope during telophase generating a micronucleus,[40] further discussed. In addition, chromosomal bridges might be generated as a consequence of lagging chromosomes where it is speculated that the micronuclei may form a chromosomal bridge in the next cell cycle,[37,41,42] or can be generated as a result of the DNA repair mechanism of double-stranded breaks by joining neighbouring DNA molecules where sister chromatids can be fused forming a “bridge” in the spindle midzone during anaphase.[43] If they are not cleaved during cytokinesis they can stretch as the daughter cells are moving apart[40] or persist to the next cell cycle by chromosome fusion due to the other double-strand break once the original bridge is broken. [43]

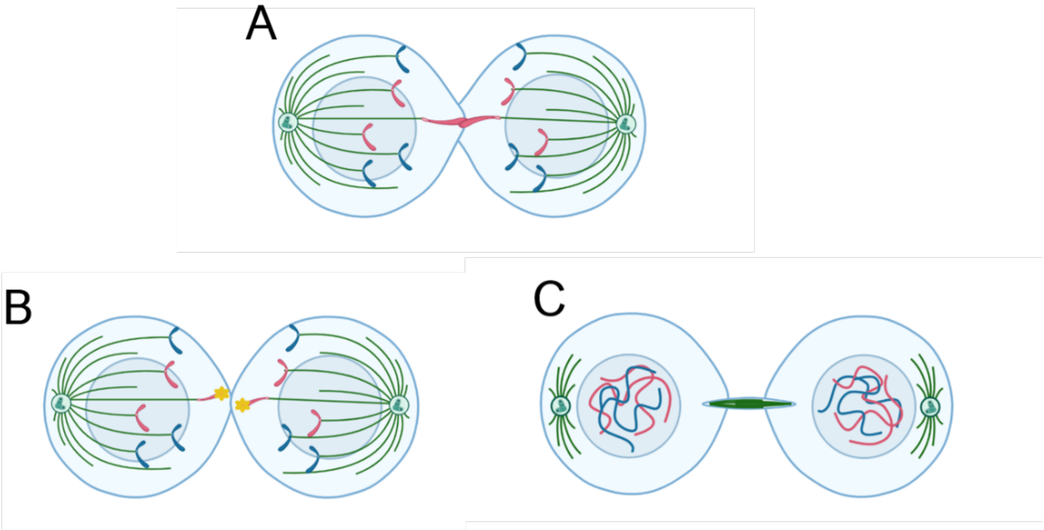

Figure 6.6: Chromosomal bridges (**A**) and their consequences where they can affect cytokinesis process by promoting a (**B**) chromosomal cleavage or an (**C**) abscission failure and extended until the next cell cycle. Adapted from reference 40 and created with Biorender.

Both mitotic defects mentioned above can cause the generation of micronuclei which are single chromosomes or fragments of chromosomes enclosed in an independent nuclear envelope. These microstructures are asynchronous with the main nucleus and have been observed in tumour cells with genomic instability. They are prone to fragmentation as they exhibit smaller nuclear pores and therefore lower nuclear import which impairs the recruitment of DNA factors for replication and repair mechanisms.[40] Chromosomes in micronuclei remain in S phase and are known to undergo premature compaction (PCC) due to their condensation influencing their structural integrity adopting a pulverized appearance.[44] In addition, micronuclei can remain present for several cell cycles before being integrated into the main nucleus and therefore, inducing chromosomal damages.[40]

6.2.2 Multipolar mitosis and mitotic defects in hPSCs

As discussed in Section 6.1.1., it is of utmost importance to maintain the genomic stability of hPSCs to be developed for personalised therapies. It is known that hPSCs can be maintained and proliferate *in vitro* almost indefinitely over long periods of time to be later differentiated into several cell types due to their self-renewal and pluripotency capacities.[3] However, several studies have reported genomic and epigenetic instability and, therefore, aneuploidy in hPSCs during *in vitro* cultures that have an impact on their molecular and phenotypic characteristics, affecting their clinical applicability.[45] Moreover, hPSCs have exhibited tumorigenic potential in animal studies[46] that ultimately can be distinguish in two categories: benign teratomas, generated from remaining undifferentiated hPSCs, and malignant transformations generated from differentiated hPSCs.[47] These characteristics with increased telomerase activity and apoptosis escaping are comparable to the hallmarks of cancer cells being the genomic instability and prone for chromosomal aberrations at a single gene or a whole chromosome level the most important.[48] There are clinical studies that have reported the development of tumours in patients after being treated with foetal and adult stem cells. Such is the case of a 12-year-old boy who developed a brain tumour after receiving foetal neural stem cells as a treatment for ataxia telangiectasia,[49] and a tumour was found in a 46-year-old woman after an autologous hematopoietic stem cell transplant to treat lupus involving the kidney.[50]

Furthermore, some studies have observed chromosomal instability in hESCs as early as 3- and 4-day-old embryos identified by single cell analysis, suggesting that these genomic abnormalities may already exist from the blastocyst stage that may persist during *in vitro* cultures.[51] For most hESCs with a low number of passage cultures, their diploid karyotype is maintained,[45] however, changes have been observed as early in passage number 3 after derivation, supporting the idea that genomic aberrations are present from the blastocyst or may arise induced by *in vitro* (culture adaptation) which could occur in any passage number. The latter has been reported in large-scale analysis for both hPSCs (hESCs and hiPSCs) (Figure 6.7).[51] Although some hPSCs lines maintain their karyotype reaching high passage culture numbers, the risk of accumulating chromosomal defects and aneuploidy is high. The International Stem Cell Initiative analysed the karyotype of 125 hESCs and 11 iPSCs lines in early and late passage numbers worldwide to investigate the genomic and epigenetic abnormalities that can affect safety and efficacy of PSCs therapies. They reported alterations in chromosome 1, 10, 12, 17, 18, 20 and 22, where the chromosome aberrations were from gaining a whole chromosome or parts of it, to loss of chromosomal regions.[52] In particular, additional copies were commonly observed in chromosomes 1, 12, 17 during prolonged culture times,[45] where the trisomy of chromosome 12 and 17q is of greatest interest as it produces global changes in gene expression increasing proliferation and tumorigenesis.[53] In addition, a chromosomal gain in the short arm of chromosome 12 has been associated with the generation of embryonic carcinomas (stem cells of teratocarcinomas)[54] and, it has been reported that two main pluripotency genes *NANOG* and *GDF3* are overexpressed due to the gain in the short arm 12p.[55] The Stem Cell Initiative also indicated that a high frequency of anomalies could be observed in the late passages almost twice as much as in the early passages.[52]

Human embryonic pluripotent stem cells also exhibit a low efficiency of the cell-cycle checkpoints, especially the arrest of G1/S checkpoint that is affected by DNA replication stress or by ionization radiation.[58] This is similar to the work reported by Crasta *et al*[44] where micronuclei containing complete chromosomes were generated in HeLa cells (cervical cancer cell line) due to mitotic mis-segregation caused by abnormal DNA replication. It is known that hPSCs have a shorter cell cycle than differentiated cells because the G1 phase is truncated where hPSCs spend about 15%

of the total cell cycle time in G1 phase and approximately 65% in S phase while 40% of cell cycle time is spent by differentiated cells. The duration of G1 phase in hPSCs is of approximately 2.5-3 hours with a total time of 16 hours to complete a cell cycle while somatic cells need 24-32 hours.[59]

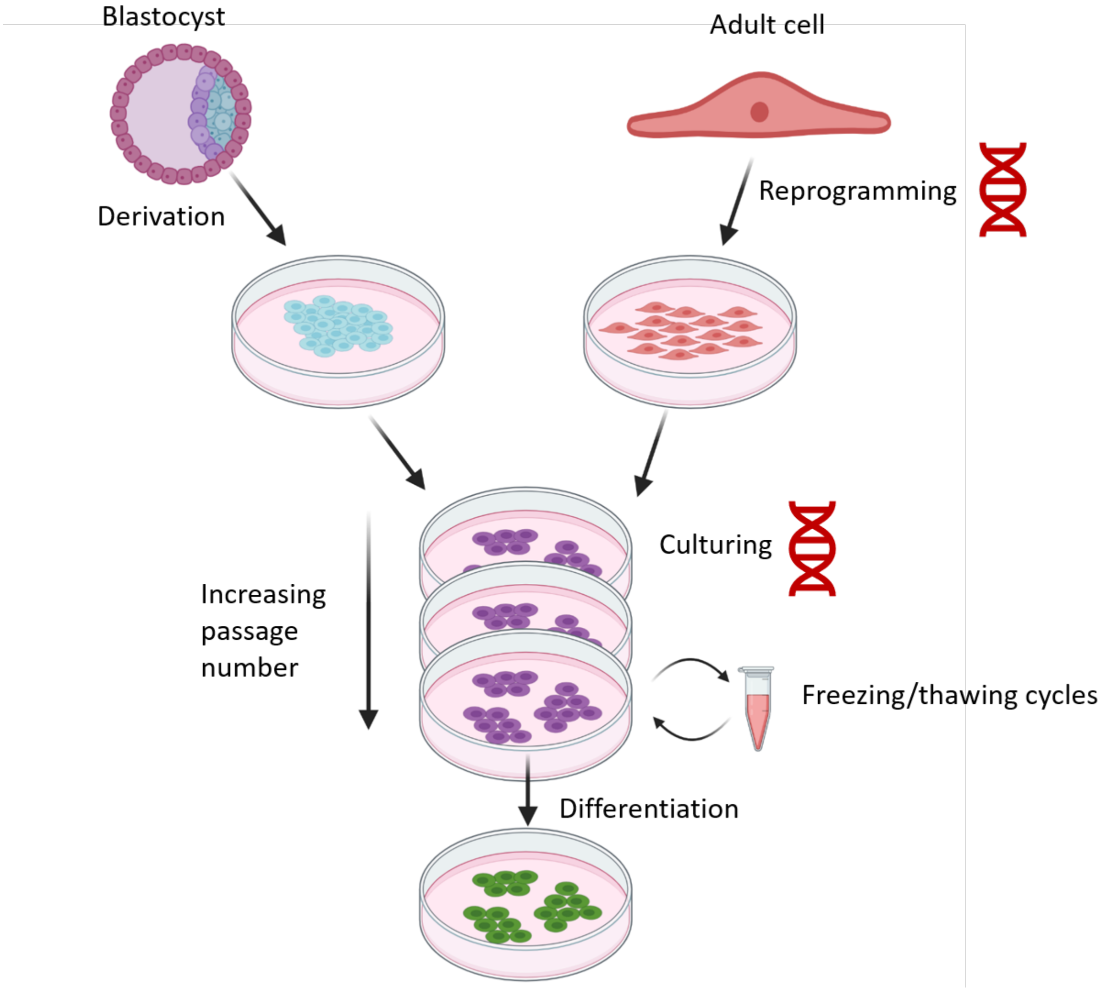

Figure 6.7: Steps taken to culture hESCs and hiPSCs indicating where genomic and epigenetic aberrations can occur. During derivation, reprogramming and culturing enrichment of aberrations may occur but also during the cycles of freezing and thawing affecting the oxygen and nutrients level. Their manifestation can occur at any time of *in vitro* culture. Adapted from reference 51 and created with Biorender.

The G1/S checkpoint is very important as it halts the DNA damaged cell from entering the S phase. Furthermore, the G2 / M checkpoint is also ineffective in hPSCs, where it normally arrests cells without the proper untangled chromosomes before entering mitosis. These deficiencies in cell cycle checkpoints make hPSCs more susceptible to genetic aberrations, accumulate them, proliferate, and cause malignant formations.[60]

As mentioned in Section 6.1.2, chromosomal instability in cancer cells can be caused by the amplification of the centrosome during mitosis, a feature that has also been observed in undifferentiated hESCs. It is speculated that the frequency of appearance of additional centrosomes is reduced if the hESCs culture time is prolonged and that their formation can be controlled if the adherence to the substrate is improved and the inhibition of the CDK2 and Aurora A cell cycle kinases is minimized.[61] Assuming the above and gathering the results of Tse *et al*[62] where they reported an increase in multipolar divisions in HeLa cells that were mechanically constrained, and Kocgozlu *et al*[63] who found that softer substrates lead to abnormal chromosomal segregation in epithelial cells, Acevedo-Acevedo *et al*[64] investigated iPSCs on different substrates varying in stiffness (i.e., glass, polyacrylamide (PA) hydrogels and tissue culture polystyrene (TCPS). The stiffness of these materials ranges from 60-64 X 10^9 Pa for glass, 2.28-3.28 X 10^9 Pa for TCPS and 5-60 X 10^3 Pa for PA hydrogels. The first materials were chosen as they are standard for *in vitro* cell culture and the latter one due to their tuneability for mechanical studies and easy fabrication. The results obtained were in discrepancy with those previously reported by Holubcova *et al*[61] who reported a frequency of mitotic anomalies of 10 to 23% and in this work was less than 10% for all substrates. Therefore, no trend was found between substrates and the percentage of supernumerary centrosomes observed. Moreover, no difference between the cellular passage number and abnormal divisions was found.

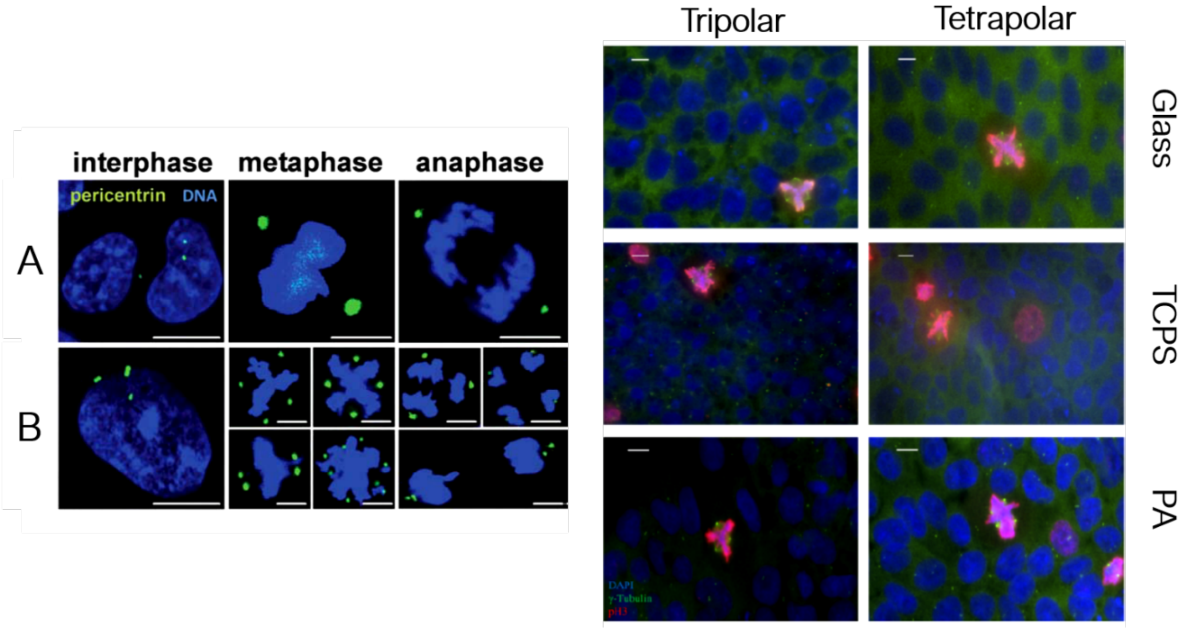

Figure 6.8: Supernumerary centrosomes found in multipolar spindles (tripolar and tetrapolar) present since interphase. Multipolar spindles observed of iPSCs cultivated on different substrates varying their stiffness. Scale bars 10µm. Taken from references 61 and 64, respectively.

A diversity of protocols and therefore great variability in results have been reported, suggesting that there are culture differences that may also be the cause of the chromosomal instability observed in hPSCs.[67] To culture hPSCs, a ROCK (Rho-associated protein kinase) inhibitor that is needed to prevent apoptosis of single hPSC cells and enhance survival by enabling aggregation to form colonies,[65] has been reported its constant use in cultures may cause an incorrect positioning and assembly of mitotic spindles.[66] This is of great importance since in vitro aggregates are necessary for the survival of hPSCs in culture, but also to recreate the normal cellular environment of native tissues where biochemical and biophysical signalling and communication between neighbouring cells is essential. Currently, 3D microenvironments called organoids are being created to mimic tissues and be used as personalised therapies in the future.[65]

6.3 Quantifications of multipolar mitosis in hPSCs

This thesis chapter reports an investigation of the dynamics of individual hPSCs *in vitro* and attempts to elucidate in real time the mitotic changes and errors they undergo. For this work, undifferentiated hESCs were used where the FUCCI and Histone 2B-HaloTag (H2B-HaloTag) constructs were previously introduced using CRISPR-Cas9 knock-in technique by Dr Seongmin Kim (senior postdoc in the Carazo Salas group) and Rosie Maddock (previous project student in the group). These constructs were introduced genetically in a stable manner to monitor the cell cycle and visualise the labelled chromatin in live cells, respectively, throughout time-lapse imaging. The reporter FUCCI or Fluorescence Ubiquitination Cell Cycle Indicator was developed by Sakaue-Sawano *et al*[68] to genetically introduce an optical sensor to monitor the cell cycle progression of individual cells going from a red to a green colour (G1 to S / G2) without altering the cell cycle. This 2-colour reporter is based on ubiquitin-mediated proteolysis that controls the cell cycle, where the 2 substrates, Cdt1 and Geminin of SCF and APC, respectively, are involved. This genetic labelling technique is possible because the protein levels of Cdt1 and Geminin are reversed, meaning there is an accumulation of Cdt1 in the G1 phase and an accumulation in Geminin in the G2 phase (Figure 6.9) but also in the S and M phases.[69] This protocol has been reported by an extensive study[70] and proved to be a reliable and safe method to study the cell cycle, control stem cell differentiation and uncover molecular mechanisms coordinating hPSCs growth and differentiation.

Additionally, a synthetic dye can be coupled to genetically encoded fluorophores to increase signal brightness and maintain photostability without affecting cell viability. As shown in Figure 6.9, a Histone 2B-HaloTag construct was previously introduced genetically in a safe locus without affecting cellular mechanisms and it was covalently coupled to a HaloTag ligand, JF646 membrane permeable to label the chromatin of individual hESCs. This HaloTag system allows the analysis of protein function, molecular interactions and *in vitro* / *in vivo* cellular and molecular imaging.[71]

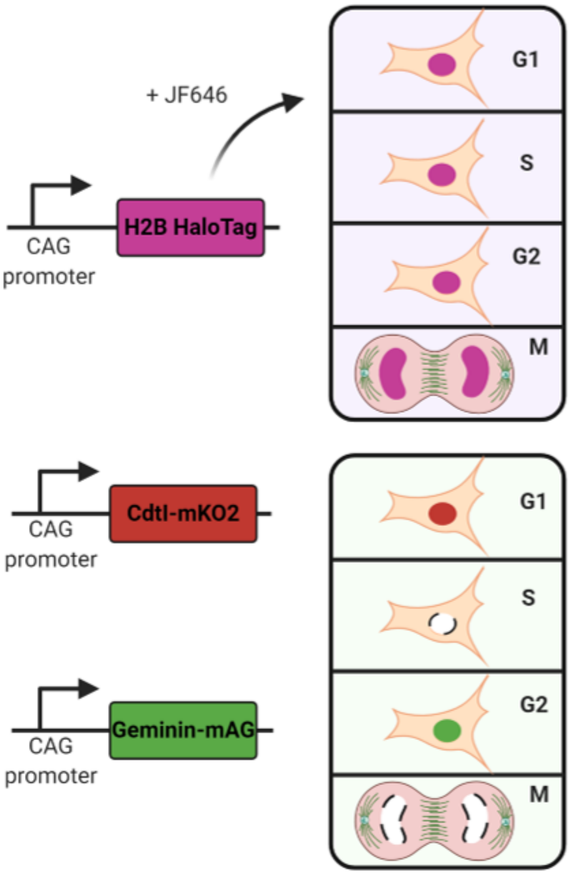

Figure 6.9: Genetically encoded constructs of H2B HaloTag covalently bound to the HaloTag ligand JF646[73] and two-colour FUCCI reporter. Adapted from R. Carazo Salas, unpublished.

A 4-day time-lapse imaging was performed with a spinal disk confocal microscope. The H2B-HaloTag JF646 (E_x / E_m: 649 / 697 nm) was imaged every 10 min and FUCCI, fused with two fluorescent proteins, GFP (green fluorescent protein) (E_x / E_m: 488 / 509 nm) and mK02, respectively, (E_x / E_m: 551 / 565 nm) was imaged every 30 minutes. The different imaging times were proposed to minimise phototoxicity in the hESCs and to avoid inducing possible genomic defects. The culture media was changed every day during a 10 min break before the next image was scheduled to be taken. At the end of the time-lapse and the data being recovered, image analysis was performed with Fiji ImageJ package where mitotic defects: lagging chromosomes, chromosomal bridges and micronuclei, were counted. In addition, the observed multipolar spindles were counted but their possible defects were not added to the total mitotic defect count (Figure 6.12). The normal mitotic divisions (Figure 6.11) were also counted for each day of the imaging to acquire a total count of mitotic divisions and thus be able to obtain a total percentage of the aforementioned defects and multipolar spindles, as further presented.

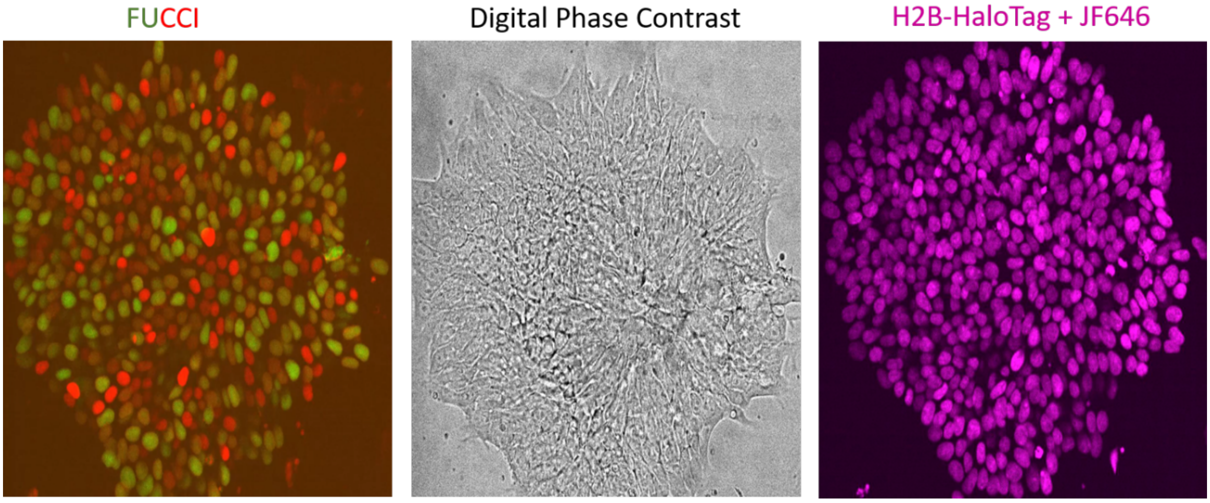

Figure 6.10: Snapshots from a time-lapse imaging experiment showing hESC colony expressing the two-colour FUCCI reporter (left) and H2B-HaloTag+JF646 labelling the nuclei of individual hESCs (right) and also imaged by digital phase contrast (middle).

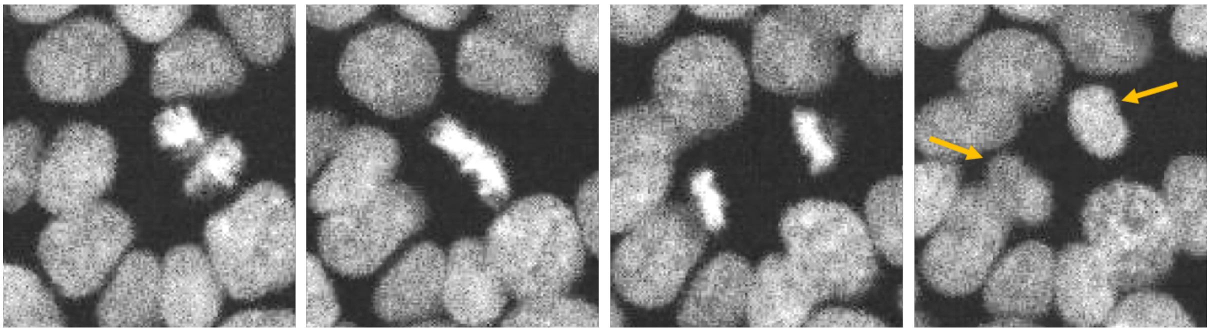

Figure 6.11: Snapshots of the 4-day time-lapse imaging in a grey scale of H2B-HaloTag showing the sequence of a normal mitosis. From left to right: condensation of chromatin (prometaphase), to metaphase, then anaphase and at last telophase / cytokinesis indicating with orange arrows the chromatin of the two hESC daughter cells.

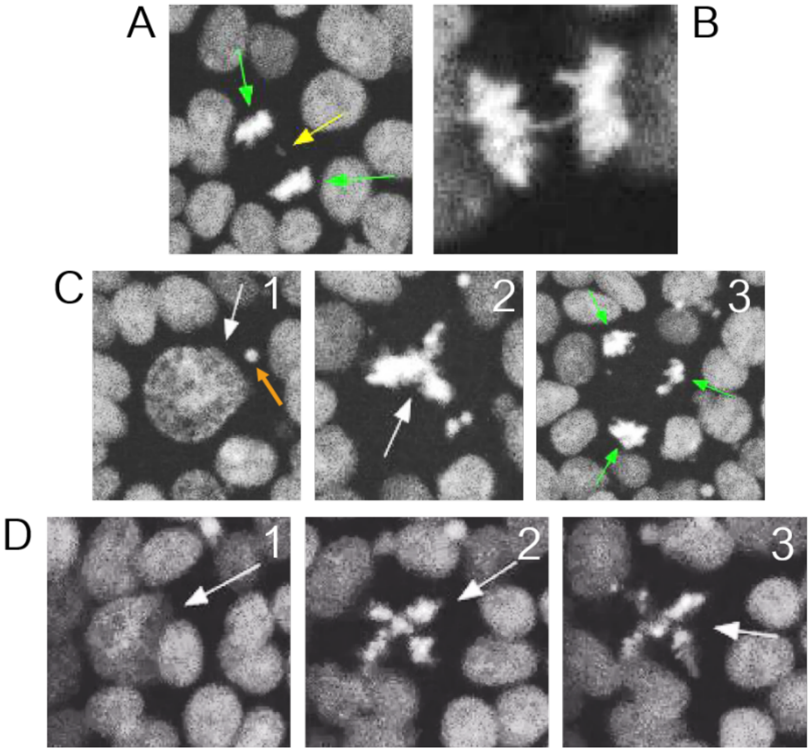

Figure 6.12: Snapshots of the 4-day time-lapse imaging in a grey scale of H2B-HaloTag showing (**A**) lagging chromosomes indicated with the yellow arrow, (**B**) chromosomal bridge and a sequence going from (**C1**) an enlarge nucleus which results in a tripolar division (**C2**) indicating the three daughter cells with green arrows (**C3**). In the case of the quadripolar or tetrapolar spindles it also starts with (**D1**) an enlarge nucleus and forming a tetrapolar shape before dividing (**D2** and **D3**). Moreover, a micronucleus is depicted in **C1** with an orange arrow very close to the enlarged nucleus, possibly present since previous mitosis.

Mitotic defects, multipolar spindles, and normal mitosis were also counted from data previously acquired by student Rosie Maddock to expand the sampling and compare the recent data as it is an independent hPSC time-lapse imaging. The percentages acquired by mitotic defects and multipolar spindles in relation to the total number of counted mitoses showed great differences as in previous time-lapse imaging there were more counted defects and less normal mitosis. Also, a clear difference was observed in the percentages of tripolar and quadripolar divisions compared to the data obtained recently. However, there are also similarities when comparing the percentages of the three mitotic defects where the chromosome bridges have almost the same percentage while the lagging chromosomes and micronuclei are very close.

These initial results may indicate that the incidence of mitotic defects does not differ much between two independent samples following the same protocol.

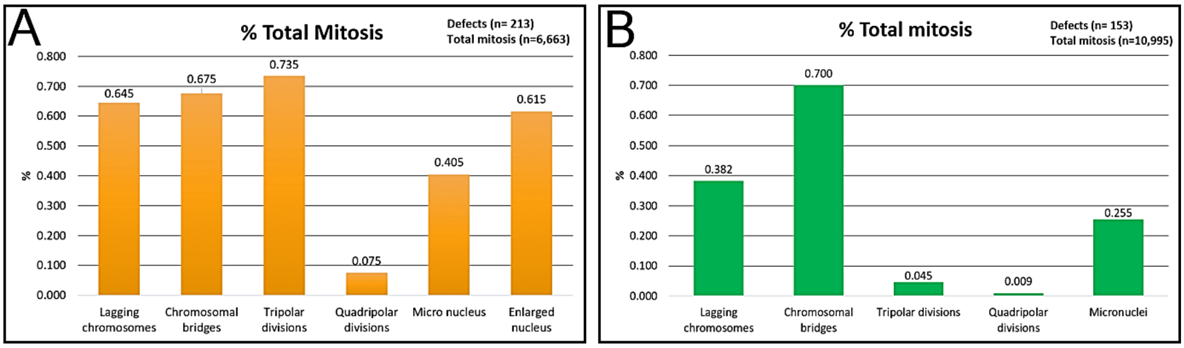

Graph 6.1: Percentages of mitotic defects from the total number of counted mitosis. (**A**) Rosie Maddocks time-lapse imaging counts with a total count of mitotic defects of 213 and (**B**) counts from recent time-lapse imaging with 153 total defect count.

The mitotic defects were taken by category to obtain the percentage of each one within the total. As can be seen from Graph 6.1 and 6.2 in the data obtained for the Rosie Maddock counts (**A**), the number of enlarged nuclei was also counted since the multiple spindle frequency was greater than the recent counts (**B**). Here a great variability within the defects is still larger where again the lagging chromosomes is the only defect that in both counts was similar. However, for the rest of the defects there is a great variability as observed in the chromosomal bridges where their incidence was 50% in recent counts while it was half in data obtained previously. Also, a notable result is the percentage of enlarged nuclei, which is very close to that of tripolar spindles, which could be speculated that there is a direct relationship. Furthermore, looking at the percentages of lagging chromosomes and micronuclei that are similar for both independent time-lapse counts, it could also be speculated that if a lagged chromosome is generated there will be a tendency to generate micronuclei. For both counts, the least frequent mitotic defect was the quadripolar or tetrapolar spindle, although for recent counts the tripolar spindles also presented low frequency, which is in agreement with the work previously reported by Acevedo-Acevedo *et al*[64] where a percentage lower than 10% of multipolar spindles was obtained.

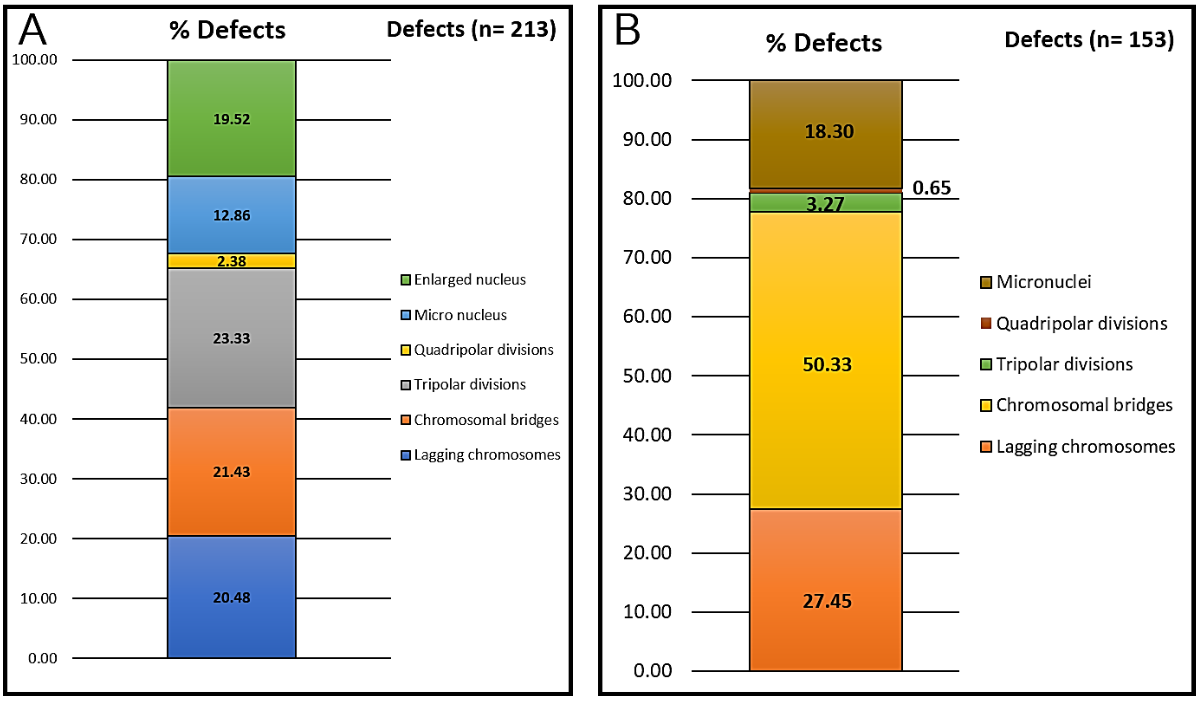

Graph 6.2: Percentages each mitotic defect from the total number. (**A**) Rosie Maddocks defects counts with a total count of 213 and (**B**) counts from recent defects with 153 total defect count.

A general table was added that gathers the counts previously presented, adding the total mitosis time of the parental cell, the size of the nucleus, the number of counted events and the percentage of all the events in reference to the total of counted mitoses. Similar tables and quantifications of hPSC mitotic defects in agreement with the general results shown here were also independently obtained by Laura Graser and Callum Kirby, two PhD students in the Carazo Salas group. In addition, the daughter cells that were followed (one generation) were added after counting their mitosis time and their mitotic defects with or without micronuclei for both time-lapse imaging. As can be seen in the complete table, the mitosis time (time from the condensation of chromatin till the separation and formation of daughter cells) of both counts presented a difference of more than 10 min. One possible reason is that the counts have not been accurate, and perhaps more time points were added, however the difference of the same line of hPSCs involved is very large and there could be already a chromosomal instability. Further discussion is presented below with FUCCI graphs.

The size of the nuclei also showed great variability, which is in agreement with the percentage results shown in Figure 6.2 (**B**), however, for mitotic defects an increase was shown compared to the bipolar divisions of the previous images. The same trend was not seen in recent data suggesting that there may be differences in handling or some problem with image exposure.

The time of daughter cell cycle is similar to that reported for the hPSCs being a total of 16 hours,[59] although a major decrease was observed for the tripolar surviving daughter cells which were only a few as observed in the column of daughter cell survival. Moreover, the lagging chromosome had a slight major frequency of generating micronuclei than chromosomal bridges which is again in agreement with what has been reported for cancer cells and hPSCs when presenting these mitotic defects, although both cell cycle time of daughter cells is lower than normal mitosis. For the quadripolar spindles, no daughter cells survive which indicates the cell may undergo apoptosis as the chromosomal damage is large. As expected, from previous graphs, the size of the nuclei of multiple spindles is larger than normal mitosis which may be an indication of a gain in chromosomal content and the cell is trying to reorder the chromatin which also correlates with the time in mitosis which is the double from normal mitosis or mitotic defects. These results are presenting some straight correlations linking multipolar spindles, size of nuclei and time in mitosis which may help further studies.

Table 1. Total numbers of undifferentiated hESCs for both independent time-lapses.

MITOTIC PHENOTYPE	NORMAL BIPOLAR	CHROMOSOMAL BRIDGE	LAGGING CHROMOSOME	TRIPOLAR SPINDLE	QUADRIPOLAR SPINDLE
Time in mitosis [min]	**31.46 ± 2.39*** **46.80 ± 0.2**	**31.15 ± 2.30*** **49.91 ± 0.99**	**33.20 ± 3.20*** **48.53 ± 3.34**	**61.09 ± 9.19*** **82 ± 31.14**	**56.66 ± 23.56*** **50**
Nucleus size [μm2]	**210.97 ± 63.84*** **151.45 ± 2.99**	**258.18 ± 106.05*** **148.68 ± 6.3**	**254.03 ± 96*** **158.84 ± 13.28**	**351.88 ± 118.98*** **279.63 ± 63.14**	**278.88 ± 101.39*** **196.57 ± 18.21**
Daughter cell survival [%]	**85.5*** **85.64**	**68.89*** **72.5**	**78.5*** **65.8**	**44.44*** **0**	**0*** **0**
Daughter cell cycle time [h]	**14.63 ± 2.00*** **15.17 ± 1.38**	**13.17 ± 0.4*** **13.12 ± 3.42**	**11.745 ± 2.25*** **13.35 ± 3.85**	**6.602 ± 4.211*** **4.71 ± 2.98**	**N/A*** **N/A**
Daughter cell with Micronuclei [%]	**N/A*** **N/A**	**2.56*** **3.89**	**53.72*** **59.5**	**34.71*** **0**	**0*** **0**
Number of events [n]	**190*** **200**	**45*** **77**	**43*** **42**	**49*** **5**	**5*** **1**
Event percentage of all mitosis [%]	**~99*** **~99**	**0.67*** **0.7**	**0.64*** **0.38**	**0.73*** **0.045**	**0.075*** **0.009**

* Rosie Maddocks final numbers of undifferentiated hESCs quantifications

As mentioned above, FUCCI reporter system was employed to monitor the cell cycle progress in live hPSCs (Figure 6.10) and images were taken every 30 min. Cell cycle times were extracted for G1 and G2 phases and were latter plotted using R Studio with a code provided by postgrad student Sam Huguet. As presented in Graph 6.3, cell cycle of 50 individual daughter cells as a result from a bipolar division, the surviving daughter cells from the multipolar spindles and mitotic defects was counted (Figure 6.13).

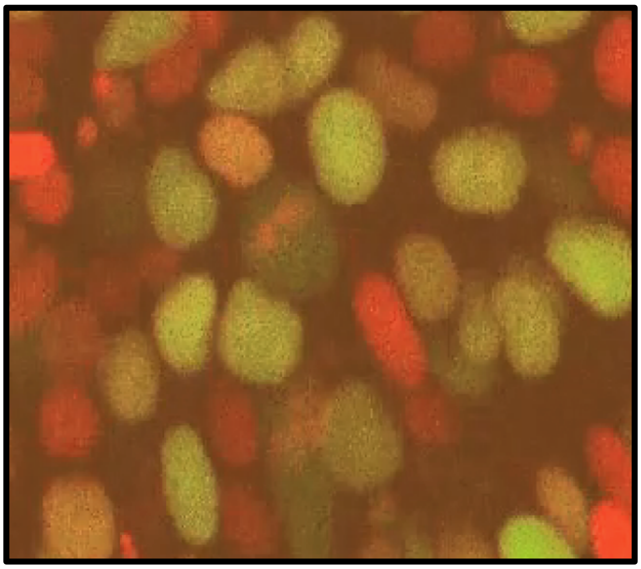

Figure 6.13: Snapshots of the two colour FUCCI reporter system. As shown at the centre of the image the chromatin in condensed and coloured in red in metaphase. The hPSCs which are coloured in bright orange and green are in G1 and G2/M phases, respectively. The bright red is the light emitted by the far-red signal from the H2B-HaloTag+JF646 construct. Objective 60X.

From the Graphs 6.3, the distribution of G1 duration phase for both time-lapse imaging data shows no difference, but a large standard error is depicted in the cells that presented chromosomal bridges (**A**). This may be an indication of a possible lengthening of the phase in order to reorganize the chromatin and thus be able to continue with the cell cycle, but in general, the duration of the G1 phase is within the range as reported by Becker *et al*[59] of 2.5-3 hours for all normal and mitotic defects. Moreover, changes in duration distribution were observed for G2 phase even for normal mitosis. In the previous time-lapse imaging (**A**), the distribution is larger, however, most of the cells had a duration between 10 and 12 hours, similar to the recent data (**B**). The distribution of multipolar spindles daughter cells for (**A**) showed a shorter G2 duration which may be another indication for further studies to focus on the molecular machinery involved in that specific cell cycle phase.

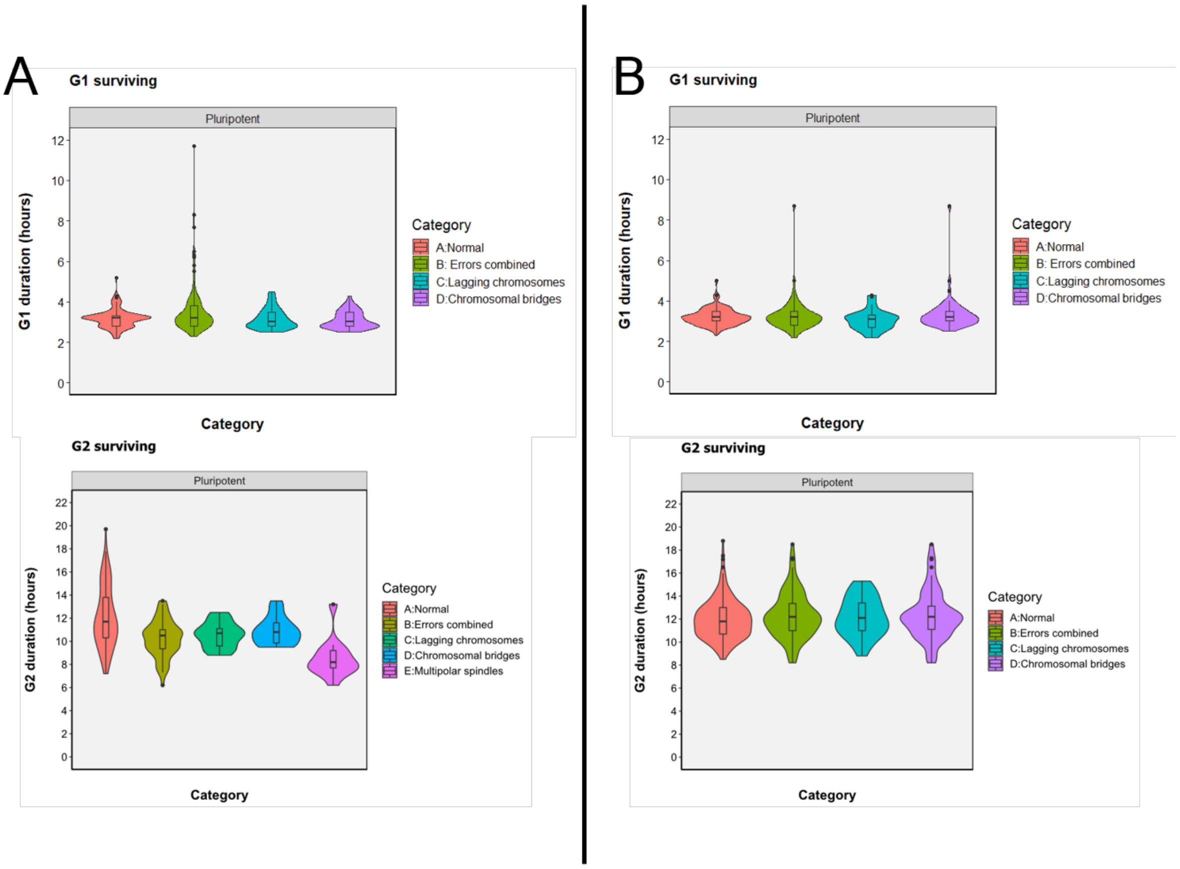

Graph 6.3: G1 and G2 duration time (hours) for (**A**) Rossie Maddock and (**B**) recent data of live undifferentiated hPSCs. For (**A**) an additional data set was included, multipolar spindles, due to the survival of a daughter cells while for (**B**) the parental cells died without completing cytokinesis.

Finally, the durations of the two phases were combined to obtain a total of hours for each undifferentiated hPSC cell. As shown in Graphs 6.4, there was more variability in the data obtained recently (**B**) and in the bipolar divisions of the previous ones (**A**). Although most show a total time within the range (16 hours) it can be speculated that in some cases the hPSC cells adapt to the culture and begin to show more variability. In this work, the same cell line as the previous data was used but they underwent a thawing cycle and although their passage number was low (less than 20) when imaged, it can be agreed that hPSC cells can undergo changes due to *in vitro* cultivation and manipulation.

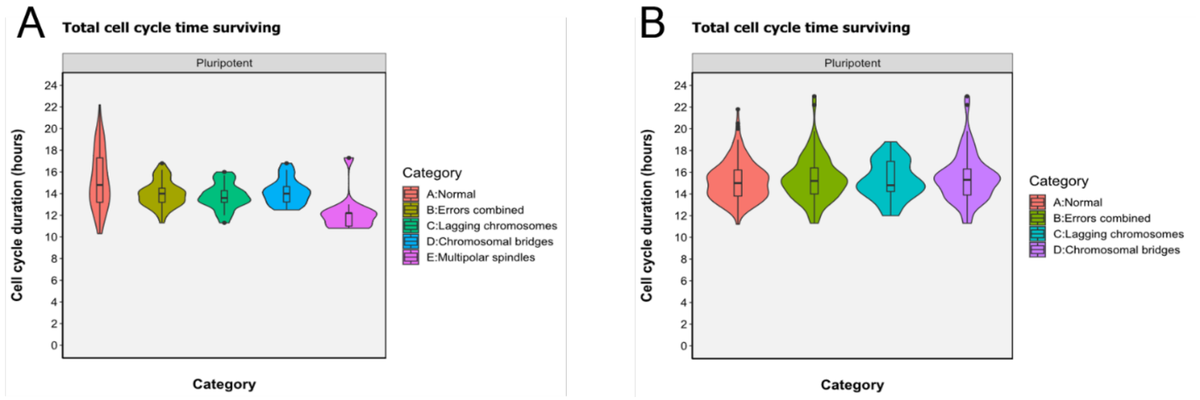

Graph 6.4: Total cell cycle time (hours) for (**A**) Rossie Maddock and (**B**) recent data of live undifferentiated hESCs.

6.4 Immunofluorescence assay for fixed hPSCs

To continue with the hPSCs mitotic defects and errors investigation, immunofluorescence (IF) labelling employing fixed hPSCs samples was done. The samples that were employed for the time-lapse imaging were fixed at the end of acquiring the images with 4% glutaraldehyde EM grade. A 3-colour immunofluorescence assay was performed where α-tubulin, a cytoskeleton building protein, was labelled in green, Cenp-E, a critical protein to bind the kinetochores and essential for a proper chromosomal segregation, was labelled in red and the centrioles, orthogonal cylinders of the centrosomes, were labelled in far red. The nuclei were labelled with a Hoechst dye (blue colour) after the immunoassaying protocol was followed.

Immunostaining is a molecular technique widely used for fixed cellular samples to detect and localise antigens within the cell/tissues by combining the tagged antibodies with a fluorophore. An antigen is usually a protein that triggers an immune response and generates the formation of a specific antibody. After the fixation which is a preliminary step in order to use IF technique, there is an antigen retrieval to restore the reactivity of epitope-antibody, which is modified during the preliminary fixation step. The most common method is the heat-induced epitope retrieval (HIER) by heating the fixed sample in a buffer solution to restore the protein structures and be able to bind the antibody to the epitope. After this first steps, an indirect IF method can be done where first a primary antibody binds to the epitope of interest and in a second step, a secondary antibody, which is tagged with a fluorophore, recognises the primary antibody that when excited, a signal is produced allowing the visualisation of the proteins of interest.[72] This two-step incubation protocol can be done simultaneously to visualise more than 2 proteins. To perform this method, several criteria must be taken when choosing the appropriate antibodies so that they do not cross-link with other endogenous proteins. The primary antibody must be chosen from a different species from the sample to be labelled and the secondary antibodies, conjugated with a fluorophore, must be against the primary antibody chosen specie.[72,73]

Table 2. Primary and secondary antibodies employed.

	Primary antibodies	Secondary antibodies	E_m/E_x wavelengths
α-tubulin	Mouse	Anti-mouse	488/520 nm
Cenp-E	Rabbit	Anti-rabbit	590/618 nm
Centrin2	Rat	Anti-rat	647/671 nm

Gathering all the criteria and considerations before performing the IF technique, the primary and secondary antibodies that were chosen are listed in Table 2. In addition, the primary antibodies were monoclonal, which allows only one epitope per antigen to be recognized, which makes it more specific, since non-desirable interactions are reduced. As shown in Figure 6.14, fluorescent labelling of mitotic hPSCs was analysed using Volocity Z-stack package to visualise the different cellular components in individual cells as hPSC colonies are compact and dense (Figure 6.15 (**A**)).

The images obtained showed that the identification of the centriole was not well identified in the mitotic cells and was found in the nuclei combined with Hoechst. This could be because the hPSC colonies are so compact that the antibody failed to recognize the epitope (Figure 6.15 (**B**)). While the kinetochores were well defined in some mitotic cells, their marking could still be improved. A very particular result was that the antibody used for the kinetochores labelling also marked the midbody, which is the place that is cleaved before the formation of two daughter cells (Figure 6.15 (**C**) which may be used for future studies. Alpha tubulin was shown to be the best-labelled cellular component that was seen in all steps of the z-stack. This may be because there is a larger surface area of these proteins, facilitating identification and therefore the labelling.

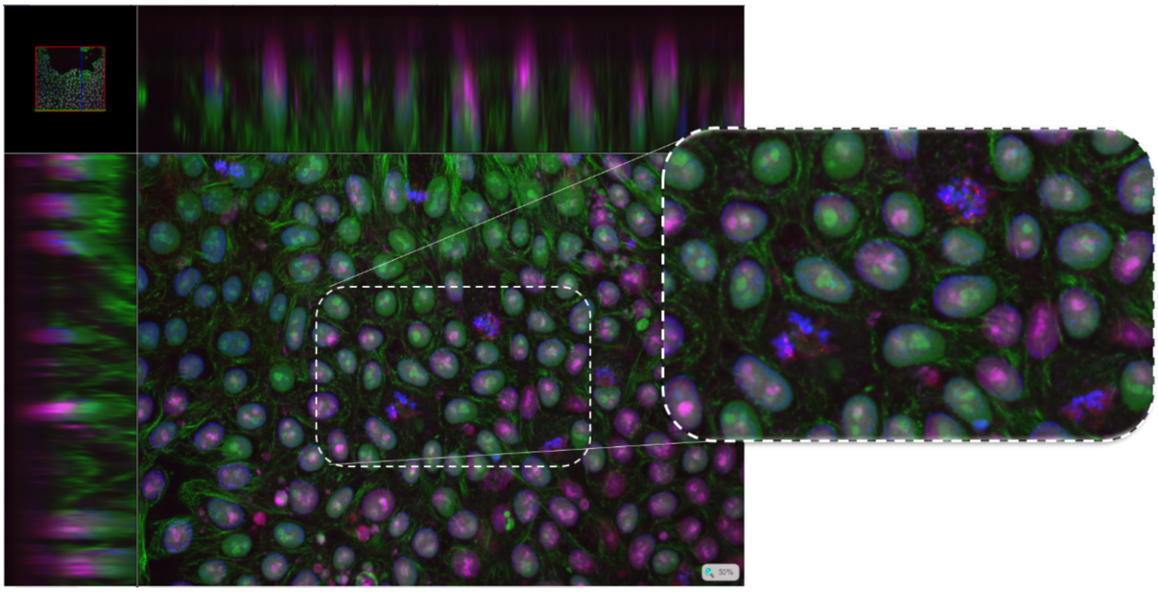

Figure 6.14: Snapshots of the 3-colour immunofluorescence assay analysed with the Volocity package provided by the Wolfson Imaging Centre at the University of Bristol. The closeup view is showing the mitotic hESC individual cells that were found within the colony.

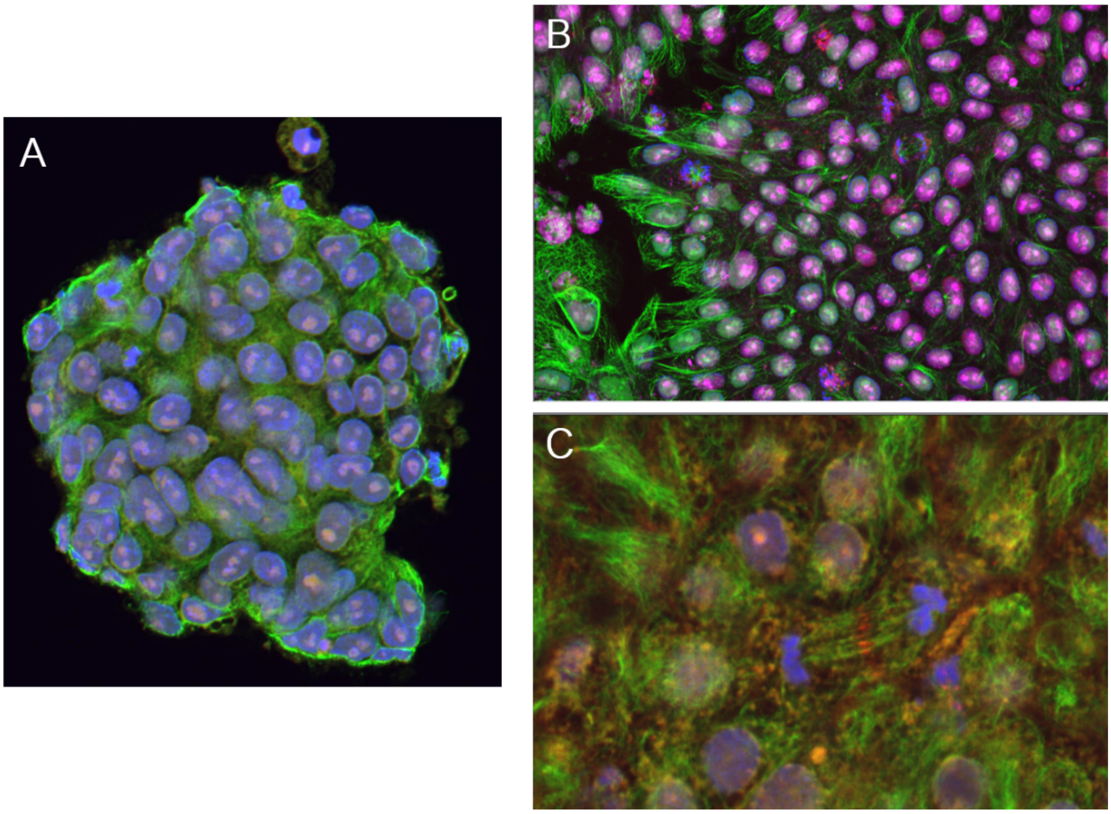

Figure 6.15: Snapshots of the 3-colour immunofluorescence assay analysed with the Volocity package where (**A**) a complete colony is shown with two mitotic cells at the right rim, a closer view (**B**) from the interior of the colony and (**C**) Cenp-E also labels the midbody present at the final stage of cytokinesis.

No merotelic attachments were observed and no multipolar spindles were identified in the analysed samples. This method presents an advantage of performing a specific labelling of proteins of interest but also the disadvantage of not being able to label at real-time therefore important events and characteristics are lost. The results suggest improving the labelling protocol and most importantly, to acquire and build more genetically encoded constructs for real-time imaging to visualise in depth the cellular components involved in the generation of mitotic defects and multipolar spindles.

6.5 References

1. P. C. Chagastelles and N. B. Nardi, *Kidney inter., Suppl*. 2011, **1**, 63–67.
2. C. Kiecker, T. Bates and E. Bell, *Cell. Mol. Life. Sci*., 2016, **73**, 923-947.
3. D. M. Choumerianou, H. Dimitriou and M. Kalmanti, *Tissue Eng Part B Rev*., 2008, **14**, 53–60.
4. T. Nii, H. Kohara, T. Marumoto, T. Sakuma, T. Yamamoto and K. Tani, *BioResearch Open Access*, Mary Ann Liebert Publishers, 2016, **51**, 127-136.
5. D. S. Kaufman, *Blood*, 2009, **114** (17), 3513-3523.
6. K. Takahashi and S. Yamanaka, *Cell*, 2006, **126**, 663-676.
7. M J. Evans and M. H. Kauffman, *Nature* 292, 154, 1981.
8. G. R. Martin. *Proc Natl Acad Sci USA*, 1981, **78**, 7634.
9. J. A. Thomson, J. Itskovitz-Eldor, S. S. Shapiro, M. A. Waknitz, J. J. Swiergiel, V. S. Marshall and J. M. Jones, *Science*, 1998, **282**, 1145.
10. Ahmed A. Shokeir, Ahmed M. Harraz and Ahmed B. Shehab El-Din, *International Journal of Urology*, 2010, **17**, 964-973.
11. D. Pralong, Alan O. Trounson and Paul J. Verma, *Stem Cell Reviews*, 2006, **2**, 331-340.
12. J. B. Gurdon, *Developmental Biology*, 1962, **5**, 68-83.
13. T. R. Elsdale, J. B. Gurdon and M. Fischberg, *J. Embryol. Exptl. Morphol*., 1960, **8**, 437-444.
14. I. Wllmut, A. E. Schnleke, J. McWhlr, A. J. Kind and K. H. S. Campbell, *Nature*, 1997, **385**, 81-0-813.
15. M. L. Condic, *Cell Prolif*. 2008, **41** (1), 17-19.
16. K. Liu, Y. Song, H. Yu and T Zhao, *Cell Death and Disease*, 2014, **5**, 1232.
17. C. A. Cowan, J. Atienza, D. A. Melton and K. Eggan, *Science*, 2005, **309**, 1369-73.
18. T. Zhao and Y. Xu, *Trends Cell Biol*, 2010, **20**, 170–175.
19. L. A. Boyer, T. I. Lee, M. F. Cole, S. E. Johnstone, S. S. Levine, J. P. Zucker, M. G. Guenther, R. M. Kumar, H. L. Murray, R. G. Jenner, *et al*. *Cell*, 2005, **122**, 947-956.
20. Y. H. Loh, Q. Wu, J. L. Chew, V. B. Vega, W. Zhang, X. Chen, G. Bourque, J. George, B. Leong, J. Liu, *et al*. *Nat. Genet*. 2006, **38**, 431-440.

21. J. Yu, M. A. Vodyanik, K. Smuga-Otto, J. Antosiewicz-Bourget, J. L. Frane, S. Tian, J. Nie, G. A. Jonsdottir, V. Ruotti, R. Stewart, I. I. Slukvin and J. A. Thomson, *Science*, 2007, **318**, 1917-1920.
22. A. Trounson, R. G. Thakar, G. Lomax and D. Gibbons, *BMC Medicine*, 2011, **9** (52), 1-7.
23. M. Serra, C. Brito, C. Correia and P. M. Alves, *Trends in Biotechnology*, 2012, **30** (6), 350-359.
24. A. S. Lee, C. Tang, M. S. Rao, I. L. Weissman and J. C. Wu, *Nature Medicine*, 2013, **19** (8), 998-1004.
25. D. Hanahan and R. A. Weinberg, *Cell*, 2000, **100** (1), 57-70.
26. D. Hanahan and R. A. Weinberg, *Cell*, 2011, **144** (5), 646-74.
27. L. A. Loeb, *Cancer Res.*, 1991, **51**, 3073-3079.
28. D. Pellman, *Nature*, 2007, **446**, 38-39.
29. S. F. Bakhoum, W. T. Silkworth, I. K. Nardi, J. M. Nicholson, D. A. Compton and Daniela Cimini, *Current Biology*, 2014, **24** (14), 148-149.
30. C. Dominguez-Brauer, K. L. Thu, J. M. Mason, H. Blaser, M. R. Bray and T. W. Mak, *Molecular Cell*, 2015, **60** (4), 524-536.
31. M. Malumbres and M. Barbacid, *Nat Rev Cancer*, 2009, **9**, 153-166.
32. D. J. Gordon, B. Resio and D. Pellman, *Nature Rev Genet*, 2012, **13**, 189-203.
33. D. A. Crompton, *Current Opinion in Cell Biology*, 2011, **23**, 109-113.
34. S. Hanks, *et al*. *Nature Genet*, 2004, **36**, 1159-1161.
35. E. Van Beneden and A. Neyt, *Bull. Acad. R Belg.*, 1887, **14**, 215-295.
36. T. Boveri, *Sitz. Der Ges. Fur Morphol. Und Physiol. Munch.*, 1887, **3**, 151-164.
37. G. Marteil, A. Guerrero, A. F. Vieira, *et al*. *Nat Commun*, 2018, **9**, 1258.
38. S. L. Thompson, S. F. Bakhoum and D. A. Compton, *Curr Biol.*, 2010, **20** (6), R285-95.
39. A. L. Manning, N. J. Ganem, S. F. Bakhoum, M. Wagenbach, L. Wordeman and D. A. Compton, *Mol. Biol. Cell.*, 2007, **18**, 2970-2979.
40. N. J. Ganem and D. Pellman, *J. Cell Biol.*, 2012, **199** (6), 871-881.
41. C. Z. Zhang, et al. Nature, 2015, 522, 179-184.
42. H. K. Lindberg, G. C. Falck, H. Jarventaus and H. Norppa, *Mutagenesis*, 2008, **23**, 371-376.

43. J. Pampalona, E. Roscioli, W. T. Silkworth, B. Bowden, A. Genescà, L. Tusell, et al. *PLoS ONE*, 2016, **11** (1), e0147420.
44. Crasta, K., N.J. Ganem, R. Dagher, A.B. Lantermann, E.V. Ivanova, Y. Pan, L. Nezi, A. Protopopov, D. Chowdhury, and D. Pellman, *Nature*, 2012, **482**, 53-58.
45. J. Zhang, A. J. Hirst, F. Duan, H. Qiu, R. Huang, Y. Ji, L. Bai, F. Zhang, D. Robinson, M. Jones, L. Li, P. Wang, P. Jiang, P. W. Andrews, I. Barbaric and Jie Na, *Stem Cell Reports*, 2019, **12**, 557-571.
46. A.S. Lee, *et al*. *Cell Cycle*, 2009, **8**, 2608–2612.
47. A. S. Lee, C. Tang, M. S. Rao, I. L. Weissman and J. C. Wu, *Nature Medicine*, 2013, **19** (8), 998-1004.
48. U. Ben-David, *Biochimica et Biophysica Acta*, 2015, **1849**, 427-435.
49. N. Amariglio, *et al*. *PLoS Med*., 2009, **6**, e1000029.
50. D. Cyranoski, *Nature*, 2010, **465**, 997.
51. R. J. Lund, E. Närvä and R. Lahesmaa, *Nat Rev Genet*, 2012, **13** (10), 732-44.
52. International Stem Cell Initiative, K. Amps, P. W. Andrews, G. Anyfantis, *et al*. *Nat Biotechnol*. 2011, **29** (12), 1132-44.
53. N. Lamm, U. Ben-David, T. Golan-Lev, Z. Storchova, N. Benvenisty and B. Kerem, *Cell Stem Cell*, 2016, **18**, 253-261.
54. J. Halliwell, I. Barbaric and P. W. Andrews, *Nat Rev Mol Cell Biol.*, 2020, **21**, 715-728.
55. Y. Mayshar, U. Ben-David, N. Lavon, J.C. Biancotti, B. Yakir, A.T. Clark, K. Plath, W.E. Lowry and N. Benvenisty, *Cell Stem Cell*, 2010, **7**, 521–531.
56. A. J. Holland and D. W. Cleveland, *Nat Rev Mol Cell Biol*,, 2009,**10**, 478–487.
57. P. H. Duijf and R. Benezra, *Oncogene*, 2013, **32**, 4727–4736.
58. U. Weissbein, N. Benvenisty and U. Ben-David, *J. Cell Biol*., 2014, **204** (2),153-163.
59. K. A. Becker, P. N. Ghule, J. A. Therrien, J. B. Lian, J. L. Stein, A. J. van Wijnen and G. S. Stein., *J Cell Physiol*., 2006, **209** (3), 883-893.
60. N. Lamm and B. Kerem, *Molecular & Cellular Oncology*, 2016, **3** (4), e1183743.
61. Z. Holubcova, P. Matula, M. Sedlackova, V. Vinarsky, D. Dolezalova, T. Barta, P. Dvorak and A. Hampi, *Stem Cells*, 2011, **29**, 46-56.
62. H. T. K. Tse, W. M. Weaver and D. Di Carlo, *PLoS ONE*, 2012, **7**, e38986.

63. L. Kocgozlu, M. Rabineau, G. Koenig, Y. Haikel, P. Schaaf, J-N. Freund, *et al.*, *Biomaterials*, 2012, **33**, 798–809.
64. S. Acevedo-Acevedo and W. Crone, *Journal of Negative Results in BioMedicine*, 2015, **14** (22), 1-7.
65. T. A. Hookway, J. C. Butts, E. Lee, H. Tang and T. C. McDevitt, *Methods*, 2016, **101**, 11-20.
66. J. Rosenblatt, L. P. Cramer, B. Baum, K. M. McGee, *Cell*. 2004,**117**, 361–72.
67. D. Ortmann and L. Vallier, *Current Opinion in Genetics & Development*, 2017, **46**,179–185.
68. A. Sakaue-Sawano, M. Yo, N. Komatsu, T.Hiratsuka, T. Kogure, T. Hoshida, N. Goshima, M. Matsuda, H. Miyoshi and A. Miyawaki, *Molecular Cell*, 2017, **68**, 626-640.
69. A. Sakaue-Sawano, H. Kurokawa, T. Morimura, A. Hanyu, H. Hama, H. Osawa, S. Kashiwagi, K. Fukami, T. Miyata, H. Miyoshi, *et al*. *Cell*, 2008, **132**, 487-498.
70. S. Pauklin and L. Vallier, *Cell*, 2013, **155**, 135-147.
71. C. G. England, H. Luo and W. Cai, *Bioconjugate Chem.*, 2015, **26**, 975−986.
72. K. Im, S. Mareninov, M. F. Palma-Diaz and W. H. Yong, *Methods Mol Biol*. 2019, **1897**, 299–311.
73. J. B. Grimm, B. P. English, J. Chen, J. P. Slaughter, Z. Zhang, A. Revyakin, R. Patel, J. J. Macklin, D. Normanno, R. H. Singer, T. Lionnet and L. D. Lavi, *Nature Methods*, 2015, **12** (3), 244-253.

7 Conclusions and outlook: Multipolar mitosis

The previous chapter provided a summary that goes back to the early work that marked a beginning in stem cell research. The development of techniques for the in vitro growth of stem cells and their derivation until the reprogramming of already differentiated adult cells so that they return to their native pluripotent state is truly outstanding achievement. These discoveries that deserved the Nobel Prize are historical and have given us a field of research that in my opinion is beginning to emerge. Also merging the investigations of the characteristics and defects that have been found in cancer cells and the similarities that have been observed with pluripotent stem cells has raised doubts about their ability to produce tissues suitable for tissue replacement therapies and organ transplantation. This field of research is new and, therefore, many investigations and studies are necessary to address each error or failure that is found on the way leading to the main goal that is to personalize the medical field and treat an endless number of diseases, seeking cures for lethal and immunological diseases.

Unfortunately, many similarities have been found and therefore it is necessary to develop new technology to reduce them. For example, one problem is extracting cells from the blastocyst to isolate and grow stem cells in vitro. This method, as mentioned in the previous chapter, shows an ethical problem but apart from its method to derive them in different cell lines it is not advantageous since during its expansion and maintenance, genetic and epigenetic changes occur that are associated with its cultivation time. In addition, the method of extraction is considered laborious and not very easy to perform. For the case of reprogrammed cells, hiPSCs, where it is required to add genetic factors to induce pluripotency, shows that although the ethical problem was reduced, changes in the genome and epigenome can be generated and probably on a larger scale than hESCs. Several factors must be considered before passing this technology *in vivo*, although several clinical trials have already emerged, such as genomic stability, reproducibility and consistency. Also monitor the tumorigenic traits that may arise, and toxicity and immunological compatibility of possible organoids formed with hPSCs.

In addition, as the topic of ultrasound was discussed and results presented in previous chapters, an emerging idea of merging hPSCs with ultrasound is possible. For example, and as presented in Chapter 1 and Chapter 4, an aggregation of cells and conjugated particles can be formed non-invasively using sound waves. As discussed previously, hPSCs grow in colonies and multicellular environments are compact therefore applying this technology to grow and study these interactions without impacting their cell viability is a viable and safe option. Additionally, a recent study investigated the response of neural stem / progenitor cells (NSPCs) to low intensity acoustic waves.[1] They assessed cell differentiation and growth by observing whether apoptosis was induced. They showed that cells maintained their cell viability and that acoustic waves improved adherence to substrates and stimulated cell differentiation. Neurite growth was improved in cells exposed to ultrasound, which is consistent with a neurite growth study, already differentiated and exposed to ultrasound, reported by Gesellchen *et al*,[2] where the direction of growth of neurites was established following the direction of propagation of ultrasonic waves. These studies provide a platform for a possible fusion of safe and effective technologies.

To complete these chapters, it can be concluded that the safety of this technology has to be ensured by determining the risks and its benefits in order to be applied in clinical therapies. Although it is of great interest to launch gene therapy as soon as possible, more studies and development of technologies to help establish stem cell applications are necessary.

7.1 References

1. I-Chi Lee, Tsu-Lin Lo, Tai-Hong Young, et al., *Ultrasound in Med & Biol.*, 2014, **40** (9), 2195-2206.
2. F. Gesellchen, A. L. Bernassau, T. Déjardin, D. R. S. Cumming and M. O. Riehle, *Lab Chip*, 2014, **14**, 2266-2275.

8 Experimental section

This chapter includes the materials and methods used to carry out in this doctoral thesis. They are described according to the order of the chapters.

8.1 Acoustic device fabrication

Procedure for Chapters 2, 3 and 4

A rectangular 2-D ultrasonic device was design with AutoCAD computational program, fabricated and assembled with two front-faced 1 mm thick piezoelectric transducers (PZT) (Noliac, NCE51, L 15 X W 2 mm). Trapping was performed in 1D so that the cells aligned parallel to the PZT faces. The acoustic device was made from PMMA [Poly(methyl methacrylate)] and mounted on a double-width glass slide (Corning, L 75 X W 50mm). The acoustic device was designed to fit a coverslip 18 X 18 mm in the central cavity. The PZT transducers were coupled with ultrasound gel (Sonatest W250) and positioned in the lateral cavities pressed to the PMMA wall by two wooden pieces, which were acting as springs. The central cavity was separated by a 3 mm boundary from the lateral cavities to ensure that there was no contact of the transducers with the medium and to avoid contamination.

8.2 Acoustic resonant and electrical impedances measurements

Undertaken by Dr Adrian Barnes for Chapter 2

The rectangular 2-D acoustic trapping was employed for resonant and electrical impedance measurements. The size of the cavity was ~20 X 20 mm with a depth of ~2 mm. The PZTs were coupled to the adjacent cavities and operated close to their third harmonic frequency, 6.74 MHz, determined experimentally previously by electrical impedance measurements. The parallel front-faced transducers were operated close to their antiresonance frequency, ~ 6.77 MHz, with a corresponding wavelength of λ = 220 μm in water. The device was operated at a cavity resonance given by w/λ is integer and are separated by ~ 0.1 MHz. The driving frequency was adjusted in small steps of 0.01 MHz until cellular alignment was observed. The standing waves were generated with a single signal generator (GwInstek SFG-2020) in parallel and monitored with an oscilloscope (Agilent Technologies DS03152A). When the PZTs were driven at 10 V_{pp} the maximum electrical power was ~1 W, delivered to the device. Impedance calculations were analysed with a 1D transmission model in SPICE computational program for the opposed PZTs with set resonant frequencies of 6.69 MHz and 6.74 MHz, as used for the cellular experiments.

8.3 Cell culture

Procedure for Chapters 2, 3 and 4

Cervical cancer (HeLa) cells and human dermal fibroblasts (HDF, for Chapter 3) were cultured in 75 cm^2 culture flasks (Greiner Bio One) and maintained under standard cell culture conditions at 37°C with a 5% CO_2 humidified atmosphere. The employed culture Dulbecco's Modified Eagle's Medium (DMEM) with 4.5g/L of D-Glucose (Gibco, Life Technologies, UK) was used for HeLa cells and Dulbecco's Modified Eagle's Medium (DMEM) with 1g/L of D-Glucose used for HDF cells. Both culture media were supplemented with 10% FBS (foetal bovine serum) (Gibco, Life Technologies, UK) and 1% penicillin/streptomycin (Gibco, Life Technologies, UK) under sterile conditions.

8.4 Cellular alignment deposition

Procedure for Chapter 3

Acoustic streaming was evaluated employing PBS (Phosphate Buffer Solution, Gibco Life Technologies, UK) as the host fluid and optical microscope observations were obtained using a Leica DMIL inverted microscope with a mounted Leica DFC295 digital camera and further analysed with LAS-MultiTime-Movie-Timelapse (Leica Microsystems Limited, UK). For cellular deposition studies, square glass coverslips (18 X 18 mm) were coated with 0.01% poly-L-lysine (A-005-C, Merck Millipore) overnight and washed with PBS 1X (pH 7.4, Gibco, Life Technologies, UK) prior to the experiments. A coated-glass coverslip was positioned inside the central chamber seeding 650µl of HeLa cells, after being dissociated from confluent cultures. The seeded HeLa cell concentration was 5 x 10^4 cells ml^{-1}. In order to induce cell trapping at the bottom of the device, two deposition methods were done: one where the acoustic field was applied immediately after the cells were seeded in the chamber (i.e., trapping the cells as they are settled) and a second one where the cells were allowed to be settled for three minutes before the field was applied (i.e., trapping after the cells had attached and deposited).

The counter-propagating waves generated in the central cavity guided the cells to the acoustic pressure nodes, where the trapping and aligning occurred. After 5, 10 and 15 min of acoustic exposure, the treated coverslips with the aligned HeLa and HDF cells, were placed in a 6-well plate for a further 24h incubation with the respective DMEM medium. Pictures and videos showing the cellular deposition over time were obtained using a Leica DMIL inverted microscope with a mounted Leica DFC295 digital camera and further analysed with LAS-MultiTime-Movie-Timelapse (Leica Microsystems Limited, UK).

8.5 Temperature-dependent measurements

Procedure for Chapter 3

Temperature measurements were made in the central chamber filled with biological media for a range of applied voltages (4 – 10 V_{pp}) to study temperature changes in relation to exposure time and intensities. The acoustic device was placed in a block heater (digital block heater SBH130D, Stuart, Cole Parmer, UK) to keep the temperature stable set at 36°C and the temperature variations were then compared to those measured when testing the same voltages in the device kept at room temperature (20°C) without temperature control. The central chamber was filled with 650µl of DMEM media and temperature recordings were taken every minute for a total of 30 min while the acoustic field was switched on. Measurements were monitored using a Type K thermocouple (Fisher Scientific, UK) and were done per triplicate.

8.6 Cell viability and metabolic activity measurements

Procedure for Chapter 3

Cell viability and metabolic activity assays were performed for HeLa and HDF cells acoustically exposed to 6, 8 and 10 V_{pp} for 5, 10 and 15 min after a 24h incubation. As a control, cells without acoustic exposure were maintained at the same temperature and for the same amount of time as exposed cells. HeLa and HDF cells were incubated at 37°C for 1h with 3µM Calcein-AM (490Ex/520Em) (Invitrogen, UK) and 5% Alamar Blue (560Ex/590Em) (Invitrogen, UK) solution in DMEM to test cell viability and metabolism, respectively. Fluorescent readings for exposed and control cells were collected from 50µl of cell culture supernatant and fluorescence readings acquired with the CLARIOstar® microplate reader (BMG LABTECH, UK). Readings were done per triplicate.

8.7 Carboxyl-modified polystyrene microspheres formulation and characterization

Undertaken by Dr Sandra Medina and Dr Sarah Michel

Dragon green-fluorescent carboxyl polystyrene microspheres (PS-COOH) (excitation/emission: 480/520 nm, Bangs Laboratories, UK) with a mean diameter of 1µm, were employed to formulate different surface charges with: 1-aminolactose, amino dextran (10,000 MW, Invitrogen), trioxa-tridecanediamine (TTDDA, Sigma-Aldrich) and acid-coated. For each coupling, 50 µl of fluorescent carboxylic microspheres were dialyzed against pure water using a dialysis membrane with a Molecular Weight Cut Off (MWCO) of 500-1000 Da for 16 hours. The aliquots were then centrifuged at 13500 rpm for 15 min. The supernatants were removed, and the pellets resuspended in 125 µl of PBS with a vortex mixer. EDC HCL (10 mg, Alfa Aesar) previously dissolved in 125 µl PBS was added to the reaction mixture. 1-aminolactose (5 mg), amino dextran 10,000 MW (10 mg) and TTDDA (5 mg) were dissolved in 125 µl of PBS, respectively, and added to the microsphere solution. The mixtures were shaken for 16 hours in darkness and then centrifuged. The supernatants were removed, and the pellets resuspended in 1 ml of pure water and centrifuged again. This last step was repeated 3 times and after 3 washes, the pellets were finally resuspended in 50 µl of PBS.

The conjugation to the microspheres was assessed by NMR using a Bruker 500 MHz equipped with a cryogenic probe. The microbeads were freeze-dried overnight and dissolved in CDCl3. 1H and HSQC were recorded at 25°C. Chemical shifts for all microspheres conjugation are reported as parts per million (ppm). For spectra analysis, MestReNova 14.0.1 was used.

The zeta potential and the dynamic light scattering (DLS) of the formulated microspheres were performed in 0.1X PBS and 0.1X DMEM medium, without FBS at 25°C by Malvern Zetasizer Nano Z and Nano S90, respectively. The polydispersity index (PDI) for each microsphere formulation was also measured and the conjugated microsphere solutions were sonicated before measurements.

8.8 Ultrasound exposure and cellular uptake

Procedure for Chapter 4

Square glass coverslips were washed with PBS after being coated overnight with 0.01% poly-L-lysine (A-005-C, Merck Millipore). The 2-D acoustic device was placed in the centre of a heating block to maintain the temperature at biological standards set at 36°C and monitored employing a Type K thermocouple (Fisher Scientific, UK). HeLa cells were dissociated from confluent cultures and seeded at a concentration of $5X10^4$ cells ml-1 into the coated-glass coverslip placed in the central cavity of the ultrasonic device. After a 15 min ultrasonic exposure (for acoustic treatment) or incubation (for basal endocytosis treatment), the coverslips with the adhered HeLa cells were incubated in a 6 well-plate for 24 hrs. The coated-glass coverslips with the attached HeLa cells were once again placed in the central cavity and 5μl of each fluorescent microsphere formulation in DMEM media without FBS was added for a further 15 min of acoustic exposure or incubation. The generated ultrasonic standing waves guided the cells and microspheres to the acoustic pressure nodes, where the trapping and aligning occurred for the acoustic treatment.

8.9 Inhibition of active cellular uptake

Conducted with assistance of Dr David Benito-Alifonso

A concentration of $5X10^4$ cells ml-1 HeLa cells were seeded at into the 0.01% poly-L-lysine coated-glass coverslips for a 15 min ultrasonic exposure or incubation, followed by an overnight incubation in a 6 well-plate. After 24 hrs, the attached cells were preincubated for 20 min with colchicine (2.5mM) which is an inhibitor for the macropinocytosis mechanism. Later, the cells were incubated (for the inhibitor basal endocytosis treatment) or exposed to ultra-sound (for the inhibitor acoustic treatment) for 15 min with 5ml of each fluorescent microsphere formulation in DMEM media. Negative controls, i.e., cells without formulated fluorescent microspheres were carried out for each treatment for cell viability and toxicity studies.

8.10 Flow cytometry and propidium iodide analysis

Conducted with assistance of Lorena Sueiro-Ballesteros and Andrew Herman

HeLa cells were seeded at the same concentration ($5X10^4$ cells ml^{-1}) onto the previously coated 0.01% poly-L-lysine glass coverslips for a 15 min ultrasonic exposure or incubation depending on the treatment and followed by an over-night incubation in 6 well-plates. After 24 hrs, the attached cells were incubated with 500µl of Accutase (A-005-C, Merck Millipore, UK) to create a single cell suspension and harvest the cells with no further washes required. Before flow cytometric analysis, 0.3mM Propidium Iodide (PI) viability staining (excitation/emission maxima: 649/697 nm, Biostatus) was performed to be able to evaluate cell viability and toxicity. Flow cytometric data was acquired using a BD LSR II (BD, San Diego, CA) and analysed using FlowJo v10.5 software (BD, San Diego, CA). A 488nm and a 633nm solid laser was used to excite Dragon green microspheres (530/30 nm) and PI (660/20 nm), respectively. Each treatment was performed and analysed in triplicate. One-way Anova analysis was done in conjunction with a Tukey’s test ($p < 0.05$).

8.11 Confocal microscopy

Conducted with assistance of Alan Leard

The attached HeLa cells from the experimental conditions (acoustic and basal endocytosis), were washed twice with Live Cell Imaging solution and labelling the cell membranes with 1X CellMask^{TM} Deep red plasma membrane stain (excitation/emission: 649/666 nm, Invitrogen, UK). The cells were fixed with warm 4% formaldehyde in PBS and the glass coverslip was mounted on a glass microscope slide using SlowFade Diamond mountant with DAPI (Invitrogen, UK), to label the nuclei. Fluorescent images of fixed HeLa cells were obtained with an inverted confocal laser scanning micro-scope (Leica SP8 AOBS) and were processed with Fiji ImageJ. Deconvolution of the fluorescent images was done employing Huygens deconvolution software, which offered 30% higher resolution of the confocal data.

8.12 Microsphere Infiltration computational analysis

Undertaken by Stephen Cross

Microspheres infiltration analysis was done using the previously deconvoluted confocal images using Fiji ImageJ workflow automation plugin MIA (v0.10.6). The fluorescent conjugated microspheres were classified based on their overlap with cells as: “overlapping” (all microsphere-labelled pixels coincident with cell-labelled pixels), “not overlapping” (no coincident pixels) or “partially overlapping” (some co-incident pixels).

8.13 Electron microscopy

Conducted with assistance of Technician Chris Neal and supported by Prof Paul Verkade

Gridded glass coverslips (ibidi®, Germany) were cut to fit in the central chamber of the acoustic device and were coated with 0.01% poly-L-lysine (A-005-C, Merck Millipore) prior experiments. The already attached and labelled cells were localized, and fluorescent images were taken employing a confocal microscope. After imaging, the samples were fixed and embedded in Epon resin and dehydrated in a graded series of ethanol from 50 to 100%). The samples were then treated with uranyl acetate for 20 min covered in foil. Serial sections from the previously trimmed regions of interest, were acquired according to the thickness for a standard TEM (~70nm) before imaging in the TEM the relocated cells.

8.14 hPSCs culture

Procedure for Chapter 6

Undifferentiated human embryonic stem cells (hESC) with genetically introduced FUCCI and H2B HaloTag reporters were grown in 6-well pre-coated plates (Greiner Bio One) and maintained under standard cell culture conditions, humidified atmosphere with 5% CO2 at 37 ° C. The hESCs were culture feeder-free well plates as they were coated with 1ml of GelTrex Matrix (Gibco, Life Technologies, UK) at a concentration of 1:100. Essential 8TM (E8) stem cell medium (Gibco, Life Technologies, UK) was used and changed every day to cultivate and maintain hESCs under sterile conditions. Prior experiments, hESCs were dissociated using 0.5mM Versene® (EDTA) (Lonza, UK) and adding Rho-associated protein kinase (ROCK) inhibitor (STEMCELL Technologies, UK) (1: 1000 of 10 µM stock solution) to improve cell survival.

8.15 Time-lapse spinning disk confocal microscopy

Procedure for Chapter 6

The undifferentiated hESC cells expressing Fucci-HaloTag were dissociated and cultured in a concentration of 1:10 in a 96-well glass bottom plate allowing the cells to adhere for 2 hours under standard culture conditions prior time-lapse imaging. The 96-well plate was placed in the heated stage inside the spinning confocal microscope (Yokogawa). Observations and recordings were done with a set time-lapse imaging for FUCCI every 30 min and HaloTag every 10 min for 4 days. The cell medium was changed every day in a 10 min break before the next schedule image session started. A 60X water immersion objective was used, and time-lapse images were analysed with Fiji Image J.

8.16 Immunofluorescence assays for fixed hPSCs

Procedure for Chapter 6

The undifferentiated hESCs were lysed with warm PEM (polymer electrolyte membrane) buffer supplemented with Triton-X100 for 1 min prior to fixation. Later, hESCs were fixed with 50ul of 1% glutaraldehyde in PEM buffer for 10 min at room temperature. Washes with 1X PBS were done after and kept the fixed cells in a 0.1% Tween 20 solution. A blocking solution of 1% BSA (bovine serum albumin) in PBST (PBS + 0.1% Tween 20) was added prior primary antibody incubation for 1 hour. Primary antibodies were diluted in 1% BSA in PBST solution and were incubated in a humidified chamber at room temperature overnight at 4°C. The primary antibodies used, and their dilutions were: mouse monoclonal anti-α tubulin (Sigma Aldrich T9026, 1:100), rabbit recombinant anti-CENPE (Abcam ab133583, 1:400) and rat purified anti-Centrin (Caltractin) (Biolegend 698602, 1:200). The secondary antibodies were added after removing the primary antibodies and carefully washing 3 times with 1X PBS. Alexa Fluor secondary antibodies were diluted in 1% BSA in PBS and incubated for 1 hour protected from the light at room temperature. The concentrations used for the secondary antibodies were followed by the manufacturer's indications, Alexa Fluor 488 (2µg/ml), Alexa Fluor 594 (4µg/ml) and Alexa Fluor 647 (1µg/ml) for α tubulin, CENPE, and Centrin, respectively. The nuclei were stained with Hoechst blue stain (1:500) 15 min prior imaging. Spinning disk confocal microscope (Yokogawa) was employed for imaging and z-stacks were acquired in steps of 0.4µm, later analysed with Volocity computational package provided by the Wolfson Imaging Centre of the University of Bristol.

Appendix Supplementary information for Chapter 4

A.1 Characterisation of carboxyl-modified polystyrene microspheres

Table A.1 Hydrodynamic size (DLS), polydispersity index and ζ- potential of conjugated fluorescent microparticles, representing the average of three measurements.

Microspheres	Diameter (nm)		PDI		ζ- potential (mV)	
	DMEM	PBS	DMEM	PBS	DMEM	PBS
Amino dextran	1070 ± 118.9	1107 ± 125	0.35	0.29	7.14 ± 2.7	8.9 ± 0.62
TTDDA	1082 ± 63.97	1078 ± 14.57	0.10	0.09	-21 ± 1.21	-22.9 ± 0.98
1-aminolactose	1004 ± 133.9	1046 ± 134	0.31	0.24	-9.6 ± 1.80	-11.6 ± 1.82
Acid	971 ± 17.6	949.9 ± 18.4	0.11	0.12	-33 ± 2.55	-46.6 ± 2.90
Commercial beads	946.7 ± 21.1	933.8 ± 48.3	0.06	0.15	-32.2 ± 1.38	-45.7 ± 2.91

A.2 Microsphere infiltration images

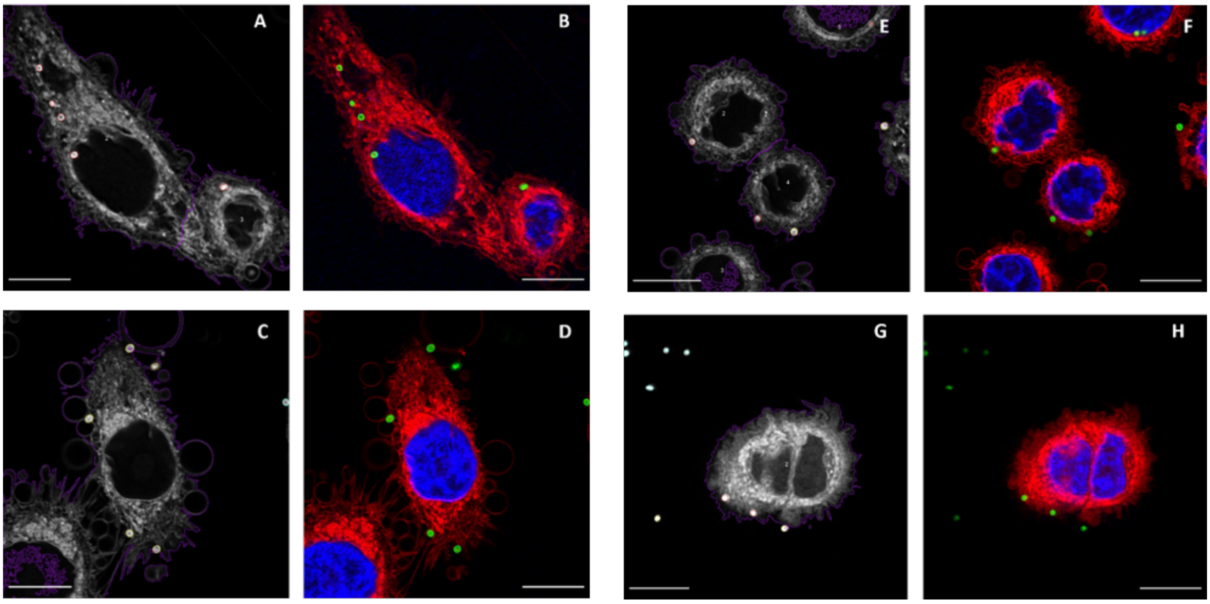

Figure 0.1: Acid microspheres infiltration analysis and deconvoluted confocal images of internalised or adjacent microspheres to HeLa cells when: acoustically aligned (**A**, **B**), unexposed only incubated particles (**C**, **D**), treated with inhibitor prior acoustic exposure (**E**, **F**) and inhibitor treatment prior particle incubation (**G**, **H**), respectively. Cell membrane in the infiltration analysis is depicted in purple. Internalised particles are surrounded in red, particles located at the edge of the cell membrane are surrounded in yellow and particles outside the cell are surrounded in blue. Scale bars 10 µm.

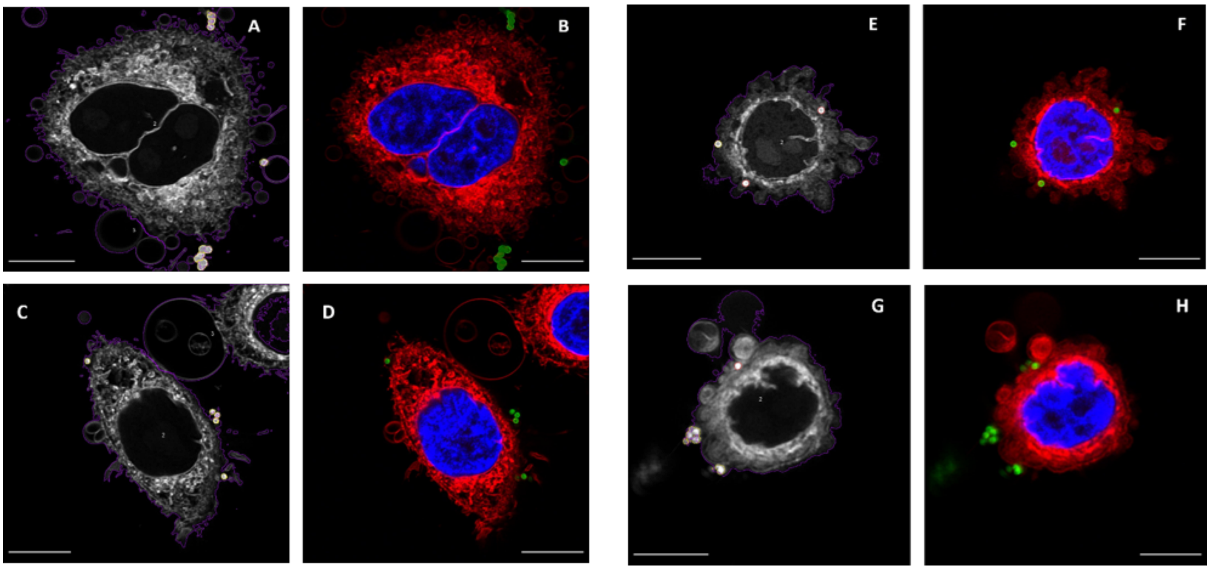

Figure 0.2: Amino dextran conjugated microspheres infiltration analysis and deconvoluted confocal images of internalised or adjacent microspheres to HeLa cell(s) when: acoustically aligned (**A**, **B**), unexposed only incubated particles (**C**, **D**), treated with inhibitor prior acoustic exposure (**E**, **F**) and inhibitor treatment prior particle incubation (**G**, **H**), respectively. Cell membrane in the infiltration analysis is depicted in purple. Internalised particles are surrounded in red, particles located at the edge of the cell membrane are surrounded in yellow. Scale bars 10 µm.

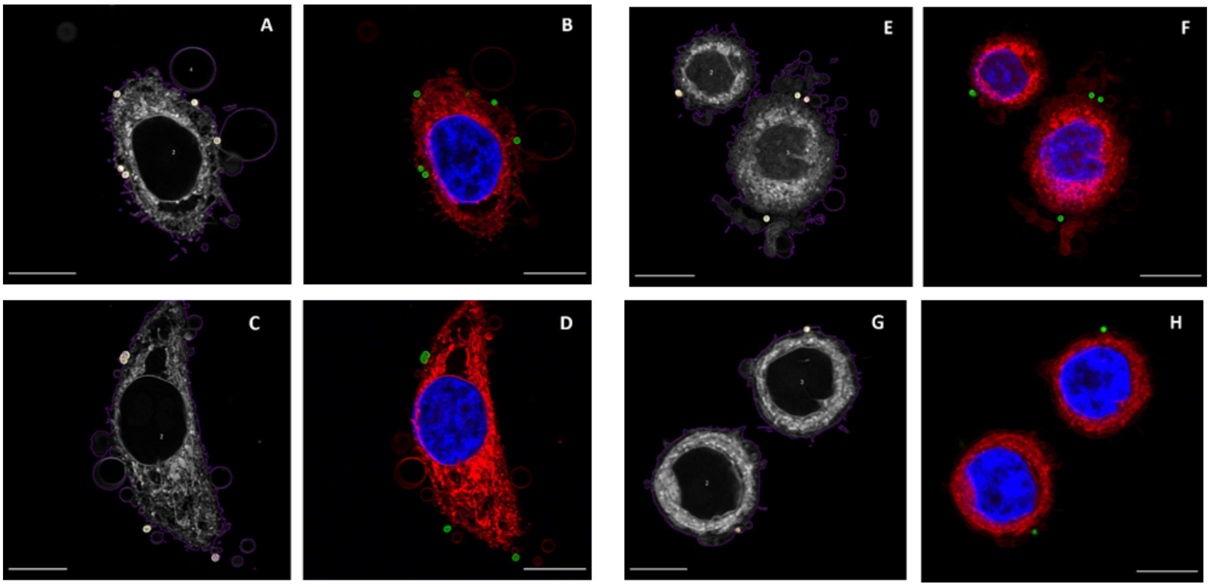

Figure 0.3: Lactose conjugated microspheres infiltration analysis and deconvoluted confocal images of internalised or adjacent microspheres to HeLa cell(s) when: acoustically aligned (**A**, **B**), unexposed only incubated particles (**C**, **D**), treated with inhibitor prior acoustic exposure (**E**, **F**) and inhibitor treatment prior particle incubation (**G**, **H**), respectively. Cell membrane in the infiltration analysis is depicted in purple. Internalised particles are surrounded in red, particles located at the edge of the cell membrane are surrounded in yellow. Scale bars 10 µm.

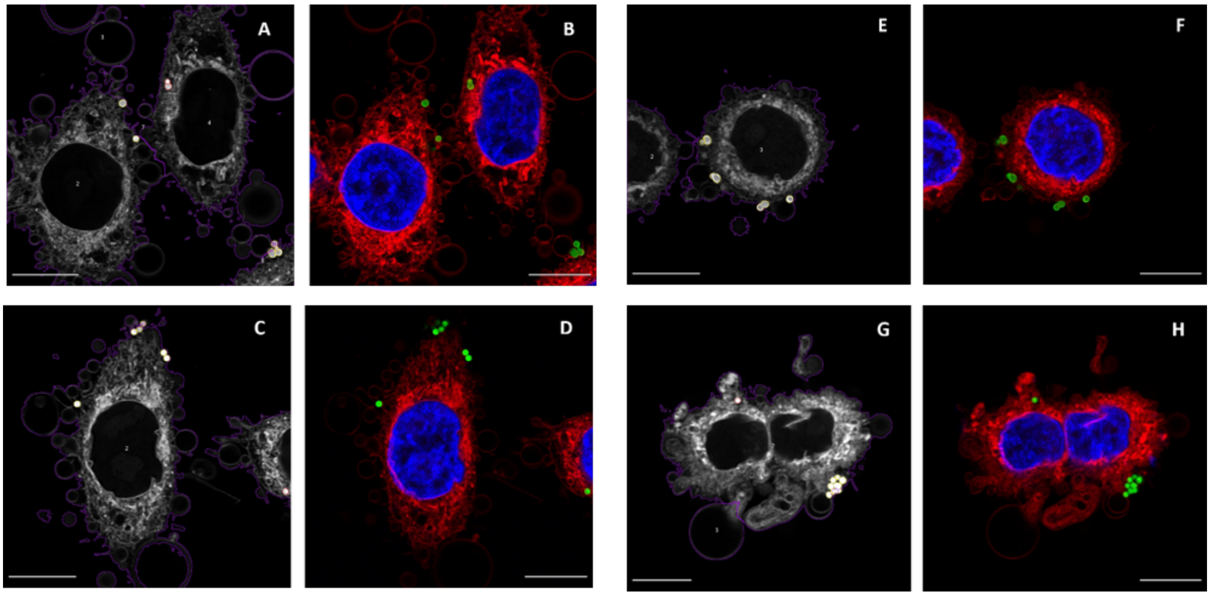

Figure 0.4: TTDDA conjugated microspheres infiltration analysis and deconvoluted confocal images of internalised or adjacent microspheres to HeLa cell(s) when: acoustically aligned (**A**, **B**), unexposed only incubated particles (**C, D**), treated with inhibitor prior acoustic exposure (**E, F**) and inhibitor treatment prior particle incubation (**G**, **H**), respectively. Cell membrane in the infiltration analysis is depicted in purple. Internalised particles are surrounded in red, particles located at the edge of the cell membrane are surrounded in yellow. Scale bars 10 µm.

A.3 Microsphere infiltration graphs

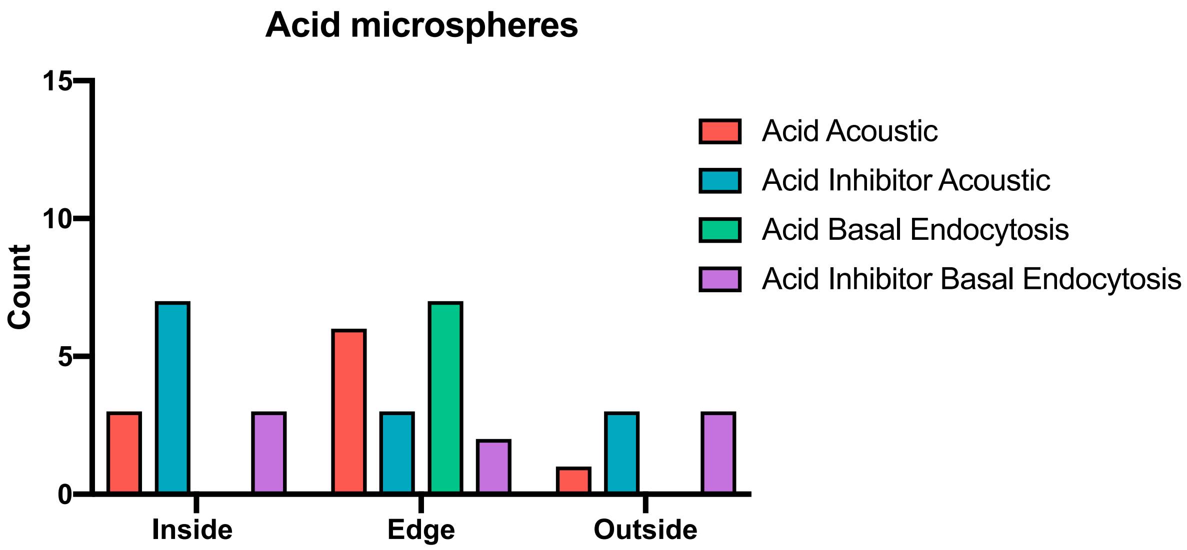

Graph 0.1: Median of acid microspheres from the infiltration analysis in all treatments.

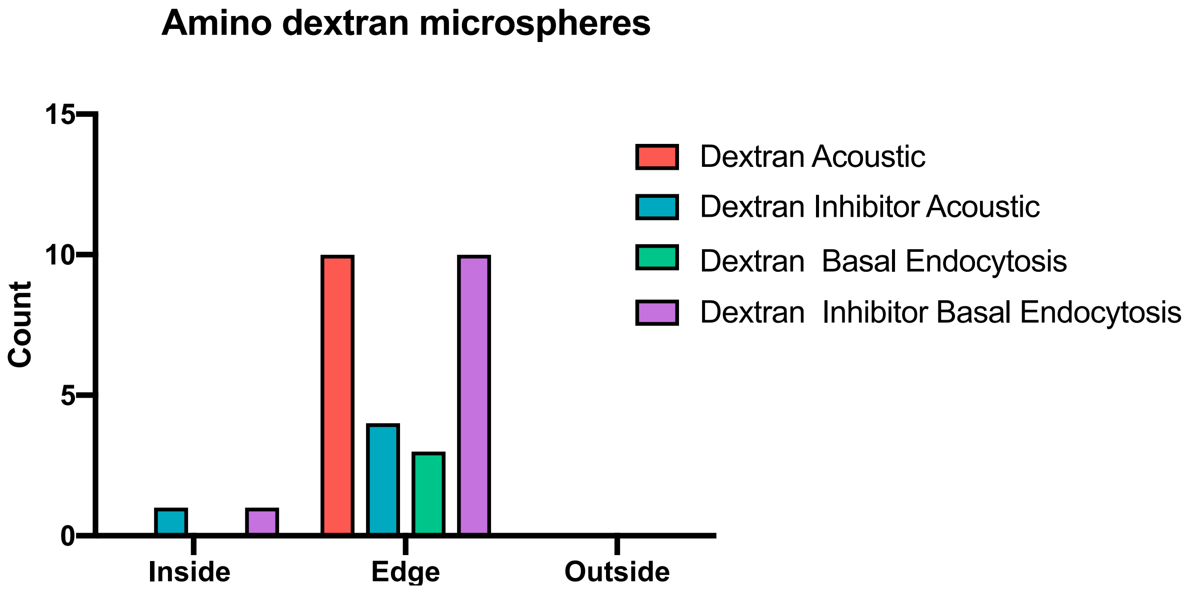

Graph 0.2: Median of amino dextran conjugated microspheres from the infiltration analysis in all treatments.

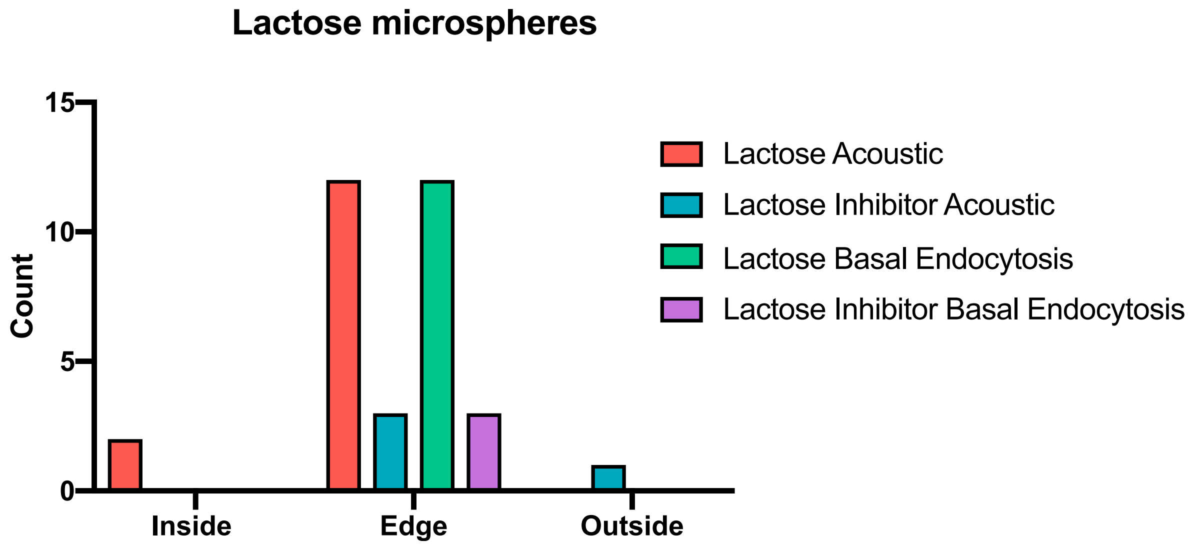

Graph 0.3: Median of lactose conjugated microspheres from the infiltration analysis in all treatments.

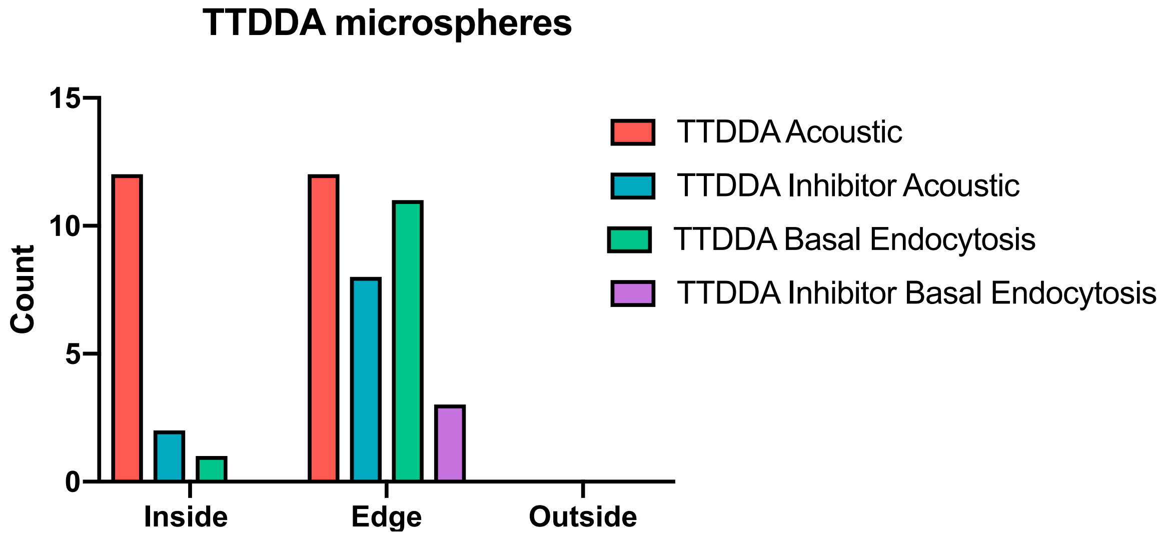

Graph 0.4: Median of TTDDA conjugated microspheres from the infiltration analysis in all treatments.

A.4 NMR microparticles characterisation

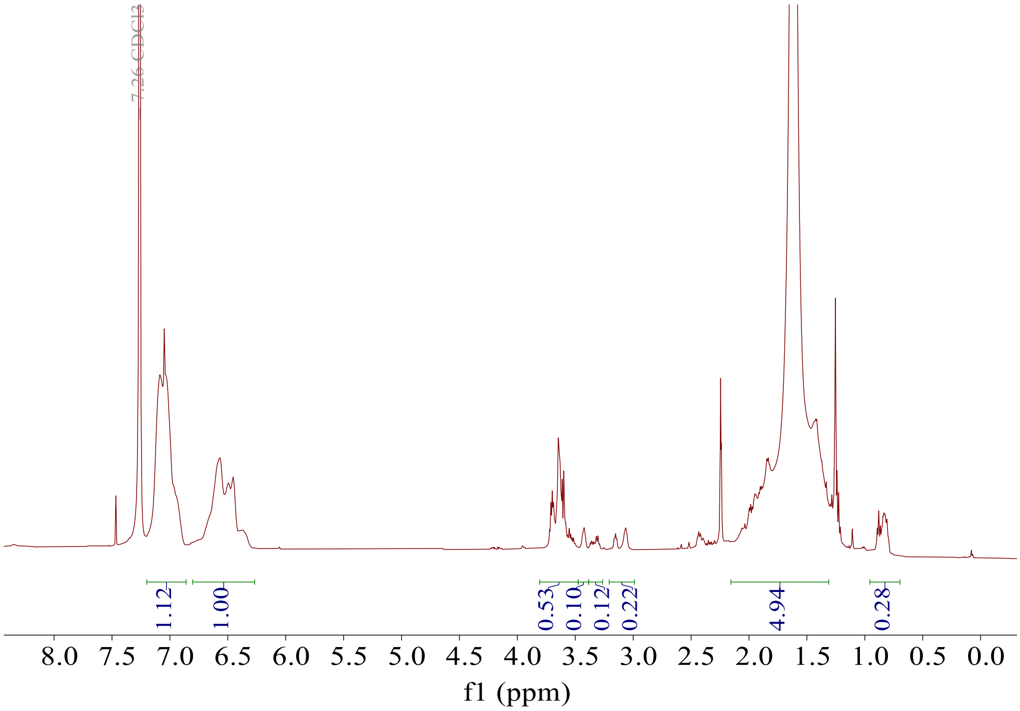

Figure 0.5: ^{1}H NMR of freeze-dried TTDDA-functionalised microspheres dissolved in $CDCl_3$.

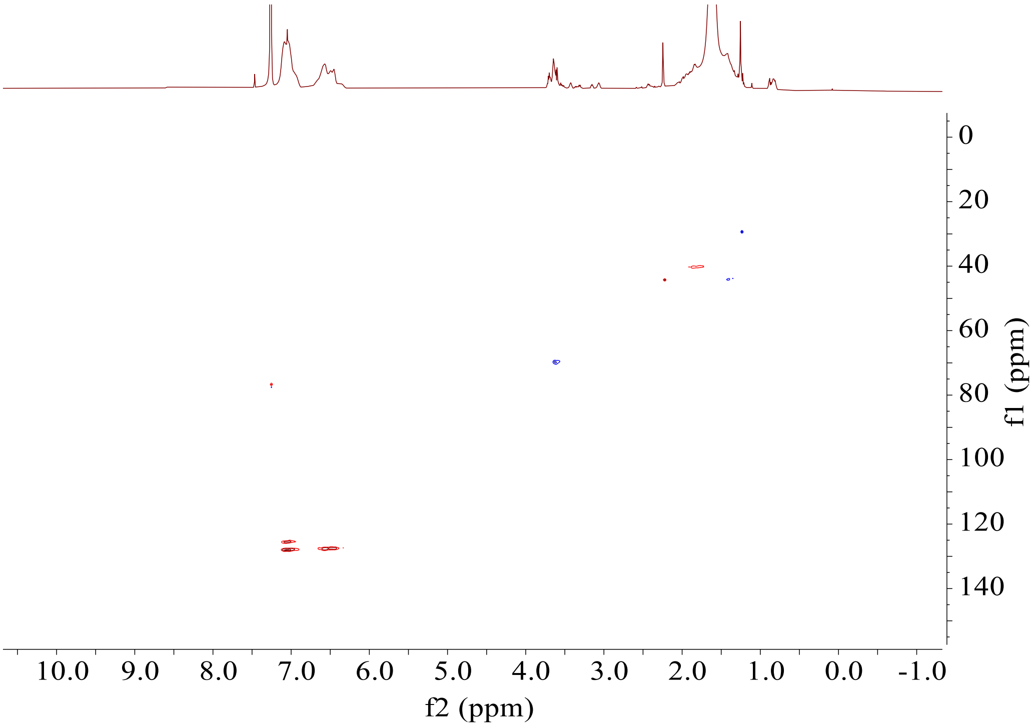

Figure 0.6: HSQC NMR of freeze-dried TTDDA-functionalised microspheres dissolved in $CDCl_3$.

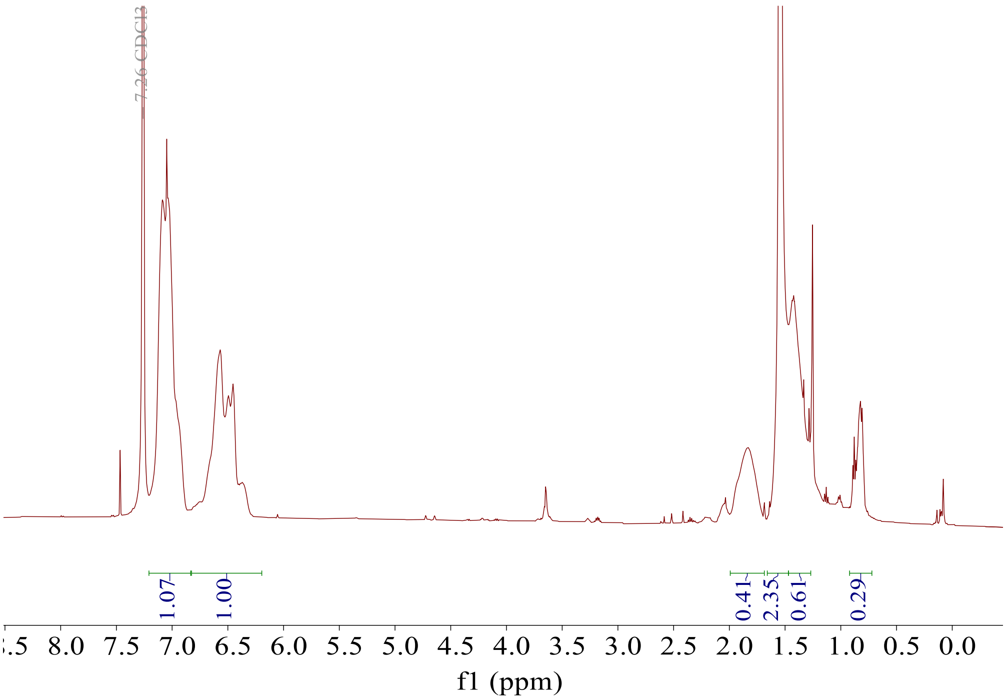

Figure 0.7: ^1H NMR of freeze-dried dextran-functionalised microspheres dissolved in $CDCl_3$.

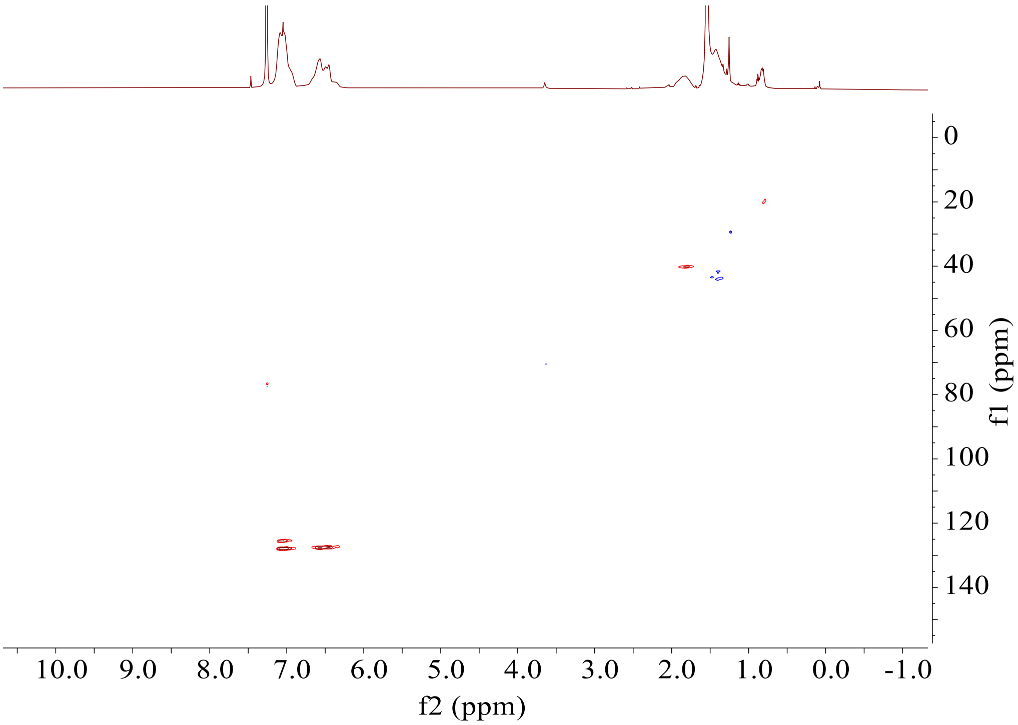

Figure 0.8: HSQC NMR of freeze-dried dextran-functionalised microspheres dissolved in $CDCl_3$.

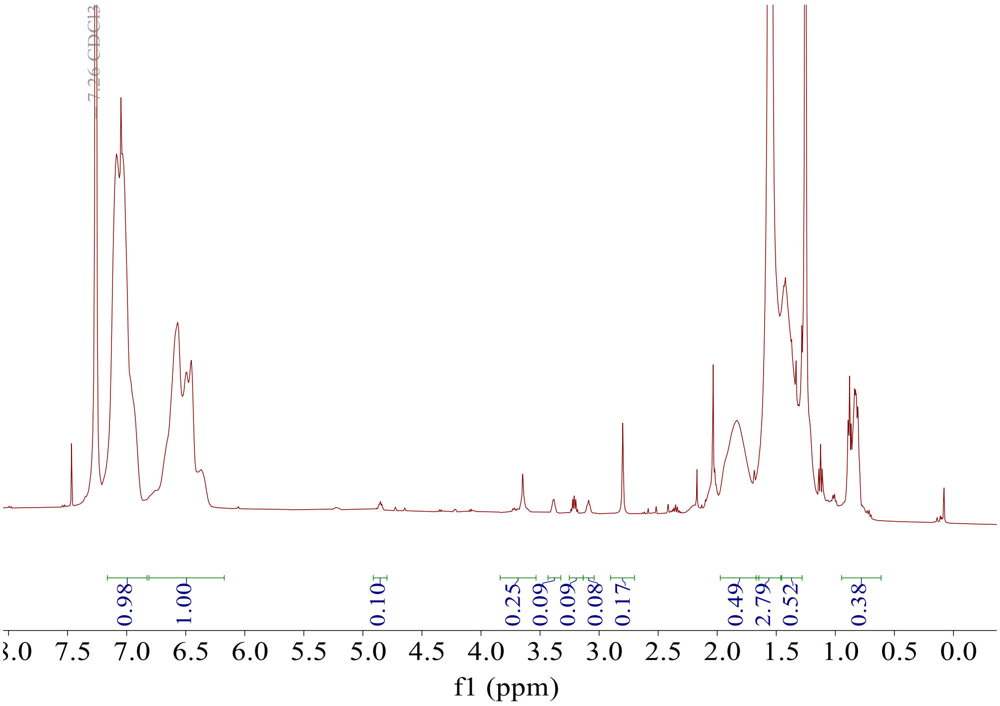

Figure 0.9: ^1H NMR of freeze-dried lactose-functionalised microspheres dissolved in $CDCl_3$.

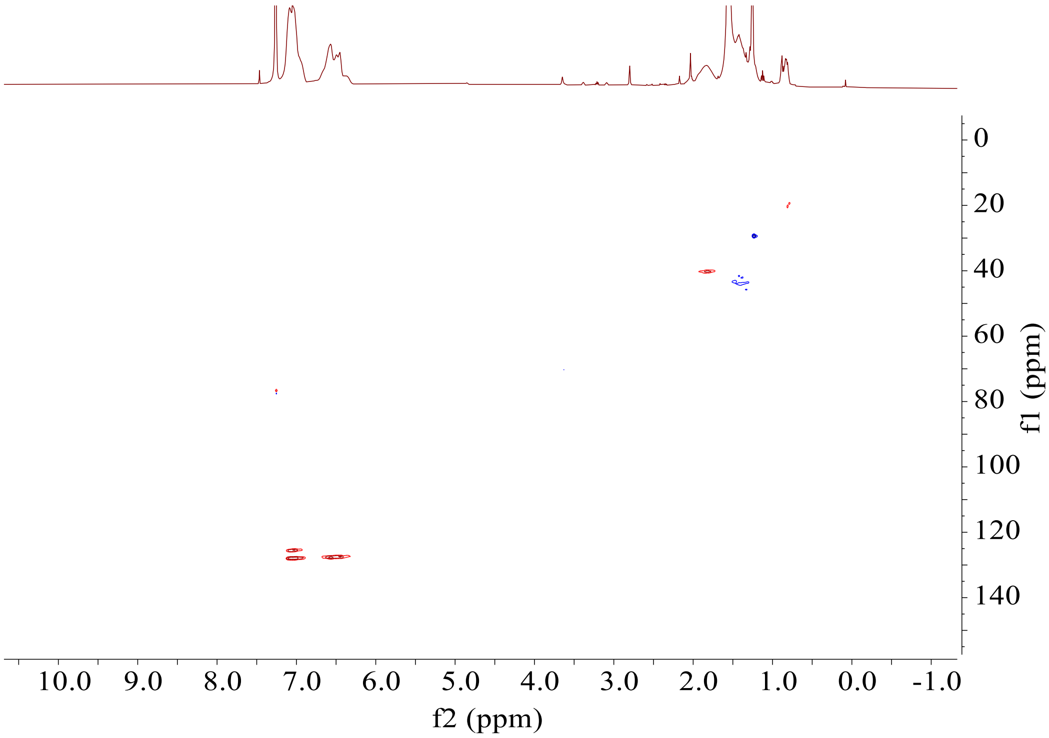

Figure 0.10: HSQC NMR of freeze-dried lactose-functionalised microspheres dissolved in $CDCl_3$.

A.5 Flow cytometry analysis

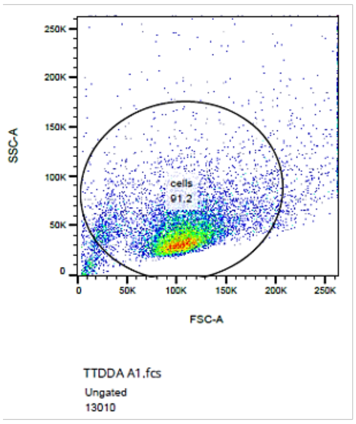

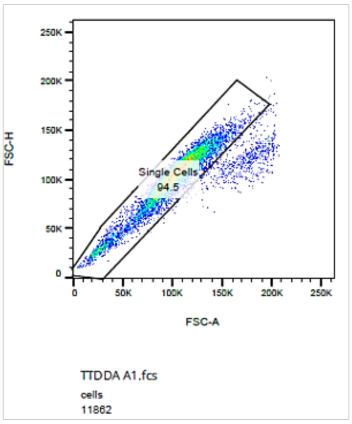

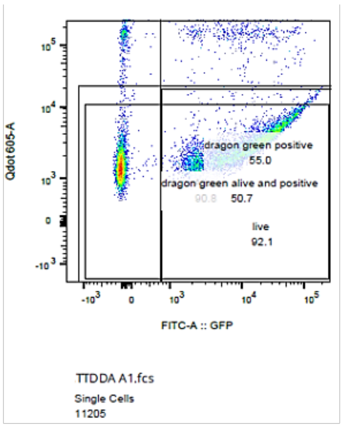

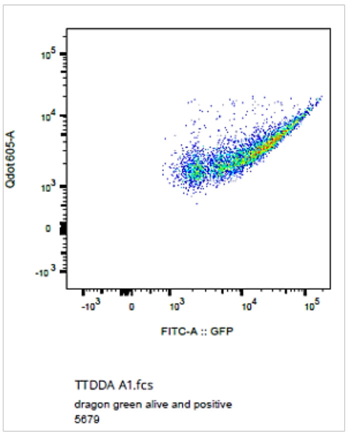

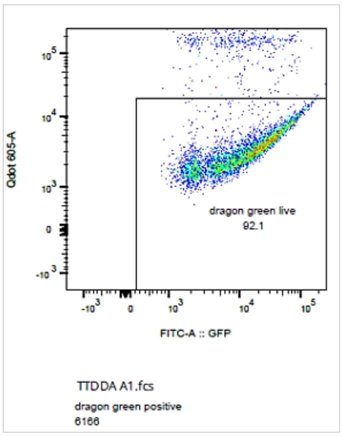

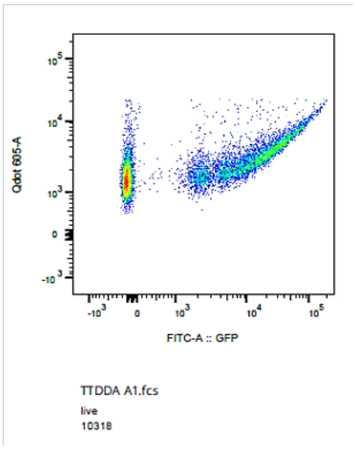

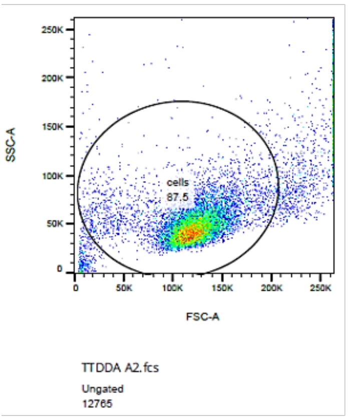

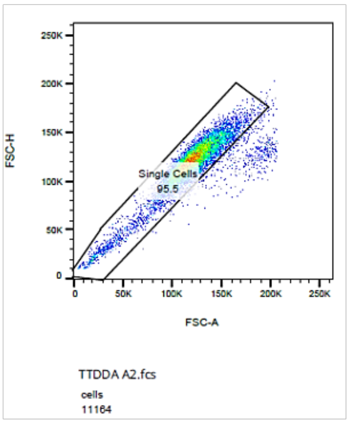

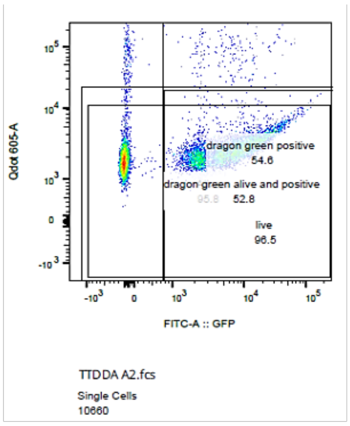

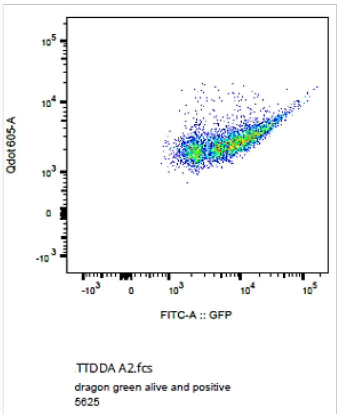

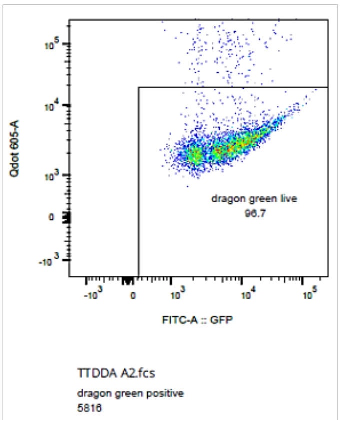

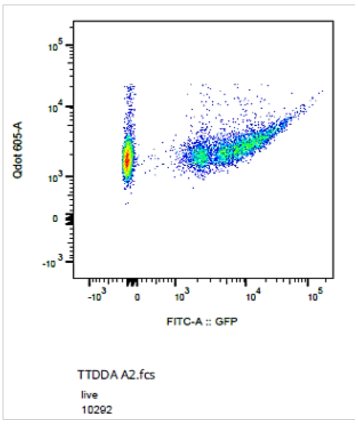

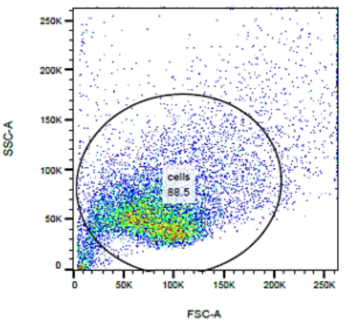

TTDDA A3.fcs
Ungated
14476

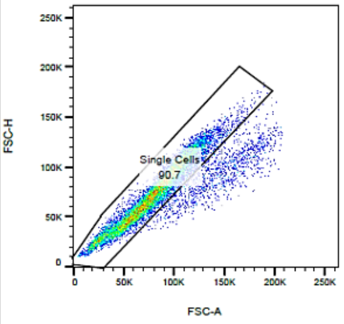

TTDDA A3.fcs
cells
12818

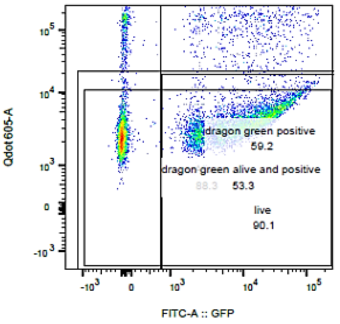

TTDDA A3.fcs
Single Cells
11623

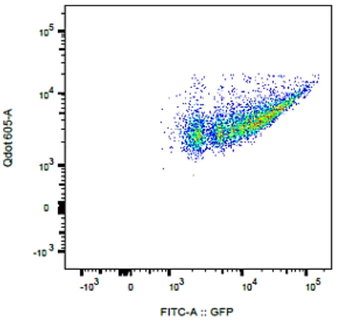

TTDDA A3.fcs
dragon green alive and positive
6198

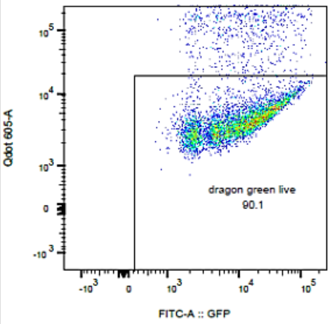

TTDDA A3.fcs
dragon green positive
6880

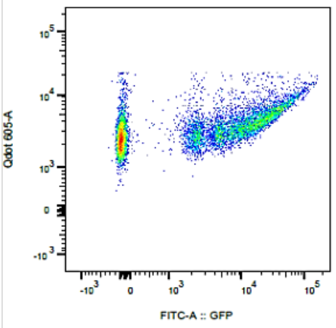

TTDDA A3.fcs
live
10474

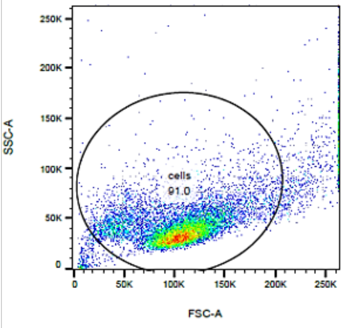

Lactose A1.fcs
Ungated
13540

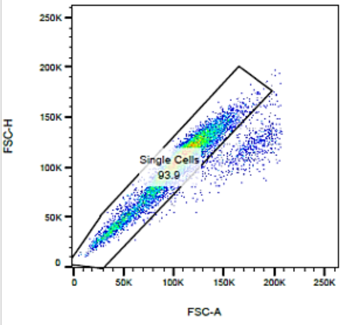

Lactose A1.fcs
cells
12328

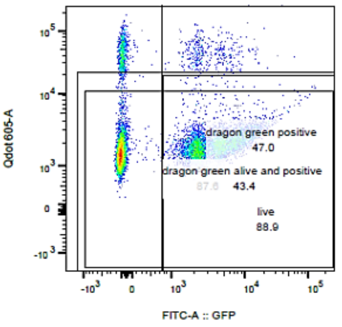

Lactose A1.fcs
Single Cells
11576

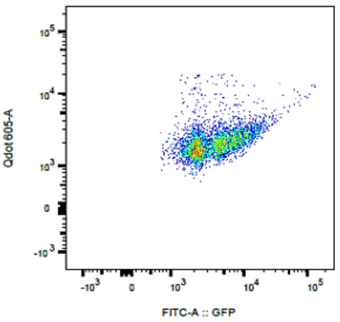

Lactose A1.fcs
dragon green alive and positive
5027

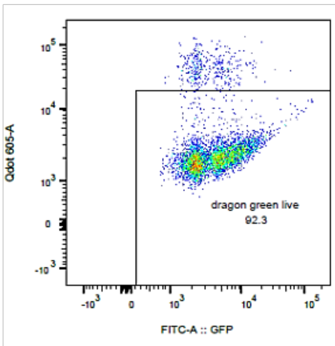

Lactose A1.fcs
dragon green positive
5438

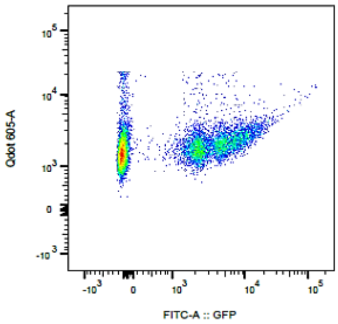

Lactose A1.fcs
live
10290

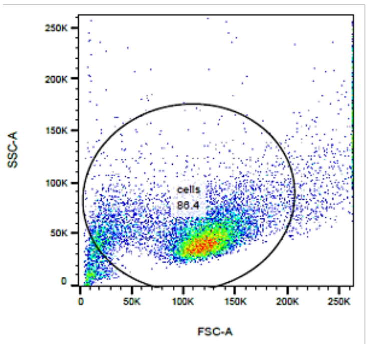

Lactose A2.fcs
Ungated
14644

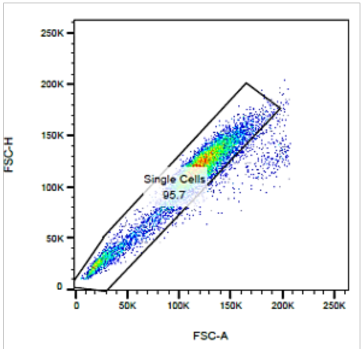

Lactose A2.fcs
cells
12649

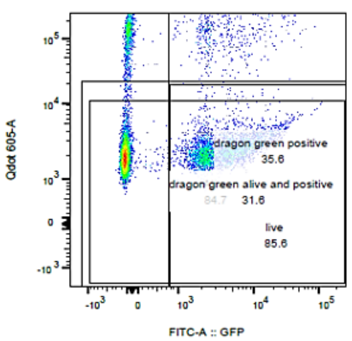

Lactose A2.fcs
Single Cells
12105

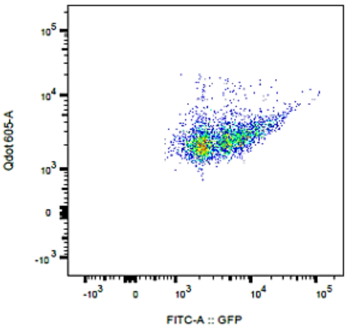

Lactose A2.fcs
dragon green alive and positive
3830

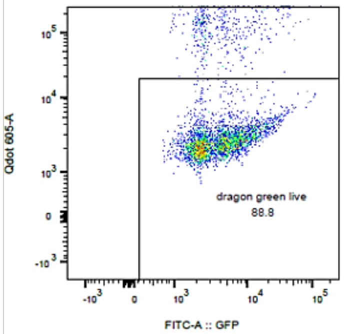

Lactose A2.fcs
dragon green positive
4315

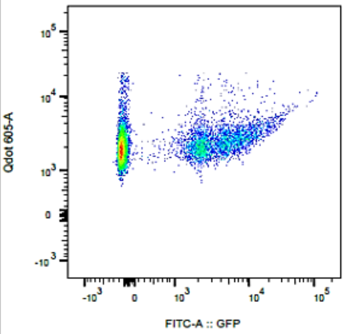

Lactose A2.fcs
live
10367

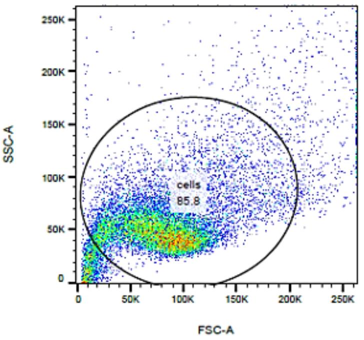

Lactose A3.fcs
Ungated
16486

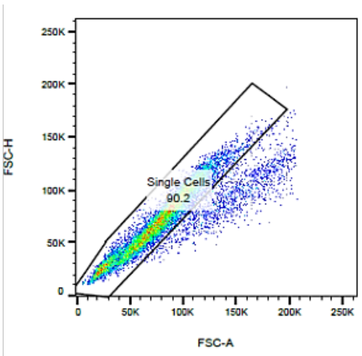

Lactose A3.fcs
cells
14145

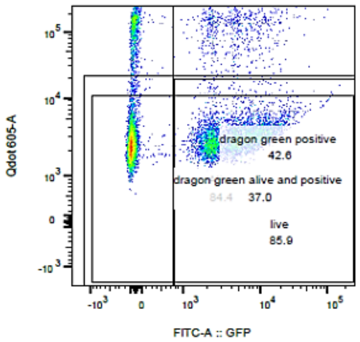

Lactose A3.fcs
Single Cells
12757

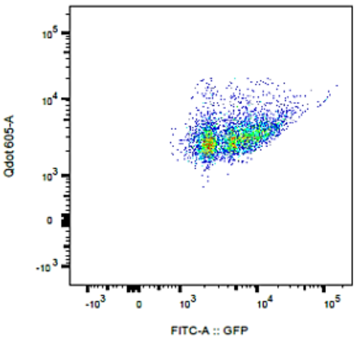

Lactose A3.fcs
dragon green alive and positive
4720

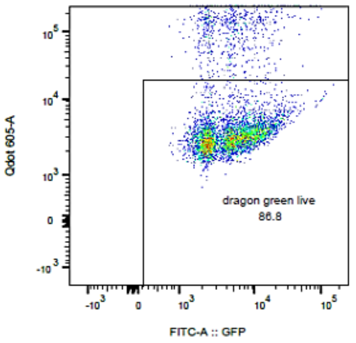

Lactose A3.fcs
dragon green positive
5429

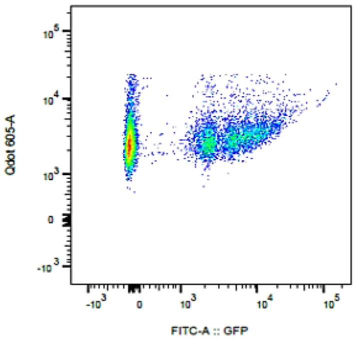

Lactose A3.fcs
live
10954

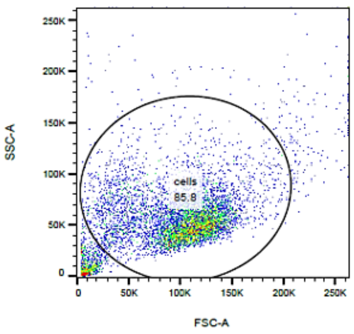

Acid A1.fcs
Ungated
7606

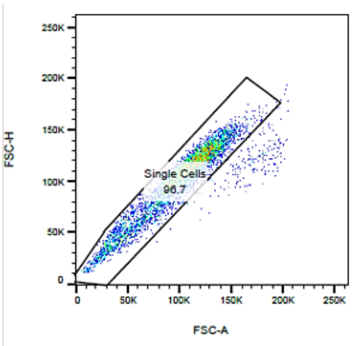

Acid A1.fcs
cells
6527

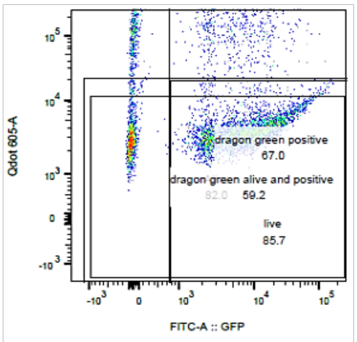

Acid A1.fcs
Single Cells
6312

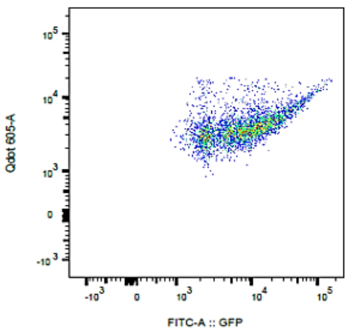

Acid A1.fcs
dragon green alive and positive
3736

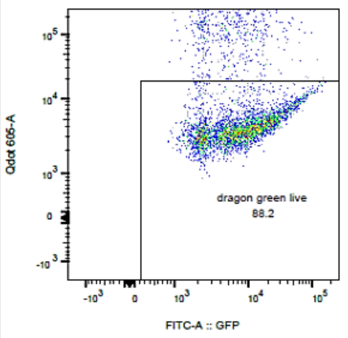

Acid A1.fcs
dragon green positive
4229

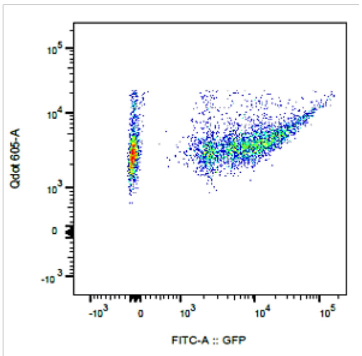

Acid A1.fcs
live
5408

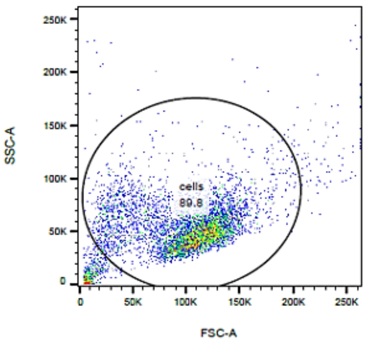

Acid A2.fcs
Ungated
6077

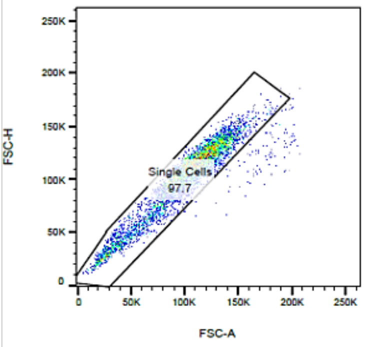

Acid A2.fcs
cells
5455

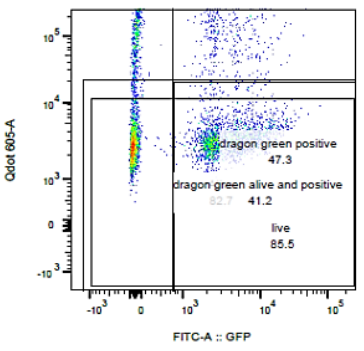

Acid A2.fcs
Single Cells
5329

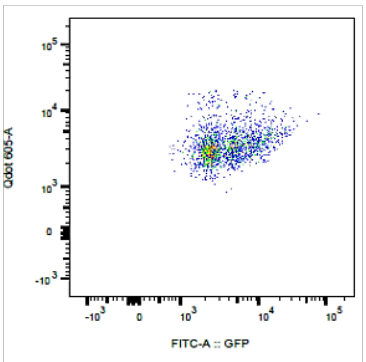

Acid A2.fcs
dragon green alive and positive
2194

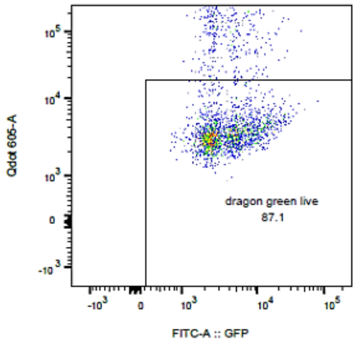

Acid A2.fcs
dragon green positive
2518

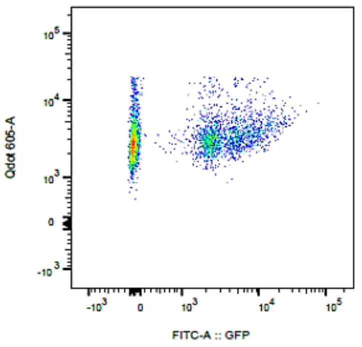

Acid A2.fcs
live
4558

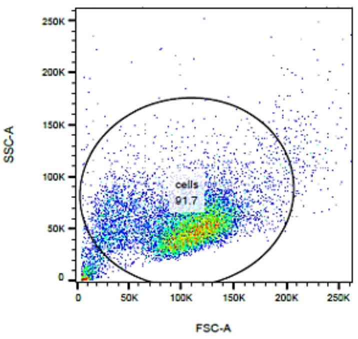

Acid A3.fcs
Ungated
13890

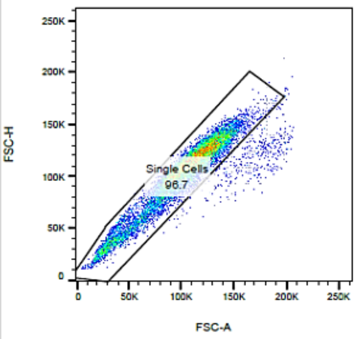

Acid A3.fcs
cells
12736

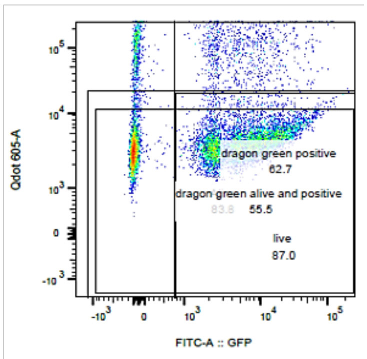

Acid A3.fcs
Single Cells
12319

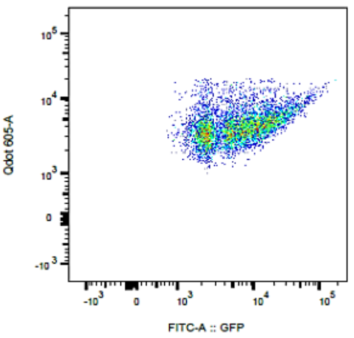

Acid A3.fcs
dragon green alive and positive
6837

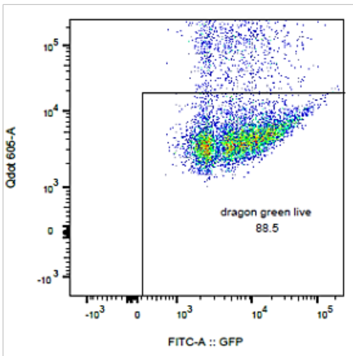

Acid A3.fcs
dragon green positive
7724

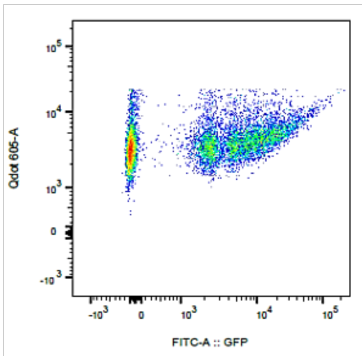

Acid A3.fcs
live
10718

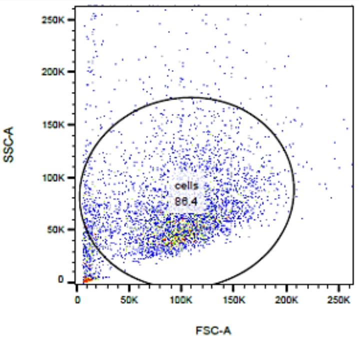

Dextran A1.fcs
Ungated
4808

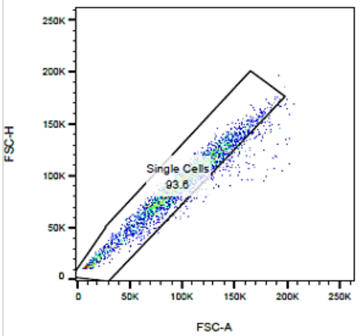

Dextran A1.fcs
cells
4152

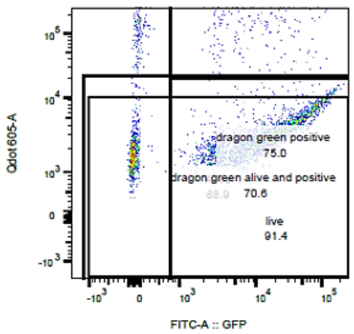

Dextran A1.fcs
Single Cells
3887

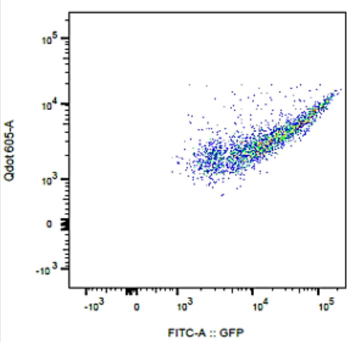

Dextran A1.fcs
dragon green alive and positive
2743

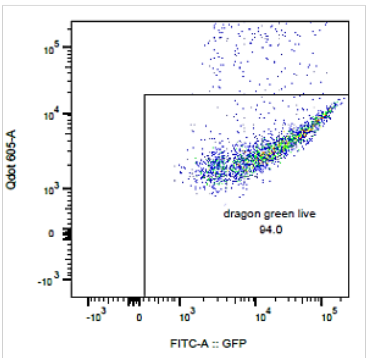

Dextran A1.fcs
dragon green positive
2917

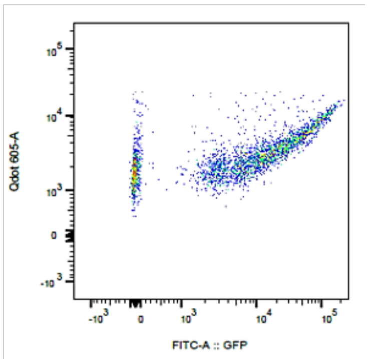

Dextran A1.fcs
live
3552

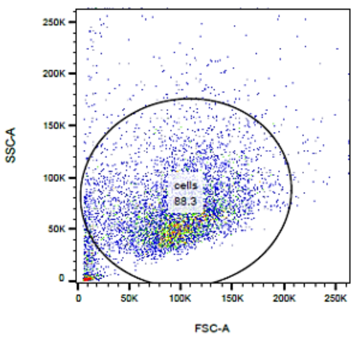

Dextran A2.fcs
Ungated
7114

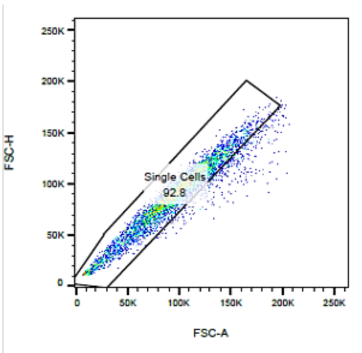

Dextran A2.fcs
cells
6282

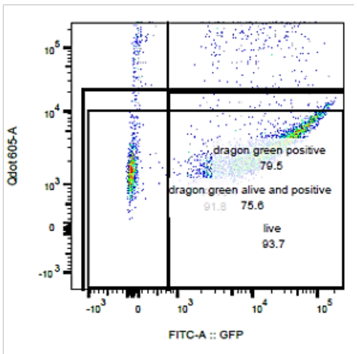

Dextran A2.fcs
Single Cells
5831

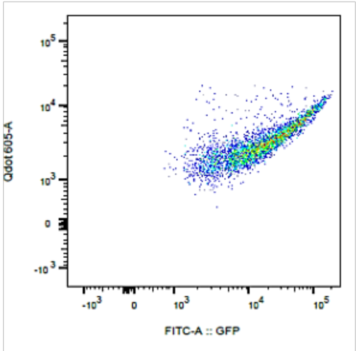

Dextran A2.fcs
dragon green alive and positive
4407

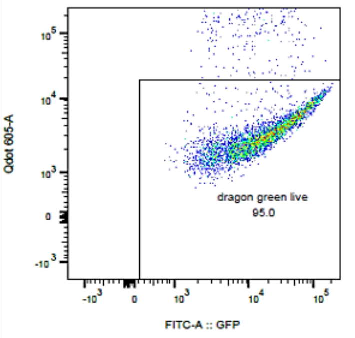

Dextran A2.fcs
dragon green positive
4637

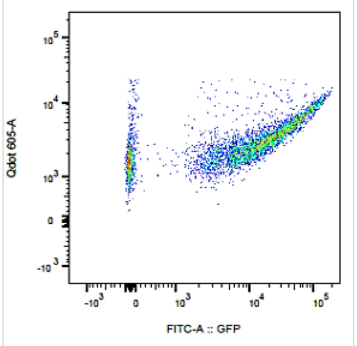

Dextran A2.fcs
live
5463

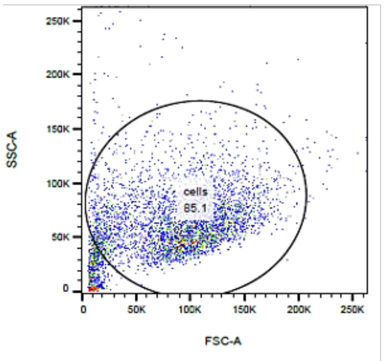

Dextran A3.fcs
Ungated
5262

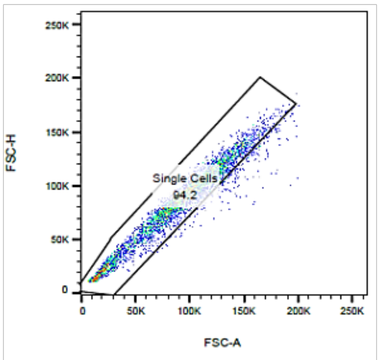

Dextran A3.fcs
cells
4478

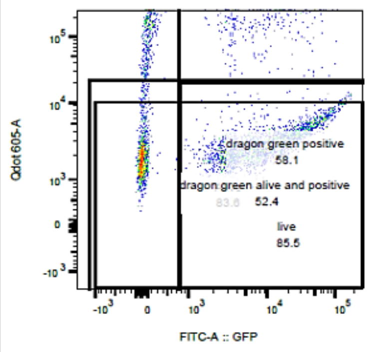

Dextran A3.fcs
Single Cells
4220

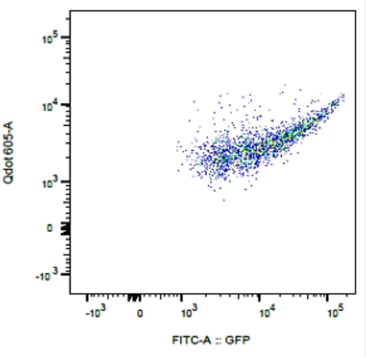

Dextran A3.fcs
dragon green alive and positive
2210

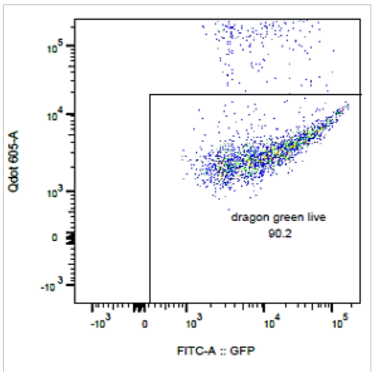

Dextran A3.fcs
dragon green positive
2451

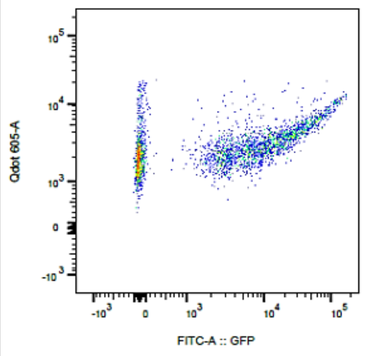

Dextran A3.fcs
live
3606

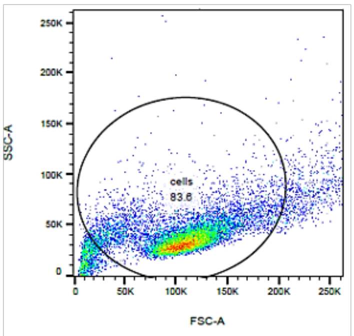

HeLa A1.fcs
Ungated
14643

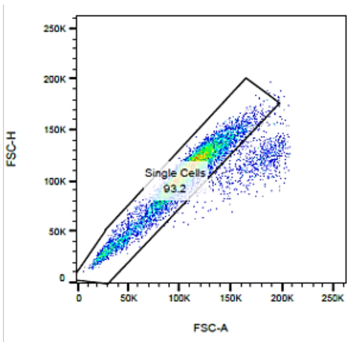

HeLa A1.fcs
cells
12239

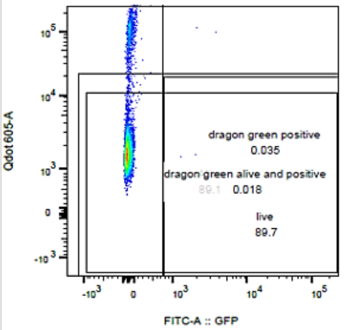

HeLa A1.fcs
Single Cells
11407

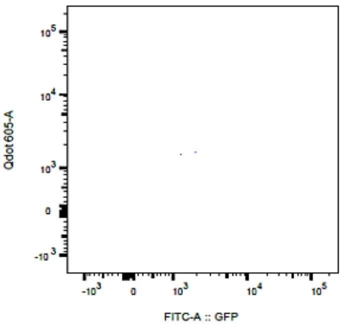

HeLa A1.fcs
dragon green alive and positive
2.00

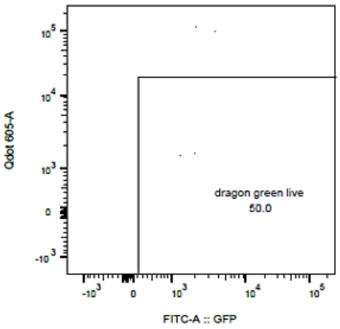

HeLa A1.fcs
dragon green positive
4.00

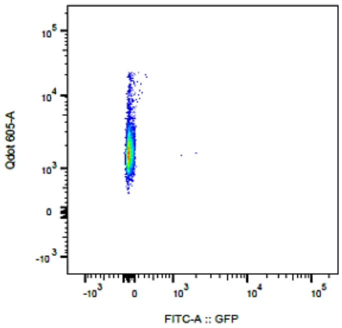

HeLa A1.fcs
live
10237

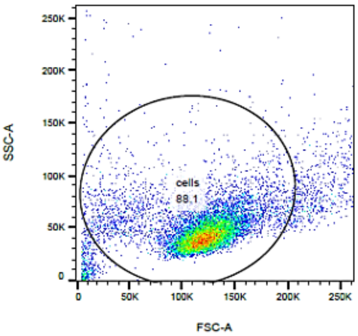

HeLa A2.fcs
Ungated
12978

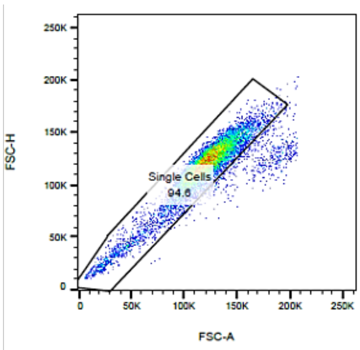

HeLa A2.fcs
cells
11438

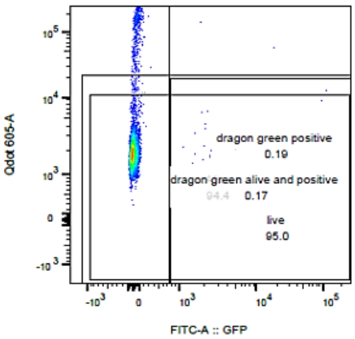

HeLa A2.fcs
Single Cells
10822

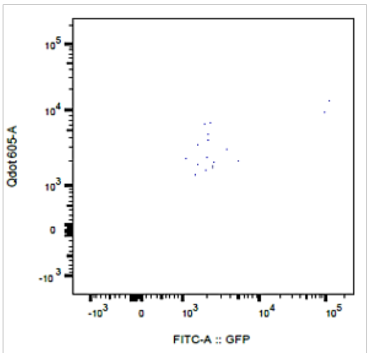

HeLa A2.fcs
dragon green alive and positive
18.0

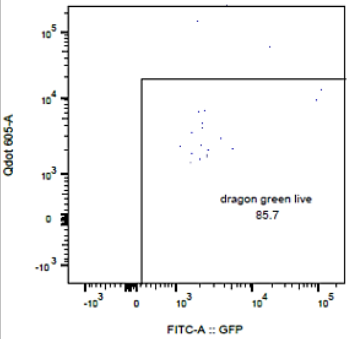

HeLa A2.fcs
dragon green positive
21.0

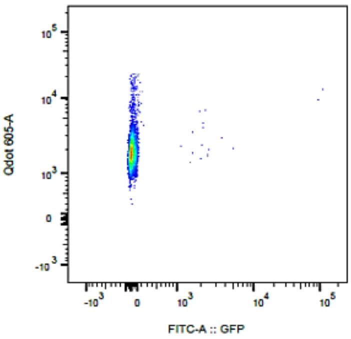

HeLa A2.fcs
live
10277

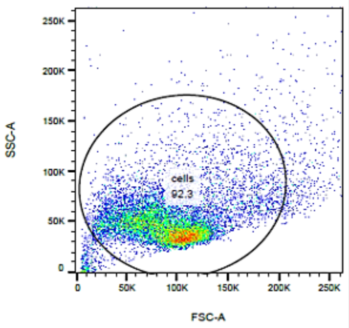

HeLa A3.fcs
Ungated
13863

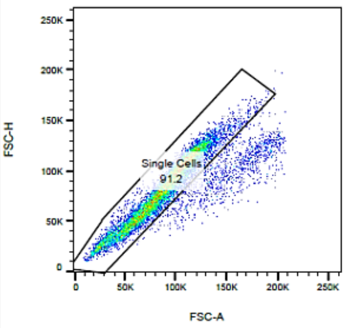

HeLa A3.fcs
cells
12795

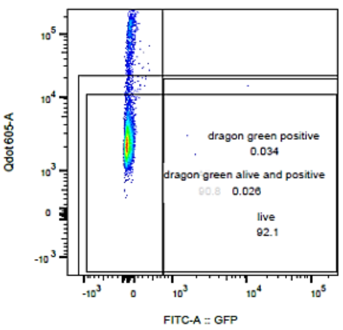

HeLa A3.fcs
Single Cells
11672

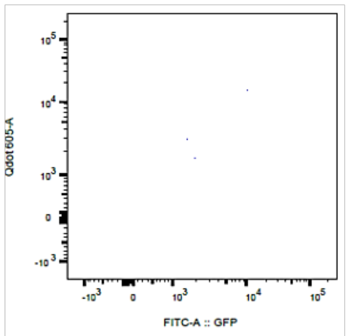

HeLa A3.fcs
dragon green alive and positive
3.00

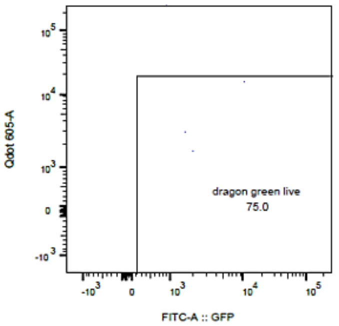

HeLa A3.fcs
dragon green positive
4.00

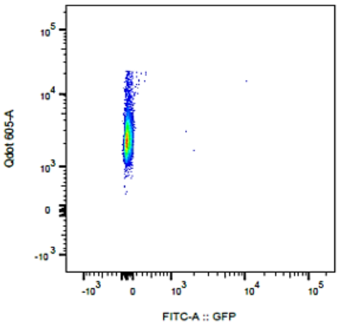

HeLa A3.fcs
live
10755

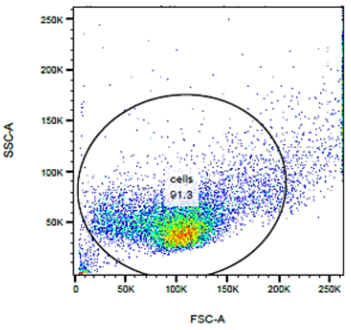

TTDDA BE 1.fcs
Ungated
13318

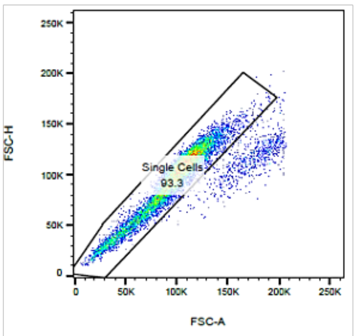

TTDDA BE 1.fcs
cells
12157

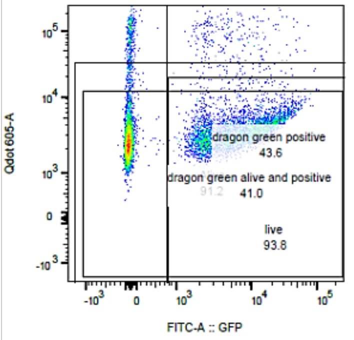

TTDDA BE 1.fcs
Single Cells
11338

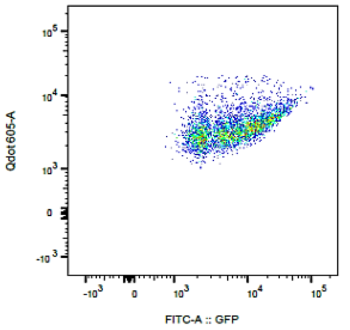

TTDDA BE 1.fcs
dragon green alive and positive
4645

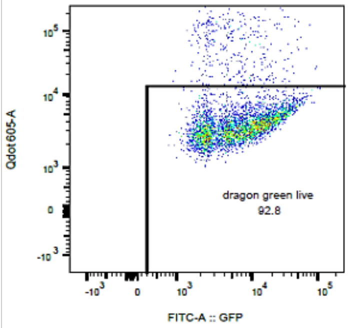

TTDDA BE 1.fcs
dragon green positive
4944

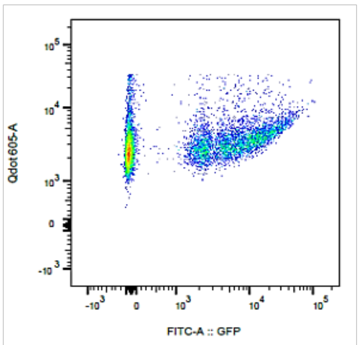

TTDDA BE 1.fcs
live
10634

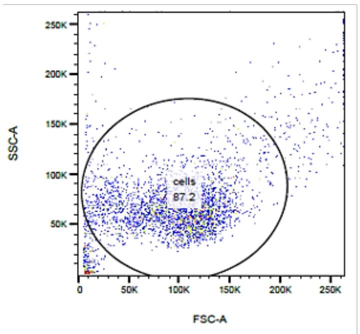

TTDDA BE 2.fcs

Ungated
3919

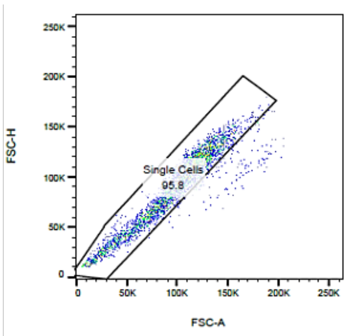

TTDDA BE 2.fcs

cells
3418

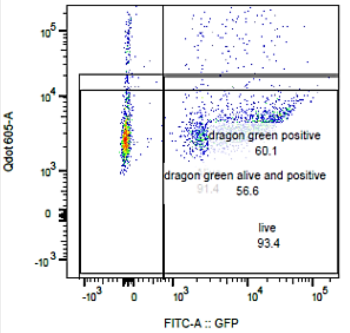

TTDDA BE 2.fcs

Single Cells
3274

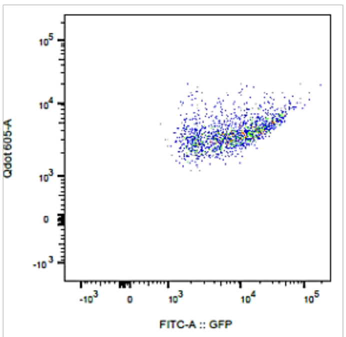

TTDDA BE 2.fcs

dragon green alive and positive
1854

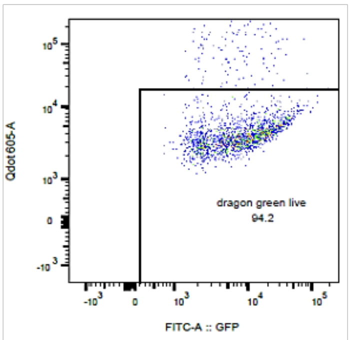

TTDDA BE 2.fcs

dragon green positive
1969

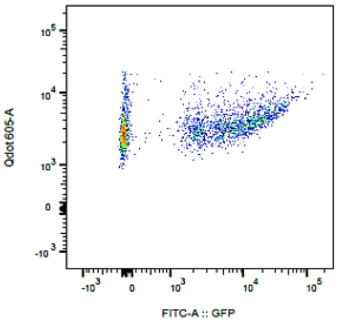

TTDDA BE 2.fcs

live
3057

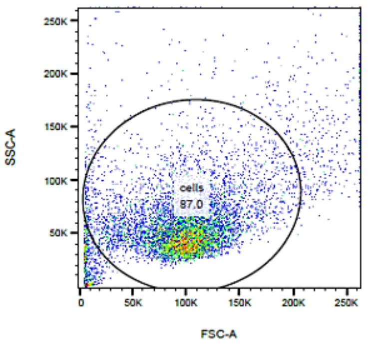

TTDDA BE 3.fcs

Ungated
9283

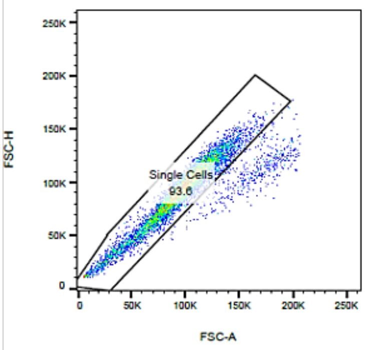

TTDDA BE 3.fcs

cells
8075

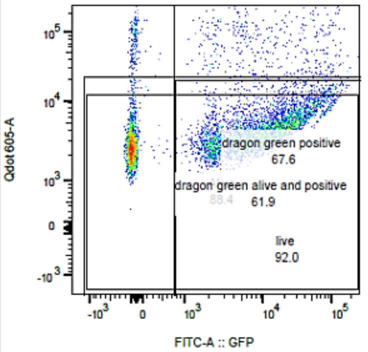

TTDDA BE 3.fcs

Single Cells
7556

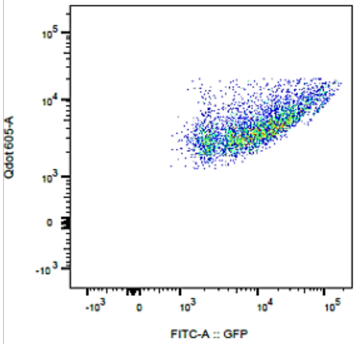

TTDDA BE 3.fcs

dragon green alive and positive
4676

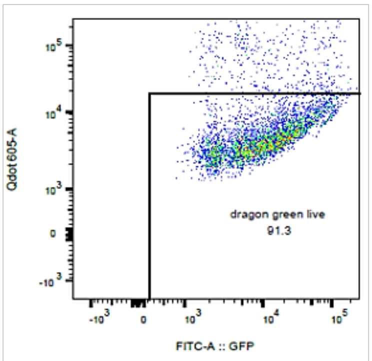

TTDDA BE 3.fcs

dragon green positive
5107

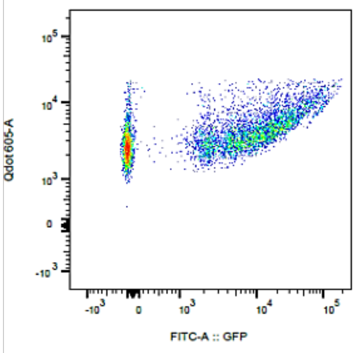

TTDDA BE 3.fcs

live
6952

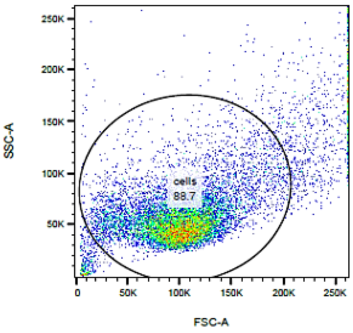

Lactose BE 1.fcs

Ungated
13935

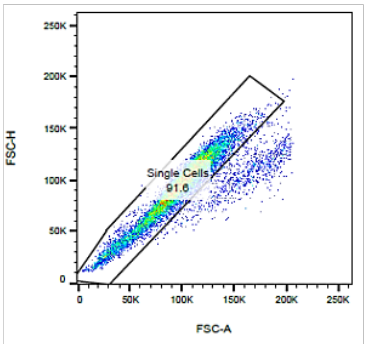

Lactose BE 1.fcs

cells
12366

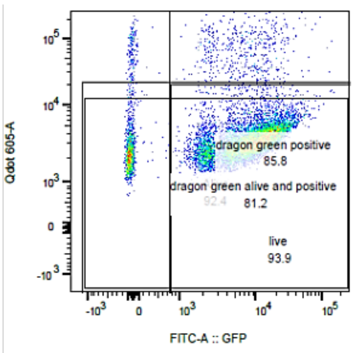

Lactose BE 1.fcs

Single Cells
11329

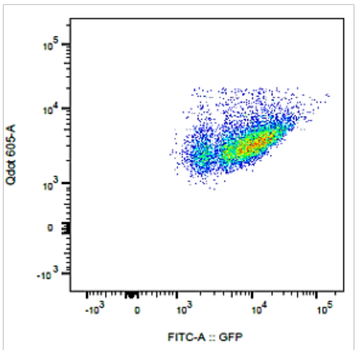

Lactose BE 1.fcs

dragon green alive and positive
9198

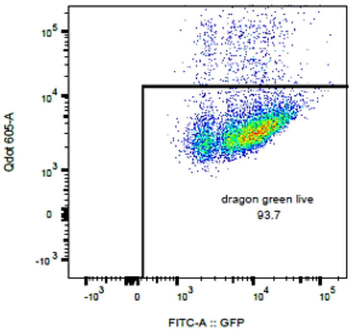

Lactose BE 1.fcs

dragon green positive
9721

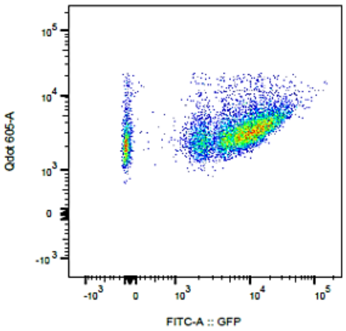

Lactose BE 1.fcs

live
10640

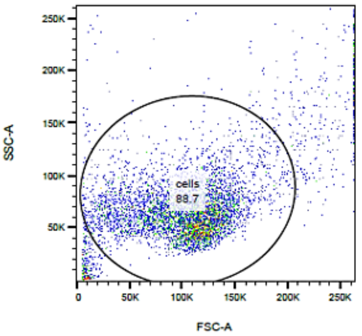

Lactose BE 2.fcs

Ungated
6348

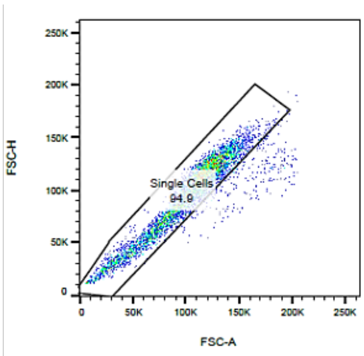

Lactose BE 2.fcs

cells
5628

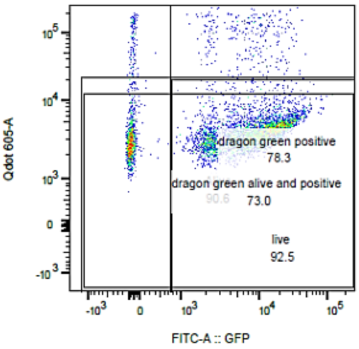

Lactose BE 2.fcs

Single Cells
5340

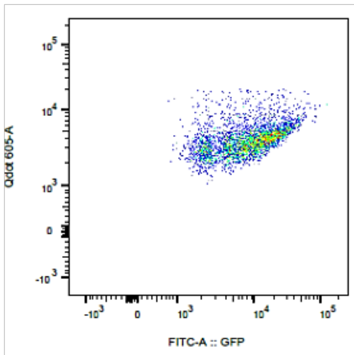

Lactose BE 2.fcs

dragon green alive and positive
3896

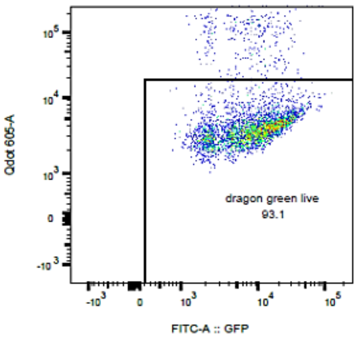

Lactose BE 2.fcs

dragon green positive
4180

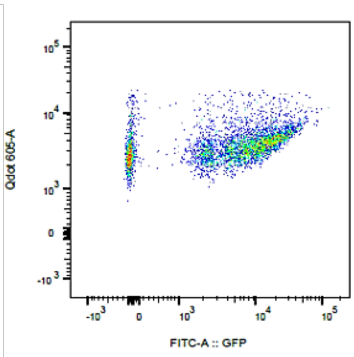

Lactose BE 2.fcs

live
4940

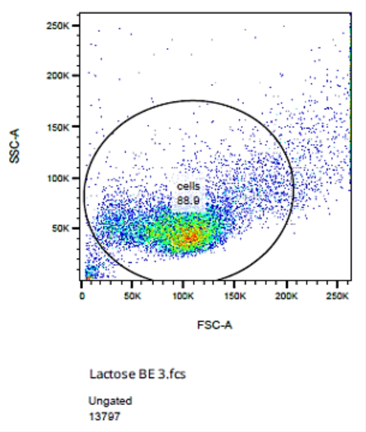

Lactose BE 3.fcs

Ungated
13797

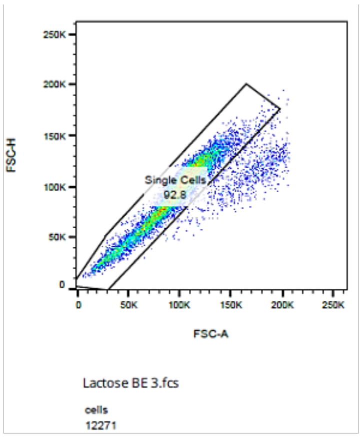

Lactose BE 3.fcs

cells
12271

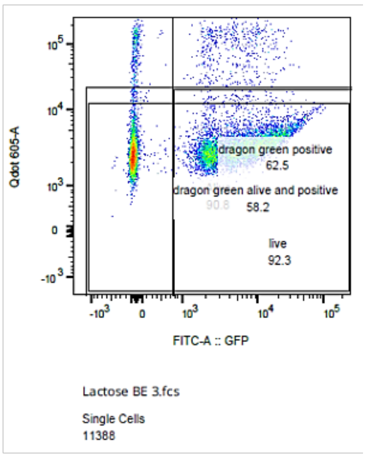

Lactose BE 3.fcs

Single Cells
11388

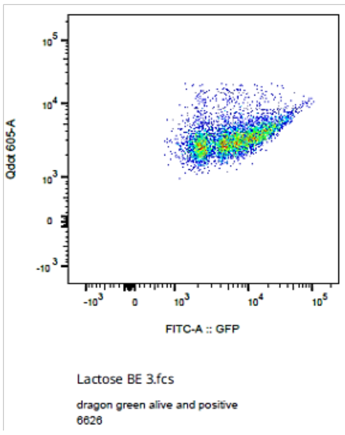

Lactose BE 3.fcs

dragon green alive and positive
6626

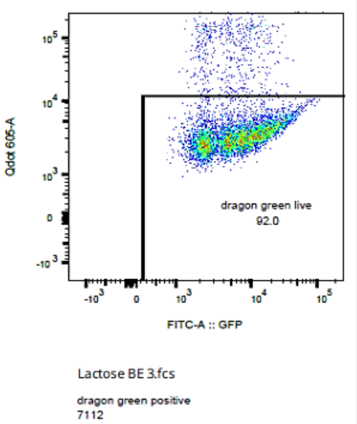

Lactose BE 3.fcs

dragon green positive
7112

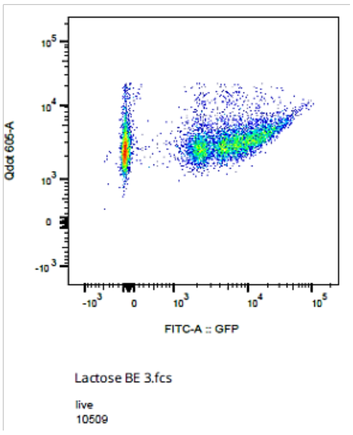

Lactose BE 3.fcs

live
10509

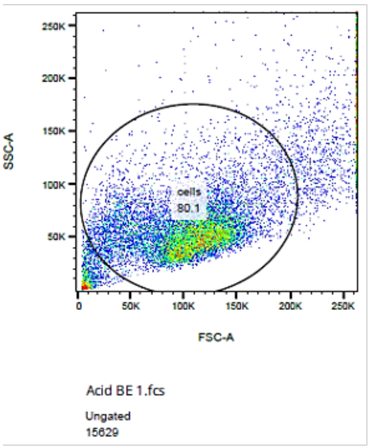

Acid BE 1.fcs

Ungated
15629

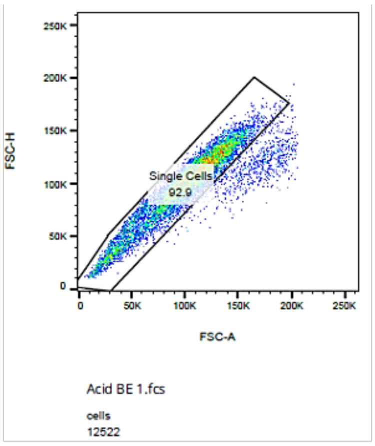

Acid BE 1.fcs

cells
12522

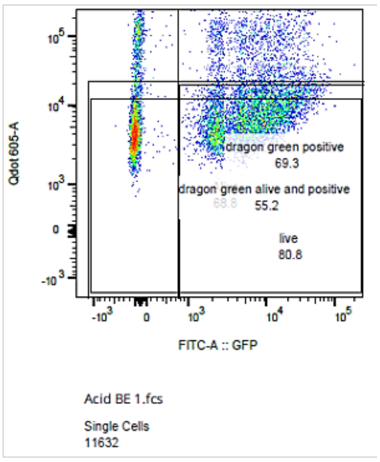

Acid BE 1.fcs

Single Cells
11632

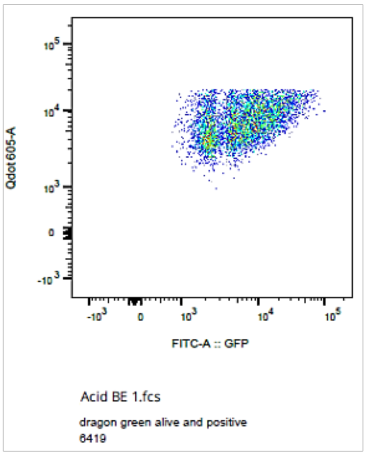

Acid BE 1.fcs

dragon green alive and positive
6419

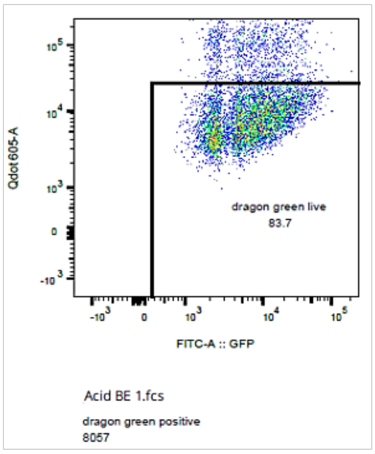

Acid BE 1.fcs

dragon green positive
8057

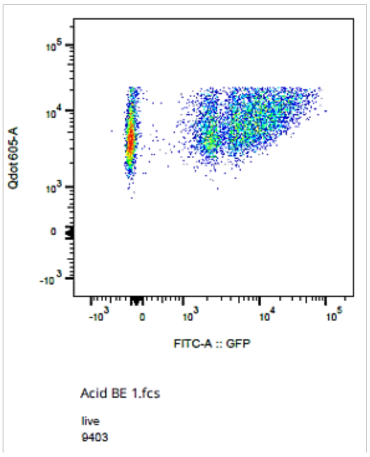

Acid BE 1.fcs

live
9403

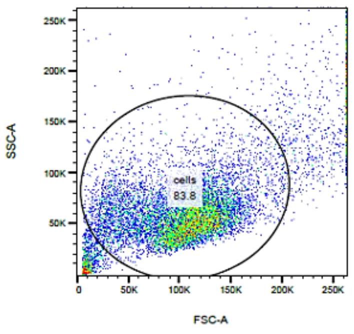

Acid BE 2.fcs

Ungated
13661

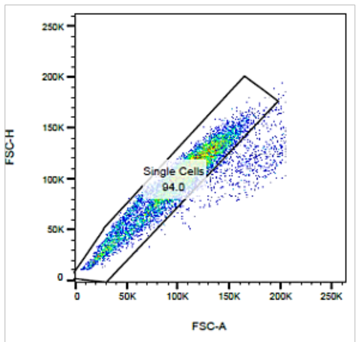

Acid BE 2.fcs

cells
11444

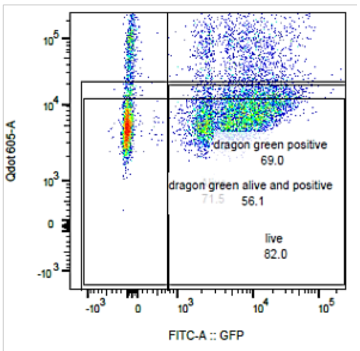

Acid BE 2.fcs

Single Cells
10759

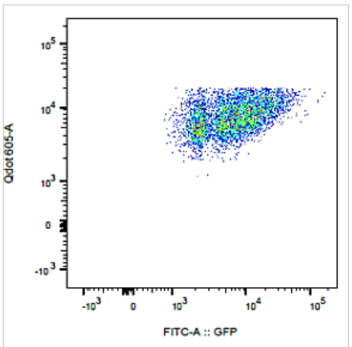

Acid BE 2.fcs

dragon green alive and positive
6039

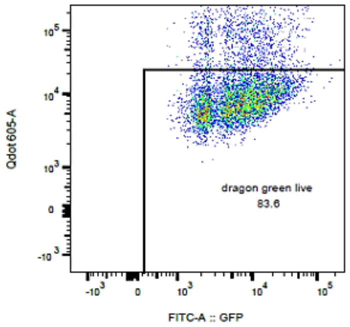

Acid BE 2.fcs

dragon green positive
7429

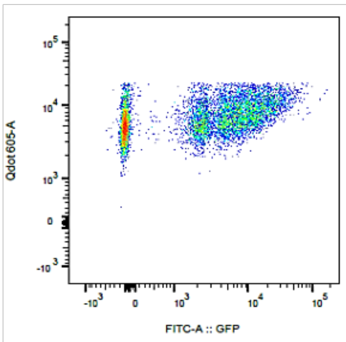

Acid BE 2.fcs

live
8826

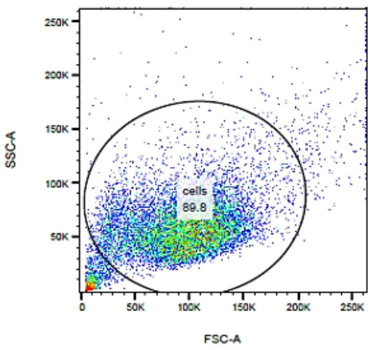

Acid BE 3.fcs

Ungated
14760

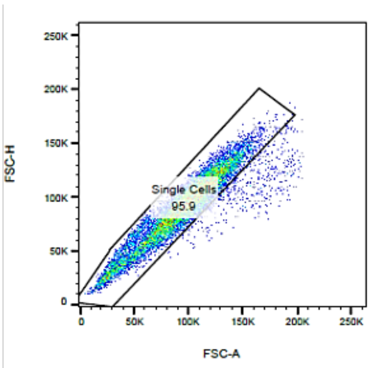

Acid BE 3.fcs

cells
13252

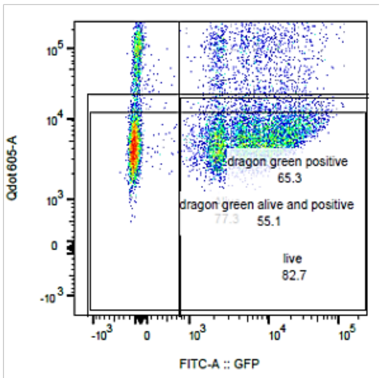

Acid BE 3.fcs

Single Cells
12711

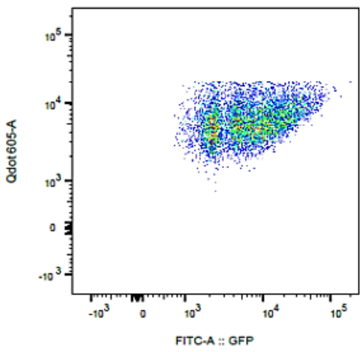

Acid BE 3.fcs

dragon green alive and positive
7008

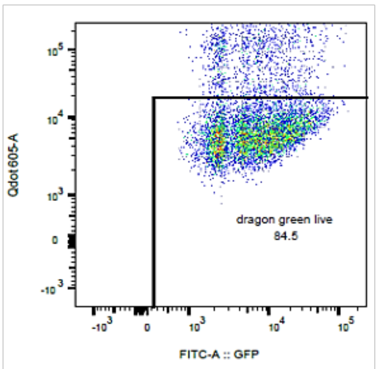

Acid BE 3.fcs

dragon green positive
8300

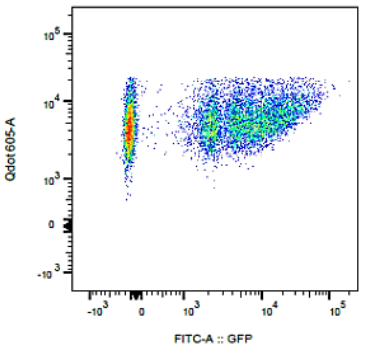

Acid BE 3.fcs

live
10510

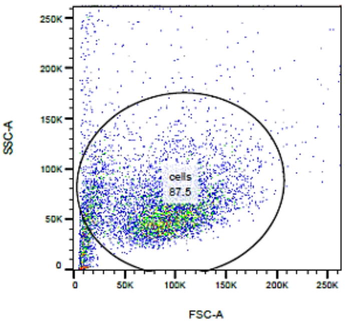

Dextran BE 1.fcs
Ungated
7317

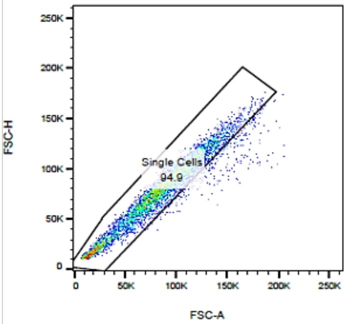

Dextran BE 1.fcs
cells
6399

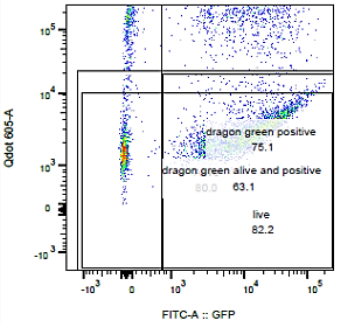

Dextran BE 1.fcs
Single Cells
6075

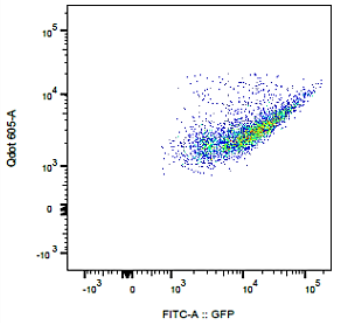

Dextran BE 1.fcs
dragon green alive and positive
3834

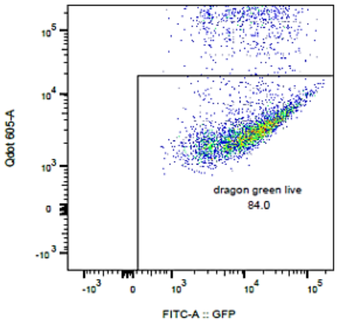

Dextran BE 1.fcs
dragon green positive
4562

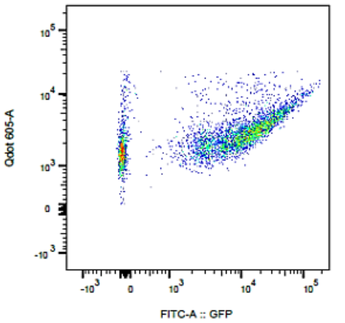

Dextran BE 1.fcs
live
4994

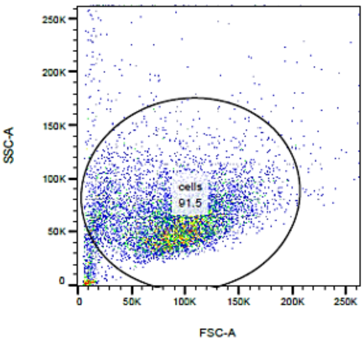

Dextran BE 2.fcs
Ungated
8468

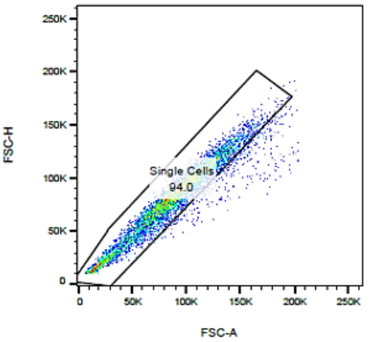

Dextran BE 2.fcs
cells
7748

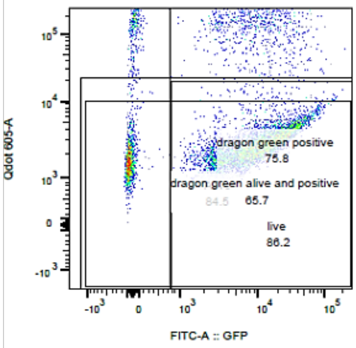

Dextran BE 2.fcs
Single Cells
7282

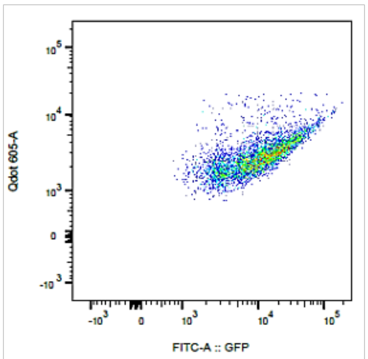

Dextran BE 2.fcs
dragon green alive and positive
4781

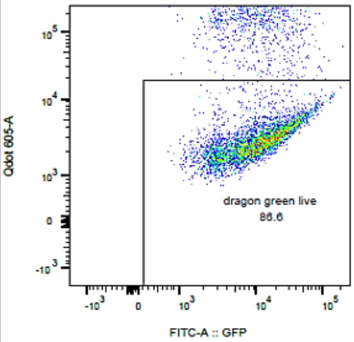

Dextran BE 2.fcs
dragon green positive
5522

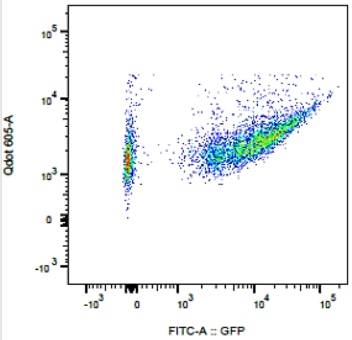

Dextran BE 2.fcs
live
6275

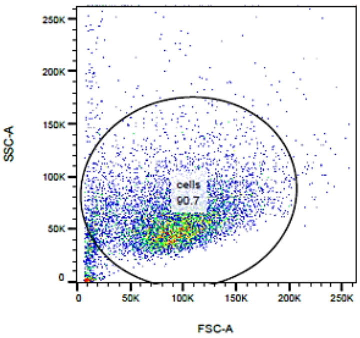

Dextran BE 3.fcs
Ungated
9188

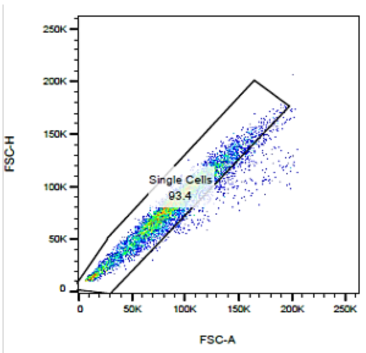

Dextran BE 3.fcs
cells
8335

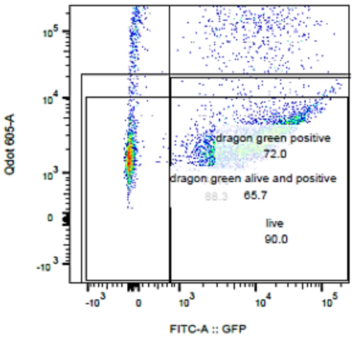

Dextran BE 3.fcs
Single Cells
7781

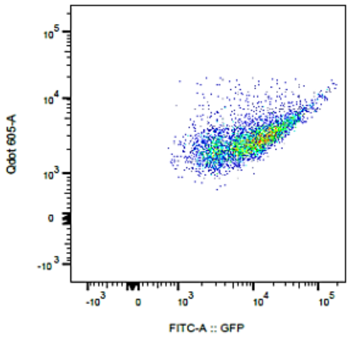

Dextran BE 3.fcs
dragon green alive and positive
5115

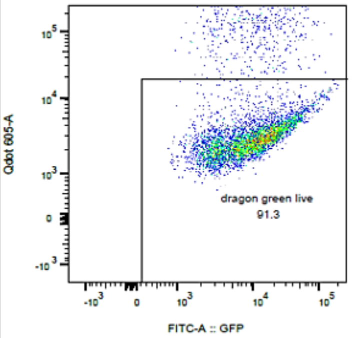

Dextran BE 3.fcs
dragon green positive
5599

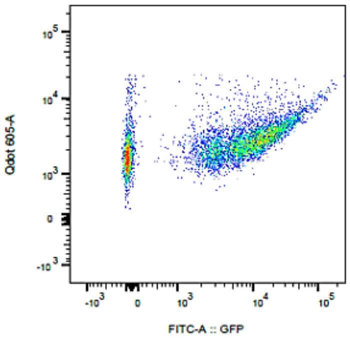

Dextran BE 3.fcs
live
7000

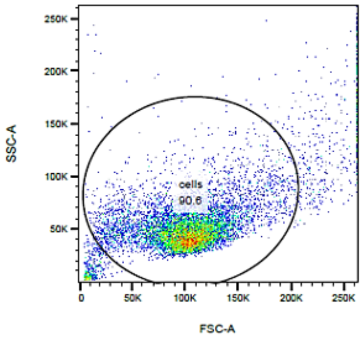

HeLa BE 1.fcs
Ungated
10405

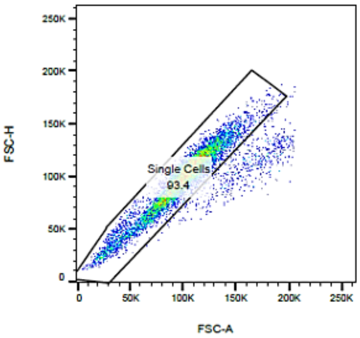

HeLa BE 1.fcs
cells
9425

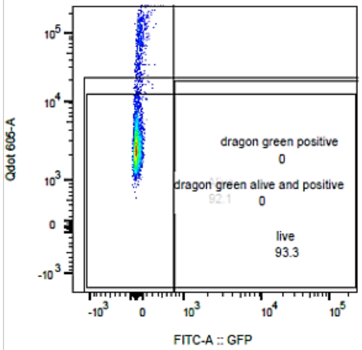

HeLa BE 1.fcs
Single Cells
8804

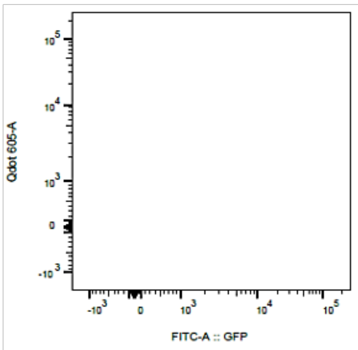

HeLa BE 1.fcs
dragon green alive and positive
0

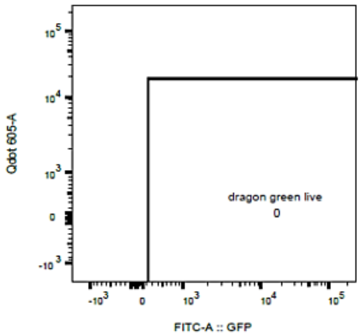

HeLa BE 1.fcs
dragon green positive
0

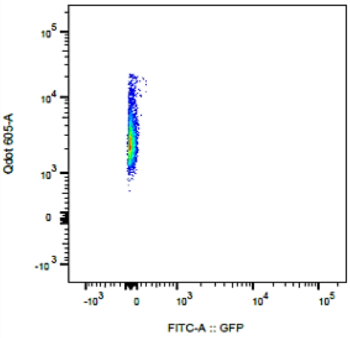

HeLa BE 1.fcs
live
8211

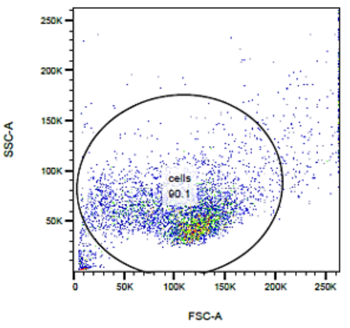

HeLa BE 2.fcs
Ungated
5480

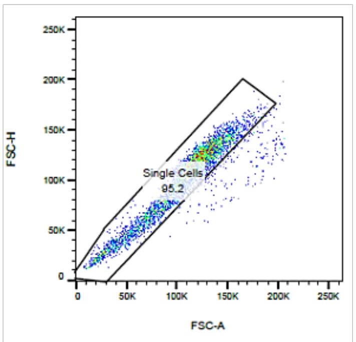

HeLa BE 2.fcs
cells
4939

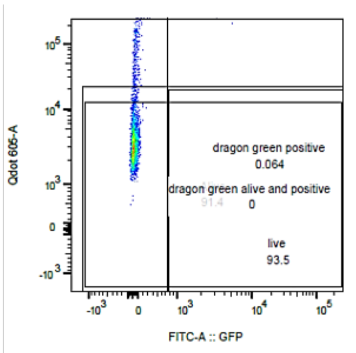

HeLa BE 2.fcs
Single Cells
4704

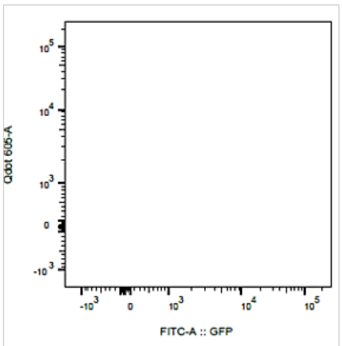

HeLa BE 2.fcs
dragon green alive and positive
0

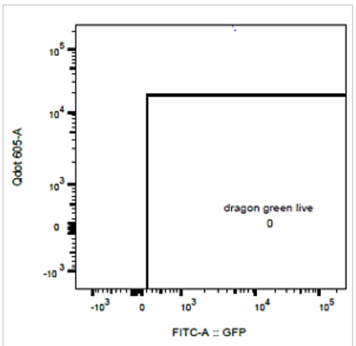

HeLa BE 2.fcs
dragon green positive
3.00

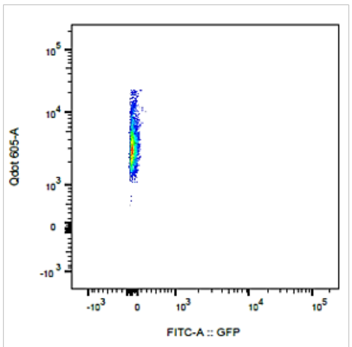

HeLa BE 2.fcs
live
4399

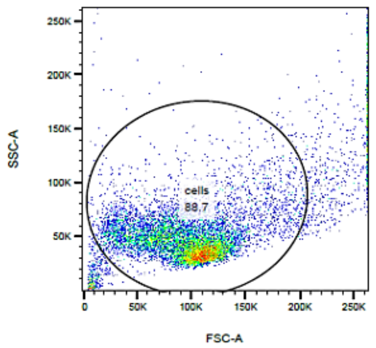

HeLa BE 3.fcs
Ungated
11225

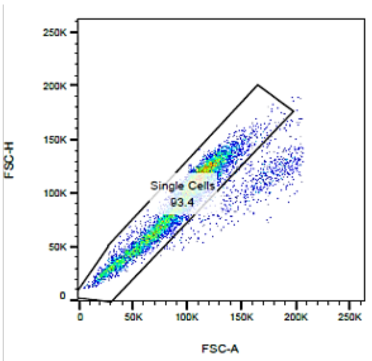

HeLa BE 3.fcs
cells
9959

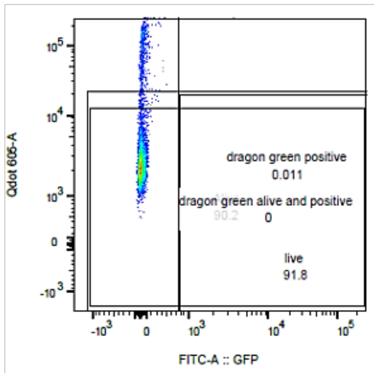

HeLa BE 3.fcs
Single Cells
9299

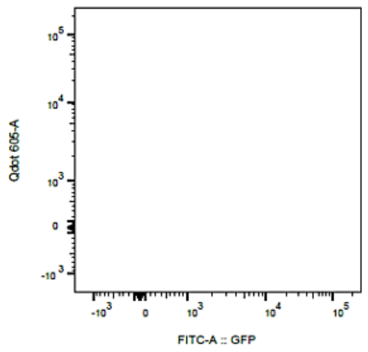

HeLa BE 3.fcs
dragon green alive and positive
0

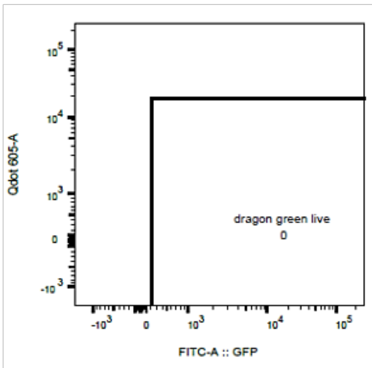

HeLa BE 3.fcs
dragon green positive
1.00

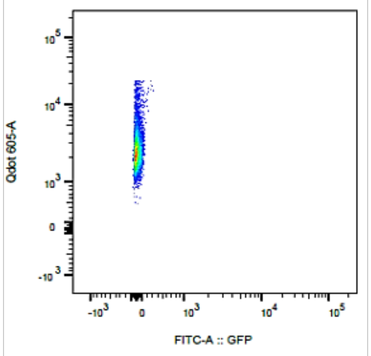

HeLa BE 3.fcs
live
8537

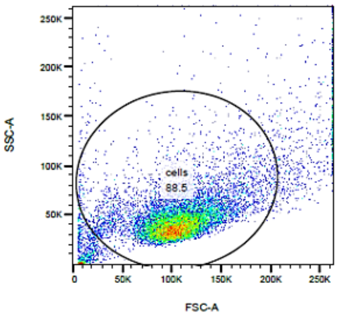

TTDDA Inh A1.fcs
Ungated
13513

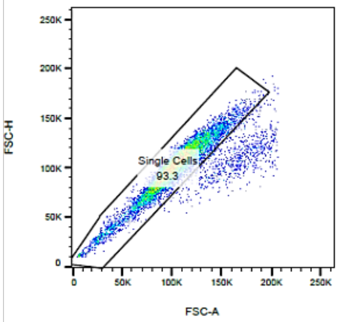

TTDDA Inh A1.fcs
cells
11958

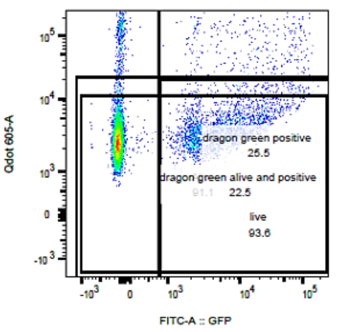

TTDDA Inh A1.fcs
Single Cells
11161

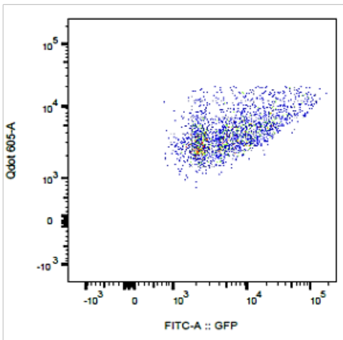

TTDDA Inh A1.fcs
dragon green alive and positive
2506

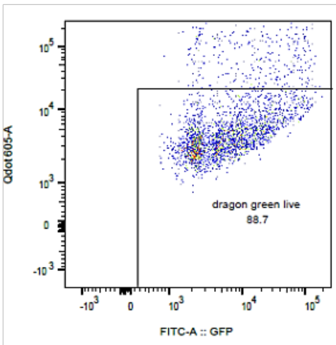

TTDDA Inh A1.fcs
dragon green positive
2843

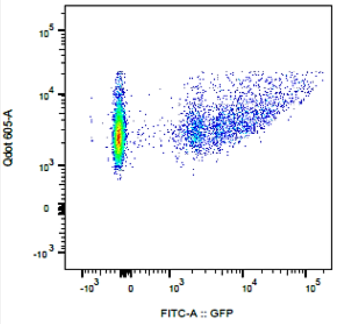

TTDDA Inh A1.fcs
live
10451

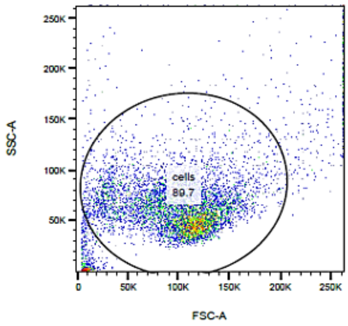

TTDDA Inh A2.fcs
Ungated
7656

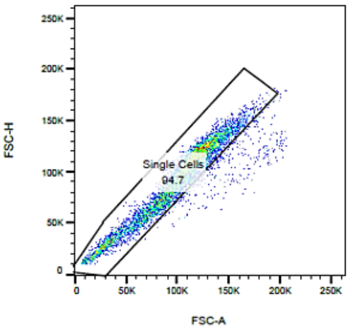

TTDDA Inh A2.fcs
cells
6870

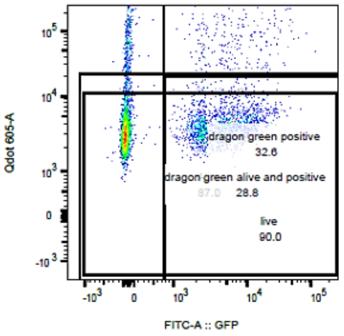

TTDDA Inh A2.fcs
Single Cells
6504

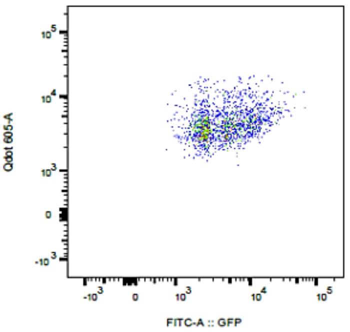

TTDDA Inh A2.fcs
dragon green alive and positive
1875

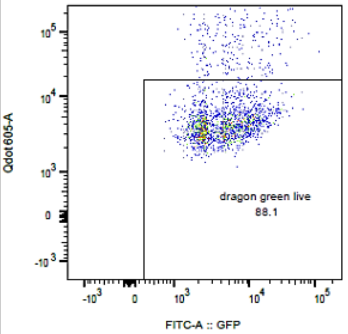

TTDDA Inh A2.fcs
dragon green positive
2122

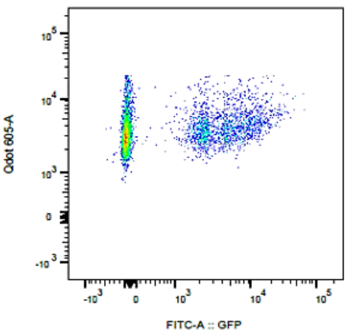

TTDDA Inh A2.fcs
live
5855

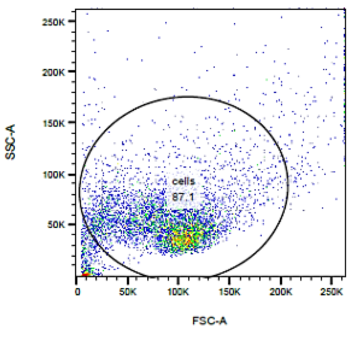

TTDDA Inh A3.fcs
Ungated
6928

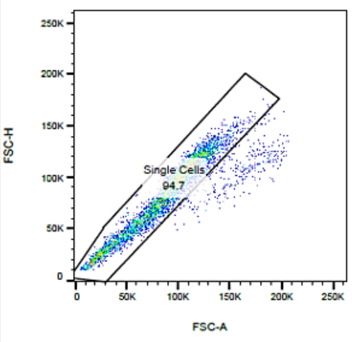

TTDDA Inh A3.fcs
cells
6032

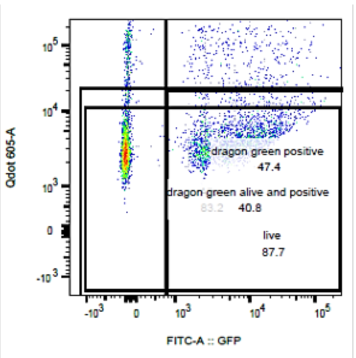

TTDDA Inh A3.fcs
Single Cells
5711

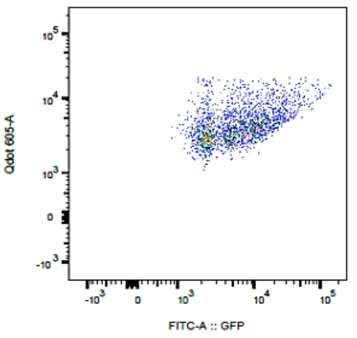

TTDDA Inh A3.fcs
dragon green alive and positive
2328

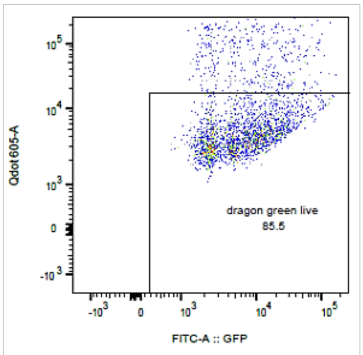

TTDDA Inh A3.fcs
dragon green positive
2708

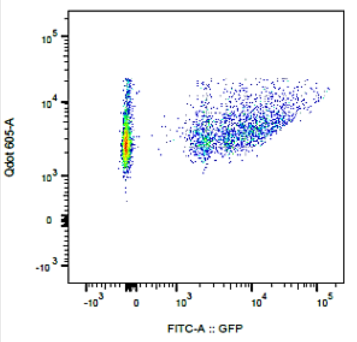

TTDDA Inh A3.fcs
live
5007

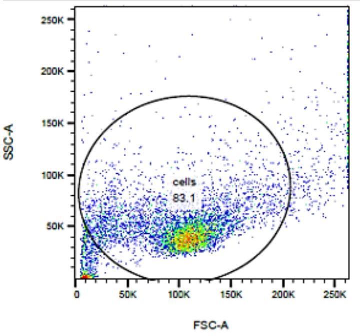

Lactose Inh A1.fcs
Ungated
8247

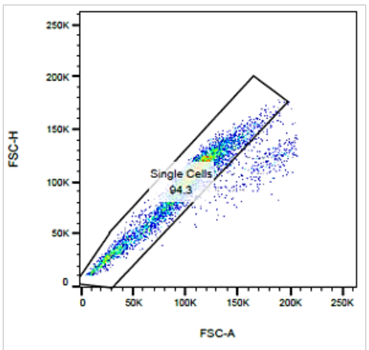

Lactose Inh A1.fcs
cells
6854

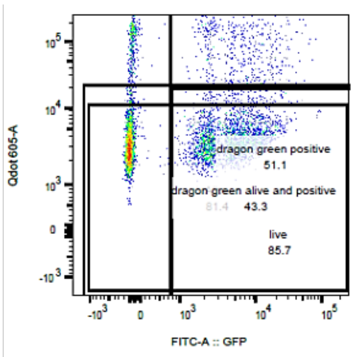

Lactose Inh A1.fcs
Single Cells
6463

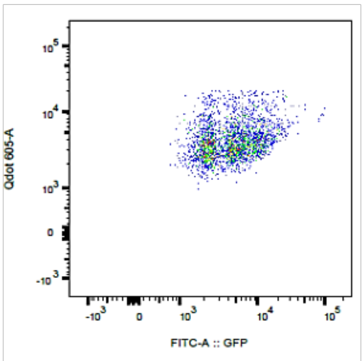

Lactose Inh A1.fcs
dragon green alive and positive
2796

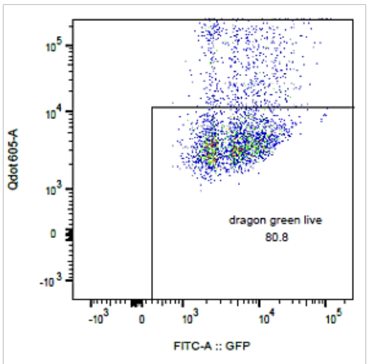

Lactose Inh A1.fcs
dragon green positive
3300

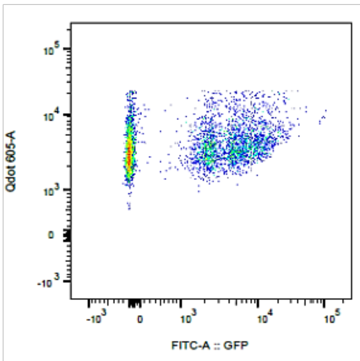

Lactose Inh A1.fcs
live
5539

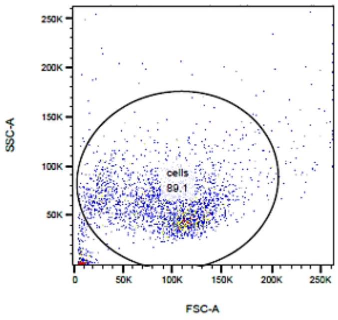

Lactose Inh A2.fcs
Ungated
3158

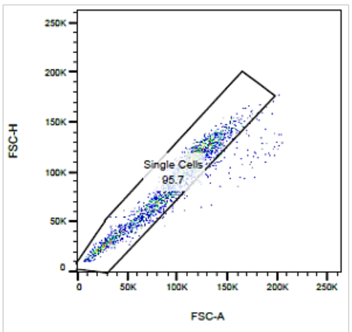

Lactose Inh A2.fcs
cells
2814

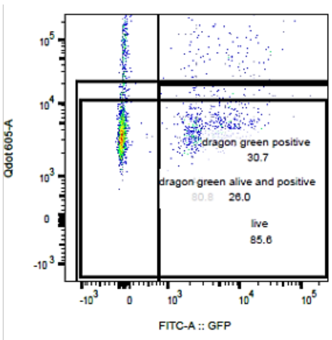

Lactose Inh A2.fcs
Single Cells
2693

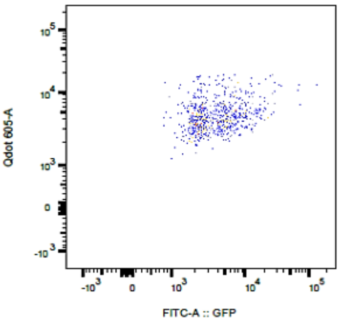

Lactose Inh A2.fcs
dragon green alive and positive
699

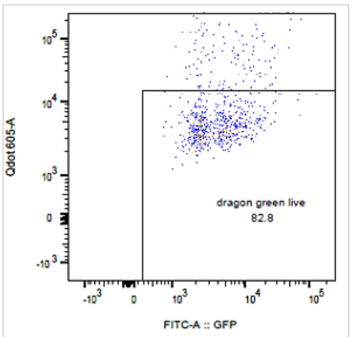

Lactose Inh A2.fcs
dragon green positive
826

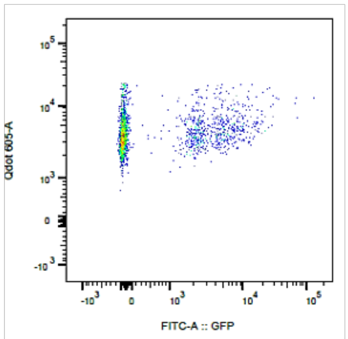

Lactose Inh A2.fcs
live
2306

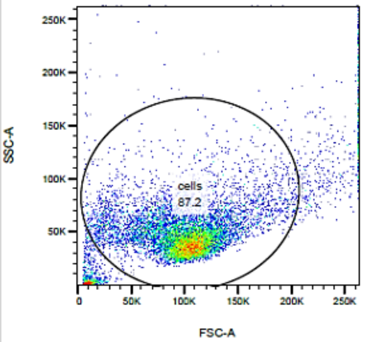

Lactose Inh A3.fcs
Ungated
12251

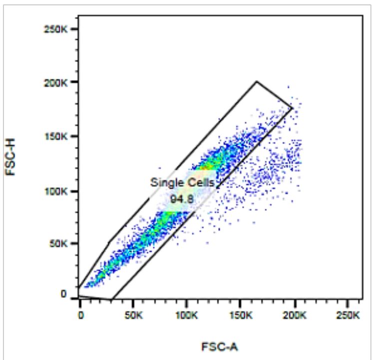

Lactose Inh A3.fcs
cells
10677

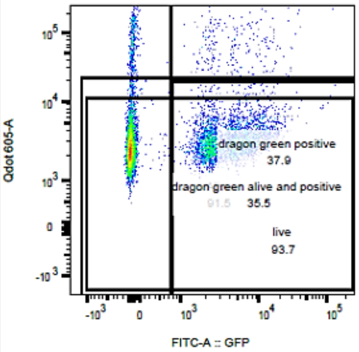

Lactose Inh A3.fcs
Single Cells
10119

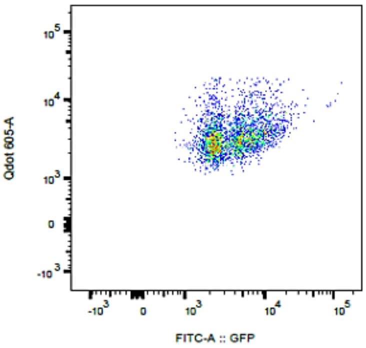

Lactose Inh A3.fcs
dragon green alive and positive
3594

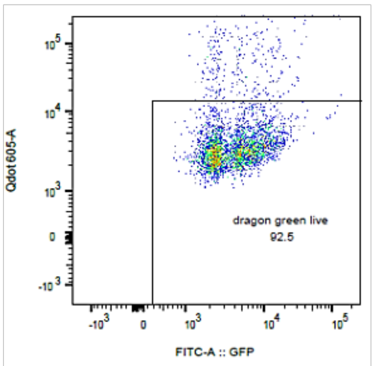

Lactose Inh A3.fcs
dragon green positive
3840

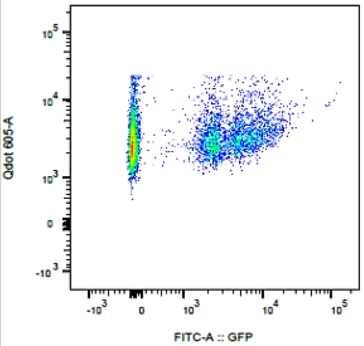

Lactose Inh A3.fcs
live
9481

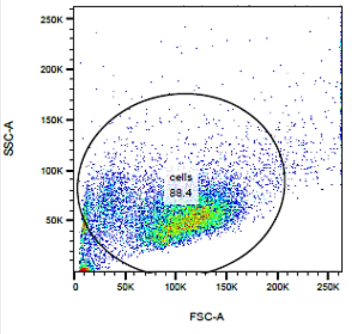

Acid Inh A1.fcs
Ungated
14933

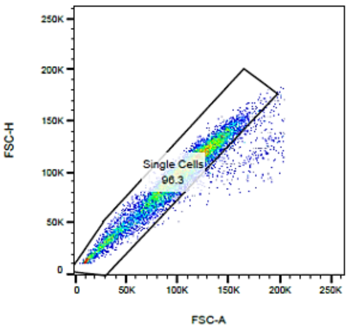

Acid Inh A1.fcs
cells
13202

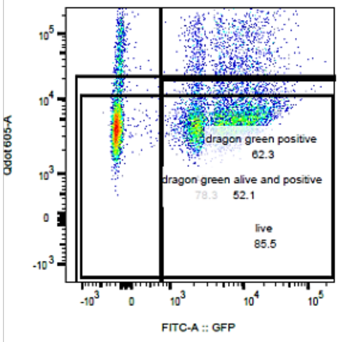

Acid Inh A1.fcs
Single Cells
12715

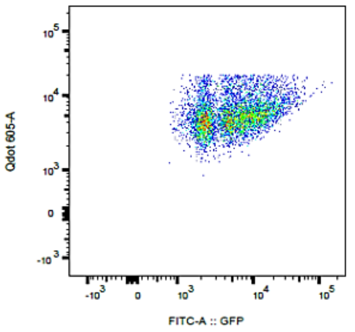

Acid Inh A1.fcs
dragon green alive and positive
6623

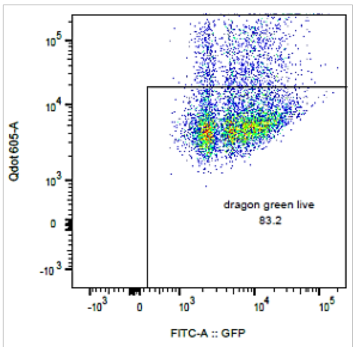

Acid Inh A1.fcs
dragon green positive
7927

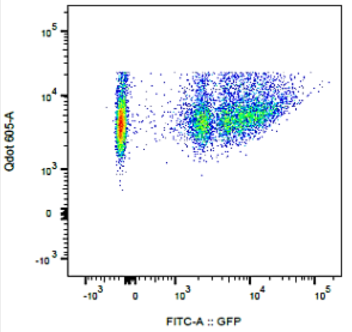

Acid Inh A1.fcs
live
10871

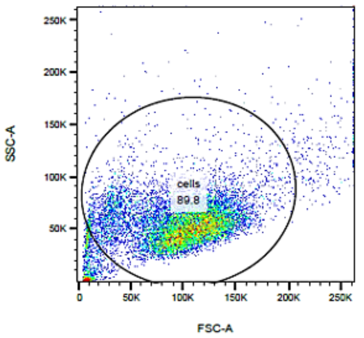

Acid Inh A2.fcs
Ungated
13918

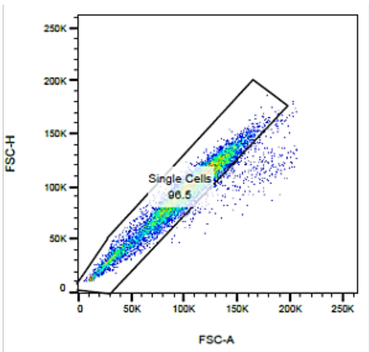

Acid Inh A2.fcs
cells
12498

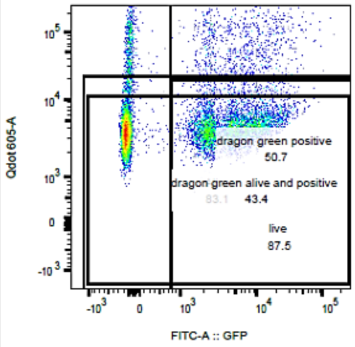

Acid Inh A2.fcs
Single Cells
12060

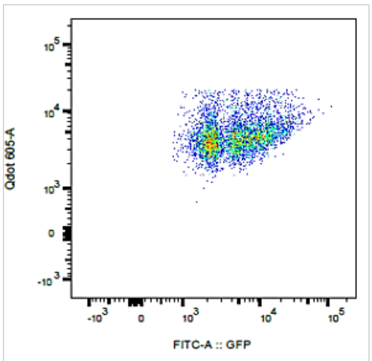

Acid Inh A2.fcs
dragon green alive and positive
5229

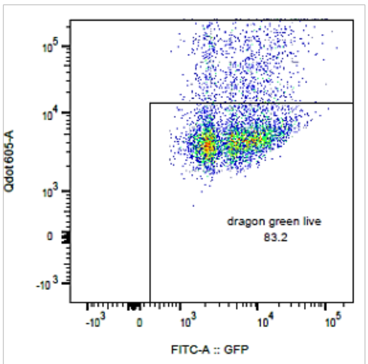

Acid Inh A2.fcs
dragon green positive
6120

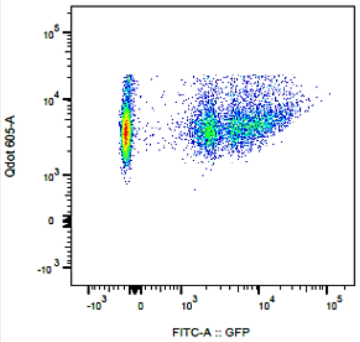

Acid Inh A2.fcs
live
10551

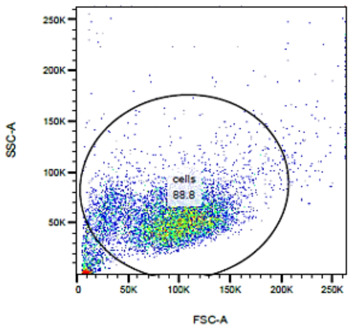

Acid Inh A3.fcs
Ungated
9836

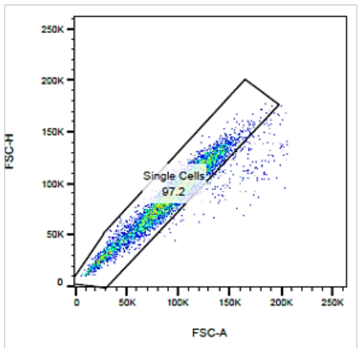

Acid Inh A3.fcs
cells
8732

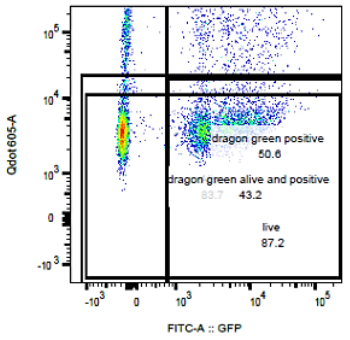

Acid Inh A3.fcs
Single Cells
8485

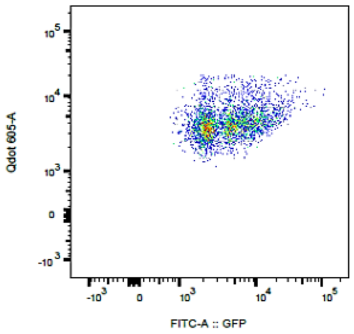

Acid Inh A3.fcs
dragon green alive and positive
3668

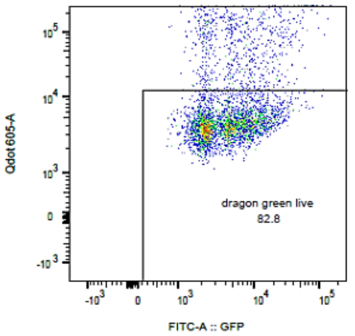

Acid Inh A3.fcs
dragon green positive
4294

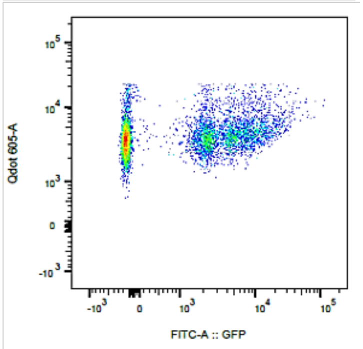

Acid Inh A3.fcs
live
7398

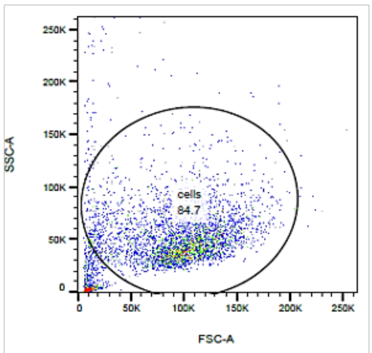

Dextran Inh A1.fcs
Ungated
4480

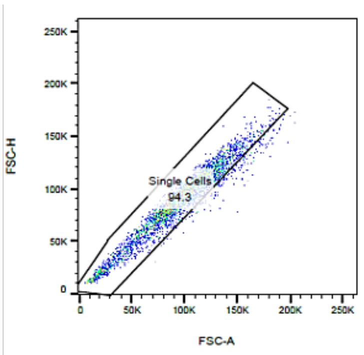

Dextran Inh A1.fcs
cells
3794

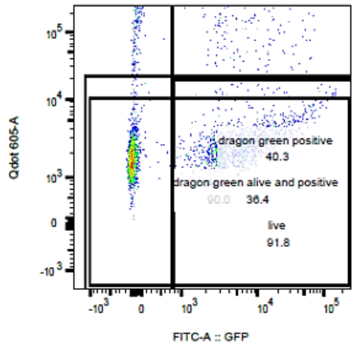

Dextran Inh A1.fcs
Single Cells
3578

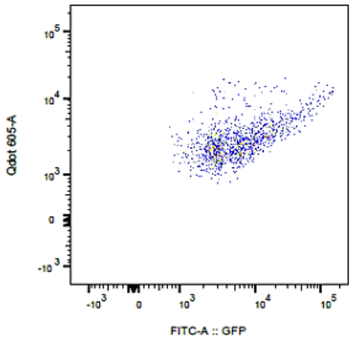

Dextran Inh A1.fcs
dragon green alive and positive
1304

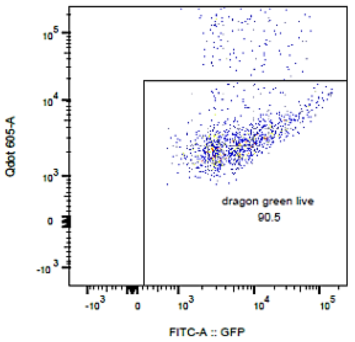

Dextran Inh A1.fcs
dragon green positive
1443

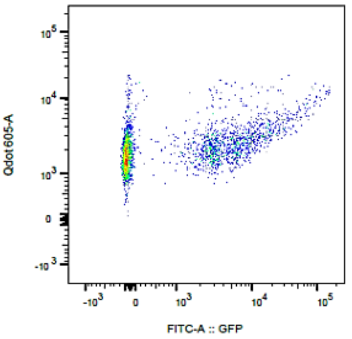

Dextran Inh A1.fcs
live
3286

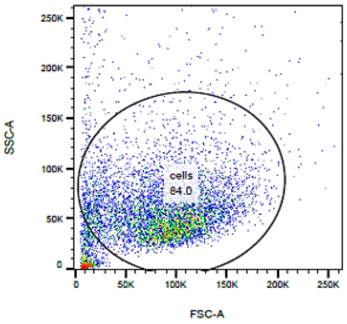

Dextran Inh A2.fcs
Ungated
8697

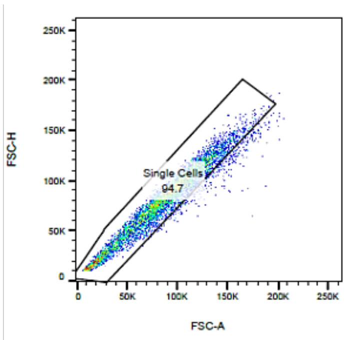

Dextran Inh A2.fcs
cells
7306

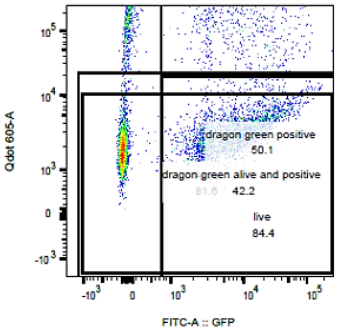

Dextran Inh A2.fcs
Single Cells
6920

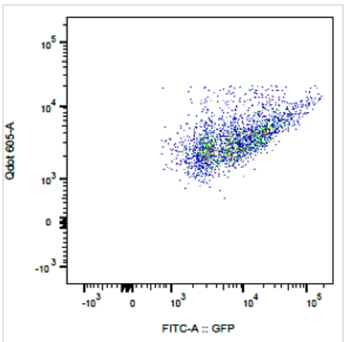

Dextran Inh A2.fcs
dragon green alive and positive
2921

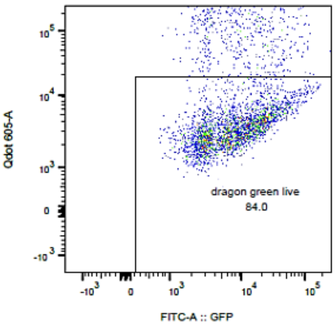

Dextran Inh A2.fcs
dragon green positive
3469

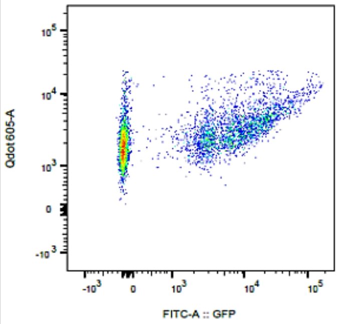

Dextran Inh A2.fcs
live
5841

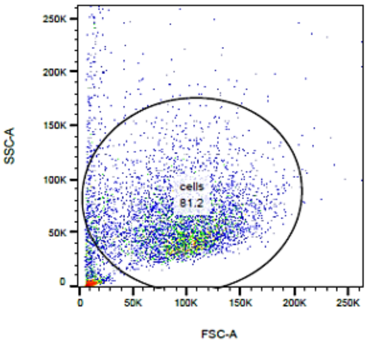

Dextran Inh A3.fcs
Ungated
6664

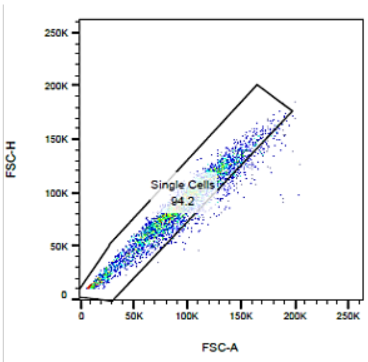

Dextran Inh A3.fcs
cells
5408

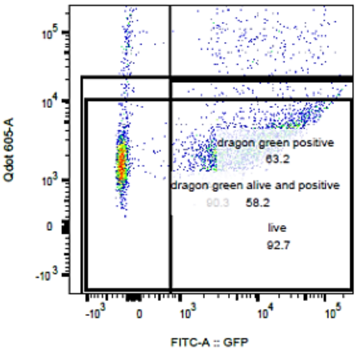

Dextran Inh A3.fcs
Single Cells
5093

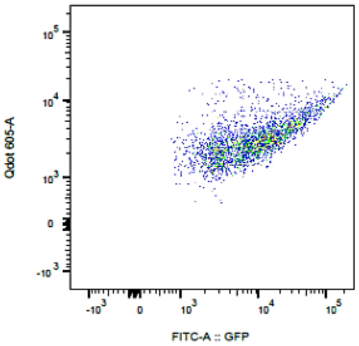

Dextran Inh A3.fcs
dragon green alive and positive
2966

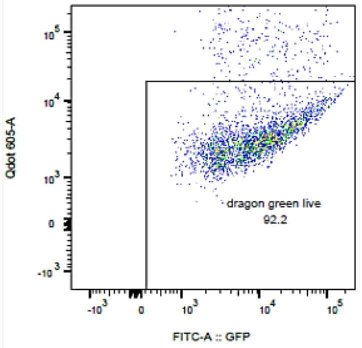

Dextran Inh A3.fcs
dragon green positive
3218

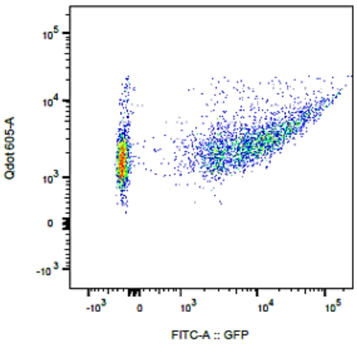

Dextran Inh A3.fcs
live
4720

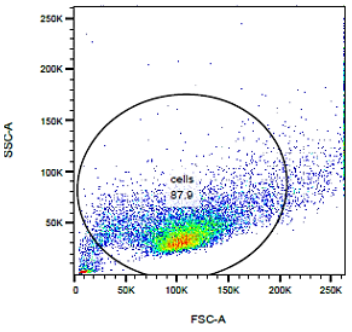

HeLa Inh A1.fcs
Ungated
13765

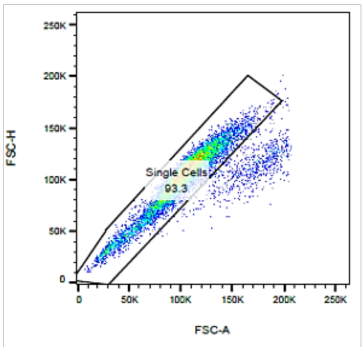

HeLa Inh A1.fcs
cells
12098

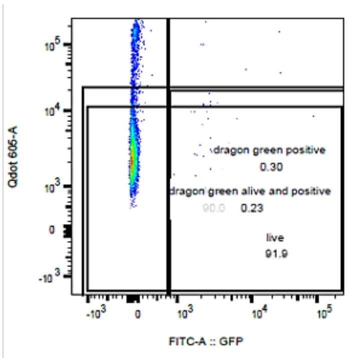

HeLa Inh A1.fcs
Single Cells
11290

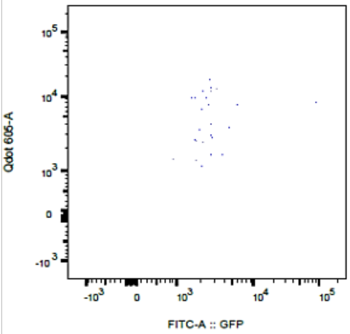

HeLa Inh A1.fcs
dragon green alive and positive
26.0

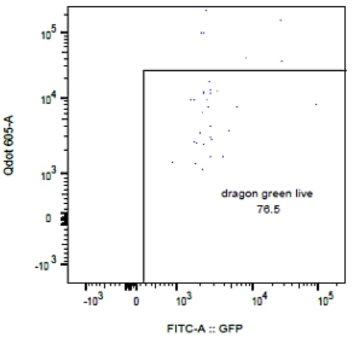

HeLa Inh A1.fcs
dragon green positive
34.0

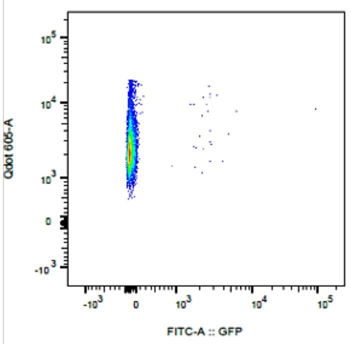

HeLa Inh A1.fcs
live
10372

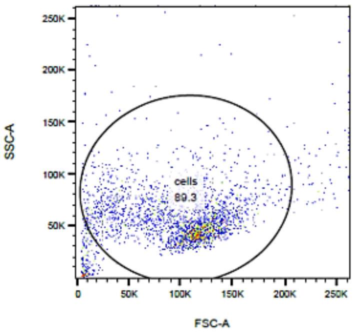

HeLa Inh A2.fcs
Ungated
2976

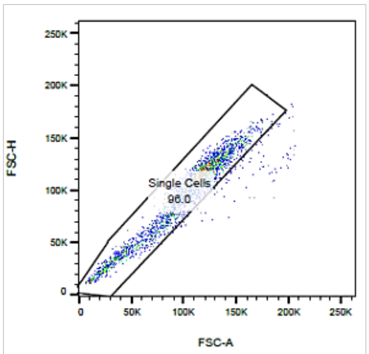

HeLa Inh A2.fcs
cells
2657

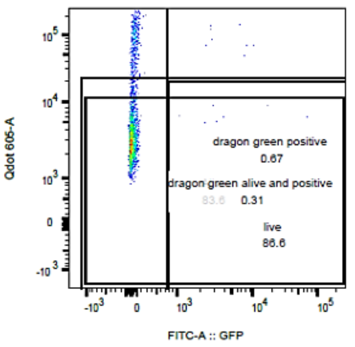

HeLa Inh A2.fcs
Single Cells
2550

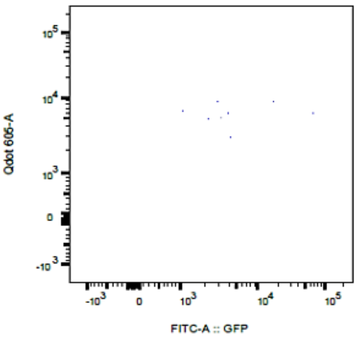

HeLa Inh A2.fcs
dragon green alive and positive
8.00

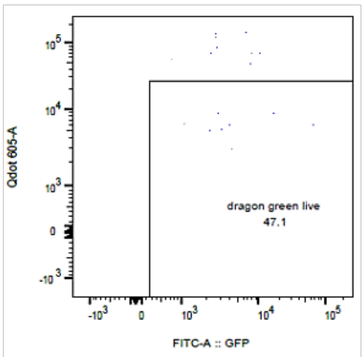

HeLa Inh A2.fcs
dragon green positive
17.0

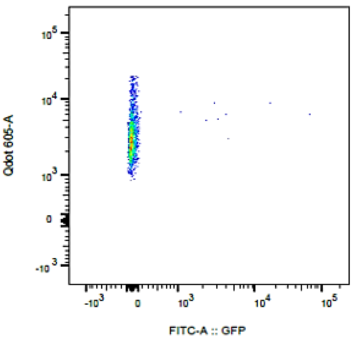

HeLa Inh A2.fcs
live
2209

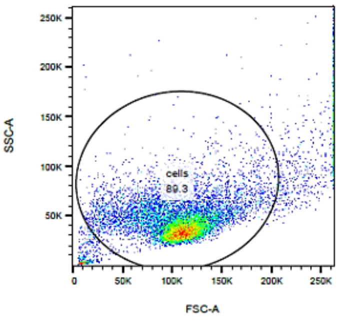

HeLa Inh A3.fcs
Ungated
13018

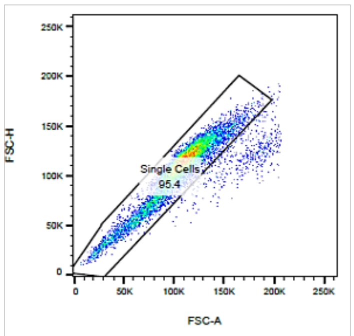

HeLa Inh A3.fcs
cells
11631

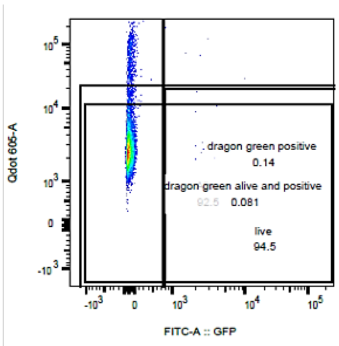

HeLa Inh A3.fcs
Single Cells
11101

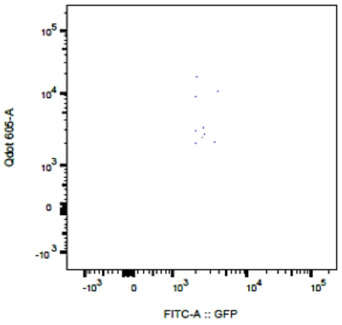

HeLa Inh A3.fcs
dragon green alive and positive
9.00

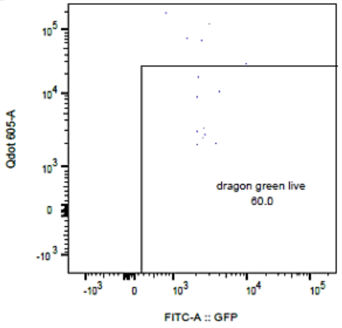

HeLa Inh A3.fcs
dragon green positive
15.0

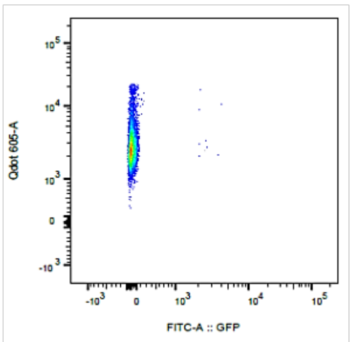

HeLa Inh A3.fcs
live
10493

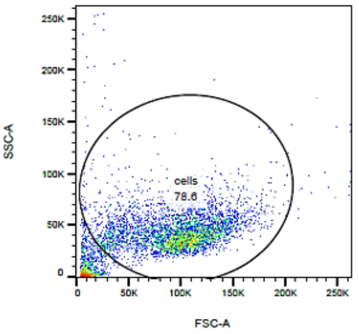

TTDDA Inh BE1.fcs
Ungated
6627

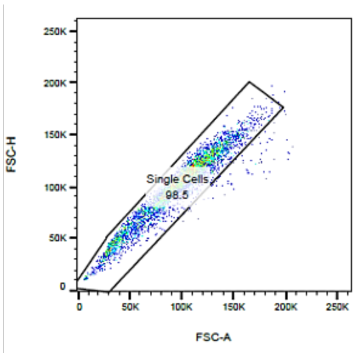

TTDDA Inh BE1.fcs
cells
5209

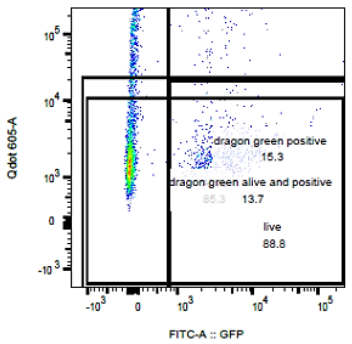

TTDDA Inh BE1.fcs
Single Cells
5129

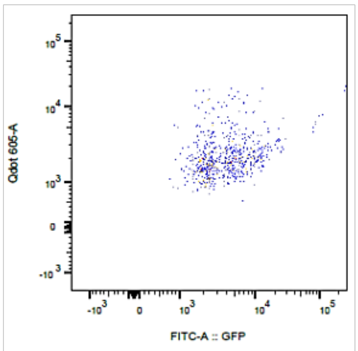

TTDDA Inh BE1.fcs
dragon green alive and positive
703

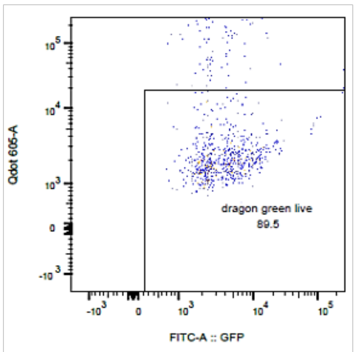

TTDDA Inh BE1.fcs
dragon green positive
787

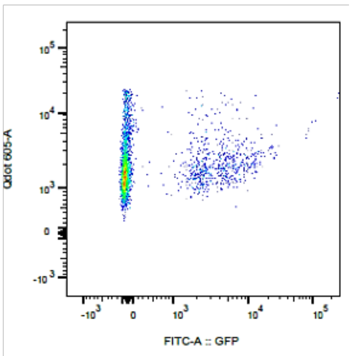

TTDDA Inh BE1.fcs
live
4554

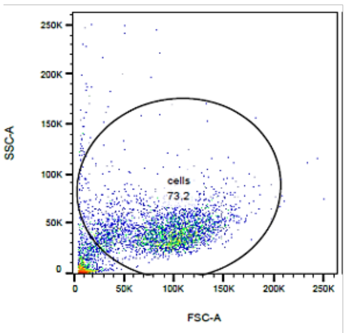

TTDDA Inh BE2.fcs
Ungated
5278

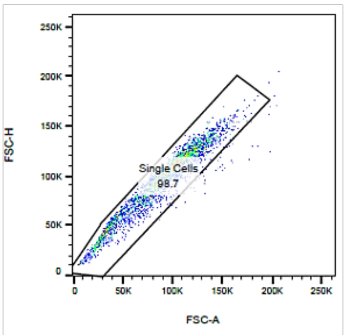

TTDDA Inh BE2.fcs
cells
3863

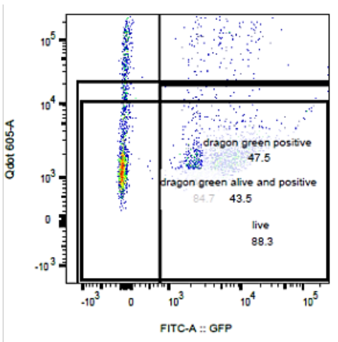

TTDDA Inh BE2.fcs
Single Cells
3814

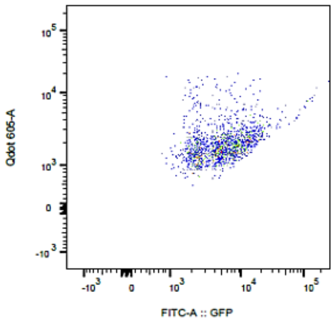

TTDDA Inh BE2.fcs
dragon green alive and positive
1659

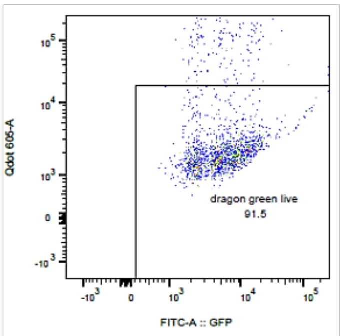

TTDDA Inh BE2.fcs
dragon green positive
1813

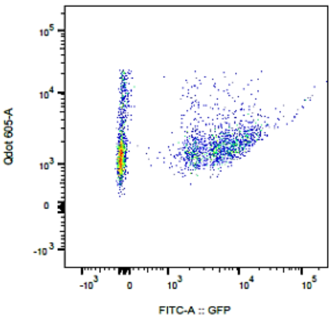

TTDDA Inh BE2.fcs
live
3369

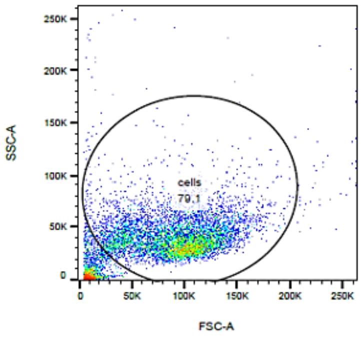

TTDDA Inh BE3.fcs
Ungated
10012

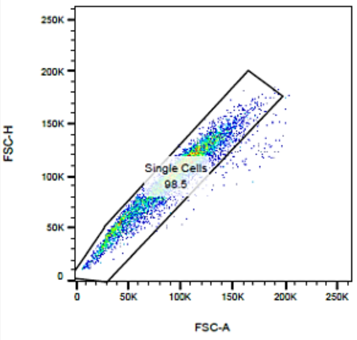

TTDDA Inh BE3.fcs
cells
7920

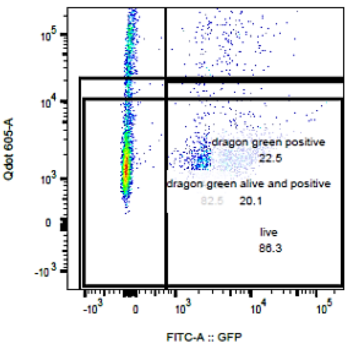

TTDDA Inh BE3.fcs
Single Cells
7800

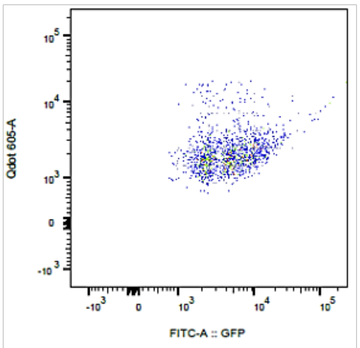

TTDDA Inh BE3.fcs
dragon green alive and positive
1566

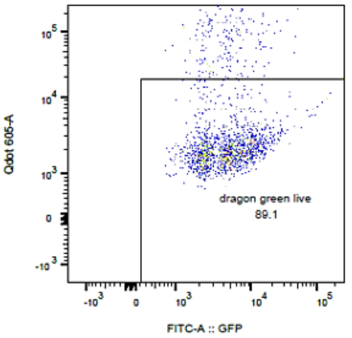

TTDDA Inh BE3.fcs
dragon green positive
1756

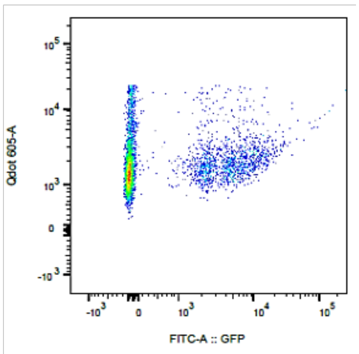

TTDDA Inh BE3.fcs
live
6734

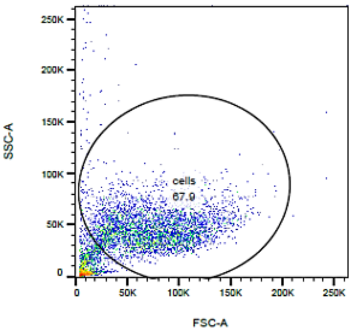

Lactose Inh BE1.fcs
Ungated
6042

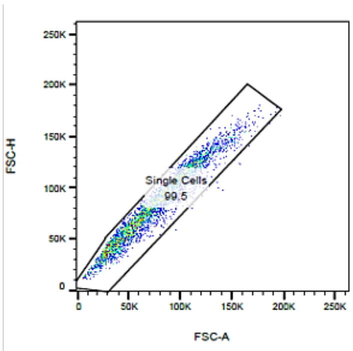

Lactose Inh BE1.fcs
cells
4100

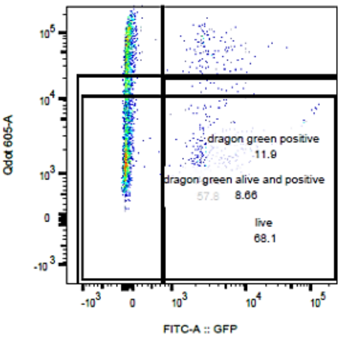

Lactose Inh BE1.fcs
Single Cells
4078

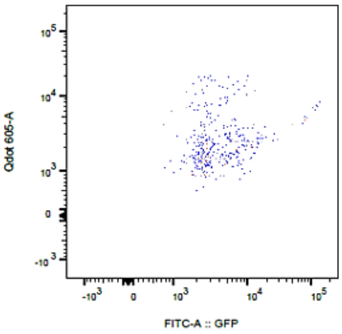

Lactose Inh BE1.fcs
dragon green alive and positive
353

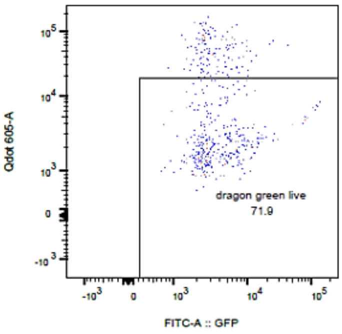

Lactose Inh BE1.fcs
dragon green positive
487

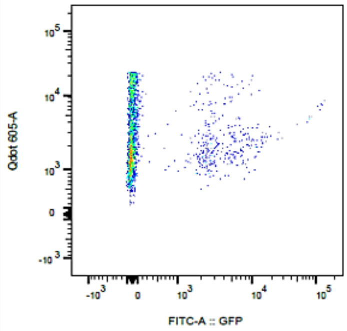

Lactose Inh BE1.fcs
live
2776

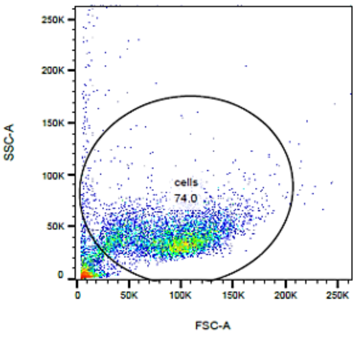

Lactose Inh BE2.fcs
Ungated
9695

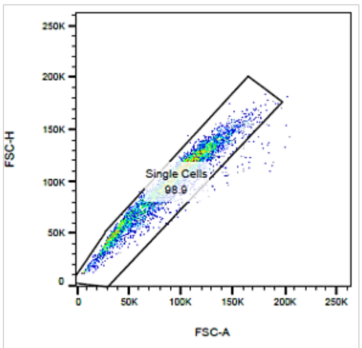

Lactose Inh BE2.fcs
cells
7179

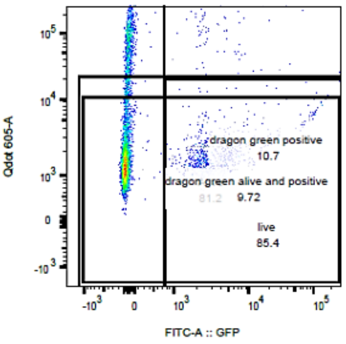

Lactose Inh BE2.fcs
Single Cells
7099

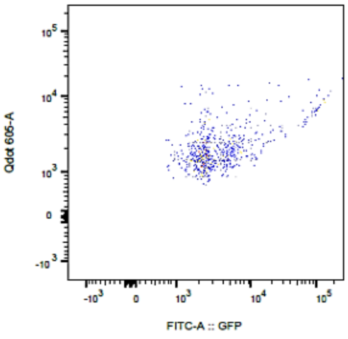

Lactose Inh BE2.fcs
dragon green alive and positive
690

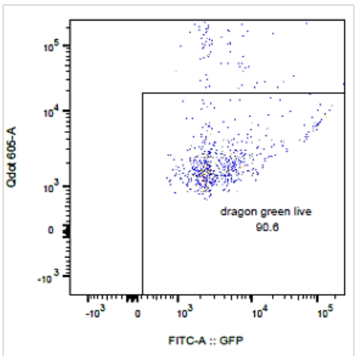

Lactose Inh BE2.fcs
dragon green positive
763

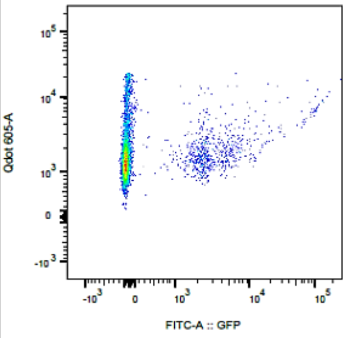

Lactose Inh BE2.fcs
live
6065

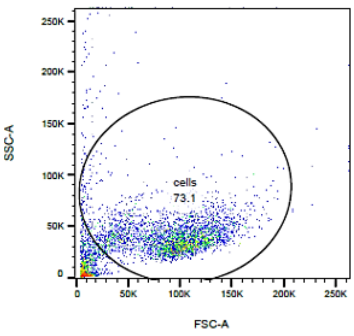

Lactose Inh BE3.fcs
Ungated
4690

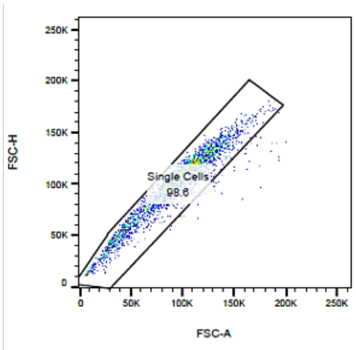

Lactose Inh BE3.fcs
cells
3429

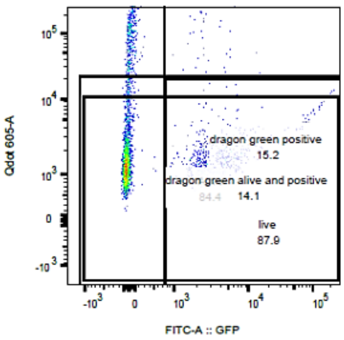

Lactose Inh BE3.fcs
Single Cells
3382

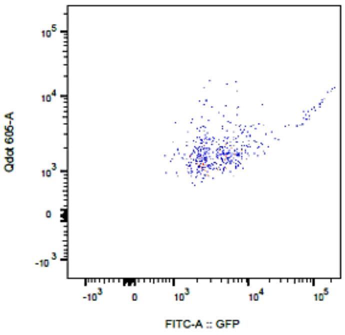

Lactose Inh BE3.fcs
dragon green alive and positive
476

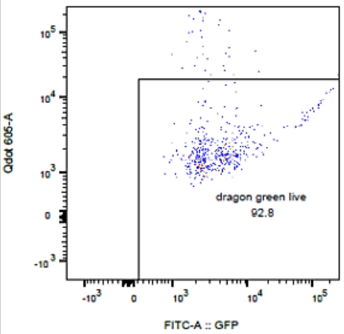

Lactose Inh BE3.fcs
dragon green positive
513

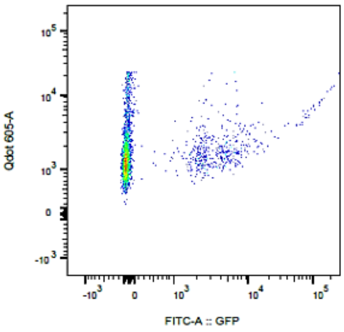

Lactose Inh BE3.fcs
live
2974

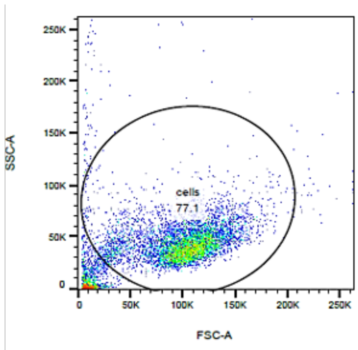

Acid Inh BE1.fcs
Ungated
8496

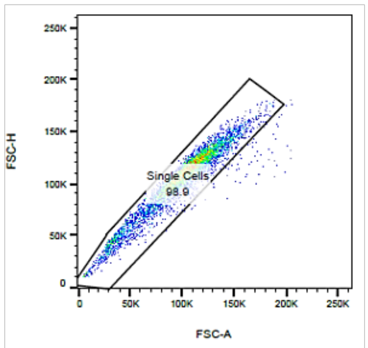

Acid Inh BE1.fcs
cells
6553

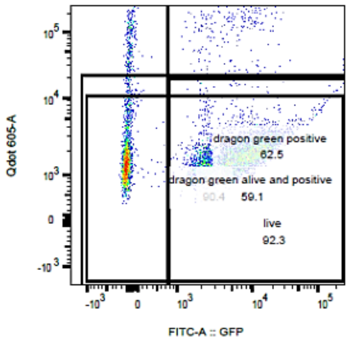

Acid Inh BE1.fcs
Single Cells
6484

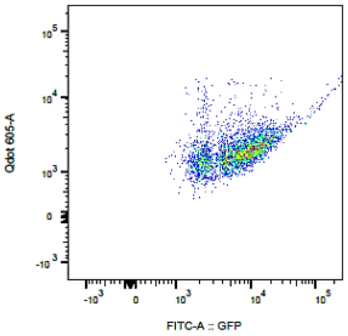

Acid Inh BE1.fcs
dragon green alive and positive
3832

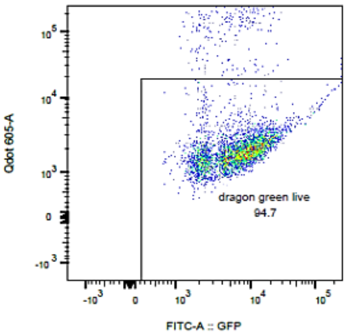

Acid Inh BE1.fcs
dragon green positive
4051

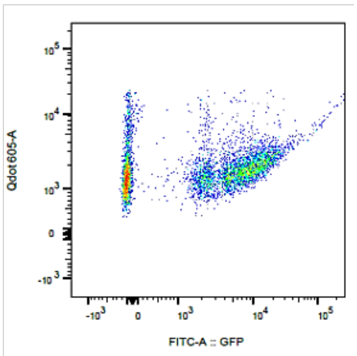

Acid Inh BE1.fcs
live
5986

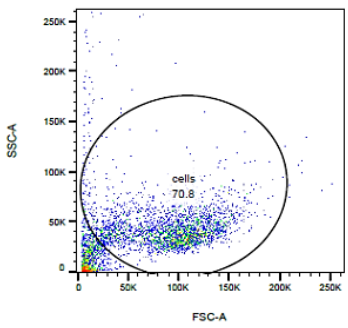

Acid Inh BE2.fcs
Ungated
4486

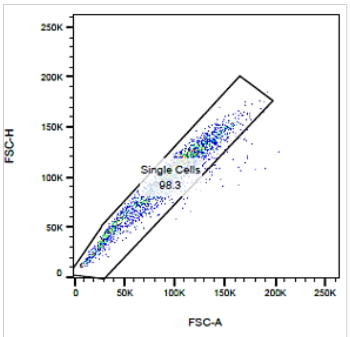

Acid Inh BE2.fcs
cells
3174

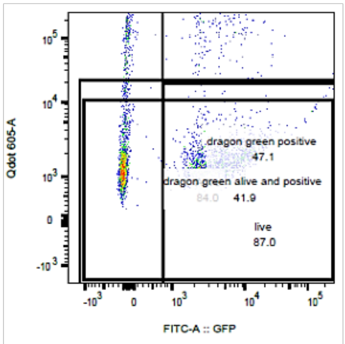

Acid Inh BE2.fcs
Single Cells
3119

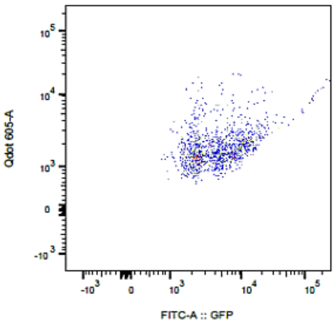

Acid Inh BE2.fcs
dragon green alive and positive
1306

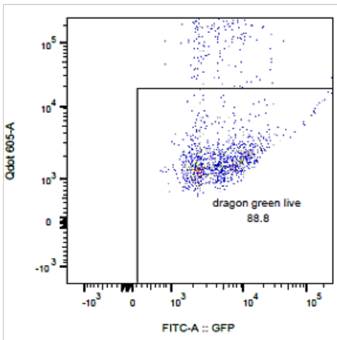

Acid Inh BE2.fcs
dragon green positive
1469

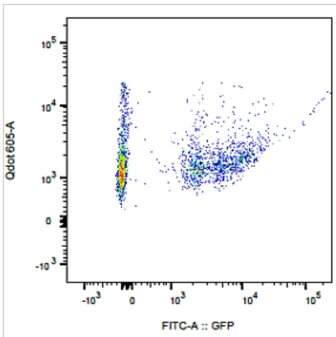

Acid Inh BE2.fcs
live
2712

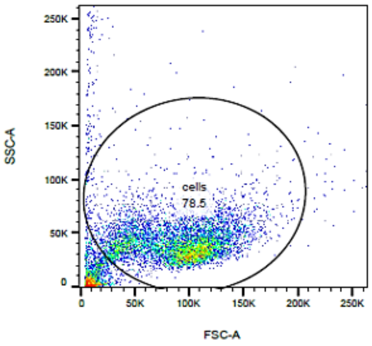

Acid Inh BE3.fcs
Ungated
9932

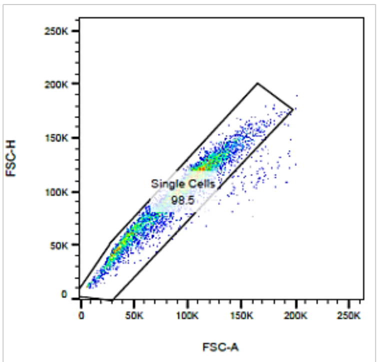

Acid Inh BE3.fcs
cells
7793

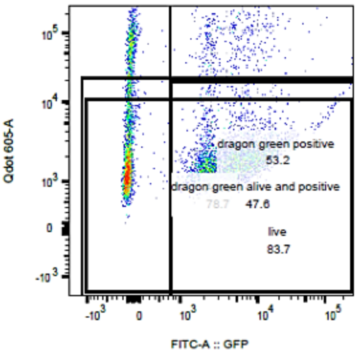

Acid Inh BE3.fcs
Single Cells
7679

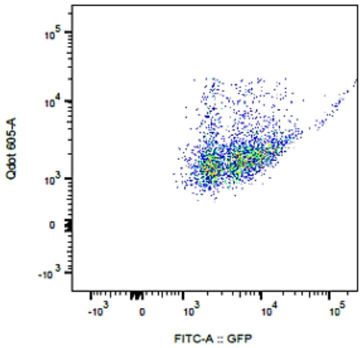

Acid Inh BE3.fcs
dragon green alive and positive
3659

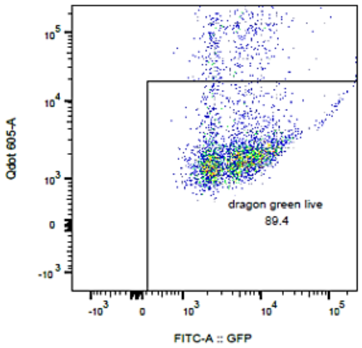

Acid Inh BE3.fcs
dragon green positive
4082

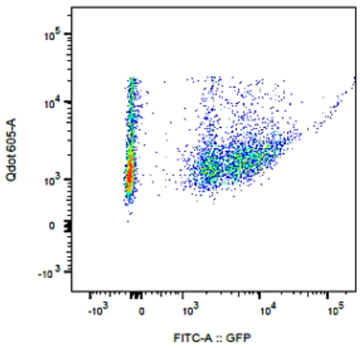

Acid Inh BE3.fcs
live
6424

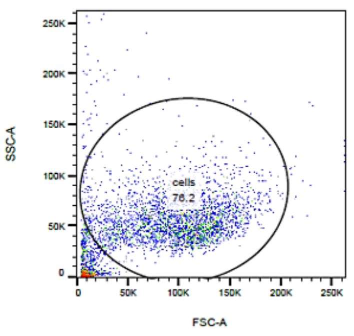

Dextran Inh BE1.fcs
Ungated
4576

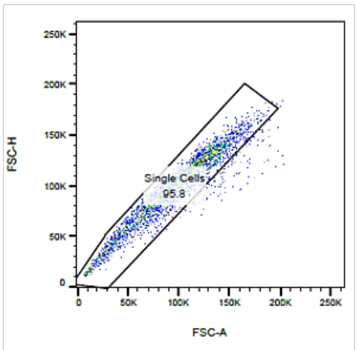

Dextran Inh BE1.fcs
cells
3485

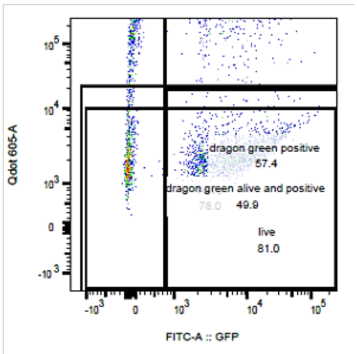

Dextran Inh BE1.fcs
Single Cells
3337

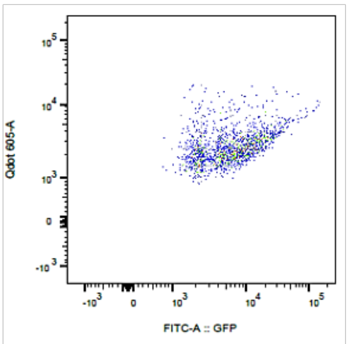

Dextran Inh BE1.fcs
dragon green alive and positive
1665

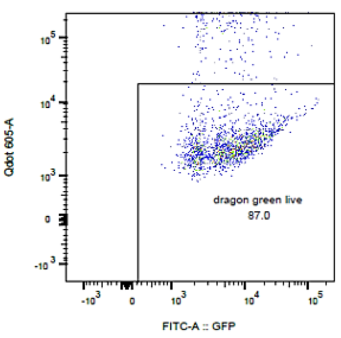

Dextran Inh BE1.fcs
dragon green positive
1914

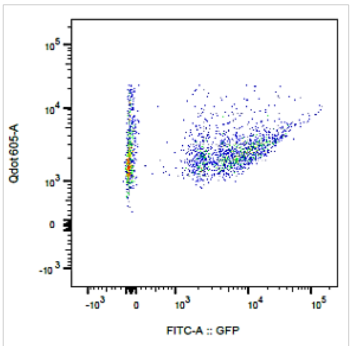

Dextran Inh BE1.fcs
live
2702

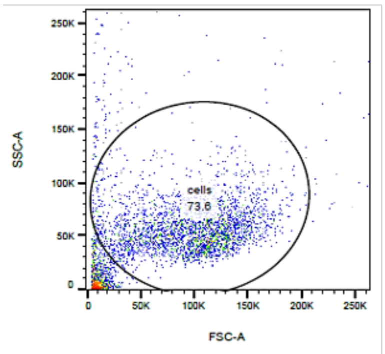

Dextran Inh BE2.fcs
Ungated
4647

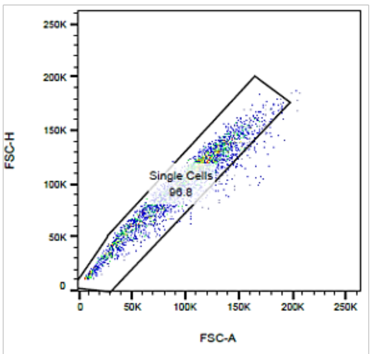

Dextran Inh BE2.fcs
cells
3422

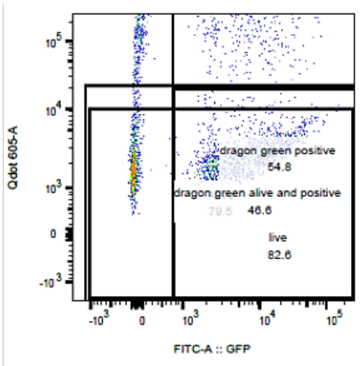

Dextran Inh BE2.fcs
Single Cells
3311

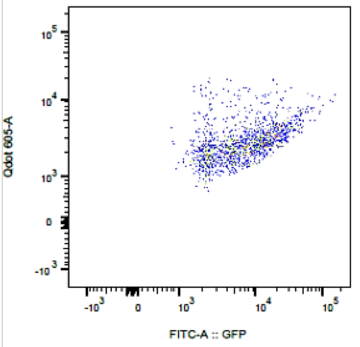

Dextran Inh BE2.fcs
dragon green alive and positive
1542

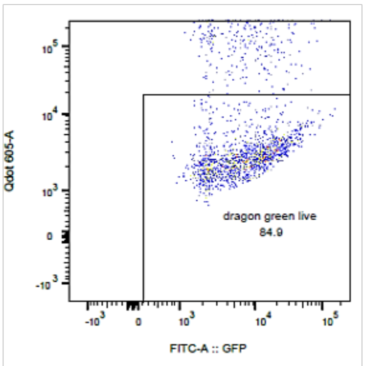

Dextran Inh BE2.fcs
dragon green positive
1816

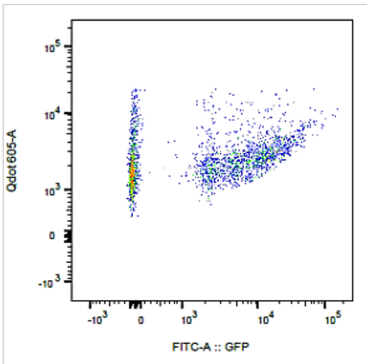

Dextran Inh BE2.fcs
live
2734

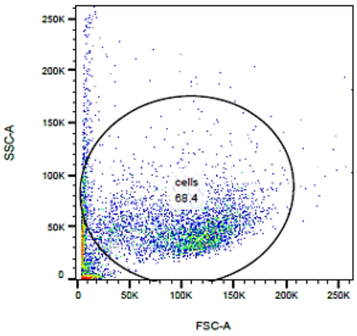

Dextran Inh BE3.fcs
Ungated
6816

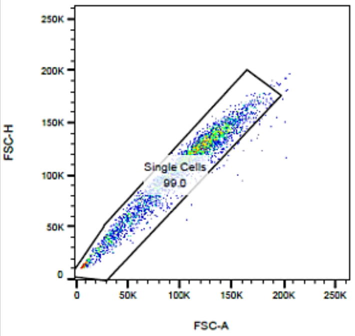

Dextran Inh BE3.fcs
cells
4663

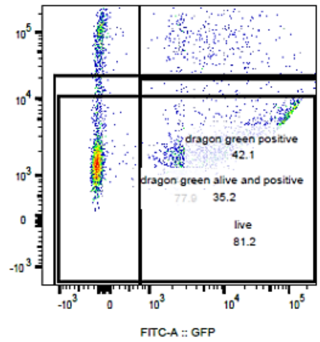

Dextran Inh BE3.fcs
Single Cells
4616

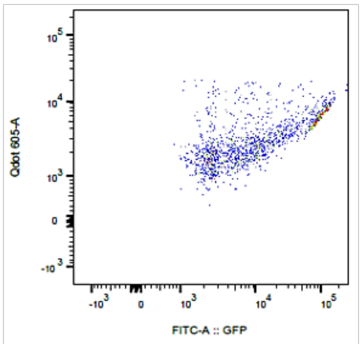

Dextran Inh BE3.fcs
dragon green alive and positive
1623

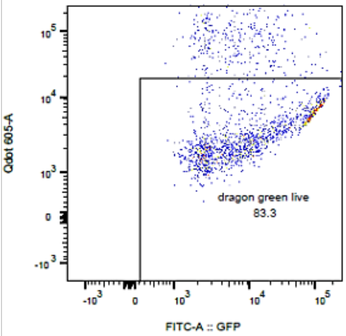

Dextran Inh BE3.fcs
dragon green positive
1943

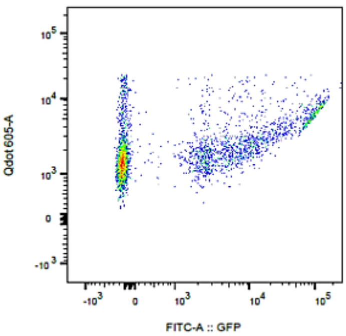

Dextran Inh BE3.fcs
live
3749

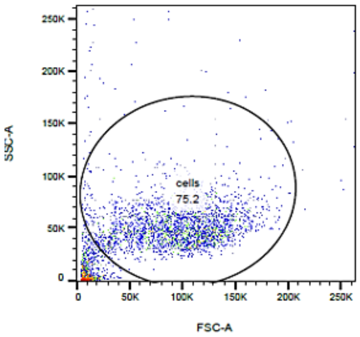

HeLa Inh BE1.fcs
Ungated
3675

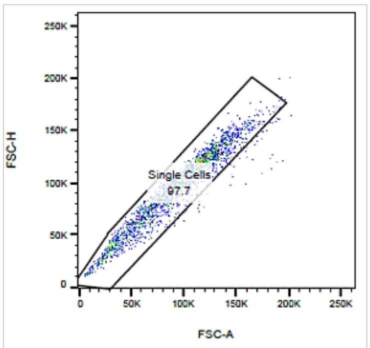

HeLa Inh BE1.fcs
cells
2762

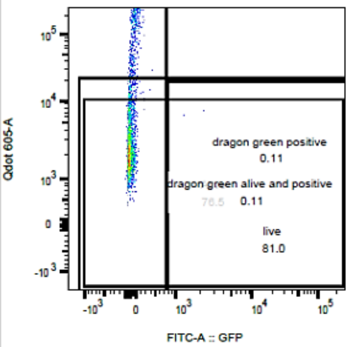

HeLa Inh BE1.fcs
Single Cells
2699

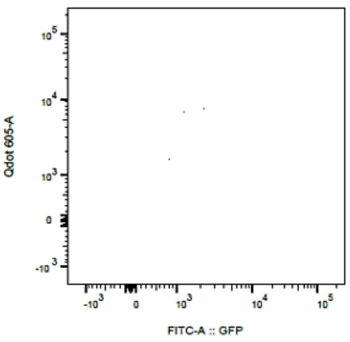

HeLa Inh BE1.fcs
dragon green alive and positive
3.00

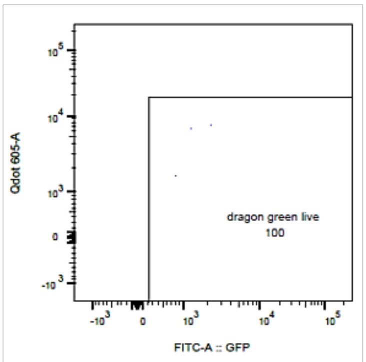

HeLa Inh BE1.fcs
dragon green positive
3.00

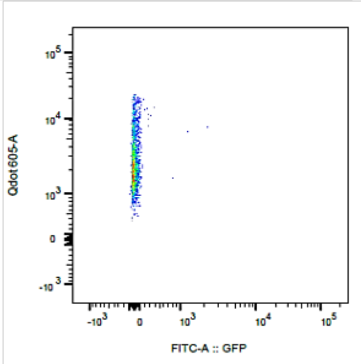

HeLa Inh BE1.fcs
live
2185

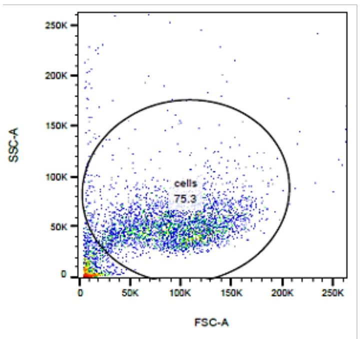

HeLa Inh BE2.fcs
Ungated
5638

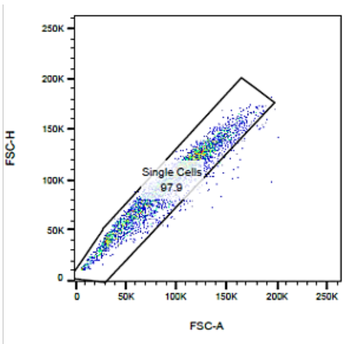

HeLa Inh BE2.fcs
cells
4243

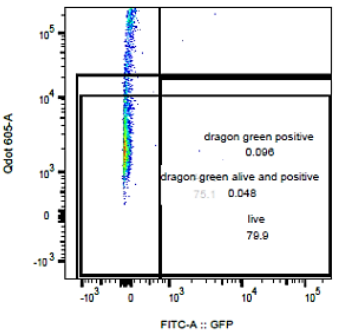

HeLa Inh BE2.fcs
Single Cells
4156

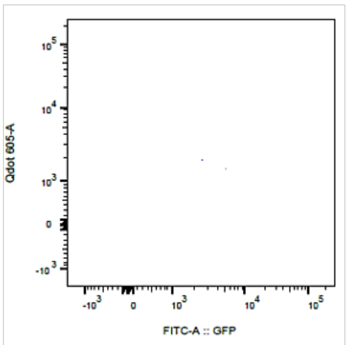

HeLa Inh BE2.fcs
dragon green alive and positive
2.00

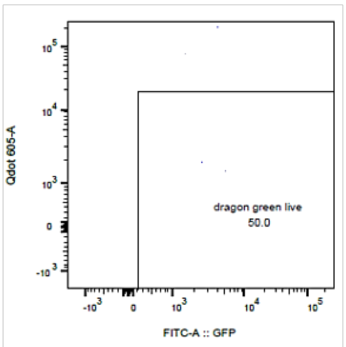

HeLa Inh BE2.fcs
dragon green positive
4.00

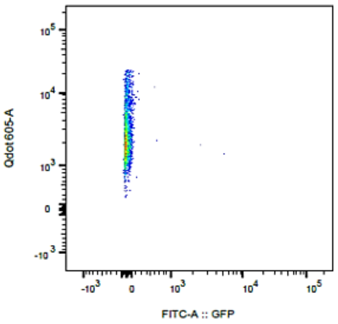

HeLa Inh BE2.fcs
live
3322

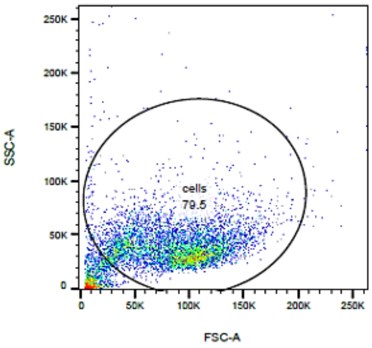

HeLa Inh BE3.fcs
Ungated
8558

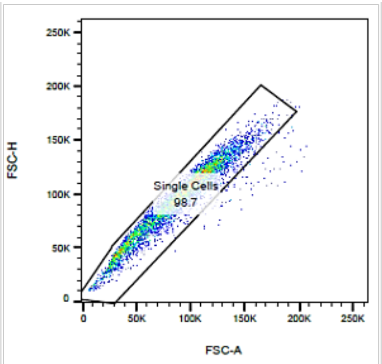

HeLa Inh BE3.fcs
cells
6802

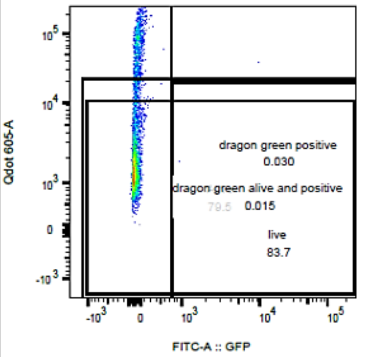

HeLa Inh BE3.fcs
Single Cells
6712

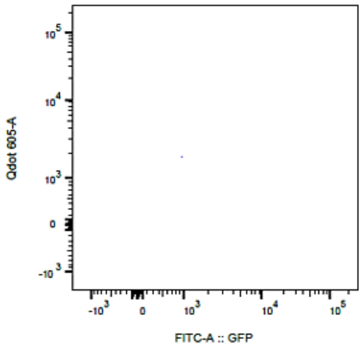

HeLa Inh BE3.fcs
dragon green alive and positive
1.00

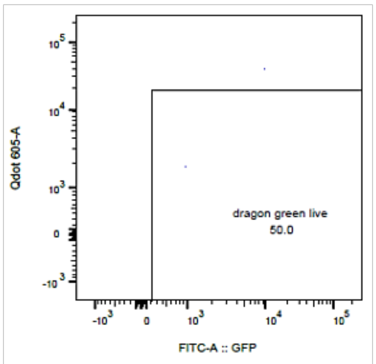

HeLa Inh BE3.fcs
dragon green positive
2.00

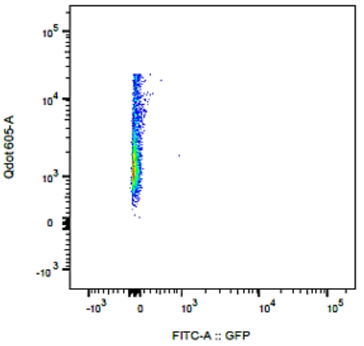

HeLa Inh BE3.fcs
live
5618